



MSc Thesis report

“Design, testing and verification of the DOT500 slip-joint support structure.”

T.P.J. Kamphuis

20-09-2016

The slip-joint connection

'Design, testing and verification of the
DOT500 slip-joint support structure.'

by

T.P.J. Kamphuis

to obtain the degree of Master of Science
at the Delft University of Technology,

to be defended publicly on Tuesday the 27th of September, 2016 at 9:30 AM.

Student number:	1528602
Project duration:	December 14, 2015 – 27 September, 2016
Thesis committee:	Prof. Dr. ir. A.V. Metrikine, TU Delft, committee chairman
	Dr. ir. M.C.M. Bakker, TU Delft, daily supervisor
	ir. J.S. Hoving, TU Delft
	Dr. ir. M.A.N. Hendriks, TU Delft
	Dr. ir. J. van der Tempel, DOT B.V., senior supervisor
	ir. R. Jorritsma, DOT B.V., daily supervisor

This thesis is confidential and cannot be made public until September 27, 2021.

Preface

This MSc thesis report describes the process of the past nine months in which a four meter diameter 'slip-joint' connection has been erected and tested on the Maasvlakte II. Needless to say, this has been a wonderful and thrilling experience, of which I appreciated every bit. Being able to witness the vibro-installation of a 125 tonne monopile and helping to build the first ever full-scale slip-joint measurement campaign has filled my soon-to-be engineering heart with joy.

First and foremost, I would like to thank Jan van der Tempel for providing me this unique opportunity and responsibility during the executing this project. Furthermore, I would like to thank the rest of my committee, including Andrei Metrikine, Maarten Bakker and Reinder Jorritsma for their time and very useful input during both individual and group meetings on my progress. Also, special thanks go out to Elbert Folmer and Robert Hasselaar, for their much appreciated support and effort during the preparation of the measurement campaign.

Love goes out to my girlfriend, Heleen, who has kindly checked the language of many pieces of the draft work and pressed the 'comma' button more times than I did during the writing process of this thesis. And finally, I would like to thank my fellow partners in misfortune, the Offshore Ponies, and above all encourage those still struggling; be brave and stay strong, it will end!

*T.P.J. Kamphuis
Delft, September 2016*

Abstract

During this MSc thesis project a full scale, real life, four meter diameter ‘slip-joint’ connection has been erected and tested on the Maasvlakte II in Rotterdam, connecting a fully operational wind turbine to its monopile foundation. Regularly, wind turbines are connected to the monopile foundation by means of a so-called transition piece. This additional piece of steel is grouted to the monopile and the wind turbine generator is subsequently bolted on top. In a slip-joint connection, a conical wind turbine tower is directly positioned over a conical top of a monopile. Hereby, a connection is created without the need for any bolts or welding, significantly reducing installation time and material costs. This is a welcome contribution to the 40% cost reduction, which is required in order to make offshore wind cost competitive with other forms of (non-renewable) electricity production.

DOT B.V. is a start-up company that has been founded with precisely that goal: make offshore wind more cost competitive by means of disruptive innovations. The current DOT500 project, a 500kW demonstration wind turbine, houses several innovations, including the slip-joint connection. Like grouted connections, static and dynamic loads from the wind turbine are transferred through contact forces between the surface contact of the two cones, mainly via friction. The structural integrity of this joint highly depends on the understanding of these load transfer mechanisms in order to quantify the effect of them in the design phase of the joint. To this end, scale experiments have been performed at the TU Delft in recent years. However, no full scale data is available up until now.

The focus of this research lies on the identification of the mechanical behaviour of the slip-joint connection, during installation and operation of the DOT500 wind turbine. Purposely, a monopile foundation was designed that allows the use of a slip-joint connection with the second hand wind turbine. A measurement campaign was organised and carried out, using several types of measuring equipment. The stresses in the slip-joint were monitored using multiple strain gauges along several circumferences over the height of the slip-joint. Additionally, several accelerometers and position sensors were installed to acquire information on the settlement of the slip-joint. Some first order models were created to predict the outcome of the measurements and acquire knowledge on the influence of the different parameters and their sensitivities on the joint.

The data of the measurements and models show promising results. The natural frequencies of the first bending modes of the total structure were identified and correspond reasonably well with the model. The settlement of the slip-joint, during installation and after a period of operation, was observed to be within predictable limits and approached a terminal level. The settlement after the installation, as a result of static self-weight only, amounts to 148 millimetres and an additional settlement of 17 millimetres was observed during the operational period of the wind turbine. The stresses within the joint, as a result of this settlement, are well below the yield stress of the material. Moreover, it is clear that in this specific case, the contact area within the slip-joint was far from optimal, as local compression was observed on the outer surface of the slip-joint. By using two purpose built cones, instead of a second hand tower, the contact area within the overlap could be improved, leading to a more desirable stress distribution.

Despite the suboptimal contact area within the slip-joint, the stresses as a result of operational loads from the wind turbine are well below the yield strength of the material and within the predictable limits. The additional hoop stresses in the wind turbine tower, as a result of a near-maximum thrust force of 70 kN, are in the order of magnitude of 20 MPa. Based on the knowledge gained from the calculations and measurements within this research, it can be concluded that the overlap length of the slip-joint connection can be shortened by at least 35% from the conventional target-level of $1.5D$ used for grouted connections to $1D$. It is recommended to continue monitoring the settlement and stresses within the slip-joint in the next phases of the DOT500 project, especially during operational intervals. This will increase the database of valuable measurement data, thereby increasing the validity of the models and understanding of the slip-joint connection. Hence, the slip-joint connection can be used in future offshore wind turbines with confidence.

List of Symbols

Greek Symbols

α	Angle of attack airfoil	[°]
α_{shear}	Wind shear profile parameter	[-]
$\bar{\lambda}_{buck}(EI, L_{buck})$	Reduced slenderness parameter	[-]
χ	Reduction factor for resistance to buckling due to normal force	[N]
δ_N	Slenderness reduction in buckling check	[-]
Δ_{air}	Air gap	[m]
δ_A	Axial displacement to reach calculated stretch of tower	[m]
δ_C	Circumference stretch of tower	[m]
δ_D	Diameter stretch of tower	[m]
δ_{mis}	Plate-to-plate misalignment	[m]
δ_o	(local) out of roundness	[m]
Δ_r	Blade element length	[m]
Δ_{storm}	Storm surge range	[m]
Δ_{tide}	Tidal range	[m]
ΔC	Deviation from specified circumference	[m]
$\Delta D_{T,MP}$	Expansion or contraction of the diameter of the cone due to settlement	[m]
Δz	Soil layer thickness	[m]
γ'	Submerged unit weight of soil	$\left[\frac{kN}{m^3}\right]$
γ_e	Environmental load safety factor	[-]
γ_g	Permanent load safety factor	[-]
γ_i	Arbitrary safety factor	[-]
γ_m	Arbitrary (material) resistance factor	[-]
γ_{tip}	Safety factor for blade tip clearance calculation	[m]
λ	Wave length	[m]
μ	Distributed tower mass	$\left[\frac{kg}{m}\right]$
μ_d	Dynamic, or sliding friction coefficient	[-]
μ_s	Static friction coefficient	[-]

ν	Poison ratio of steel	[—]
Ω	Angular rotation speed	$\left[\frac{rad}{s}\right]$
ω	Wave frequency	$\left[\frac{rad}{s}\right]$
ω_0	An arbitrary natural frequency	$\left[\frac{rad}{s}\right]$
$\omega_{0,d}$	An arbitrary damped natural frequency	$\left[\frac{rad}{s}\right]$
ω_{n1}	Radial natural frequency of the n-th mode	$\left[\frac{rad}{s}\right]$
ω_{n2}	Circumferential natural frequency of the n-th mode	$\left[\frac{rad}{s}\right]$
ϕ	Angle of internal friction of soil	[°]
ϕ_{buck}	Global buckling calculation parameter	[—]
ϕ_e	Angle of inflow	[°]
ϕ_{max}	Maximum pile rotation	[°]
ϕ_{seabed}	Pile rotation at seabed	[°]
ρ_{air}	Air density	$\left[\frac{kg}{m^3}\right]$
ρ_{steel}	Density of steel	$\left[\frac{kg}{m^3}\right]$
ρ_{water}	Density of sea water	$\left[\frac{kg}{m^3}\right]$
σ	Standard deviation	[%]
σ_{axial}	Resulting design stress from axial load	$\left[\frac{N}{m^2}\right]$
$\sigma_{hoop,a}$	Tangential, or hoop stress according to alternative proposed method	$\left[\frac{N}{m^2}\right]$
$\sigma_{hoop,l}$	Tangential, or hoop stress according to literature	$\left[\frac{N}{m^2}\right]$
σ_{hoop}	Tangential, or hoop stress	$\left[\frac{N}{m^2}\right]$
$\sigma_{m,NF3}$	Stress due to bending moment at strain gauge 'NF3'	[MPa]
σ_m	Resulting design stress due to bending moment	$\left[\frac{N}{m^2}\right]$
σ_{VM}	Resulting Von Mises equivalent stress	$\left[\frac{N}{m^2}\right]$
σ_{yield}	Yield stress of material	$\left[\frac{N}{m^2}\right]$
τ	Resulting design stress from shear force	$\left[\frac{N}{m^2}\right]$
θ_{cone}	Angle of cones	[°]
ζ	Wave amplitude	[m]
ζ_d	Damping ratio	[—]

ζ_{block}	Current blockage factor	[–]
ζ_{spread}	Wave spreading factor	[–]
Roman Symbols		
$\dot{u}(z)_{water}$	Total water particle acceleration	$[\frac{m}{s^2}]$
$\dot{u}(z)_{wave}$	Water particle acceleration due to waves	$[\frac{m}{s^2}]$
$\hat{u}(z)_{wave}$	Amplitude of water particle velocity due to waves	$[\frac{m}{s}]$
A	Factor to account for static or cyclic loading	[–]
a	Induction factor	[–]
A_{disk}	Area of the actuator disk	$[m^2]$
$A_{MP}(D, t)$	Area of steel in cross section	$[m^2]$
a_{NF}	Natural frequency calculation constant	[–]
A_{rotor}	Area of the rotor	$[m^2]$
C_1	Soil coefficient 1	[–]
C_2	Soil coefficient 2	[–]
C_3	Soil coefficient 3	[–]
C_d	Drag coefficient	[–]
$C_d(\alpha)$	Drag coefficient of air foil as function of angle of attack	[–]
$C_l(\alpha)$	Lift coefficient of air foil as function of angle of attack	[–]
C_p	Power coefficient of wind turbine	[–]
C_{actual}	Actual circumference of the tower	$[m]$
c_e	Chord length of blade element e	$[m]$
C_m	Inertia coefficient	[–]
$C_{specified}$	Specified circumference of the tower	$[m]$
C_{tower}	Circumference of the tower	$[m]$
D	Calculation constant	$[Nm]$
$D(z)$	Diameter of tower or monopile as function of height	$[m]$
$D(z)_{T,MP}$	Diameter at height z of the cone of tower or monopile	$[m]$
D_t	Decommissioning and other costs in year t	$[€]$
D_{av}	Average outer diameter of wind turbine tower	$[m]$
D_f	Total fatigue damage	[–]
D_{max}	Maximum diameter	$[m]$
D_{min}	Minimal diameter	$[m]$

D_{MP}	Monopile outer diameter	[m]
D_{nom}	Specified or nominal diameter	[m]
$D_{pile}(z)$	Cylinder diameter at depth z	[m]
$D_{t,i}$	Tower inner diameter	[m]
$D_{t,slip}$	Tower diameter at top of the slip-joint	[m]
d_{water}	Water depth	[m]
E	Environmental loading	[-]
E_f	Total energy to overcome friction	[J]
E_k	Kinetic energy	[J]
E_p	Potential energy	[J]
E_t	Electrical energy generated in year t	[€]
E_{cur}	Current load	[-]
E_{ice}	Ice load	[-]
E_{tower}	Tower elasticity modulus	[Pa]
E_{water}	Water level	[-]
E_{wave}	Wave load	[-]
E_{wind}	Wind load	[-]
EI	Tower flexural rigidity	[Nm ²]
$EI(D, t)$	Bending stiffness	[Nm ²]
F_D	Drag force on blade element	[N]
F_L	Lift force on blade element	[N]
F_R	Radial force	[N]
f_s	Shaft friction during cone penetration test (CPT)	[Pa]
F_z	Vertical downward force	[N]
$f_{1,fa}$	First natural frequency of wind turbine system fore-aft	[Hz]
$f_{1,ss}$	First natural frequency of wind turbine system side-side	[Hz]
F_{axial}	Axial force on rotor, or thrust force	[N]
$f_d(z)$	Drag force on a cylinder per unit length	[$\frac{N}{m}$]
$F_{f,z}$	Vertical component of the friction force	[N]
F_f	Friction force	[N]
F_{hydro}	Total horizontal hydrodynamic load on structure	[N]
$f_i(z)$	Inertia force on a cylinder per unit length	[$\frac{N}{m}$]

$f_{Morison}(z)$	Hydrodynamic load on a cylinder per unit length	$\left[\frac{N}{m}\right]$
F_M	Summated contact forces due to a moment	$[N]$
$F_{N,z}$	Vertical component of the normal force	$[N]$
$f_{nat,1}$	First natural frequency of wind turbine system	$[Hz]$
F_N	Normal force	$[N]$
F_{wind}	Total wind drag force	$[N]$
$F_{x,e}$	Total force in x-direction on element e	$[N]$
f_y	Factored yield strength	$\left[\frac{N}{m^2}\right]$
G	Gust factor for duration t	$[-]$
G	Permanent loads	$[N]$
g	Gravitational acceleration	$\left[\frac{m}{s^2}\right]$
$G(t)$	Gust factor	$[-]$
$G_{MP,tower}$	Permanent load of monopile or wind turbine tower	$[N]$
H_s	Significant wave height	$[m]$
H_{design}	Design wave height	$[m]$
h_{drop}	Drop height of slip-joint	$[m]$
h_{foc}	First point of contact during settlement	$[m]$
$h_{overlap,a}$	Minimal slip-joint overlap length using alternative method	$[m]$
$h_{overlap,l}$	Minimal slip-joint overlap length using literature method	$[m]$
$h_{overlap}$	Slip-joint overlap length	$[m]$
$H_{s,50}$	50 year return period significant wave height	$[m]$
$H_{s,5}$	5 year return period significant wave height	$[m]$
h_{total}	Total height of upper cone hanging over lower cone	$[m]$
h_{to}	Target overlap length	$[m]$
H_{wave}	Arbitrary wave height	$[m]$
I	Tower area moment of inertia	$[m^4]$
i_r	Reflection coefficient	$[-]$
I_t	Investment costs in year t	$[€]$
i_t	Transmission coefficient	$[-]$
$I_{w,t}$	Wind turbulence intensity	$[%]$
K	Calculation constant	$\left[\frac{N}{m}\right]$
k	Initial modulus of subgrade reaction	$\left[\frac{MPa}{m}\right]$

K_1	Stiffness factor 1	$\left[\frac{N}{m}\right]$
K_2	Stiffness factor 2	$\left[\frac{N}{m}\right]$
k_l	Translational spring constant	$\left[\frac{N}{m}\right]$
k_r	Rotational spring constant	$\left[\frac{Nm}{rad}\right]$
k_w	Wave number	$[m^{-1}]$
L	Schematised wind turbine length	$[m]$
$l(z)$	Distance from height z to arbitrary point x	$[m]$
L_{buck}	Buckling length of structure	$[m]$
L_{NF3}	Length between rotor and 'NF3' strain gauge	$[m]$
L_{COE}	Levelized cost of energy	$\left[\frac{\text{€}}{kWh}\right]$
M_t	Operation and Maintenance costs in year t	$[€]$
m_{cone}	Mass of upper cone	$[kg]$
m_{growth}	Marine growth	$[m]$
M_{NF3}	Bending moment at strain gauge 'NF3'	$[kNm]$
m_{other}	Any other contributing mass	$[N]$
$m_{platform}$	Platform mass	$[N]$
M_{rd}	Resistance to buckling due to overturning moment	$[Nm]$
m_{top}	Top mass of the wind turbine	$[kg]$
m_{tower}	Total mass of schematised wind turbine tower	$[m]$
$M_{x,aero}$	Total moment at arbitrary point x resulting from aerodynamic forces on rotor	$[Nm]$
$M_{x,hydro}$	Total moment resulting from hydrodynamic load on structure	$[Nm]$
$M_{x,wind}$	Total moment resulting from wind drag force at arbitrary point x	$[Nm]$
$M_{y,ed}$	Governing overturning moment	$[Nm]$
n	Vibration mode n	$[-]$
n_e	Expected lifetime of structure	$[years]$
N_i	Maximum number of cycles at stress range i	$[-]$
n_i	Actual number of cycles at stress range i	$[-]$
N_{blades}	Number of blades	$[-]$
N_{ed}	Governing normal force	$[N]$
N_{rd}	Resistance to buckling due to normal force	$[N]$
O	Ovality of arbitrary tower section	$[\%]$

P	Pressure	$\left[\frac{N}{m^2} \right]$
$p(X)$	Lateral soil reaction as function of depth X	$\left[\frac{kN}{m} \right]$
P_w	Produced power of the wind turbine	$[W]$
P_{max}	Maximum contact pressure	$\left[\frac{N}{m^2} \right]$
$p_u(X)$	Ultimate lateral soil resistance at depth X	$\left[\frac{kN}{m} \right]$
$P_{w,max}$	Maximum available power in the wind at actuator disk	$[W]$
$q(z)_{wind}$	Wind drag force at height z	$\left[\frac{N}{m} \right]$
q_t	Cone resistance during cone penetration test (CPT)	$[Pa]$
q_{hydro}	Distributed hydrodynamic load	$\left[\frac{N}{m} \right]$
$q_{hydro}(z)$	Total hydrodynamic force on a cylinder per unit length	$\left[\frac{N}{m} \right]$
q_{wind}	Distributed wind load	$\left[\frac{N}{m} \right]$
r	Discount rate	$[-]$
r_{blade}	Distance from root to blade element	$[m]$
R_d	Design resistance	$[-]$
R_k	Characteristic resistance	$[-]$
R_{mean}	Mean radius of cone	$[m]$
R_{rotor}	Rotor blade radius	$[m]$
S_i	Stress range i	$[-]$
S_d	Design load	$[-]$
S_k	Characteristic load	$[-]$
T	Thrust force of the rotor	$[N]$
t	Time	$[s]$
$t(z)$	Wall thickness of tower or monopile as function of height	$[m]$
T_p	Peak wave period	$[s]$
t_y	year number	$[-]$
T_z	Mean zero crossing period	$[s]$
t_{MP}	Monopile wall thickness	$[m]$
t_M	Layer thickness of Micanti	$[m]$
$t_{t,MP}$	Tower or monopile wall thickness	$[m]$
t_{tower}	Tower wall thickness	$[m]$
t_{wall}	Average wall thickness of wind turbine tower	$[m]$

$u(x, t, z)_{wave}$	Water particle velocity due to waves	$[\frac{m}{s}]$
$u(z)_{cur}$	Current speed at depth z	$[\frac{m}{s}]$
$u(z)_{water}$	Total water particle velocity	$[\frac{m}{s}]$
u_M	Overtuning moment contribution in buckling check	$[-]$
u_N	Normal force contribution in buckling check	$[-]$
$u_{0,cur}$	Arbitrary stationary current speed at sea surface	$[\frac{m}{s}]$
U_r	Reference wind speed at height r	$[\frac{m}{s}]$
u_{seabed}	Pile deflection at seabed	$[m]$
u_{toe}	Pile toe kick foundation	$[m]$
UC	Unity check	$[-]$
$V(z)$	Wind speed at height z	$[\frac{m}{s}]$
V_0	Undisturbed wind velocity	$[\frac{m}{s}]$
v_{cone}	Maximum velocity of cone during controlled dropping	$[\frac{m}{s}]$
V_{disk}	Wind velocity at actuator disk	$[\frac{m}{s}]$
V_{ed}	Governing base shear	$[N]$
$V_{gust,N}(z)$	Extreme wind speed at height z with return period N	$[\frac{m}{s}]$
V_{mean}	Arbitrary mean wind speed	$[\frac{m}{s}]$
$V_N(z)$	Mean wind speed at height z with return period N	$[\frac{m}{s}]$
V_{rel}	Relative velocity experienced by blade element	$[\frac{m}{s}]$
V_{rot}	Rotational velocity of blade element	$[\frac{m}{s}]$
V_{wind}	Wind speed	$[\frac{m}{s}]$
$W_{MP}(D, t)$	Section modulus of steel	$[m^3]$
W_{NF3}	Section modulus of tower at position of strain gauge 'NF3'	$[m^3]$
X	Depth below soil surface	$[m]$
x	Position	$[m]$
X_R	Reference depth	$[m]$
y	Lateral soil displacement	$[m]$
z	Height z	$[m]$
z_r	Reference height	$[m]$
z_0	Roughness parameter, typically 0.0001 for open seas	$[m]$
z_{hub}	Hub height	$[m + LAT]$
$z_{platform}$	Platform clearance level with sea level	$[m + LAT]$

z_{settle}	Settlement of slip-joint in z-direction	[m]
$z_{tipclearance}$	Blade tip clearance with platform	[m]
z_{tip}	Blade tip height	[m + LAT]
z_{toe}	Penetration depth	[m + LAT]

List of Figures

1.1	LCoE for different electricity sources	2
1.2	Definitions typical offshore wind turbine	3
1.3	DOT drive train system now (left) and in the future (right)	5
1.4	DOT concept for a typical wind farm	5
1.5	DOT500 project	6
1.6	The slip-joint connection	7
1.7	Thesis approach	8
2.1	Design cycle monopile DOT turbine	13
2.2	Different data acquisition methods	14
2.3	Common data processing techniques	15
2.4	Offshore wind turbine design elevations (left) and clarification of platform clearance level (right)	16
2.5	One degree-of-freedom mass-spring-damper system	17
2.6	Three response regimes. From left to right: Quasi-static, resonance, inertia dominated. Solid blue line: excitation, dashed red line: response.	18
2.7	Wind turbine schematisation	19
2.8	Frequency Assessment Diagram	20
2.9	Four main loads acting on a typical wind turbine	21
2.10	Logarithmic and shear wind profile extrapolation	22
2.11	Momentum and Blade element theory [43]	24
2.12	From time series to spectrum spectrum notation [22]	26
2.13	Sea surface elevation (left) and accompanying wave spectrum (right) [43]	26
2.14	Wave Kinematics by Airy wave theory (left) and Wheeler stretching (right)	27
2.15	Characteristic loads to design load with different load cases	30
2.16	Modelling of soil-structure interaction by means of (non-linear) springs	31
2.17	Design graphs to determine C-coefficients and k-value	32
2.18	Pile displacement due to design load	33
2.19	Typical SN-curves for structural steel	35
3.1	Slip-joint connected offshore wind turbine	37
3.2	Vertical force equilibrium slip-joint	38
3.3	Hoop stress as result uniform pressure due to radial force	39
3.4	Internal forces resulting from moment on slip-joint	41
3.5	Internal forces resulting from moment on slip-joint	42
3.6	Individual plate sections make up the total monopile	44
3.7	Different fabrication tolerances relevant for slip-joint design [13]	44
4.1	Overview of different structural components of the DOT500	49
4.2	Ovality	51
4.3	Schematic overview of modular monopile	52
4.4	Schematic overview of design heights DOT500 and DOT3000 offshore	53
4.5	Frequency calculation and resulting spectrum of the DOT500 onshore wind turbine	54
4.6	Governing load case and resulting strength and stability checks	55
4.7	Different inner cone angles slip-joint	56
4.8	Governing load case for slip-joint design; DOT500 offshore conditions	56
4.9	Schematic overview of DOT500 test site at Maasvlakte II	57
4.10	Overview of DOT500 test site at Maasvlakte II	58

5.1	Fourier transformation from time- to frequency domain	60
5.2	Schematic overview placement strain gauges and accelerometer	62
5.3	Natural frequency sensor overview	62
5.4	Schematic overview of decay in acceleration signal	63
5.5	Schematic overview of settlement sensors	64
5.6	Settlement sensor overview	64
5.7	Schematic overview of placement of strain sensors	67
5.8	Strain distribution sensor overview	67
5.9	Overview of sensors on (actual) wind turbine structure	70
5.10	Schematic overview of the measurement instrument on the wind turbine tower	70
6.1	Schematic overview of foundation model for natural frequency	72
6.2	Schematic overview of discretisation steps in model	73
6.3	Graphical illustration of settlement parameters	75
6.4	Schematic overview of settlement model	75
6.5	Stress distributions within slip-joint for base case and increased friction coefficient	79
6.6	Schematic overview of FEM for non-uniform pressure application	80
6.7	Different load cases simulating non-uniformly applied pressure	80
6.8	Schematic overview of FEM for oval tower simulation	81
6.9	Results of two FEM calculations	81
7.1	Installation phases of day one, the 6th of May	84
7.2	Installation phases of day two, the 18th of May	84
7.3	Installation phases of day two, the 18th of May	85
7.4	Settlement of slip-joint day two (left) and numerically approximated settlement velocity (right)	87
7.5	Total settlement of the slip-joint and approximated settlement velocity over the days	88
7.6	Settlement definitions	88
7.7	Schematic overview monopile misalignment direction (left) and measurement staff cross-check (right)	89
7.8	Global hoop elongations	90
7.9	Additional hoop stresses due to settlement of the slip-joint	91
7.10	Non-contact area between sensor 'G5' and 'G6'	92
7.11	Principle stresses as result of slip-joint settlement	93
7.12	Response signal of acoustic device	94
7.13	Difference in friction 'contact area' and measurable contact area	95
8.1	Frequency spectrum of NF strain gauges during heavy wind conditions	98
8.2	Frequency spectrum of NF3 and NF5 strain gauges during operational window	98
8.3	Time domain response of strain gauges during emergency stops	99
8.4	Frequency spectrum of strain gauge sensors during emergency stops	100
8.5	Three different (emergency) stops have been used for a decay test	100
8.6	Fitted exponential decay in structure's response after (emergency) stop to obtain the damping. Test 3	101
8.7	Settlement of the slip-joint over the total test phase	103
8.8	Total overlap length as can be read from the measuring staffs on the monopile	104
8.9	Settlement behaviour as a result of thrust forces	104
8.10	Hoop stress distribution after settlement during operation	106
8.11	Sensor indication	107
8.12	Evaluated operational interval	107
8.13	Additional hoop stresses within the slip-joint as result of thrust force	108
9.1	Frequency domain response of DOT500 turbine during operational interval at a rotor speed of 24-28 RPM	112
9.2	Settlement of slip-joint as result of additionally installed wind turbine items	112
9.3	Settlement of the slip-joint over the total test phase	113
9.4	Settlement definitions	113

9.5	Additional hoop stress in tower wall due to settlement slip-joint	114
9.6	Modelled local strains (left) and observed non-contact area (right)	114
9.7	Principle stresses and direction after settlement of slip-joint	115
9.8	Most probable reason for not being able do detect a difference in contact and non-contact areas	115
9.9	Additional hoop and vertical stresses in the slip-joint during operational interval	116
A.1	Lower tower dimensional data based on simple diameter and wall thickness measurements	120
A.2	Lower tower dimensional data based on simple diameter and wall thickness measurements with reference to actual site heights.	120
A.3	Lower tower weight information based on test in workshop	121
A.4	Lower tower dimensional data based on 3D measurements	121
A.5	Upper tower dimensional based on simple diameter and wall thickness measurements	122
A.6	Lower upper weight information based on test in workshop	122
A.7	Tensile and chemical test report turbine tower	123
A.8	Monopile dimensions according to technical drawing	124
A.9	Monopile dimensions according 3D-scan	125
A.10	Nacelle and rotor weight information	125
A.11	Environmental input parameters OWEZ	126
A.12	Environmental input parameters Maasvlakte II	126
A.13	Structural input parameters Vestas V90	126
A.14	Frequency spectrum of DOT3000 at OWEZ with average diameter of 4.00 m and wall thickness of 0.055 m	127
A.15	Frequency spectrum of DOT500 at OWEZ with average diameter of 4.00 m and wall thickness of 0.055 m	127
A.16	Load calculation and strength checks for DOT500 offshore turbine	128
A.17	Load calculation and strength checks for DOT3000 offshore turbine	129
A.18	Penetration depth optimisation for DOT500 onshore	130
A.19	Penetration depth optimisation for DOT3000 offshore	131
A.20	Dimensions control report SIF monopile	132
B.1	Rosette strain gauge specification sheet	133
B.2	Full bridge strain auge specification sheet part 1	134
B.3	Full bridge strain auge specification sheet part 2	135
B.4	Accelerometer specification sheet	136
B.5	Position sensor specification sheet	137
C.1	Input sheet soil interaction model - soil parameters as function of depth (brown is input, yellow is calculated)	139
C.2	Input sheet soil interaction model - dimensions monopile (brown is input, yellow is calculated)	140
C.3	Output Bladed natural frequency calculation with clamped foundation fore-aft (a) and side-side (b) direction	140
C.4	Output Bladed natural frequency calculation with spring-foundation fore-aft and side-side direction	141
C.5	Output RFEM natural frequency calculation with clamped and spring-foundation (no difference in direction)	142
C.6	Input scheme of target penetration model	143
C.7	Output of the model: target overlap length and accompanying hoop stresses	143
C.8	Deformations (left) and accompanying stresses as result of load case 1 in RFEM	144
C.9	Deformations (left) and accompanying stresses (right) as result of load case 2 in RFEM	144
C.10	Deformations (left) and accompanying stresses (right) as result of load case 3 in RFEM	145
C.11	Deformations (left) and accompanying stresses (right) as result of oval tower case	145
D.1	Example of a couple of log lines directly obtained from the data logger	147
D.2	Main function file decompression and decoding tool	147
D.3	Script that decompresses the data to actual numeric values	148

D.4	First part of the ordering script. The rest is the same for all sensors	149
D.5	Script that processes the the sensor signal into required output values, pt1.	150
D.6	Script that processes the the sensor signal into required output values, pt2., rest is same for all sensors	151
E.1	Predicted and measured penetration speed in relation with soil characteristics	154
E.2	Slip-joint settlement as result of different subcomponents installed	155
E.3	Horizontal strain gauge ring A response as result of installation of subcomponents	155
E.4	Horizontal strain gauge ring D response as result of installation of subcomponents	156
E.5	Horizontal strain gauge ring G response as result of installation of subcomponents	156
E.6	Acceleration of slip-joint during installation of different subcomponenets	157
E.7	Additional stresses due to settlement during operation interval	158
E.8	Additional stresses due during operation interval on 11th of August	158
E.9	Histogram and fitted normal distribution of additional stress due to operational interval on 11th of August	159
E.10	Additional stresses due during operation interval on 10th of August	159
E.11	Histogram and fitted normal distribution of additional stress due to operational interval on 10th of August	160
E.12	Stresses within slip-joint as result of thrust force near rated conditions	160
E.13	Fitted exponential decay in structure's response after (emergency) stop to obtain the dampging. Test 1	161
E.14	Fitted exponential decay in structure's response after (emergency) stop to obtain the dampging. Test 2	161
E.15	Fitted exponential decay in structure's response after (emergency) stop to obtain the dampging. Test 3	162
E.16	Acoustic report page 1	163
E.17	Acoustic report page 2	164
E.18	Acoustic report page 3	165
E.19	Acoustic report page 4	166
E.20	Acoustic report page 5	167
E.21	Acoustic report page 6	168
E.22	Acoustic report page 7	169
E.23	Acoustic report page 8	170
E.24	Acoustic report page 9	171
E.25	Acoustic report page 10	172
E.26	Acoustic report page 11	173

List of Tables

2.1	Return periods for different environmental load cases	30
3.1	Input values for hoop stress calculation	43
3.2	Theoretical maximum fabrication tolerances of tower and monopile cone	45
4.1	Wind turbine tower dimensions	50
4.2	Detailed dimensions of tower slip-joint section	51
4.3	Weight and centre of gravity, measured from bottom of cone, of two tower pieces	51
4.4	Masses and dimensions of RNA	52
4.5	Return periods values for different environmental load cases	53
4.6	Load cases for DOT3000 offshore	55
6.1	First natural bending frequency estimations	74
6.2	Influence of sensitivities on settlement parameters	78
6.3	Influence of sensitivities on settlement parameters	78
7.1	Masses of the subcomponents of the wind turbine	85
7.2	Settlement and relative settlement of slip-joint	86
7.3	Measured and anticipated settlement values	88
7.4	Elongation of position sensors Pos A through Pos G	90
8.1	Identified and measured natural frequencies	101
8.2	Normalised standard deviations during operational interval	107
9.1	Measured and anticipated settlement values	113

Contents

Preface	iii
Abstract	v
List of Symbols	vii
List of Figures	xvii
List of Tables	xxi
1 Introduction	1
1.1 Background	1
1.1.1 Wind Energy?	2
1.1.2 Offshore wind.	3
1.1.3 DOT B.V.	4
1.1.4 DOT500 Project	6
1.1.5 Slip-joint connection	6
1.2 Research objective and scope	7
1.3 Research Approach.	8
1.4 Method statement	8
1.5 Thesis Structure	9
2 Theory on wind turbine support structure design	13
2.1 Introduction	13
2.2 Data collection and processing.	14
2.3 Design heights	16
2.4 Dynamic analysis	17
2.5 (initial) Monopile dimensions	19
2.6 Load calculations	21
2.6.1 Permanent loads	21
2.6.2 Wind drag loads	22
2.6.3 Aerodynamic loads	23
2.6.4 Hydrodynamic loads	25
2.7 Limit states and load combinations	29
2.7.1 Limit states	29
2.7.2 Load combinations	29
2.8 Foundation design	31
2.8.1 Soil modelling	31
2.8.2 Soil parameters	32
2.8.3 Design checks.	32
2.9 ULS: Strength and stability checks	33
2.10 FLS: Fatigue damage check	34
2.11 Conclusion	35
3 Theory on slip-joint principle and design	37
3.1 Introduction	37
3.2 Slip-joint working principle.	38
3.2.1 Static vertical force equilibrium	38
3.2.2 Static bending moment at slip-joint connection	40
3.3 Fabrication tolerances	43
3.3.1 Deviation from specified circumference.	44
3.3.2 Ovality of the object	44
3.3.3 (local) out-of-roundness	44

3.3.4	Misalignment of welded plate sections	45
3.3.5	Tolerances	45
3.4	Slip-joint installation	45
3.4.1	Controlled dropping	46
3.4.2	Introducing vibrations	47
3.5	Conclusion	47
4	DOT500 onshore test set-up	49
4.1	Introduction	49
4.2	DOT500 Wind turbine tower and RNA	50
4.2.1	Wind turbine tower information	50
4.2.2	Additional tower information	51
4.2.3	Rotor and nacelle dimensions	52
4.3	DOT500 monopile	52
4.3.1	Design heights	53
4.3.2	Frequency analysis and monopile dimensions	54
4.3.3	Loads and design checks	54
4.4	DOT500 slip-joint	55
4.4.1	Slip-joint design	56
4.4.2	3D measurement monopile	57
4.5	Test site set-up	57
4.6	Conclusion	58
5	Measurement Campaign	59
5.1	Introduction	59
5.2	Natural frequency identification	59
5.2.1	Measuring natural frequency	60
5.2.2	Approach	60
5.2.3	Chosen sensors	61
5.2.4	Sensor positioning	61
5.3	Slip-joint settlement	62
5.3.1	Approach	62
5.3.2	Chosen sensors	63
5.3.3	Sensor positioning	64
5.4	Slip-joint stress distribution	65
5.4.1	Approach	65
5.4.2	Chosen sensors	66
5.4.3	Sensor positioning	67
5.5	Calibration of the sensors	68
5.5.1	Strain gauges	68
5.5.2	Accelerometers	68
5.5.3	Position sensors	68
5.6	Sensor data acquisition	68
5.7	Conclusion	69
6	Modelling and predictions	71
6.1	Introduction	71
6.2	Natural frequency model	71
6.2.1	Model information	71
6.2.2	Assumptions and details	72
6.2.3	Sensitivities	74
6.2.4	Predictions	74
6.3	Slip-joint settlement	74
6.3.1	Model information	75
6.3.2	Assumptions and details	76
6.3.3	Sensitivities	77
6.3.4	Predictions	78

6.4	Slip-joint global stress distribution	78
6.4.1	Predictions and sensitivities	79
6.5	Slip-joint local stress distribution	79
6.5.1	Model information	79
6.5.2	Model outcome	81
6.6	Conclusion	81
7	Results during installation	83
7.1	Introduction	83
7.2	Installation process.	83
7.2.1	Monopile installation day: 6th of May.	83
7.2.2	Wind turbine installation day one: 18th of May.	84
7.2.3	Wind turbine installation day two: 19th of May.	85
7.2.4	Conclusion and discussion	86
7.3	Slip-joint settlement	86
7.3.1	Settlement during installation	86
7.3.2	Settlement after installation	87
7.3.3	Final overlap compared to model	88
7.3.4	Conclusion and discussion	89
7.4	Slip-joint stress distribution	90
7.4.1	Global hoop stresses	90
7.4.2	Local hoop stresses	91
7.4.3	Principle stresses	92
7.4.4	Conclusions and discussion	93
7.5	Acoustic measurement	94
7.5.1	Measurements	94
7.5.2	Conclusions and discussion	95
7.6	Conclusions.	96
8	Results during operation	97
8.1	Introduction	97
8.2	Natural frequency	97
8.2.1	Heavy wind conditions and non operational	97
8.2.2	Operation conditions near rated speed	98
8.2.3	Emergency stop.	99
8.2.4	Damping estimation	100
8.2.5	Conclusions and discussion	101
8.3	Slip-joint settlement	102
8.3.1	Settlement during operational period	102
8.3.2	Settlement behaviour.	104
8.3.3	Conclusions and discussion	105
8.4	Slip-joint stress distribution	105
8.4.1	Additional stress due to extra settlement	105
8.4.2	Analysis on dynamic stresses	106
8.4.3	Stresses due to peak loads	107
8.4.4	Conclusions and discussion	109
8.5	Conclusion	109
9	Conclusions and recommendations	111
9.1	Conclusions	111
9.2	Recommendations and future research	116
9.2.1	Recommendations to the academic society	116
9.2.2	Recommendations to the industry.	117
9.2.3	Recommendations to DOT B.V.	117
A	DOT500 support structure dimension	119
A.1	Introduction	119

B	Measurement campaign details	133
B.1	Introduction133
B.2	Sensor details133
B.2.1	Strain gauges133
B.2.2	Accelerometers136
B.2.3	Position sensors137
C	Model details	139
C.1	Introduction139
C.2	Natural Frequency139
C.2.1	Model input.139
C.2.2	Model output140
C.3	Slip-joint settlement143
C.3.1	Model input.143
C.3.2	Model output143
C.4	Local stress distribution144
D	Post processing tool details	147
D.1	Introduction147
D.2	Decompression and decoding tool.147
E	Measurement results details	153
E.1	Introduction153
E.2	Monopile installation.154
E.3	Slip-joint installation.155
E.4	Measurements during operation.158
E.5	Acoustic measurement report163
	Bibliography	175

Introduction

1.1. Background

The global energy trends do not lie. At this point in time, it is predicted that the global energy demand is going to increase by an extra 30% with respect to today's levels of 104,426 *TWh*. Alongside, a growing trend is observed in the world's effort to reduce the environmental impact of this power generation [24]. Furthermore, the world's demand for (green) electricity rises with an estimated 70% from today's levels of 20,900 *TWh* [24]. This last increase can primarily be explained by the global concerted effort to reduce CO_2 emissions.

This incentive finds its roots back in 1992 when the first international environment treaty was signed, the so called 'United Nations Framework Convention on Climate Change'; or UNFCCC [40]. This treaty's main goal was to 'stabilise' the emission of greenhouse gases. From then on a number of rectification and update-meetings were held, including the Kyoto-Protocol of 1992. The key element in the Kyoto-Protocol lies in the fact that it demanded and quantified actual targets with respect to the emission of greenhouse gases. Most recently, the Paris Agreement of 2015 put down the agreement that the committing countries will, "as soon as possible" do their utmost best to keep global warming "to well below 2 degrees C" increase above pre-industry levels [41]. This means that countries will have to cut down on their CO_2 emission and energy use, whilst increasing the percentage of zero-carbon electricity production facilities.

The main theme in these outlooks and accords is that, one way or the other, mankind is going to need more energy. And above all, there is a growing demand for this energy to be produced and consumed in a 'green' and sustainable manner. One of the most obvious levers country's governments can pull is the production of electricity. It accounts for a rough 25% [25] of the total energy demand and is relatively easy to change course on as almost all electricity production plants are government owned or initiated. As of today, there are five main alternatives for fossil fuel electricity generation:

1. Wind Energy
 - Onshore Wind Energy
 - Offshore Wind Energy
2. Solar PV
 - Solar PV Residential
 - Solar PV commercial
3. Nuclear Energy
4. Hydro power
5. Others, including: geothermal, bio-fuels and hydrogen and fuel cells

From this list, the top four looks most promising at this point, considering production on large scale and technological developments. However, due to the different nuclear disasters the past decades and change of view on nuclear waste, there is an increasing incentive to reduce or even stop the electricity production from nuclear power plants. In the Netherlands, due to the absence of great heights to generate large heads for hydro-plants, the most interesting large scale sustainable energy sources therefore turn to be either wind or solar energy. So let's do what our Dutch ancestors did in the 16th century: build a vast amount of wind turbines and become world leader in this area [10]. This time not to replace one-third of the labour force, but one-third of the total electricity production of the Netherlands as a start.

1.1.1. Wind Energy?

Is wind energy a viable form of electricity production? To answer this question, one must look at the cost of (offshore) wind energy at this point and how it can be competing with other forms of (renewable) energy. Because in the end, all that matters for the government and investors is the value and revenue of the investment. In the light of the developments discussed in section 1.1, people are prepared to pay something extra for renewable energy sources, but it must be competitive at the least. A common way to compare cost-effectiveness of different types of energy production methods is the levelized cost of energy (*LcOE*) calculation. In this calculation the indexed sum of costs over the lifetime of the production is divided by the levelized energy yield over the lifetime.

$$LcOE = \frac{\sum_{t_y=1}^{n_e} \frac{I_t + M_t + D_t}{(1+r)^{t_y}}}{\sum_{t_y=1}^{n_e} \frac{E_t}{(1+r)^{t_y}}} \quad (1.1)$$

An extension to this formula, proposed by the International Energy Agency (IEA), is to add the carbon-fees for nonrenewable sources of energy in the 'other costs' D_t . In 2015, these were set to 30 US dollars per ton CO_2 . When we take this into account and graph the *LcOE* for the three renewables and some non-renewable electricity sources we obtain graph 1.1 [23].

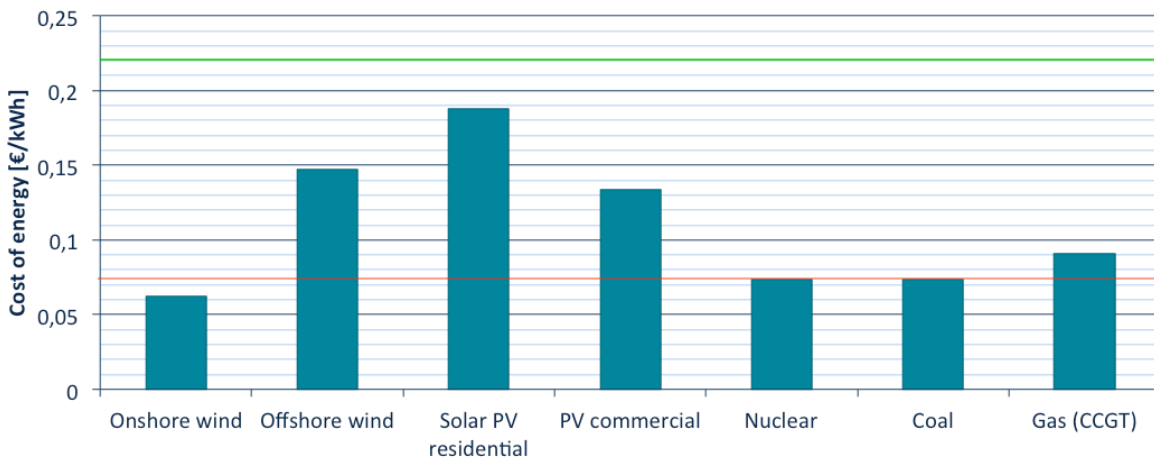


Figure 1.1: LCoE for different electricity sources

In this graph, the green line indicates the price the customer pays for electricity (including VAT and taxes), which lies at around $0.22 \frac{\text{€}}{\text{kWh}}$. The red line indicates the market price of energy, i.e. the price the industry receives for selling its produced electricity. This price lies at around $0.07 \frac{\text{€}}{\text{kWh}}$. The conclusion on this graph is threefold:

1. Residential solar panels are competitive, since the energy price for customers exceeds the cost of installing and maintaining solar panels on your roof. So every kWh one does not have to 'buy' from the energy market because you produce it yourself, is pure profit. On the other hand, the

use of commercial solar panels is not competitive yet and requires a cost reduction of about 40% in order to compete with the market price of $0.07 \frac{\text{€}}{\text{kWh}}$.

2. Onshore wind is highly competitive with nonrenewable forms of energy.
3. Like commercial solar PV, offshore wind requires a cost reduction. A reduction of about 50% would enable offshore wind to be a competitive form of electricity production.

1.1.2. Offshore wind

As far as wind energy is concerned it is concluded that on- and offshore wind could be good alternatives for energy production. To ensure a common speech figure 1.2 shows a typical offshore wind turbine accompanied with some definitions for several parts. These definitions will be used throughout this thesis.

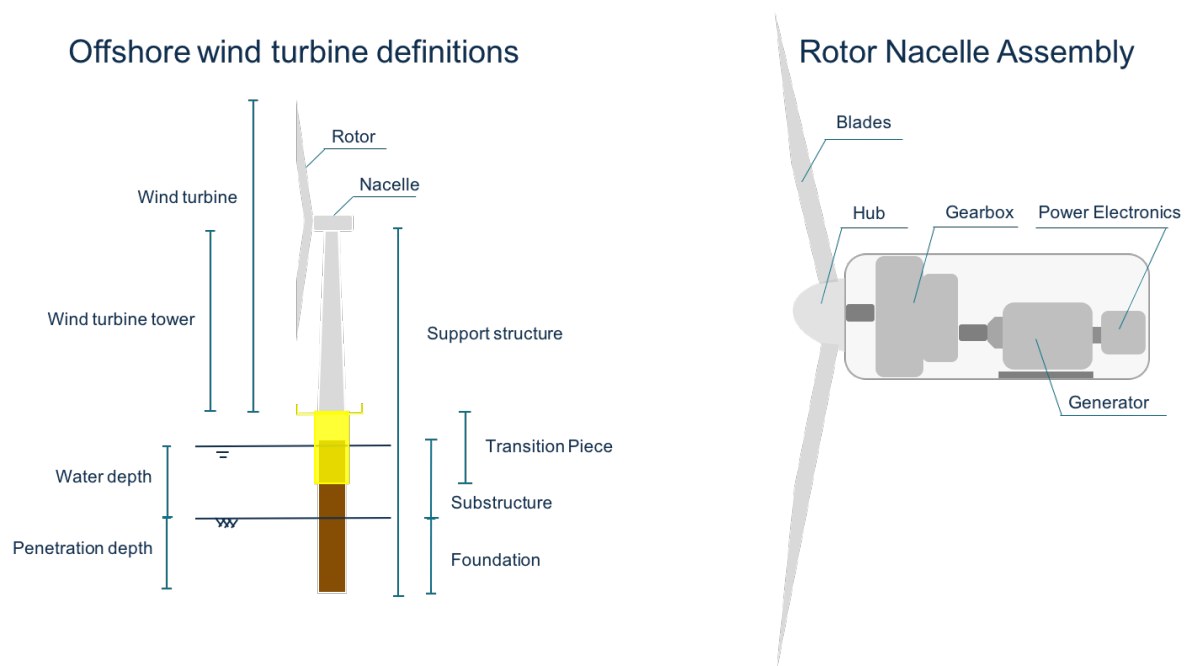


Figure 1.2: Definitions typical offshore wind turbine

As can be concluded in section 1.1.1, onshore wind is a very good alternative for greener energy production. However, a continuing trend of wind turbines moving offshore can be observed these days. This contra-intuitive movement can be explained by three major factors. First of all, the most prominent reason to go offshore is to find areas with more constant and higher average wind speeds. This greatly increases the amount of power that can be captured by the wind turbine, as the power generation from the wind follows a cubed relation:

$$P_w = \frac{1}{2} C_p \rho_{air} A_{rotor} V_{wind}^3 \quad (1.2)$$

Secondly, increasing land occupation prohibits the placement of large scale wind farms onshore, while there is plenty of space available offshore. Thirdly, public opinion comes into play. People simply do not like to have big wind turbines in their back yard. So as a final reason the 'horizon pollution' that people experience from installing wind turbines onshore is pushing wind turbines offshore. The latter three reasons have been the major driving force for wind turbines to move offshore.

The offshore wind industry is a rather young industry with the first commercial offshore wind farm being the 'Vindeby' wind farm in Denmark build in 1991 [2]. This wind farm consists of 11 turbines with a capacity of 450 kW each, generating a total of 4.95 MW of installed peak power. Since then,

offshore wind farms have grown bigger and bigger. The biggest offshore wind farm as of today is the 'London Array', with a total installed peak capacity of 630 MW, generated by 175 turbines of 3.6 MW rated power each [1]. As the shallow water spots in the North Sea are getting more crowded, another trend can be observed these days; a move to further offshore locations with deeper waters. These spots bring higher costs for offshore wind farms for obvious reasons. The support structures will need to reach deeper, making them bigger and therefore more expensive. Moreover, the already costly export power cables need to reach bigger distances, also adding to higher costs per wind turbine. With the already established levelized cost of energy of current offshore wind farms in section 1.1.1, one can conclude that offshore wind is a potential source of sustainable energy production, as long as the margin for profit is increased by an approximate 50%.

The solution to this can be twofold; increase the earnings for the investors or cut the cost. The first part of this solution has been laid out by the Dutch government in the form of the proposed long horizon subsidy scheme's for the wind farms on the dutch coast of the North Sea. However, subsidies are not a durable solution. This means that the costs have to be cut down as well, e.g. by cutting cost on capital or simply the costs of the product itself. This can be achieved by better integration of different sectors of the wind industry and by innovation in the wind industry. Since the 1990's there has not been any significant innovation in the (offshore) wind energy sector. The sector is ready for it and that is where the startup company DOT B.V. comes in.

1.1.3. DOT B.V.

The Delft Offshore Turbine B.V. (DOT) is a start-up company founded with the goal to commercialise the idea of the DOT drive train-concept. This idea is a new and innovative concept for the drive train system of an offshore wind turbine. It is based on a hydraulic transmissions. Regularly, wind turbines make use of a mechanical transmission system and produce electricity individually. This requires the placement of big and heavy gearboxes and generators in the top of the wind turbine. That weight has to be supported, typically by a monopile which has to endure the complicated cocktail of loads in the rough offshore climate. This creates the need for large diameter monopiles to control the dynamic behaviour, for this greatly influences the fatigue damage of the turbine. This will be discussed in more detail in chapter 2. Furthermore, the fact that every wind turbine generates its own electricity means that a lot of copper is being used in the offshore environment to connect every wind turbine to a transmission station and eventually to the grid.

The DOT concept tries to tackle these problems by using a hydraulic transmission system (in combination) with water pumps. This concept states that every wind turbine in a wind park will be equipped with a hydraulic transmissions system, effectively consisting of an oil pump connected to the rotor and a oil motor driving a water pump. In a later stage of the design, when the market is ready and willing to produce low RPM, high displacement water pumps, the oil transmission will be disregarded and only the water pump will be equipped in the wind turbine. Consequently, all turbines will pump their water to one or more power stations, a Pelton Turbine, located centrally within the wind farm, hence generating electricity only on one central location [11]. This concept is illustrated in figure 1.3 and figure 1.4.

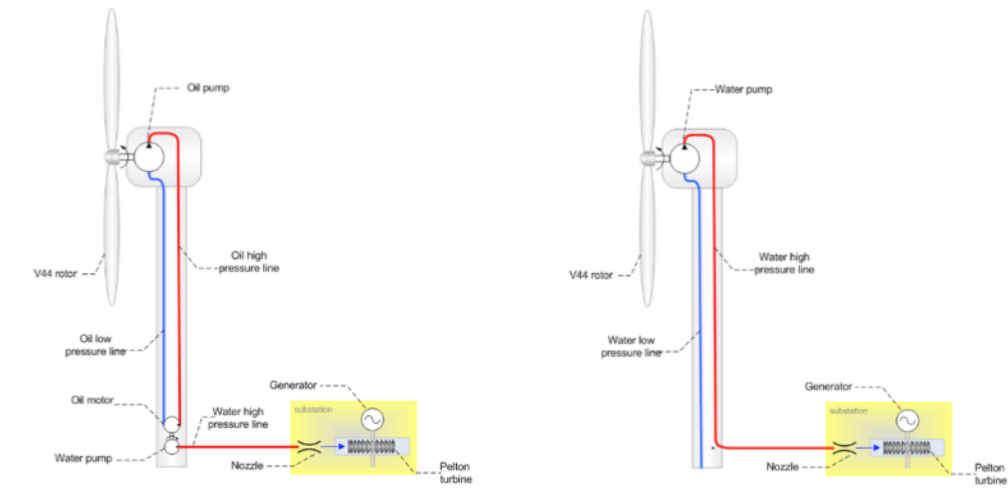


Figure 1.3: DOT drive train system now (left) and in the future (right)



Figure 1.4: DOT concept for a typical wind farm

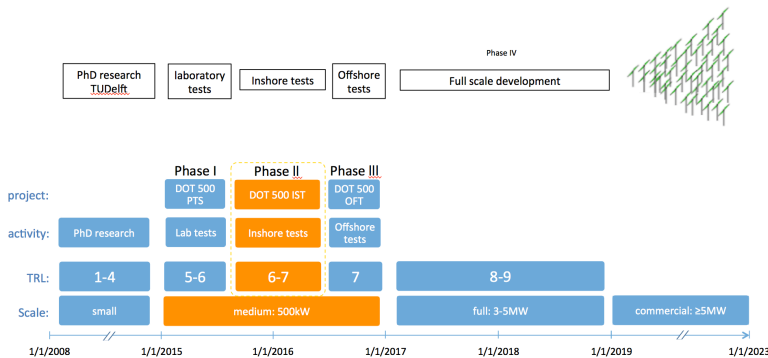
By doing so, the top mass of the wind turbine can be reduced by an estimated 50% to 60% [11]. This means that the support structure of the wind turbine can be potentially significantly reduced in size, saving lots of cost for fabrication and construction per turbine. Considering the fact that a typical wind farm consists of 100 to 150 wind turbines it is not hard to image the immense cost savings that can be realised considering the support structure alone. Apart from this, the positive effect of generating electricity at one central location reduces the amount of generators and subsea power cables throughout the wind farm, also cutting down on the installation and material (copper) costs. Although the efficiency per turbine is somewhat reduced due to the hydraulic drive train, the overall cost per kWh can be drastically reduced with an estimated magnitude of 30% to 50% [11].

1.1.4. DOT500 Project

As indicated DOT strives to have its share in the required cost reduction specified in section 1.1.1, by means of innovation. To succeed in this goal DOT focusses on three main targets in the near future:

1. Proof of concept on medium scale, hydraulic equipment only: Phase I: DOT 500 PTS
2. Demonstration project medium scale onshore with a Vestas V44: Phase II: DOT 500 ONT
3. Demonstration project medium scale offshore with a Vestas V44: Phase III: DOT 500 OST

This part of the overall DOT planning, graphically displayed in figure 1.5a, will hereafter be referred to as the DOT500 project in which the 500 stands for the size of the scale: 500kW. The first part of this project has been completed. A second hand Vestas V44 was bought and the nacelle has been refurbished to house the DOT 500kW drive train, which can be seen in figure 1.5b. The purpose of this first phase was to perform failure and performance tests to map the system's performance. These tests have taken place from January to April 2016. Consequently, the DOT drive train system has been fitted in the real Vestas V44 turbine for its next destination: the onshore and offshore test. The onshore is currently up and running and the installation started in May 2016 on the Maasvlakte II. This will be elaborated on in chapter 4. The offshore test is scheduled for February 2017. In these tests the DOT drive train will be tested with real wind on an outdoor location for the first time.



(a) Overall planning DOT project



(b) Completed Phase I: DOT500 PTS

Figure 1.5: DOT500 project

The focus of these tests will be on the proof of concept of the hydraulic drive train in a real-wind environment. However, since this is a demonstration project, or test wind turbine, the project houses great opportunities to test other innovations. The DOT500 will be supported by means of a monopile in both the on- and offshore test. This monopile will be vibrated into the soil. Furthermore, the connection of the wind turbine and monopile will be done by means of a slip-joint. This innovation will also be tested on the DOT500 project and will be the focus of this thesis. A small introduction to the principle is given in section 1.1.5.

1.1.5. Slip-joint connection

A slip-joint connection is an alternative form of connecting the wind turbine tower to its foundation. Up until today, over 70% of offshore wind turbine foundations are monopiles and a staggering 97% of the total support structures for wind turbines installed in 2015 where monopiles [19]. Monopiles are regularly connected with the wind turbine tower by means of a transition piece that is grouted and fixed on top of a monopile. Consequently, the turbine tower is bolted on top the of the transition piece. However, a monopile foundation provides an ideal base for the slip-joint connection. A slip-joint consists of two conically shaped steel tubulars, that slide over each other as can be seen in figure 1.6.

The idea originates from a Dutch company named WindMaster, that used this joint to connect two wind turbine tower parts of the "Duinvogel" at Scheveningen back in 1995 [27]. The main goal of the use of

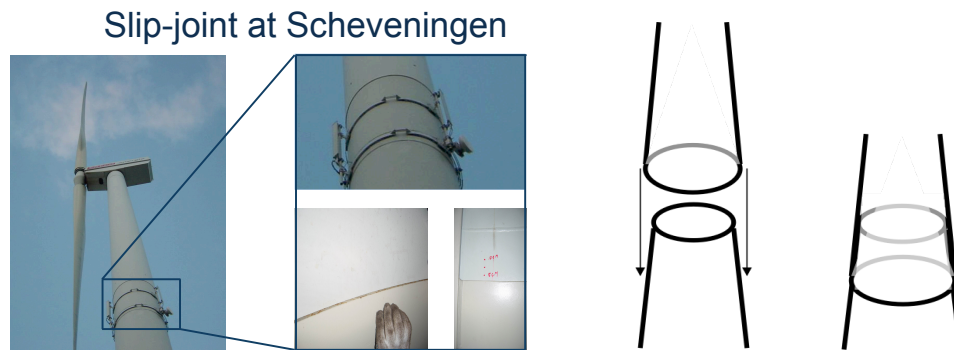


Figure 1.6: The slip-joint connection

this joint was to reduce installation time caused by the many bolts commonly used to connect turbine tower parts. WindMaster went bankrupt in 1998 and the innovation went in abeyance. However, in 2003 the idea was picked up by Jan van der Tempel (the founder of DOT B.V.), who figured this connection technique of monopile and wind turbine could bring huge benefits to the offshore wind industry. Not only could this joint reduce costly offshore installation time, but on top of that it could possibly reduce material cost as the need for a transition piece is absent in this type of connection. The conclusion of a DOWEC report investigating the possibility of using this joint offshore was that there are no major problems foreseen in the use of it offshore [27]. No structural reliability problems were found in investigating 'the Duinvogel' slip-joint and the installation method saved critical installation time. The verticality of the monopile should be guaranteed as the slip-joint holds no correction possibilities. However, current industry standards seem to meet this requirement.

In 2008 it was observed that several grouted connections of a transition piece in the North Sea were settling. It was found to be a design error and the conclusion was drawn that a lot of other transition pieces might eventually encounter the same problem. This led to a change in the design code of offshore structures by Det Norske Veritas (DNV) [15]. This development holds yet another motivation to further speed up the investigation of the use of a slip-joint for (offshore) wind turbines. That is why the DOT500 project will also make use of a slip-joint connection between the monopile and the wind turbine.

As of today, there are still some areas to discover concerning the use of the joint. These include the structural strength and stability of the joint and its behaviour in the offshore corrosive environment. Furthermore, the settlement of the joint and the stress distribution resulting from this settlement are not fully understood at this point in time. The goal of this thesis is to add an extra case study on the application of the slip-joint focussing on identifying the two latter named items.

1.2. Research objective and scope

The features as described on the DOT500 turbine support structure are innovations that have never, or a limited number of times been tried in the offshore wind sector. The DOT500 project provides a great opportunity to test these new features and aid to the innovation process for the whole industry. This research will contribute in this matter. As pointed out, the focus of the research will be on the slip-joint connection. Therefore, the main objective of this thesis will be described as: *"Design, testing and verification of the DOT500 slip-joint support structure."* The main research question is formulated as follows:

Main research question:

"What is the mechanical behaviour of the slip-joint connection during installation and operation of the DOT500 wind turbine support structure?"

To answer this question the following sub-questions have been formulated. These questions will gradually pave the way towards a complete answer to the main research question.

1. What are the loads acting on a wind turbine support structure?
2. What are the relevant parameters that need to be taken into account in support structure design?
3. What is the theory behind the slip-joint working principle?
4. What are the relevant parameters that need to be taken into account in slip-joint design?
5. How can the relevant structural parameters be measured?
6. How can the relevant structural parameters be modelled and predicted?
7. What is the DOT500 slip-joint's settlement behaviour during installation and operation?
8. What is the stress distribution of the DOT500 slip-joint and how does it development during installation and operation?
9. How can the contact area of the slip-joint be determined?

The research approach based on the objective described in this section is presented in section 1.3.

1.3. Research Approach

The approach of this thesis is threefold. First of all, a literature study will be performed identifying the important parameters in the design of an offshore wind turbine support structure and slip-joint design. This knowledge is of great importance to generate a sound measurement campaign to measure these parameters. Secondly, a number of models will be created to anticipate on the sensitivities of these parameters and predict their potential influence on the slip-joint during installation and operation. Thirdly, the processed measurement results will be compared with the models and predicted output to conclude on the mechanical behaviour of the DOT500 slip-joint during installation and operation. This is graphically displayed in figure 1.7.

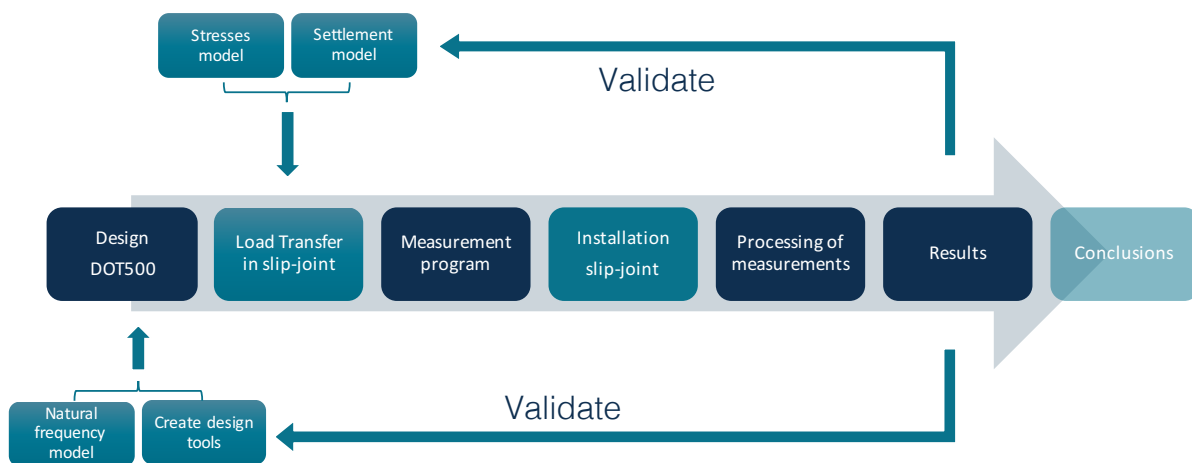


Figure 1.7: Thesis approach

1.4. Method statement

The DOT500 project provides a unique opportunity to acquire data from an actual full-scale operating wind turbine connected with a slip-joint. Therefore, it was chosen to mainly focus the research on the preparation, execution and interpretation of the result of the measurement campaign that will be set up within the DOT500 project.

The relevant theoretical background will be researched in a literature study in the beginning of the research. This information shall be used to optimise the measurement campaign. Also, some first order

models shall be made to anticipate on the results and understand the influence of different sensitivities. This will add to a better understanding and interpretation capability of the measurement results.

Most of the focus of the research lies on the acquisition, processing and interpretation of the data of the measurement campaign. To this extent post processing tools will be made to facilitate the investigation of the raw data. Based on the conclusions of this data and backed up by the knowledge gained from the models, conclusions on the mechanical behaviour of the DOT500 slip-joint shall be drawn.

1.5. Thesis Structure

In the consecutive subsections the structure of the report shall be elaborated on. Every chapter will provide the background to answer the stated subquestions in the research objective. These subquestion will be listed and the content of the chapter shall be evaluated.

Chapter 1

The current houses the introduction to the thesis. The background information about the thesis subject is presented as well as the research object and research questions. Furthermore, the approach of the research is elaborated on in combination with a method statement and scope definition.

Chapter 2

Subquestion 1:

"What are the loads acting on a wind turbine support structure?"

Subquestion 2:

"What are the relevant parameters that need to be taken into account in support structure design?"

Chapter 2 is part of the theoretical background of the thesis and explores the theory behind wind turbine support structure design. The design cycle of an offshore wind farm as presented in literature shall be explored and the relevant design parameters for the DOT500 project will be identified. Furthermore, the relevant theory and formula's that will serve as input for the models is explored in this chapter. This provides the reader with the theoretical background required for the clarify of the rest of the thesis.

Chapter 3

Subquestion 3:

"What is the theory behind the slip-joint working principle?"

Subquestion 4:

"What are the relevant parameters that need to be taken into account in slip-joint design?"

Chapter 3 is part of the theoretical background of the thesis and investigates the theory behind the slip-joint principle. Any performed researches found in literature shall be investigated and discussed. Also, the considerations for the slip-joint design of the DOT500 support structure will be evaluated and the most important parameters shall be identified. This provides the reader with the relevant theoretical background required throughout the remainder of the thesis.

Chapter 4

Chapter 4 is an informative chapter that presents the DOT500 onshore test site setup. The details of the different components of the wind turbine shall be elaborated on such as, the wind turbine tower, RNA, monopile and slip-joint. The dimensional data will be presented as well as the design considerations for the monopile and slip-joint. Also, an overview of the test site will be provided.

Chapter 5

Subquestion 5:

"How can the relevant structural parameters be measured?"

Chapter 5 presents the measurement campaign that was set up to monitor the DOT500 slip-joint. The background information and motivations to the important decisions that have been taken shall be presented. Also, the different types and the positioning of the sensors shall be discussed. This provides the reader with the necessary information to interpret the results from the measurements in the thesis.

Chapter 6

Subquestion 6:

"How can the relevant structural parameters be modelled and predicted?"

Chapter 6 present the models that have been made in order to anticipate and better understand the outcome of the measurements. Three first order models have been made for this purpose, including a model to predict the natural frequency, settlement and stress distribution along the slip-joint connection. The detailed steps, assumptions and sensitivities of the models shall be elaborated on in this chapter.

Chapter 7

Subquestion 7:

"What is the DOT500 slip-joint's settlement behaviour during installation and operation?"

Subquestion 8:

"What is the stress distribution of the DOT500 slip-joint and how does it develop during installation and operation?"

Subquestion 9:

"How can the contact area of the slip-joint be determined?"

Chapter 7 presents the results of the DOT500 measurement campaign during the installation phase. A vast amount of data has been gathered with the sensors and this chapter presents the most relevant findings contributing to the main research question. Data on the settlement and stress distribution shall be presented and compared with the models. Also, the results of the contact area measurement will be presented.

Chapter 8

Subquestion 7:

"What is the DOT500 slip-joint's settlement behaviour during installation and operation?"

Subquestion 8:

"What is the stress distribution of the DOT500 slip-joint and how does it develop during installation and operation?"

Chapter 8 presents the results of the DOT500 measurement campaign that have been gathered during various instants in the operational period of the wind turbine. Data on the natural frequency, settlement and stress distributions shall be presented and compared to the models.

Chapter 9

Finally, chapter 9 presents the conclusions of this research answering the posed subquestions and main research question of this thesis. Furthermore, a number of recommendations to the academic society as well as to industrial society shall be presented.

2

Theory on wind turbine support structure design

2.1. Introduction

Offshore wind energy is a vast multidisciplinary industry in which expertise from a lot of different fields is combined to create structures that are put out at sea. It is due to this industry's nature that the design process of an offshore wind turbine is a quite complex one. Part of this process is the design of the offshore wind turbine's support structure. The enormous wind turbines that will generate the clean energy at sea, have to be able to withstand the complex cocktail of loads that the harsh offshore environment throws at them. This chapter will elaborate on the theory behind a typical offshore wind turbine support structure design cycle. Since the DOT500 structure will be founded by a monopile, the focus in this chapter lies on the monopile design.

The goal of this chapter is to create a theoretical background that will serve as a foundation for further steps in this thesis. Furthermore, the theory and calculations serve as input for chapter 4 and 6. The design cycle of an offshore wind turbine will be explored taking into account the most important aspects in this design cycle. The focus herewith lies on the identification and understanding of the most important design parameters accompanying an offshore wind turbine design process. A typical offshore design cycle is presented in figure 2.1. This will serve as the main guidance throughout this chapter and will be treated step by step in the subsequent sections.

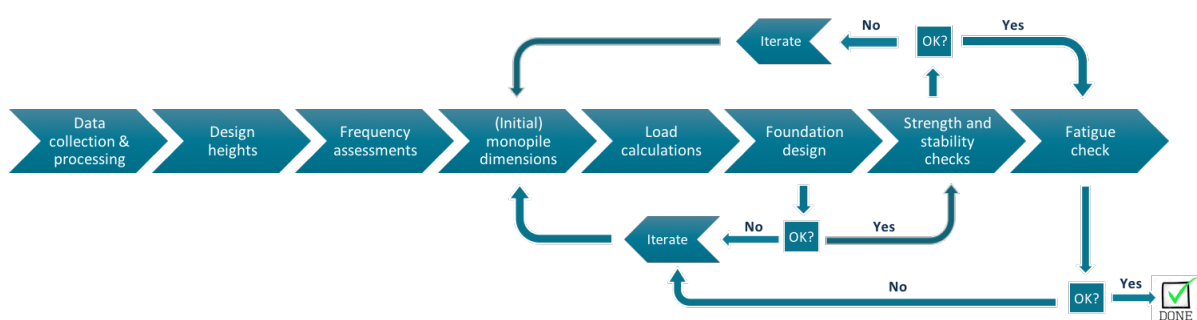


Figure 2.1: Design cycle monopile DOT turbine

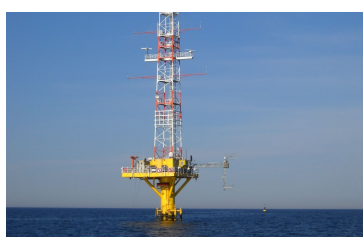
First of all section 2.2 will elaborate on the data collection and processing process. This data serves as input for the design cycle. Sections 2.3 and 2.4 explain the first steps in the design process consisting of the determination of the design heights and a preliminary frequency assessment, respectively. On the basis of this, the preliminary monopile dimensions can be established as is explained in section 2.5. From here on, sections 2.6 through 2.10 will elaborate on the iterative design cycle the calculation of loads, different design checks and optimising the dimensions of the structure.

2.2. Data collection and processing

When designing a proper wind turbine it is of crucial importance to obtain the right data as input for this design cycle. Therefore, the first step in the design of an offshore wind turbine is the process of collecting data. The required data can be split into a number of categories:

- **MetOcean data.** MetOcean data consists of information on wind, wave, current and water level data. Wind speeds and direction as well as wave heights and periods are typical examples of this type of data. This data is crucial for calculating environmental loads on the structure as a result of these forces of nature. Moreover, it is of vital importance when establishing installation and maintenance weather windows.
- **Site specific data.** Apart from the MetOcean data there is a lot of other site specific data that needs to be gathered. For example, data on the seabed soil-conditions as well as the bathymetry. Furthermore, data on the air and water characteristics like, temperature, density salinity and other constituents should be gathered. Also, it is important to make an inventory of already existing infrastructure and waterway- and seabed occupation that is already existent.
- **Other data.** Finally, there is all sorts of other data that needs to be collected to be able to design and optimise the wind turbine support structure. This data may include information on the structural parts like the wind turbine.

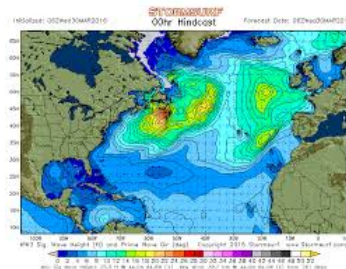
Data like this can be acquired through different methods, namely in-situ measurements, ex-situ measurements and by means of hind cast models displayed in figure 2.2.



(a) In-situ measurements, e.g. MetMasts



(b) Ex-situ measurements, e.g. satellite



(c) Models, e.g. hindcasting

Figure 2.2: Different data acquisition methods

In-situ measurements

In-situ measurements are performed at the exact location where the data is required. These can be for example wave buoys for wave data and anemometers for wind data. These in-situ measurements are generally bundled on the North Sea in the form of a MetMast. In the Dutch North-Sea there are a total of nine of these MetMasts of which the data can be freely accessed. The upside of this kind of data is that is a long and continuous form of collecting the environmental data. Also, it is open and freely available. The most important limitation is that the data is collected only on a single location as opposed to a bigger area.

Ex-situ measurements

Ex-situ measurements are measurement that are not taken on the exact site, for example satellite measurements. Satellites can be used to collect MetOcean data of big area's at once. However, since satellites circle around the earth the measurements are not continuous and more inaccurate than most in-situ measurements.

Models

Finally, models can be used to create new data or extrapolate data from different locations to a wider area. Hind casting is a method of testing and validating a mathematical model. Models that calculate

the required MetOcean data can be validated by using the measured and actual acquired data. In this way, model 'predictions' of past data sets can be made and validated using the actual measured data. The model can then be used to extrapolate this data into the future to acquire the new and required data [36].

After having acquired the data listed above it needs to be processed in order to use it for the right purposes. Most importantly this holds for the MetOcean data. Typically this data is acquired in the form of time-series at different locations. This raw data will then have to be processed into usable data. This is done by means of statistics. A number of the most common products of data processing are displayed in figure 2.3.

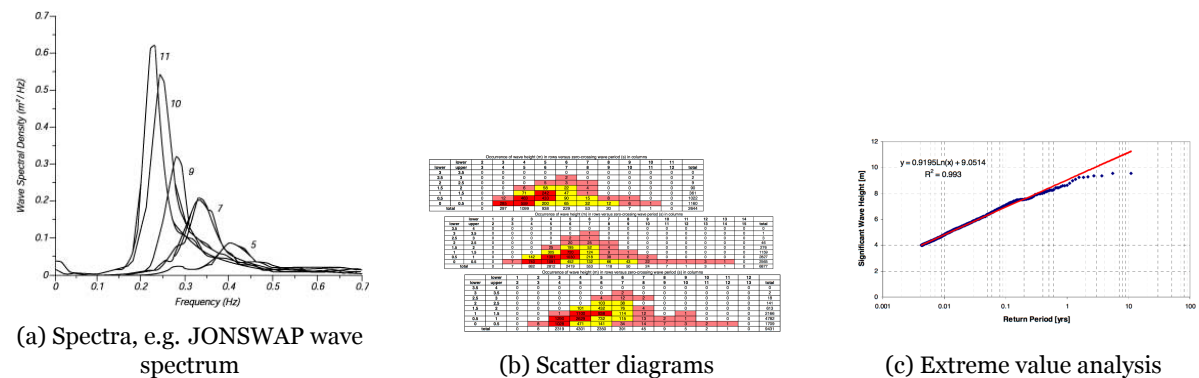


Figure 2.3: Common data processing techniques

Spectral representation

A common way to process data, especially wave data, is in the form of spectra. By means of a Fourier Transform the data in the time domain, e.g. a time series of sea surface elevation, can be converted to the frequency domain. In this manner, an irregular sea-state can be represented in a single diagram, showing the amount energy in the wave as a function of the frequency of the wave. In this way an entire irregular sea-state is represented in a single diagram with only two parameters, the significant wave height H_s and peak period T_p of this sea-state. A typical spectrum of fetch-limited sea, such as the North Sea, is a JONSWAP spectrum [22].

Scatter diagrams

A convenient way to bundle information on wave heights, wave periods and wind speeds is by means of a scatter diagram, or plot. Such diagrams show the occurrence of different combinations and intensity of wave height, wave period and wind speed. In this way an entire year of time-series can be displayed in a couple of diagrams [43].

Extreme value analysis

Apart from the latter two named short term statistical representation techniques, it is also important to acquire long term statistical data. This is important for extreme load calculations for example. The generalised extreme value distribution can be used for this purpose. Such methods are used to present a statistical distribution of maxima or minima of a very large collection of independent random variables from the same arbitrary distribution [29]. By means of this analysis one can gain a statistically reliable estimate of an extreme value of for example a once in a 50 year returning wave height, or $H_{s,50}$.

Of course, there are multiple other aspects in processing this data ranging from directional information of wind, wave and current to the interpretation of soil investigation. In this thesis, raw time-series have been used to perform extreme value analysis as input for design calculations. Furthermore, soil investigations have been performed in the form of a CPT, which have been processed to generate the relevant soil parameters.

2.3. Design heights

The first real step in the design process is to determine specific design heights of the wind turbine. These elevation levels are important for several reasons as will be elaborated on in the subsequent subsections. Therefore, it is crucial to set these heights in an early stage of the design. The following design heights need to be calculated or determined, graphically displayed in left picture in figure 2.4. These levels will be shortly elaborated on from bottom to top.

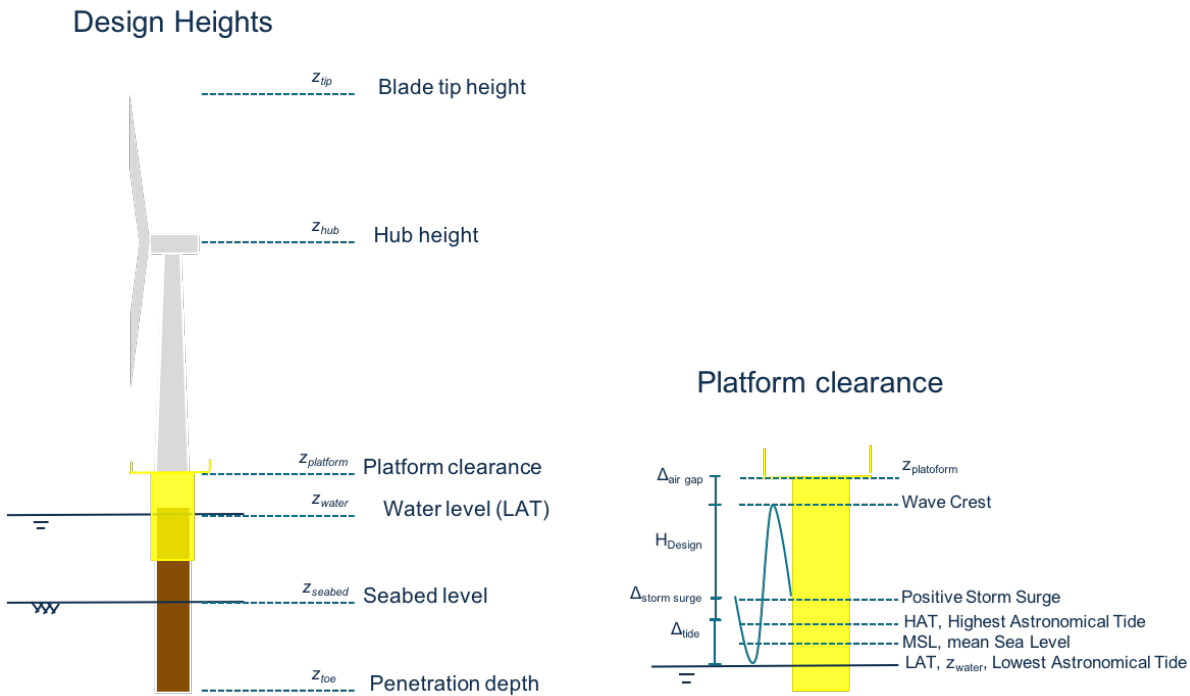


Figure 2.4: Offshore wind turbine design elevations (left) and clarification of platform clearance level (right)

Penetration depth

The toe level of the foundation, or penetration depth (z_{toe}), is the deepest point of the structure. This level is determined by requirements for the stability of the foundation, i.e. the foundation must be deep enough to withstand the loads acting on the turbine, as will be elaborated on in section 2.8. This level is highly location dependent, due to the soil properties can vary, even throughout one wind farm. At the start of the design cycle, when the foundation stability analysis has not yet been performed, this level is determined by means of a rule of thumb. A typical value for this first estimate is seven times the monopile diameter (D_{MP}), $z_{toe} = 7D_{MP}$.

Water level and seabed level

The seabed level is obviously determined as the position where the seabed is located. It is important to have a proper reference frame with a single reference point. This point is usually taken at the water level, or more specifically the lowest astronomical tide (LAT). This is the lowest level that the water will reach during the shifting of the tides. This water level can then be extended to the mean sea level (MSL), which is the average level in the tidal ranges and the highest astronomical tide (HAT). The latter obviously is the highest level that the water will reach during tidal shifts. Finally, on top of these tidal variations a so called storm surge level is added. This is the water level rise due to long fetch of storm-winds, blowing land inwards.

Platform clearance level

The platform clearance level is a level established in such a manner that the platform on the wind turbine shall not be hit by a wave within an established statistical certainty. This level is therefore determined by means of taking the highest water level possible, adding the maximum design crest height of a wave, plus a safety factor [45].

$$z_{platform} = \Delta_{tide} + \Delta_{storm} + H_{design} + \Delta_{air} \quad [m + LAT] \quad (2.1)$$

In which,

$$H_{design} = 0.65 \cdot (1.86 \cdot H_{s,50}) \quad [m] \quad \text{and} \quad \Delta_{air} = 1.5 \quad [m] \quad (2.2)$$

Hub height

Another important design height is the hub height of the turbine. This height is determined as the distance of the water level to the hub. The hub of the turbine is the middle point of the rotor to where the blades are attached. This level is usually set by the turbine manufacturer as it influences the power production of the turbine. However, a brief check needs to be performed to see if the blade-tip has enough clearance with the platform. The following relation must hold in order for a safe distance between blade tip and working platform.

$$z_{tipclearance} = z_{hub} - R_{rotor} - z_{platform} - \gamma_{tip} > 0 \quad [m + LAT] \quad (2.3)$$

In this formula γ_{tip} is a safety distance specified between the tip of the blade and the platform, e.g. 5m.

Blade tip height

The final elevation of the wind turbine that needs to be determined is the blade tip height at the highest possible position. This is obviously determined by the hub height plus the rotor radius.

$$z_{tip} = z_{hub} + R_{rotor} \quad [m + LAT] \quad (2.4)$$

2.4. Dynamic analysis

Commonly, the next stage of the wind turbine design is to perform a brief dynamic analysis. The goal of this analysis is to identify both the eigenfrequencies of- and the excitation frequencies on the dynamic system, i.e. the wind turbine. The importance of this exercise can be most conveniently explained by means of a one degree-of-freedom mass-spring-damper system, as displayed in figure 2.5.

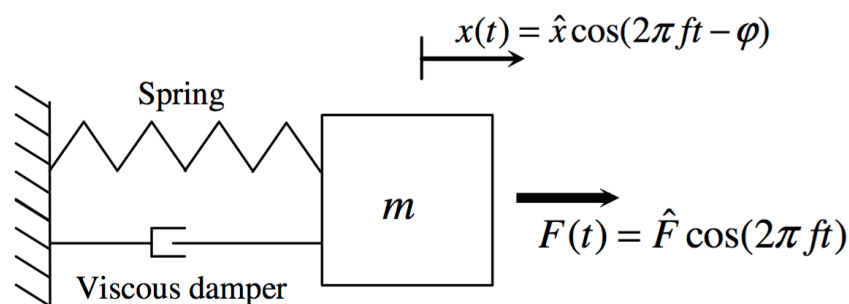


Figure 2.5: One degree-of-freedom mass-spring-damper system

When such a system is excited by a pulse load it becomes a harmonic vibration, characterised by an eigenperiod or natural frequency. This frequency characterises the free vibration of the system. However when the system is excited with a harmonic force $F(t)$, the amplitude \hat{x} and phase ϕ of the response is highly dependent on the frequency f of this force [17]. One can distinguish three steady state response regimes, displayed in figure 2.6 [43].

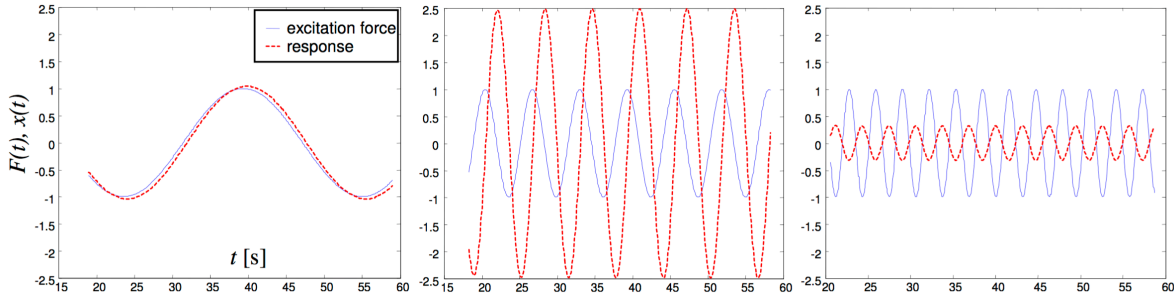


Figure 2.6: Three response regimes. From left to right: Quasi-static, resonance, inertia dominated. Solid blue line: excitation, dashed red line: response.

- **Quasi-static:** for excitation frequencies well below the system's natural frequency of the system, the system reacts quasi-static. The displacement of the system almost exactly follows the time varying excitation force, as if it was a static load.
- **Resonance:** when the excitation frequency on the system is in a narrow region around the system's natural frequency the amplitude of the response will be a number of times bigger than the input amplitude. It will even be theoretically infinite if the excitation- and natural frequency are exactly similar. The energy dissipating forces, or damping, of the system limit the amplitude of the response in this regime.
- **Inertia dominated:** for excitation frequencies well above the system's natural frequency the response of the system is inertia dominated. The system cannot 'follow' the excitation any more. This produces a response that has an amplitude which is lower than if it were excited statically and which move almost in counter-phase with the excitation force.

It shall be clear from the previous discussion that the natural frequency of the system should lie sufficiently far away from the excitation frequencies present on the wind turbine to decrease the chance of resonance of the system. A state of resonance will significantly increase the amplitude of the response of the wind turbine leading to higher stresses and reduced (fatigue) life time. The most common low frequency excitation sources on a wind turbine system are [43]:

- **Wave frequencies:** wave frequencies come in a range and are usually modelled using a wave-spectrum formulation. A common way to do so in fetch-limited seas is by means of the JONSWAP-formula notation. The region from 0 to $2\omega_{peak}$ should be avoided to prevent resonance problems [45].
- **1P excitation:** this is the rotational frequency of the turbine. Excitations at this frequency can for example happen due to a mass imbalance in one of the three blades of the turbine. For a variable speed wind turbine this gives a frequency range which can be calculated by: $f_{1P} = \frac{RPM-range}{60}$ [Hz]. A buffer of 10% is added to both ends of the range as a safety factor.
- **3P excitation:** this is the blade passing frequency of the turbine. Excitations at this frequency can happen due to turbine blades passing the tower, creating small pressure disturbances, exciting the tower. Again, for a variable speed wind turbine this gives a frequency range, which can be calculated by: $f_{3P} = \frac{3 \cdot RPM-range}{60}$ [Hz]. A buffer of 10% is added to both ends of the range as a safety factor.

To avoid resonance the natural frequencies of the turbine support structure should lie outside the previously discussed zones. The first natural frequency of the system is herewith the most important one, as the second- and higher order frequencies generally lie outside the discussed excitation frequency zones. In the preliminary design phase a first estimate of the first natural frequency can be calculated using an approximation formula. For this purpose the wind turbine is modelled as a cantilever beam with a top mass as displayed in figure 2.7.

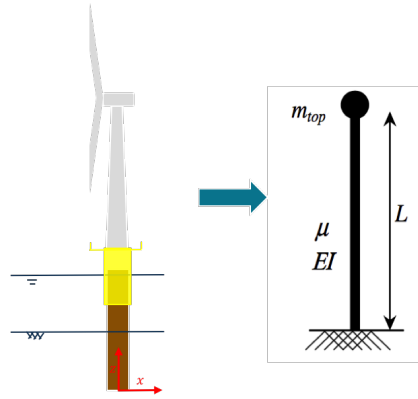


Figure 2.7: Wind turbine schematisation

The length of the model is taken as the total length of the turbine from seabed to hub-height [45]. With this schematisation, the first natural frequency can be calculated using the following formula [43]:

$$f_{nat,1}^2 = \frac{3.04}{2\pi^2} \cdot \frac{EI}{(m_{top} + 0.227\mu L)L^3} \quad [Hz] \quad (2.5)$$

In this formula EI is the tower bending stiffness, μ is the distributed mass of the tower, m_{top} is the top mass of tower (the total Rotor Nacelle Assembly) and L is the length of the schematised tower. To more easily understand the dependance of the structural parameters that influence the natural frequency the following relations, valid for thin walled cylinders, are substituted equation 2.5:

$$I \approx \frac{1}{8}\pi D_{av}^3 t_{wall} \quad [m^4], \quad \mu = \rho_{steel}\pi D_{av} t_{wall} \quad [kg/m], \quad a_{NF} = \frac{m_{top}}{\rho_{steel}\pi D_{av} t_{wall} L} \quad [-] \quad (2.6)$$

In these relations D_{av} and t_{wall} are the average diameter and wall thickness of the total structure, respectively. After this substitution the following relation for the first natural frequency of the turbine is obtained:

$$f_{nat,1} \approx \frac{D_{av}}{L^2} \cdot \sqrt{\frac{E_{tower}}{104(a_{NF} + 0.227)\rho_{steel}}} \quad (2.7)$$

The resulting equation 2.7 quite elegantly shows the influence of the most important structural parameters in the wind turbine support structure design. First of all it can be concluded that the first natural frequency is proportional to the average diameter, as well as inversely proportional to the squared length of the turbine support structure. Furthermore, the first natural frequency is inversely proportional to the square root of the ratio between the top mass and mass of the support structure's tower. These relations can be used to establish initial dimensions of the monopile structure to avoid overlap of the structure's natural frequency and excitation frequencies.

It must be noted that this initial approach does not include the effect that the soil has on the foundation of the monopile. Also, any lumped masses, such as grout layers or bolt flanges, are not taken into account. Even more so, taking the average diameter and wall thickness of a conical tower, results in an approximation for the stiffness of the tower. Among others, these aspect have an influence on the structure's natural frequency [30]. Therefore, it is a crucial to perform a more detailed dynamic analysis with inclusion of these aspects to be even more accurate on the predication of the structure's natural frequency.

2.5. (initial) Monopile dimensions

The initial dimensions of the monopile structure can now be established based on the criteria posed in section 2.4. A convenient way to combine the information of the excitation frequencies as well as the

estimated first natural frequency of the system, is to display this information in the frequency domain in the form of a diagram. Such a diagram instantaneously visualises the ranges in which the natural frequency may lie. Typically, three regions can be distinguished. These ranges lie left of the 1P excitation range (soft-soft), between the 1P and 3P excitation range (soft-stiff) and right of the 3P excitation range (stiff-stiff), respectively.

Commonly, the soft-stiff region is preferred as the soft-soft region yields very flexible structures that are in range of the wave excitation forces and the stiff-stiff region leads to very stiff, thus big and (too) expensive structures. An example of such a diagram, for an arbitrary Vestas V90 turbine with an average tower diameter and wall thickness of 4 meter and 0,05 meter respectively, is displayed in figure 2.8. It is common practise to avoid the whole 1P and 3P excitation range, so it is depicted in blocks. However, it is good to note that this obviously is a simplification of reality. It is reasonable to assumed that in the lower RPM-ranges of the rotor the energy that is put into the excitation is much lower than at the higher RPM-ranges. Moreover, the energy in these excitations might even not be high enough to put the system into resonance. It is not that easy to quantify the latter discussed, but future studies should provide more clarity on this subject.

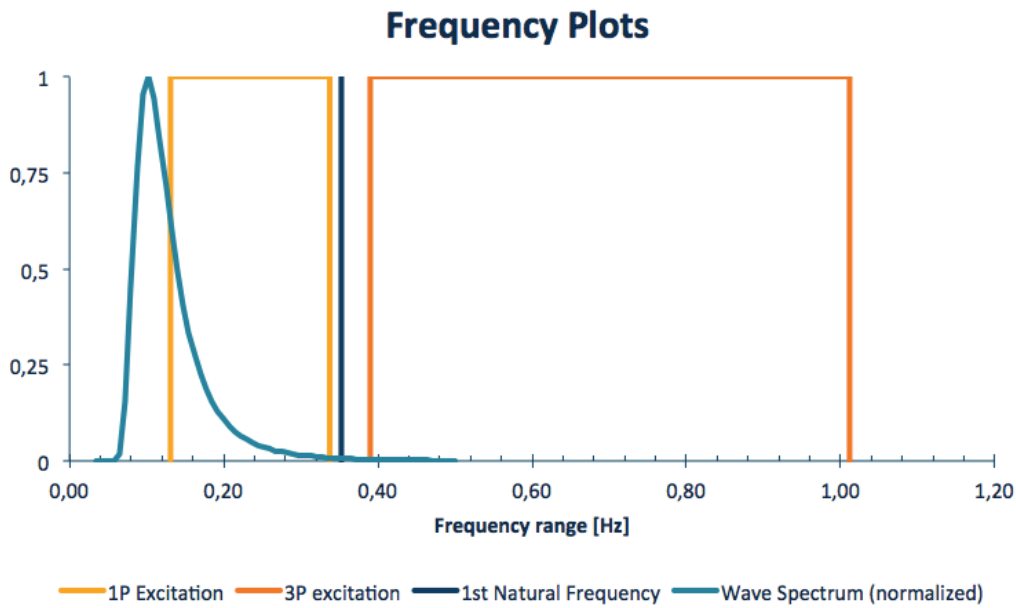


Figure 2.8: Frequency Assessment Diagram

The structural parameters in equation 2.7, along with other relevant structural input shall be used to create a support structure with natural frequency in the soft-stiff zone. As a rule of the thumb the following proportionality relations, as derived in section 2.4, can be used:

$$f_{nat,1} \propto D_{av}, \quad f_{nat,1} \propto \frac{1}{L^2}, \quad f_{nat,1} \propto \frac{1}{\sqrt{\frac{m_{top}}{m_{tower}}}} \quad (2.8)$$

Typically, the wind turbine tower's dimensions are specified by the turbine manufacturer thus can be used as input. This also holds for the top mass of the wind turbine. Moreover, the design heights, thus the length of the total turbine structure, have already been set in section 2.3. This means that the only two parameters that need to be altered in order to reach the required stiffness criteria is the (average) diameter and wall thickness of the monopile. As a start, one can start by trying different diameters and choosing a accompanying wall thickness according to rules of thumb based on industry practise [45]:

$$\frac{D_{av}}{t_{wall}} \approx 60 [-] \quad (2.9)$$

Of course, multiple iterations, preferably also including the other structural parameters like the design heights and wind turbine tower dimensions, are required to come to a sufficiently optimised design.

2.6. Load calculations

Now that the initial monopile dimensions are known, the next step in the design cycle will be to calculate the different loads acting on the turbine structure. For this purpose only permanent and environmental loads will be considered. This results in the following four main loads. The first is a permanent load while the second, third and fourth are environmental loads.

1. Permanent loads, G . These loads are the result of the weight of the total structure.
2. Wind drag loads, q_{wind} . These loads are the result of the wind blowing against the turbine structure.
3. Aerodynamic loads, T . The rotor of the turbine structure creates a thrust force as a result of the power production.
4. Hydrodynamic loads, q_{hydro} . These loads result from the waves and currents moving along the structure creating drag and inertia loads.

It must be noted that there is a wider variety of loads, including variable loads due to personnel present and boat landing session. However, these are insignificant compared to the previously mentioned four main load categories and will therefore not be elaborated on in this thesis. Furthermore, the only static load acting on the wind turbine is the permanent load G . All the other loads are of dynamic nature, creating a complex cocktail of time-varying actions on a typical wind turbine structure. The four load categories are graphically displayed in figure 2.9 and will be elaborated on in the subsequent sections.

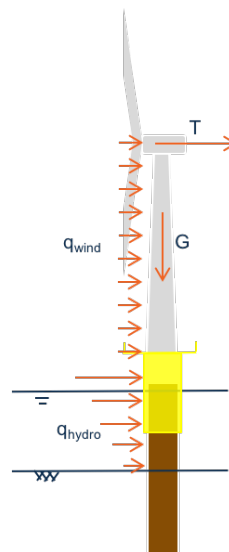


Figure 2.9: Four main loads acting on a typical wind turbine

2.6.1. Permanent loads

Permanent loads are static of nature and on a typical wind turbine are only caused by the self-weight of the structure and its accompanying components. In a monopile design, the main structural components are the wind turbine tower, possible transition piece and the monopile foundation. Their permanent load is calculated by the area of steel multiplied by the density of steel and gravitational acceleration:

$$G_{MP,tower} = \pi t(z)(D(z) - t(z)) \cdot L \cdot \rho_{steel} \cdot g \quad [N] \quad (2.10)$$

Furthermore, the permanent load consists of the remaining structural elements, such as the top mass m_{top} , access platform mass $m_{platform}$ or any other (lumped) masses such as bolt flanges and inter-

mediate platforms in the tower, etc. Their contribution is bundled under m_{other} for convenience sake. Consequently, the total permanent load G consists of the addition of these individual elements:

$$G = G_{MP,tower} + (m_{top} \cdot g) + (m_{platform} \cdot g) + (m_{other} \cdot g) \quad [N] \quad (2.11)$$

2.6.2. Wind drag loads

The first of the environmental loads considered is the wind drag load. Wind blowing along the wind turbine structure creates drag forces along the height of the tower. Wind speeds are both not uniform over the height and not stationary. Therefore, a mean wind speed cannot directly be used in a load calculation. First of all, a given mean wind speed must be extrapolated to the height that it will be used to calculate a wind drag load at. Two methods are commonly used for this purpose. One uses a logarithmic profile while the other uses a power law, as described in equations 2.12a and 2.12b, respectively, [15],[20].

$$V(z) = U_r \left(\frac{\ln(\frac{z}{z_0})}{\ln(\frac{z_r}{z_0})} \right) \left[\frac{m}{s} \right] \quad (2.12a)$$

$$V(z) = U_r \left(\frac{z}{z_r} \right)^{\alpha_{shear}} \left[\frac{m}{s} \right] \quad (2.12b)$$

In these equations, U_r is the wind speed at reference height z_r and z is the height at which the wind speed $V(z)$ is to be determined. Furthermore, the logarithmic profile uses z_0 , the roughness parameter, for extrapolation purposes, while the power law profile uses α_{shear} , the shear parameter, for this purposes. Appropriate for these parameters are prescribed in the design guides [15] and [20] and typical values include $z_0 = 0.002$ and $\alpha_{shear} = 0.14$, which correspond to rough sea-states offshore. It should be noted that these profiles do give different wind speeds extrapolation results as can be seen in figure 2.10. In this plot an average wind speed at 10 meters of $U_r = 12 \text{ [m/s]}$ was used along with the roughness and shear parameter values listed above.

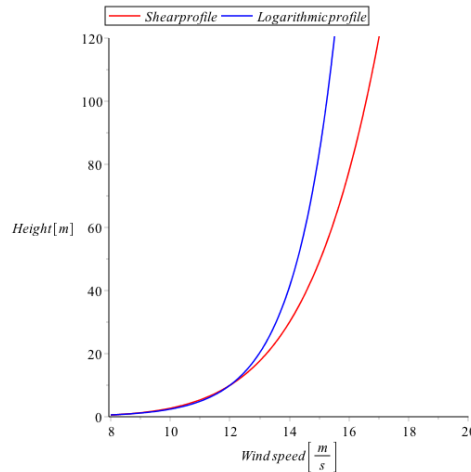


Figure 2.10: Logarithmic and shear wind profile extrapolation

The difference in these profiles at a hub height of $z_{hub} = 80 \text{ m}$ is already 10% in this case. This can have a significant effect on the calculated power production and resulting drag and thrust forces. Therefore, one profile shall be chosen in the beginning of the design phase to avoid any conflicts on the latter. Wind drag loads are not of too much influence as can be seen in 4.3, therefore a constant, average profile can be assumed to ease the calculation process. Other than this, there exist no real preference for one of the two profiles.

Secondly, the time varying character of the wind speed should be taken into account. First of all, there is the effect wind turbulence. Wind turbulence intensity is defined as the standard deviation of the time varying wind signal divided by the mean wind speed.

$$I_{w,t} = \frac{\sigma}{V_{mean}} \quad [\%] \quad (2.13)$$

This time varying character shall be modelled in accordance with the limit state and load case that is used for the calculation, for example normal turbulence model for fatigue limit state (FLS) calculations and extreme turbulence model for ultimate limit state (ULS) calculations. DNV and GL guidelines supply different models for this modelling [15], [20].

Next to the turbulence, the possibility of wind gusts should be taken into account, especially in ultimate load calculations. Guidelines prescribe values for such extreme gusts and wind speeds, however preference is given to site specific information. Yearly maxima can be extrapolated by means of Gumbel extreme analysis to find extreme wind speeds with a given return period N . To find values for such an extreme gust the tail of the wind spectrum can be used, but an approximated formula was derived by [47]. In this method a gust factor is defined as:

$$G(t) = 1 + 0.42I_{w,t} \cdot \ln\left(\frac{3600}{t}\right) \quad [-] \quad (2.14)$$

The extreme hourly mean wind speed $V_N(z)$ with return period N at height z can now be converted to an extreme gust wind speed $V_{gust,N}(z)$ with duration t by:

$$V_{gust,N}(z) = G \cdot V_N(z) \quad \left[\frac{m}{s}\right] \quad (2.15)$$

With a given (extreme) wind speed, calculated according to any of the above described methods, the wind drag force as a function of z along the wind turbine can be calculated. For example, using the extreme wind gust calculated in equation 2.15 this yields:

$$q(z)_{wind} = \frac{1}{2} \rho_{air} C_d D(z) V_{gust,N}(z)^2 \quad \left[\frac{N}{m}\right] \quad (2.16)$$

In this equation $D(z)$ is the diameter of the tower structure at height z and C_d is the drag coefficient accompanying this surface which is commonly set to $C_d = 1.0$ and $C_d = 0.7$ for a flat surface and a cylinder respectively [15]. Drag forces result from wind blowing along the tower, nacelle and parked rotor. The integral of these drag forces along the total height of the turbine L exposed to the wind yields the total horizontal wind drag force.

$$F_{wind} = \int_{z=sealevel}^{z=L} q(z)_{wind} dz \quad [N] \quad (2.17)$$

The horizontal drag force will also create a moment at any arbitrary reference point x separated by distance $l(z)$. The summation of these provides the total overturning moment due to the wind drag loads at point x :

$$M_{x,wind} = \sum q(z)_{wind} dz \cdot l(z) \quad [Nm] \quad (2.18)$$

2.6.3. Aerodynamic loads

Apart from drag loads on the tower, the wind also generates loads on the rotor, i.e. the wind turbine blades. Next to the drag forces, the blades also generate lift forces. The combination of momentum theory and blade element theory, commonly referred to as BEM-theory, was developed by Betz and Glauert (1935) to calculate these lift and drag forces along the wind turbine blade. To this extend the rotor area is modelled as an actuator disk in a stream tube, whereas the blades are split in blade elements, graphically shown in figure 2.11.

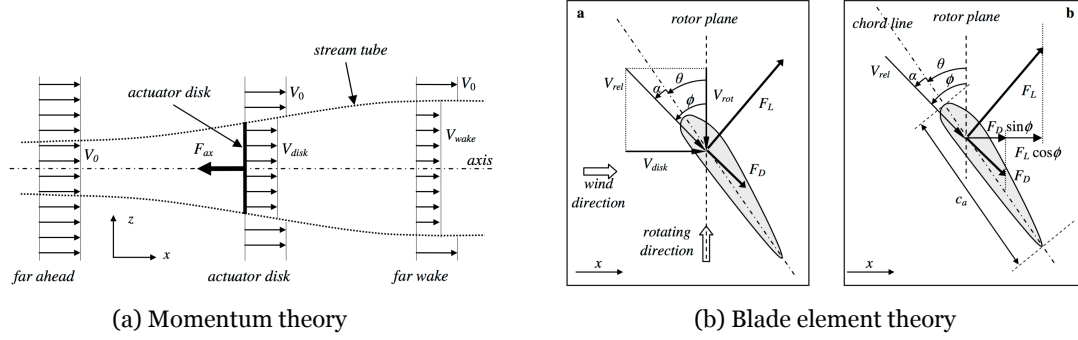


Figure 2.11: Momentum and Blade element theory [43]

In the momentum theory the relation between the undisturbed wind velocity V_0 and the velocity at the actuator disk V_{disk} is given by the induction factor is defined as:

$$a = \frac{V_0 - V_{disk}}{V_0} \quad [-] \quad (2.19)$$

Using the Bernoulli equation to calculate the resulting axial force F_{axial} on the actuator disk, one finds [39]:

$$F_{axial} = \frac{1}{2} A_{disk} \rho_{air} V_0^2 \cdot 4a(1-a) \quad [N] \quad (2.20)$$

With a given wind speed at the rotor, there are still two unknown variables in this equation, namely the axial force F_{axial} and the induction factor a . Therefore another equation is required to solve this problem. For this purpose the blade element theory is used. The blade elements each have their own aerodynamic properties such as a drag coefficient and lift coefficient $C_d(\alpha)$ and $C_l(\alpha)$, as a function of the angle of attack α . The forces on these blade elements are caused by the relative wind velocity V_{rel} , which is a result of the incoming wind velocity V_{disk} and the velocity due to the rotation of the blades V_{rot} . The latter is defined as the angular rotation speed Ω times the distance of the considered blade element to the root of the blade, r_{blade} .

$$V_{rel} = \sqrt{V_{disk}^2 + V_{rot}^2} \quad \left[\frac{m}{s} \right] \quad (2.21)$$

Where,

$$V_{disk} = V_0 \cdot (1 - a) \quad \text{and} \quad V_{rot} = \Omega \cdot r_{blade} \quad \left[\frac{m}{s} \right] \quad (2.22)$$

The lift and drag forces, as depicted in figure 2.11b, can then be defined as:

$$F_L = \frac{1}{2} C_l(\alpha) \rho_{air} V_{rel}^2 c_e \Delta_r \quad \text{and} \quad F_D = \frac{1}{2} C_d(\alpha) \rho_{air} V_{rel}^2 c_e \Delta_r \quad [N] \quad (2.23)$$

In these equation c_e is defined as the chord length of the blade and Δ_r is the length of the considered blade element. The total force in the x-direction of the blade element r is defined as the summation of the x-components of the lift and drag forces:

$$F_{x,e} = F_L \cdot \cos(\phi_e) + F_D \cdot \sin(\phi_e) \quad [N] \quad (2.24)$$

The total axial force is simply the summation of the x-components of the forces of all the blade elements of one blade, times the number of blades on the rotor.

$$F_{axial} = N_{blades} \cdot \sum_{e=root}^{e=tip} F_{x,e} \quad [N] \quad (2.25)$$

Combining the expressions of the momentum theory 2.20 and the blade element theory 2.25, yields a set of two equations with two unknowns, namely the total axial force, or thrust force T on the rotor and the induction factor, which can be solved for any given angle of attack.

Generated power

The generated power of the rotor can by definition be calculated by multiplying the total force with the velocity of the incoming wind speed:

$$P_w = F_{axial} \cdot V_{disk} \quad [W] \quad (2.26)$$

Rewriting equation 2.19 and substituting it in 2.26 to remove the actuator disk velocity V_{disk} from the equation, yields:

$$P_w = \frac{1}{2} A_{disk} \rho_{air} V_0^3 \cdot 4a(-1+a)^2 \quad [W] \quad (2.27)$$

The theoretical power that is present in the wind in the actual disk is:

$$P_{w,max} = \frac{1}{2} A_{disk} \rho_{air} V_0^3 \quad [W] \quad (2.28)$$

Using this expression, the ratio of the actual power extracted from the wind versus the available power in the wind can be established, which is defined as the power coefficient C_p :

$$C_p = \frac{P_w}{P_{w,max}} = 4a(-1+a)^2 \quad [-] \quad (2.29)$$

The maximum of this relation is $C_p = \frac{16}{27}$ at $a = \frac{1}{3}$, which is commonly known as the Betz-limit, as Albert Betz was the first to derive this relation [5]. It is obvious to understand that the power production of a wind turbine is to optimised at any given wind speed V_{disk} . Equation 2.26 elegantly shows that this implicitly means that the axial force F_{axial} , or thrust force T as it shall be called from now on, is to be maximised.

Modern variable speed wind turbines experience this situation near their 'rated wind speed'. After this wind speed the power output is kept constant when wind speed increases. This effectively means that the lift- and drag forces are decreased by means of pitching the blades. Due to this pitching the lift- and drag coefficients decrease making the air foil less efficient and thereby reducing the total thrust force acting on the rotor.

Obviously, the thrust force T at the rotor also results in a moment at an arbitrary point x with distance $l(z)$ from the rotor. This moment due to the aerodynamic load is given by:

$$M_{x,aero} = T \cdot l(z) \quad [Nm] \quad (2.30)$$

2.6.4. Hydrodynamic loads

Finally, hydrodynamic loads are present on the turbine. This environmental load is essentially caused by the speed and acceleration of the water particles in the water. There are two sources for these movements, namely currents and waves.

Currents

Currents are mainly caused due to the influences of the gravitational pull by the sun and the moon, known as tides, but can also be caused by other forces. These include the wind, the Coriolis effect, as well density gradients due to difference in temperature and salinity of different oceanic regions. In any case currents can be considered as stationary flows which therefore do not accelerate the water particles. The velocity of the water particles due to currents can be measured at the sea surface. As the water gets deeper the effect of these forces decrease, thereby reducing the velocity of the water particles. Different methods are used to model this effect, including a commonly used power law, prescribed by DNV in offshore wind turbine design [15]:

$$u(z)_{cur} = u_{0,cur} \cdot \left(\frac{z + d_{water}}{d_{water}} \right)^{\frac{1}{7}} \left[\frac{m}{s} \right] \quad (2.31)$$

In this equation $u_{0,cur}$ is an arbitrary current speed at sea surface, d_{water} is the water depth and $u(z)_{cur}$ is the current speed at height z .

Waves

The translation from waves to water particle velocities and accelerations is more complicated process. When looking at any given sea state, waves seem to come from any direction with widely varying amplitudes and periods. Intensive study has been performed on trying to describe such seemingly random sea states in mathematical models in order to perform calculations with this data. This process starts with measuring sea-surface elevation on a single point as function of time. These time-series of sea surface elevations in the time domain can then be converted to the frequency domain by a Fourier Transform to turn it into a spectrum notation. The sea surface elevation can be well represented by a large number of sinusoids each having their own amplitude and period, thus frequency. In figure 2.12 this is graphically depicted.

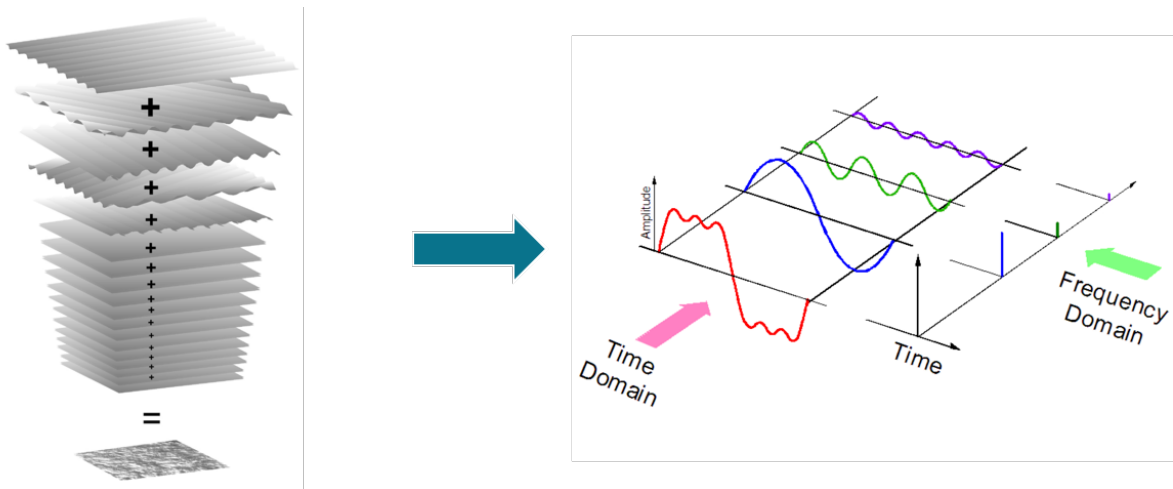


Figure 2.12: From time series to spectrum notation [22]

In reality the time-signal looks much more random, since the signal contains a lot more individual sinusoids than three. However, the working principle is the same. A more realistic time signal of a sea state and accompanying spectrum is given in figure 2.13.

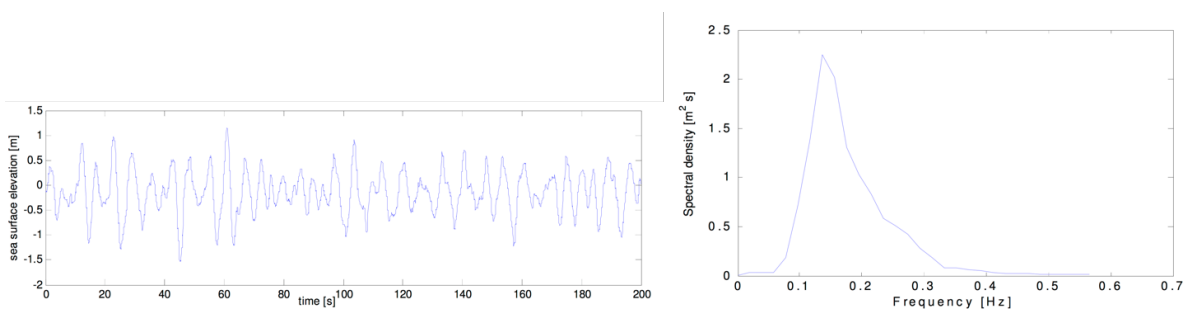


Figure 2.13: Sea surface elevation (left) and accompanying wave spectrum (right) [43]

The wave height that is used in calculations is the so called significant wave height H_s . From the time-series it can be defined as the average value of the highest one-third of the wave peaks. For a statistically stationary time series this equals four times the standard deviation σ of the time series. The square root of the zeroth order spectral moment of the time series equals the standard deviation again [22].

The mean zero crossing period T_z of the time signal is defined as the length of the time signal divided by the number of up-crossings in this signal. This period can also be found by the square root of the

zeroth order spectral moment divided by the second order spectral moment. The peak period T_p of the spectrum is the frequency at which the peak of the spectrum is located [22].

Many attempts have been undertaken to try and fit a formula for such wave spectra. The two most commonly used spectra are the Pierson-Moskowitz spectrum [31] and the JONSWAP-spectrum [18] for fetch unlimited and fetch limited sea-states respectively. These formula's try to recreate a wave spectrum with only a few parameters as input such as for example the significant wave height and peak- or zero crossing period. In this manner, a random sea-state can be created via an Inverse Fourier Transform that is statistically similar to a typical sea state at that particular location.

Airy wave theory

With a given wave height and period the motion of the water particles can be described by the linear Airy wave theory [22]. This theory describes the water particle motion orbital as a function of depth. These orbits move from circular to elliptical with decreasing water depths. Since Airy theory is only valid until the mean still water level, it does not account for the water particle motions in the wave crest. A common method to include water kinematics in the wave crests above still water level is to use the Wheeler Stretching method [46]. In this method the calculated wave kinematics up to still water level and stretches it up to the actual water level. The wave particle kinematics according to Airy wave theory and the Wheeler stretching method are displayed in figure 2.14.

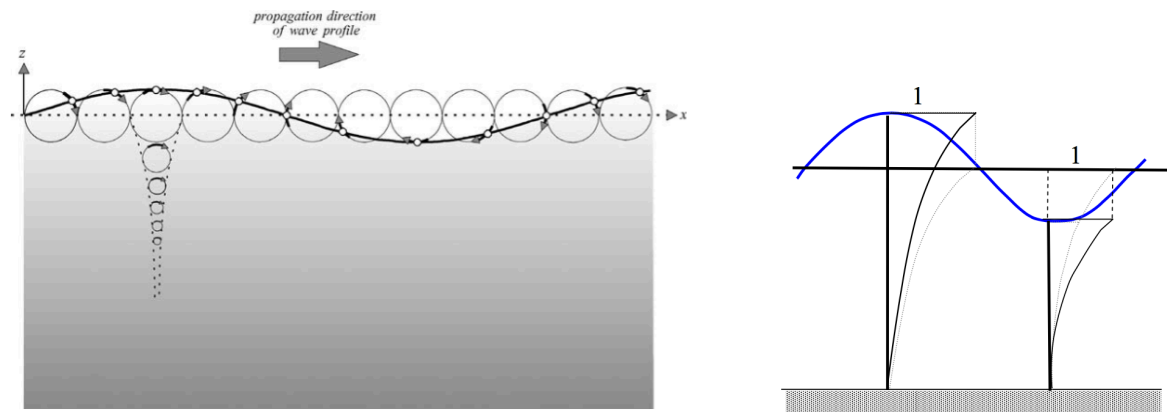


Figure 2.14: Wave Kinematics by Airy wave theory (left) and Wheeler stretching (right)

According to Airy wave theory the water particle velocity as a function of depth is described by:

$$u(x, t, z)_{wave} = \hat{u}(z)_{wave} \sin(\omega t - k_w x) \quad \left[\frac{m}{s} \right] \quad (2.32)$$

The amplitude of this wave particle velocity is most interesting as this will create the biggest load in the time and space varying wave particle motion. The value of this amplitude at height z is given by:

$$\hat{u}(z)_{wave} = \omega \zeta \frac{\cosh(k_w(d_{water} + z))}{\sinh(k_w d_{water})} \quad \left[\frac{m}{s} \right] \quad (2.33)$$

In these equations d_{water} is the water depth, furthermore ω is the wave frequency, k_w is the wave number and ζ is the wave amplitude which can be calculated by:

$$\omega = \frac{2\pi}{T_p} \quad \left[\frac{rad}{s} \right] \quad \text{and} \quad k_w = \frac{2\pi}{\lambda} \quad [m^{-1}] \quad \text{and} \quad \zeta = \frac{H_{wave}}{2} \quad [m] \quad (2.34)$$

In these equations H_{wave} is an arbitrary wave of which the wave kinematics needs to be calculated, for example a design wave H_{design} and λ is the wave length which can be calculated via the dispersion relationship [22]:

$$\lambda = \frac{g T_p^2}{2\pi} \cdot \tanh\left(\frac{2\pi d_{water}}{\lambda}\right) \quad [m] \quad (2.35)$$

The wave particle acceleration can be found by the derivative of equation 2.32 with respect to ω . Likewise the velocity, the most interesting parameter is the amplitude of this equation, which is described by:

$$\dot{u}(z)_{wave} = \omega \cdot \hat{u}(z)_{wave} \left[\frac{m}{s^2} \right] \quad (2.36)$$

The combined effect of currents (2.31) and waves (2.33 and 2.36) lead to the total water particle velocity and acceleration. To account for possible current blockage effects of nearby structures and the effect of wave spreading, which is neglected in this harmonic wave approach, possible scaling factors ζ_{block} and ζ_{spread} can be incorporated [45]. For offshore wind structures typical values include $\zeta_{block} = 1.0$ and $\zeta_{spread} = 0.906$. This leads to the following expressions for the wave particle kinematics:

$$u(z)_{water} = \hat{u}(z)_{wave} \zeta_{spread} + u(z)_{cur} \zeta_{block} \left[\frac{m}{s} \right] \text{ and } \dot{u}(z)_{water} = \dot{u}(z)_{wave} \zeta_{spread} \left[\frac{m}{s^2} \right] \quad (2.37)$$

Morison equation

The most common way to translate wave kinematics into forces on slender cylinders is by using the Morison equation [45]. This is a semi-empirical equation that calculates the drag and inertia forces due to the wave particle velocity and acceleration per unit length of the cylinder. Using equation 2.37 as input for the water kinematics, this equation is given by:

$$f_{Morison}(z) = f_d(z) + f_i(z) \left[\frac{N}{m} \right] \quad (2.38)$$

The drag load and inertia load are given by equation 2.39a and 2.39b respectively.

$$f_d(z) = \frac{1}{2} \rho_{water} C_d D_{pile}(z) \cdot |u(z)_{water}| u(z)_{water} \left[\frac{N}{m} \right] \quad (2.39a)$$

$$f_i(z) = \frac{\pi}{4} \rho_{water} C_m D_{pile}(z)^2 \cdot \dot{u}(z)_{water} \left[\frac{N}{m} \right] \quad (2.39b)$$

In these equations C_d and C_m are the drag- and inertia coefficients. These depend on the Reynolds number of the flow and the surface roughness of the pile. Typical offshore values include $C_d = 0.7 - 1.0$ and $C_m = 2.0$. However, in every load calculation these coefficient should be defined according to industry guidelines [15]. Furthermore, $D_{pile}(z)$ is defined as the diameter of the cylinder experiencing the hydrodynamic load. This diameter should include the presence, if applicable, of marine growth. The total diameter that should be used for calculation of hydrodynamic loads on an arbitrary monopile should therefore be:

$$D_{pile}(z) = D_{MP} + 2m_{growth} [m] \quad (2.40)$$

The total hydrodynamic load is not a simple summation of the drag and inertia load. Since the drag load is proportional to the velocity of the water particles and the inertia load is proportional to the acceleration, the two loads are 90 deg out of phase. Therefore, care should be taken when adding these individual loads to come to the total load. An approximation for the total hydrodynamic load is given by [45]:

$$q_{hydro}(z) = \sqrt{f_d(z)^2 + f_i(z)^2} \left[\frac{N}{m} \right] \quad (2.41)$$

The total horizontal hydrodynamic load along the submerged length of the structure L is given by the integral of the distributed horizontal load:

$$F_{hydro} = \int_{z=seabed}^{z=L} q_{hydro}(z) dz [N] \quad (2.42)$$

The total resulting moment at an arbitrary point x separated by distance $l(z)$ from the horizontal load at height z is given by:

$$M_{x,hydro} = q_{hydro}(z) dz \cdot l(z) [Nm] \quad (2.43)$$

Near future monopiles

It is important to note that the Morison equation describes the load on a cylinder in oscillatory flows quite well for slender structures. The slenderness ratio is defined as the cylinder diameter $D_{pile}(z)$ divided by the wave length λ . If this ratio tends to go to 1.0 i.e., the pile diameter reaches equal size as the wave length the validity of the Morison equation can be questioned. This can very well be the case for big monopile structure supporting offshore wind turbines in relatively shallow waters, leading to small wave lengths. The structure influences the wave field and diffraction effects begin to play a role [22]. A simple engineering approximation to correct for this effect is by means the MacCamy-Fuchs correction [8]. This correction describes a reduction of the inertia coefficient as a function of the above described slenderness ratio.

This effect is not of importance for the DOT500 monopile design, however attention should be paid to this matter when monopile size increases.

2.7. Limit states and load combinations

The loads calculated in section 2.6 are so called characteristic loads. When designing any kind of structure there is always an uncertainty in the calculation methods of the both the loads and the resistance of the material. Design guides like [15] and [20] specify methods to incorporate these uncertainties in the design and guarantee a structurally safe result. A common method that is used in the industry is the so called Load and Resistance Factor Design (LRFD) method. In this method the factored design load must equal or smaller than the design resistance:

$$S_d \leq R_d, \text{ where } S_d = S_k \gamma_i \text{ and } R_d = \frac{R_k}{\gamma_m} \quad (2.44)$$

This relation is commonly expressed in the form of a so called unity check, in which the design load is divided by the design resistance. This ratio should be smaller than one in order pass the check.

$$UC = \frac{S_d}{R_d} \leq 1.0 \quad [-] \quad (2.45)$$

Regularly one would like to keep the unity check as close to $UC = 1.0$ as possible. This means that the amount of steel in the structure is just enough to keep it safe thereby, reducing the cost of the structure as much as possible.

2.7.1. Limit states

This basic check should be performed for different limit states and different load combinations that could possibly be acting on the structure. Possible limit states include Ultimate Limit State (ULS), Serviceability Limit State (SLS), Accidental Limit State (ALS) and Fatigue Limit State (FLS). Within every limit state the design guides prescribe a number of load combination that the structure should be checked for. The ULS describes extreme survival conditions, while the ALS describes accidental events, such as boat collisions. The SLS describes criteria in every day operational states, such as maximum deflections and accelerations in the nacelle, while the FLS describes methods to calculate the accumulative fatigue damage due to every day conditions. The structure should be able to meet all criteria in every limit state in order to be structurally safe. The FLS calculations will be briefly touched upon in section 2.10, while the other two limit states will not be discussed as it is not of importance in the rest of this thesis. In the subsequent chapter a brief explanation of a simple ULS calculation shall be presented.

2.7.2. Load combinations

In offshore wind turbine design ULS design is an important step as the wind turbines are situated in a harsh unforgiving environment. The design load in such a case is given a load combination, consisting of the summation of relevant characteristic loads multiplied by their safety factor:

$$S_d = \gamma_g G + \gamma_e E \quad (2.46)$$

In this equation G is the permanent load and E is the environmental load, which consists of wind, wave, current and possibly ice loads. Furthermore, γ_e is the environmental load factor and γ_g is the permanent load factor. Typical ULS factors include $\gamma_e = 1.35$ and $\gamma_g = 1.1$ (unfavourable direction) or $\gamma_g = 0.9$ (favourable direction) respectively, however every load combination might be accompanied by different load factors. Guidelines like [15] and [20] prescribe numerous load combinations that should all be checked in order to ensure a structurally safe design. These load combinations include the use of different combinations of return periods and directionality's for the environmental parameters. However, a first order estimation of the ultimate strength of an offshore wind turbine structure can be obtained using the following load combination:

$$E = E_{wind} + E_{wave} + E_{cur} + E_{ice} + E_{water} \quad (2.47)$$

Since there is regularly no ice load in the North Sea this load will be disregarded from now on. In this basic, unidirectional load combination, DNV prescribes three load cases with combinations of return periods to use for the different environmental parameters. These values should then be used as input parameters in the load calculations discussed in section 2.6. The three load cases with different combinations of return periods are specified in table 2.1.

Table 2.1: Return periods for different environmental load cases

Load Case	Wind	Waves	Current	Ice	Water
Load case 1	50 years	5 years	5 years	-	50 years
Load case 2	5 years	50 years	5 years	-	50 years
Load case 3	Rated	5 years	50 years	-	50 years

Every one of these three load cases should be checked and one yielding the highest load is the governing load case. These design loads can then be bundled into one design load case at an arbitrary location consisting of a normal force N_{ed} , a base shear V_{ed} and an overturning moment $M_{y,ed}$. Typically, the highest reaction force is found near the seabed, as the moment resulting from the environmental loads is the highest near this point. The above described process for a design load located at the seabed is graphically displayed in figure 2.15.

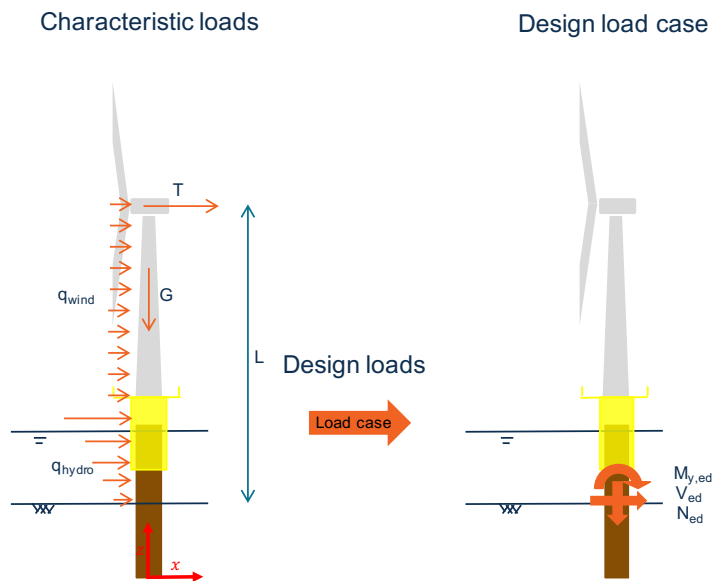


Figure 2.15: Characteristic loads to design load with different load cases

2.8. Foundation design

2.8.1. Soil modelling

Now that the design loads are calculated, the first check on the support structure can be performed. In the design of a monopile two main checks are performed to determine the stability of the foundation in both vertical and horizontal direction. The soil around the monopile will generate reaction forces depending on the type of soil and the dimensions of the monopile. These reaction forces must be big enough to resist the design loads that act on the monopile. These reaction forces are typically modelled by means of (non-linear) springs. A graphical overview is displayed in figure 2.16.

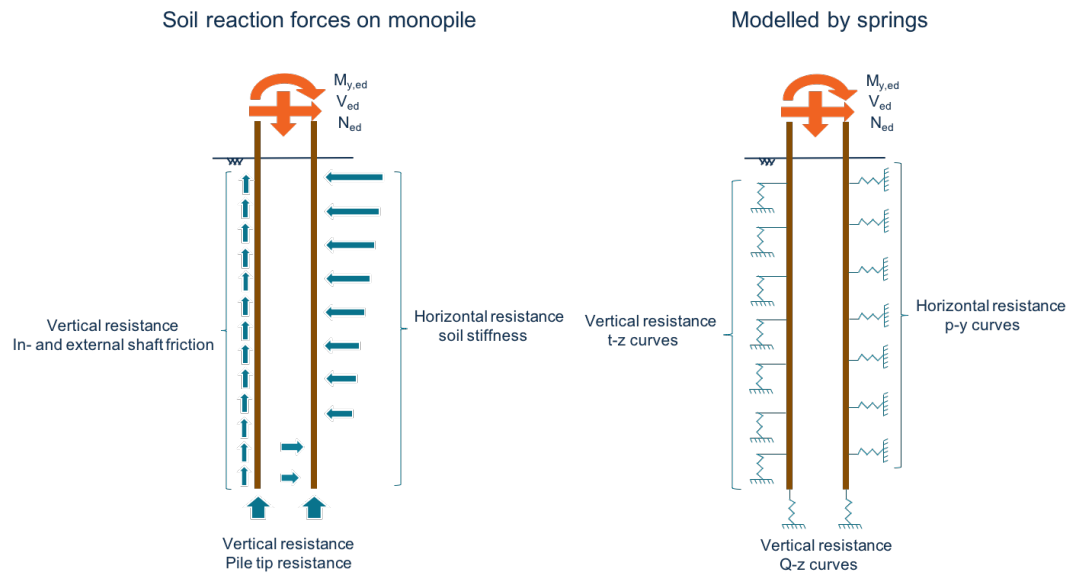


Figure 2.16: Modelling of soil-structure interaction by means of (non-linear) springs

The characteristics of these model springs highly depend on the type of soil and its accompanying parameters. Furthermore, the depth of the soil layer is of importance and the pile diameter also influences that spring's characteristics. Commonly, the vertical resistance springs are modelled using so called Q-z curves and t-z curves. They describe the amount of frictional resistance and tip resistance the soil is able to deliver. Furthermore, the horizontal soil resistance is commonly modelled using so called p-y curves. This non-linear spring model, models the soil's resistance to the horizontal displacement of the pile. Design guides like [26] and [3] prescribe the methods and formula's to calculate the spring characteristics.

For clarity's sake the method to quantify the p-y curve's characteristics is elaborated on shortly for sand, as it will be used in subsequent chapters of this thesis. First of all, an ultimate strength shall be determined per soil layer, given by:

$$p_u(X) = \begin{cases} (C_1X + C_2D_{MP})\gamma'X & \text{if } 0 < X \leq X_R \\ C_3D_{MP}\gamma'X & \text{if } X > X_R \end{cases} \left[\frac{kN}{m} \right] \quad (2.48)$$

In this equation C_1 , C_2 and C_3 are coefficients dependant on the friction angle of the soil ϕ . They can be obtained from design graphs in figure 2.17a [12]. Furthermore, γ' is the submerged unit weight of the soil and $hDmp$ is the monopile diameter. Lastly, X is the depth below the soil surface and X_R is the reference depth below which $C_3D_{MP}\gamma'X$ exceeds the value of $(C_1X + C_2D_{MP})\gamma'X$.

The p-y curve is established for every soil layer, as a function of depth via:

$$p(X) = A \cdot p_u(X) \cdot \tanh\left(\frac{kX}{Ap_u(X)} \cdot y\right) \left[\frac{kN}{m} \right] \quad (2.49)$$

In this equation k is the initial modulus of subgrade reaction and can be determined from a design graph displayed in figure 2.17b. Furthermore, $p(X)$ is the lateral soil resistance and y is the lateral soil deflection which create p-y curve together. Lastly, A is a factor that accounts for static or cyclic loading conditions. This factor is given by:

$$A = \begin{cases} 0.9 & \text{for cyclic loading} \\ \left(3 - 0.8 \cdot \frac{X}{D_{MP}}\right) & \text{for static loading} \end{cases} \quad [-] \quad (2.50)$$

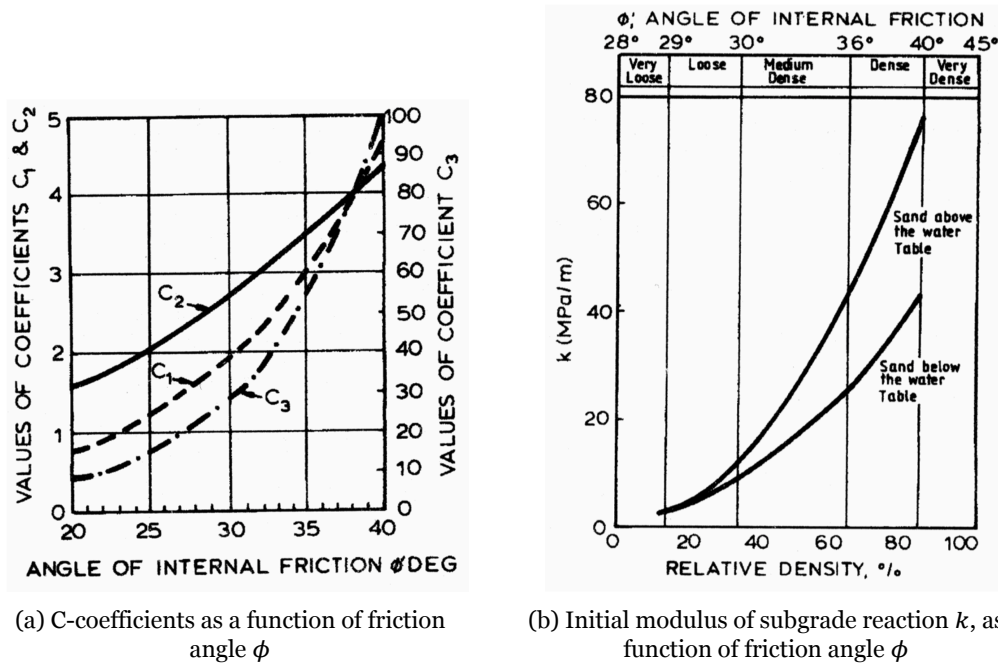


Figure 2.17: Design graphs to determine C-coefficients and k-value

2.8.2. Soil parameters

The most important input in the calculation methods to determine these soil-spring characteristics are the soil parameters, as they directly influence stiffness of the spring and can be quite a challenge to obtain. In the case of sand these are the effective soil unit weight γ' and the internal friction angle of the sand ϕ . They must be obtained by means of in-situ soil investigations. A common investigation that is done is a Cone Penetration Test (CPT). Such a test delivers two main parameters, namely the cone tip resistance (q_t) and shaft friction (f_s) as a function of depth. From these parameters the soil type can be predicted relatively accurately. However, it is not that straight forward to obtain the relevant soil parameters from these CPT's. To this extend, laboratory tests should be performed, which require actual soil samples from the site obtained from boreholes. This is a time consuming process, therefore a lot of research has been done to try and obtain (semi-)empirical formula's to accurately predict soil parameters directly from CPT's [6], [33], [28].

2.8.3. Design checks

When the soil-structure interaction has been properly modelled, the two design checks can be performed, including a vertical and horizontal stability check. For this purpose the design load case in the ULS shall be used as load input. First of all, the vertical check is quite straight forward. The maximum reaction force in vertical direction that the soil can generate, by means of friction on the sides of the pile and resistance on the tip of the pile, should be larger than the design force in vertical direction.

Secondly, the lateral stability of the foundation shall be checked. The design horizontal load and over-turning moment is introduced on the horizontally spring-supported foundation. The displacement of

the foundation pile as a result of this load case and non-linear soil resistance should be calculated as a function of depth. This is displayed in figure 2.18.

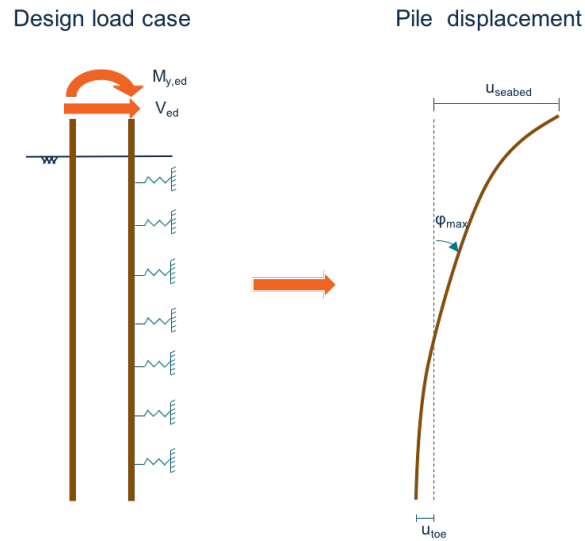


Figure 2.18: Pile displacement due to design load

The displacement graph of the foundation pile should suffice a number of criteria prescribed in the design guides like [26], [3]:

$$u_{seabed} < 0.03 \cdot D_{MP} [m] \quad \text{and} \quad u_{toe} < 0.02 [m] \quad \text{and} \quad \phi_{max} < 0.5 [^\circ] \quad (2.51)$$

The criteria for both the vertical strength and horizontal stability of the foundation result in the optimal length of the foundation. In other words, the total length of the pile should be long enough to mobilise enough soil for the reaction forces to be big enough. This design check yields the total penetration depth for the monopile z_{toe} .

2.9. ULS: Strength and stability checks

With an optimised foundation present the first checks with regard to the structural strength of the structure can be performed. Design guides prescribe a range of checks that should be performed in order to guarantee a structurally safe design. Two basic strength and stability checks will be described subsequently, namely a yield stress check and a global buckling check. It is important to note that there are many other checks that need to be performed in order to ensure a safe design which are all described in the design guides like [15] and [20].

Strength check

The first check is to see if there is any point in the structure where the stresses will be so high that it will cause the material to yield. When steel starts to yield it means that it deforms plastically i.e., permanent deformation. This is something that one in general would like to prevent from happening. A number of points along the structure should be checked. For this example the seabed is chosen as reference point to check the stresses, as this is where the load are the highest. For this check to be ok, the stresses in the monopile due to the factored loads should be lower than the factored yield stress. The stresses due to the different loads in the design load cases shall be found by:

$$\sigma_{axial} = \frac{N_{ed}}{A_{MP}(D, t)} \left[\frac{N}{m^2} \right], \quad \sigma_m = \pm \frac{M_{y,ed}}{W_{MP}(D, t)} \left[\frac{N}{m^2} \right], \quad \tau = \frac{V_{ed}}{0.5\pi D_{MP} t_{MP}} \left[\frac{N}{m^2} \right] \quad (2.52)$$

To find the total stress resulting from these different stress components the Von Mises equivalent stress formula can be used. In this uni-directional load case the simplified version can be used to find the total

equivalent stress to be:

$$\sigma_{VM} = \sqrt{(\sigma_m + \sigma_{axial})^2 + 3\tau^2} \left[\frac{N}{m^2} \right] \quad (2.53)$$

In this equation the positive value of σ_m shall be used to find the highest total stress due to the combination of axial and bending load. This design stress should be smaller than the factored yield stress in order to pass this check.

$$UC = \frac{\sigma_{VM}}{f_y} > 1.0 \quad \text{with} \quad f_y = \frac{\sigma_{yield}}{\gamma_m} \left[\frac{N}{m^2} \right] \quad (2.54)$$

From these formulas it can be concluded that these stresses can be decreased by increasing D_{MP} or t_{MP} . Since D_{MP} is already fixed with regard to the stiffness criterion set in 2.4, the most prominent parameter that can be used to optimise this check is the wall thickness of the monopile t_{MP} . However, optimising offshore wind structures for ULS calculations is commonly not done as the most important design driver is fatigue [43]. Therefore, in this early design phase the unity check can be set to $UC \approx 0.6 - 0.7$ as a maximum to find an 'optimised' value for the wall thickness.

Global stability check

The global buckling check is a check on the total stability of a structure. So instead of failure due to yielding, the structure can fail if the total load combination is big enough in order to compromise the stability of the structure. Guidelines provide semi-empirical formulas to check for the resistance to global buckling [20]. The stability of the structure is reduced due to normal loads and overturning moments. Therefore, the reduced resistance to the normal force χN_{rd} and the overturning moment M_{rd} , combined with a slenderness reduction δ_N should be bigger than the design loads.

$$u_N = \frac{N_{ed}}{\chi N_{rd}}, \quad [-] \quad u_M = \frac{M_{y,ed}}{M_{rd}}, \quad [-] \quad \delta_N = \min(0.25 \cdot \chi \phi_{buck}, 0.1) \quad [-] \quad (2.55a)$$

$$UC = (u_N + u_M + \delta_N) < 1.0 \quad [-] \quad (2.55b)$$

The global buckling check's most important parameter is the reduced slenderness ratio $\bar{\lambda}_{buck}(EI, L_{buck})$, which is most of all dependent on the buckling length L_{buck} and the bending stiffness of the structure $EI(D, t)$. Likewise the yield check this check can be optimise to find satisfying values for the unity check $UC \approx 0.6 - 0.7$. With the diameter and length of the structure fixed the most important parameter to tune is the wall thickness of the monopile t_{MP} .

2.10. FLS: Fatigue damage check

As a final check in the design the structure must be checked on fatigue damage in the FLS. Fatigue failure is the effect of the cumulative damage that a structure experiences due to continuously varying stresses levels. A structure can withstand a maximum number of cycles N_i at any given stress range S_i before cracks start to occur which will eventually lead to failure. In the ULS-case the number of cycles is 1. However, for lower stress levels the number of cycles n_i before failure is bigger. The limit of these cycles are typically depicted in so called SN-curves, depicted in figure 2.19. Guidelines prescribe specific SN-curves for different types of steel and locations in the structure [14].

When the number of cycles n_i at every stress range S_i is known the total fatigue damage on the structure can be calculated via Miner's fatigue damage rule [34]. This rule states that the cumulative fatigue damage D_f is the sum of the actual number of cycles n_i divided by the maximum number of cycles N_i at every stress range i .

$$D_f = \sum_i \frac{n_i}{N_i} \quad [-] \quad (2.56)$$

If the fatigue damage is smaller than $D_f < 1.0$, then the structure is considered structurally safe with regard to fatigue. Of course, the challenge in this method is to find the number of stress cycles at every

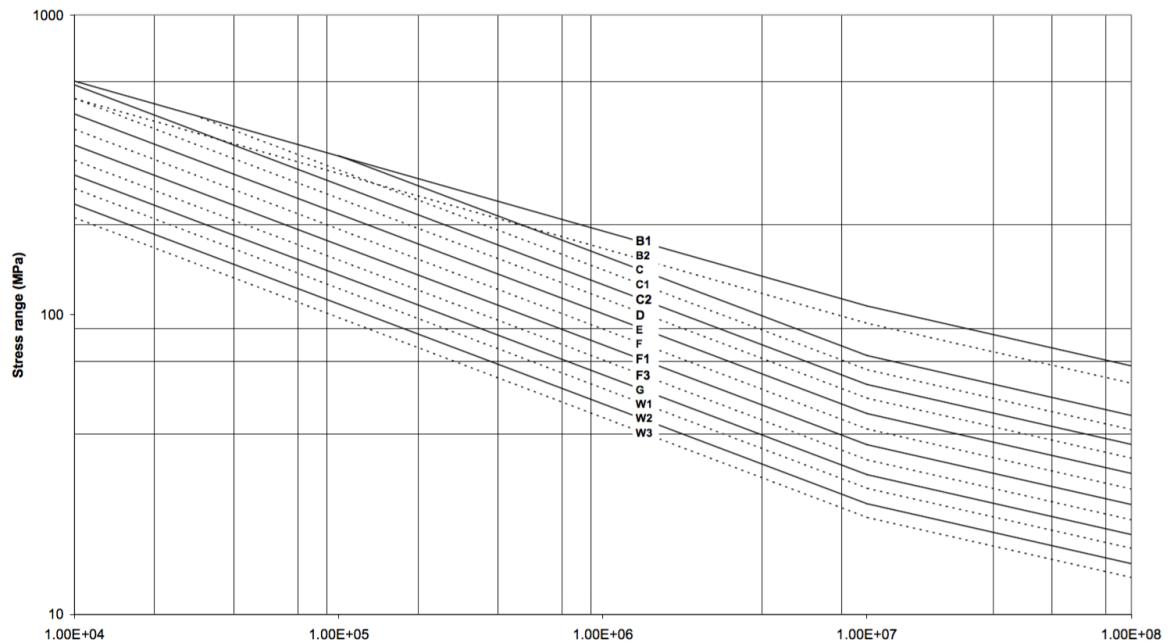


Figure 2.19: Typical SN-curves for structural steel

stress range in the structure. Typically, time domain simulations are performed in programs such as Bladed, simulation the structure's response in a lot of different common sea states. With methods like peak- and rain-flow counting [43] the number of stress cycles can be counted after which the total fatigue damage can be checked in that specific statistically equivalent sea state.

Fatigue calculations are typically very time consuming calculations as a lot of points in the structure, especially structure details such as welds and joints, need to be checked simulating the structure's response for a great amount of sea states. If any of these points fail the structure's resistance to these stresses should be increased by for example increasing the diameter or wall thickness or eliminating sharp edges or any other irregularities in the shape that cause stress concentrations.

2.11. Conclusion

The design cycle of an offshore wind support structure has been explored in this chapter, touching upon the relevant aspects in the design with respect to this thesis. As for the loads acting on the wind turbine, four main load categories can be distinguished. These consist of permanent load (G), thrust force due to the operational turbine (T), wind drag loads along the tower (q_{wind}) and finally hydrodynamic loads (q_{hydro}) as a result of waves and currents flowing around the support structure. The relative influence of these shall be explored in section 4.3.

The main design parameters that can be played with are the monopile diameter and wall thickness (D_{MP}) and (t_{MP}) and the length of the total structure (L). The latter is most prominently influenced by the different design heights that shall be established in the design process. The diameter (range) of the monopile is most prominently influenced by the stiffness criteria of the structure to minimise resonance possibilities by moving any of the structure's natural frequencies outside excitation ranges. It can be questioned whether the total excitation ranges should be avoided, considering the (limited) energy in the excitation compared to the damping in the structure. This might provide some thought for future research. In any case, it is concluded that the natural frequency of the DOT500 support is an important parameter to know and shall thus be measured in the measurement campaign.

The structure's wall thickness mainly results from design checks with respect to a number of load cases in different limit states. From industry practise it can be concluded that the offshore wind turbine support structure's main design driver, are the design checks in the fatigue limit state as a result of the

dynamic load input from the harsh offshore environment. Careful identification and prediction of the natural frequency is therefore of great importance and shall be treated in section 6.2.

Finally, it must be noted that the dimensions of the tower structure are generally fixed by the wind turbine manufacturer. This limits the design freedom that the engineer has in optimising the total structure to possibly reduce the cost by saving on the amount of steel that is used in the structure. This design freedom is especially relevant in the process of reaching the stiffness criterion in the dynamic analysis of the structure. Being able to play dimensions of the wind turbine tower could eventually reduce the size, weight and therefore cost of the monopile foundation structure.

Theory on slip-joint principle and design

3.1. Introduction

Normally, the wind turbine tower is connected to the monopile by means of a transition piece. This piece of steel is fixed to the monopile by means of a grouted connection and the wind turbine tower is subsequently bolted on top. The slip-joint connection is an alternative way of connecting the wind turbine tower to its foundation. The two cones are directly fitted on each other without the use of extra bolts or welding. Likewise grouted connections, static and dynamic loads are transferred through contact forces between the surface contact of the two cones, mainly via friction. However, without the use of an extra structural element. This potentially saves material costs and above all, valuable offshore installation time.

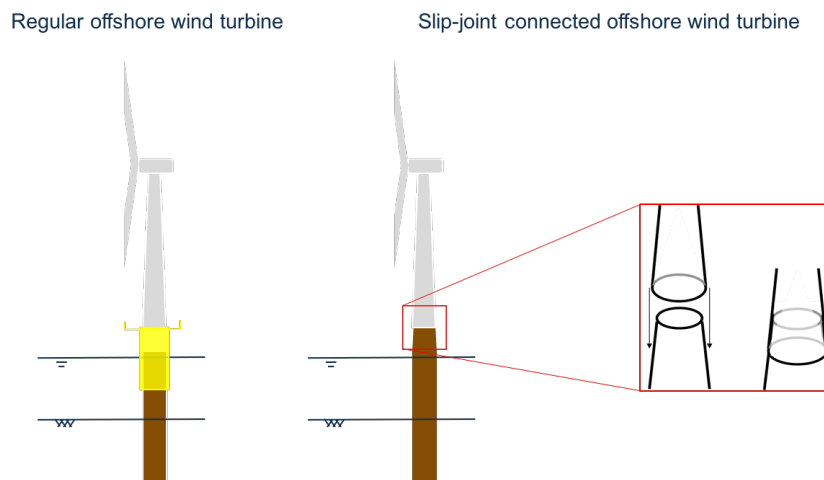


Figure 3.1: Slip-joint connected offshore wind turbine

The aim of this chapter is to describe and elaborate on the current theory on the slip-joint connection for offshore wind turbines. Furthermore, any other considerations with regard to the installation and design of a slip-joint connection will be treated. This will lay the theoretical bases for the next steps in the thesis.

Section 3.2 presents the theory on the working principle of a slip-joint connection, elaborating on the stresses within the slip-joint during static equilibrium and (ultimate) bending moments. The parameters that influence the stresses will be identified. Section 3.3 elaborates on the influence of fabrication tolerances on the slip-joint's stresses and section 3.4 presents some notes on the installation of a slip-joint connection. Finally, section 3.5 lists the main conclusions from the above described evaluation.

3.2. Slip-joint working principle

Although the slip-joint connection has been used on some occasions in the last twenty years, limited research has been performed on this alternative connection. In 2003 a prospective study was performed by DOWEC, which used the 'Duinvogel' slip-joint as case study. It was concluded that the use of a slip-joint connection onshore did not yield any structural reliability problems. It shortened installation considerably and no unwanted settlement or failure of the steel within the joint was observed. Also, no major problems were foreseen with the usage of this connection offshore [27]. The primary equations shown in this section are based on the latter named report.

When in 2008 grout connection started to fail aplenty, the research on the topic started to pick up and scale experiments were performed on the TU Delft [16], [35]. The focus of this research was mainly on the installation side of the slip-joint as shall be elaborated on in section 3.4. Both studies assume that friction force is the main basis for the working principle of the joint.

3.2.1. Static vertical force equilibrium

To get a feeling for this basic working principle, an arbitrary slip-joint connection is presented. To this extent, the vertical equilibrium of forces is inspected as a start, depicted in figure 3.2. In this example, the upper cone represents the wind turbine tower and the lower cone represents the monopile.

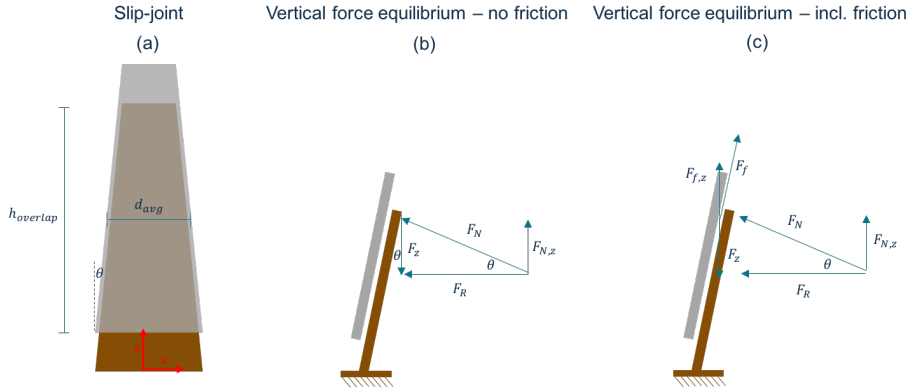


Figure 3.2: Vertical force equilibrium slip-joint

No friction

For a proper fixation of the two cones, the vertical downward force F_z , the gravitational force due to the self-weight of the upper cone, must be in equilibrium with counter-acting forces. In the fictional case where no friction is present (figure 3.2b) this is the vertical component of the normal force F_N .

$$F_z = F_{N,z} = F_N \sin(\theta_{cone}) \quad [N] \quad (3.1)$$

As a result a radial component of this normal force is exerted on the inside of the upper cone. This radial force is given by 3.2a or as a function of F_z by 3.2b.:

$$F_R = F_N \cos(\theta_{cone}) \quad [N] \quad (3.2a)$$

$$F_R = \frac{F_z}{\tan(\theta_{cone})} \quad [N] \quad (3.2b)$$

For this example's sake it is assumed that the two cones perfectly fit together, thus that the radial force F_R is divided along the total surface area of the overlap of the joint to create a uniform pressure P , in accordance with the pressure vessel assumption. The pressure is then given by:

$$P = \frac{F_R}{h_{overlap} \cdot D_{t,i} \pi} \left[\frac{N}{m^2} \right] \quad (3.3)$$

This uniform pressure then results in a tangential- or hoop stress σ_{hoop} in the upper cone of the turbine tower, given by:

$$\sigma_{hoop} = \frac{PD_{t,i}}{2t_{tower}} \left[\frac{N}{m^2} \right] \quad (3.4a)$$

$$\sigma_{hoop} = \frac{F_R}{2t_{tower} \cdot \pi \cdot h_{overlap}} \left[\frac{N}{m^2} \right] \quad (3.4b)$$

Substituting equation 3.2b in equation 3.4b, yields an expression for the hoop stress as a function of the vertical gravitational force:

$$\sigma_{hoop} = \frac{F_z}{2t_{tower} \cdot h_{overlap} \cdot \pi \cdot \tan(\theta_{cone})} \left[\frac{N}{m^2} \right] \quad (3.5)$$

Formula 3.5 gives the average hoop stress in the tower that is introduced in the tower to meet the vertical force equilibrium criteria. This expression is valid, assuming a linear varying diameter $D_{t,i}$ over the height of the slip-joint overlap length $h_{overlap}$. This is graphically displayed in figure 3.3.

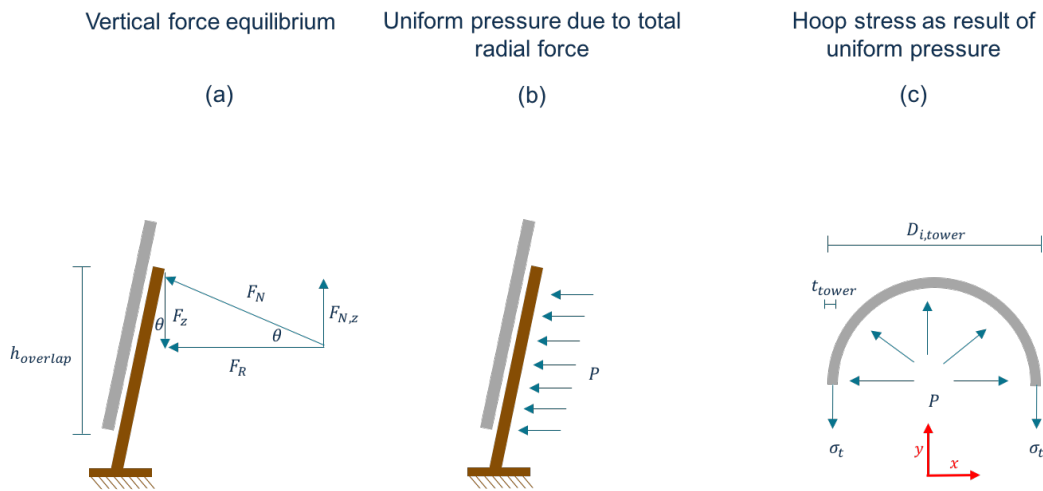


Figure 3.3: Hoop stress as result uniform pressure due to radial force

Including friction

Of course, in an actual situation a friction force will be present as a result of the two conical sections touching each other. This is displayed in figure 3.2c. Assuming a linear coulomb friction model, the friction force F_f in the static situation is dependent on the normal force F_N via a static friction coefficient μ_s :

$$F_f = \mu_s F_N \quad [N] \quad (3.6)$$

This friction force acts by definition in the perpendicular direction of the normal force. The vertical component of this friction force is:

$$F_{f,z} = F_f \cdot \cos(\theta_{cone}) \quad [N] \quad (3.7)$$

The total vertical equilibrium is now found by:

$$F_z = F_{N,z} + F_{f,z} \quad [N] \quad (3.8a)$$

$$F_z = F_N \cdot \sin(\theta_{cone}) + \mu_s F_N \cdot \cos(\theta_{cone}) \quad [N] \quad (3.8b)$$

Dividing equation 3.8b by $\cos(\theta_{cone})$ and rewriting this expression, yields the following relation:

$$\frac{F_z}{\cos(\theta_{cone})} = F_N \cdot (\tan(\theta_{cone}) + \mu_s) \quad [N] \quad (3.9)$$

Rewriting equation 3.2a as a function of F_R and substituting the resulting expression in equation 3.9, yields:

$$F_z = F_R \cdot (\tan(\theta_{cone}) + \mu_s) \quad [N] \quad (3.10)$$

The latter equation can easily be rewritten as a function of F_z to obtain:

$$F_R = \frac{F_z}{(\tan(\theta_{cone}) + \mu_s)} \quad [N] \quad (3.11)$$

Now substituting equation 3.11 in equation 3.4b, yields the following relation for the average hoop stress in the tower σ_{hoop} :

$$\sigma_{hoop} = \frac{F_z}{2t_{tower} \cdot h_{overlap} \cdot \pi \cdot (\tan(\theta_{cone}) + \mu_s)} \quad \left[\frac{N}{m^2} \right] \quad (3.12)$$

Equation 3.12 quite elegantly shows the effect of the friction coefficient μ_s on the average hoop stress in the tower σ_{hoop} . For any small value of this friction coefficient, the magnitude of the hoop stress decreases considerably. Using typical values for the friction coefficient and tower angle, $\mu_s = 0.1$ [–] and $\theta_{cone} = 0.5$ [°] respectively and the formula's above, the following relations can be found:

- For a small value for the friction coefficient $\mu_s = 0.1$ the total normal force F_N is reduced by 481%.
- At this given friction coefficient the friction takes up 79.3% of the total upward vertical force, while the vertical component of the normal force only accounts for 20.7%.

Furthermore, one finds from equation 3.12 that the hoop stress in the tower is inversely proportional to the tower wall thickness t_{MP} and the total overlap length of the slip-joint $h_{overlap}$. Also, the hoop stress is inversely proportional to the friction coefficient μ_s and the tangent of the cone angle $\tan(\theta_{cone})$.

$$\sigma_{hoop} \propto \frac{1}{t_{MP}}, \quad \sigma_{hoop} \propto \frac{1}{h_{overlap}}, \quad \sigma_{hoop} \propto \frac{1}{\tan(\theta_{cone})}, \quad \sigma_{hoop} \propto \frac{1}{\mu_s} \quad (3.13)$$

In the preceding derivation it is assumed that the conical sections have a perfectly linear diameter variation over the height. Furthermore, the assumption is made that the tower has perfectly circular cross-section in the x-y plane. In a real situation, this is not the case. The cause and magnitude of this, together with the implications of this will be elaborated on 3.3. A first order model taking into account these variations shall be discussed in section 6.3. The change on the friction force over time, due to for example the relaxation of the steel, are not touched upon, but can influence the total equilibrium.

3.2.2. Static bending moment at slip-joint connection

Apart from the static vertical load, the slip-joint will also have to endure horizontal loads as a result of the environmental and operational loads of the turbine discussed in section 2.6. These loads will also cause stresses in the tower and monopile, especially due to the resulting moment of the horizontal forces. Therefore, this will be the focus of the subsequent evaluation. Limited literature is available on this matter, although [27] briefly touches upon this subject. This will be elaborated on in the next section. Also, a new proposed first order method is discussed subsequently.

Literature method

In the DOWEC report [27] the effect of the bending moment is taken into account by assuming that the bending moment shall introduce horizontal contact forces within the slip-joint. These forces are assumed to have a linearly increasing distribution over height. This is graphically displayed in figure 3.4.

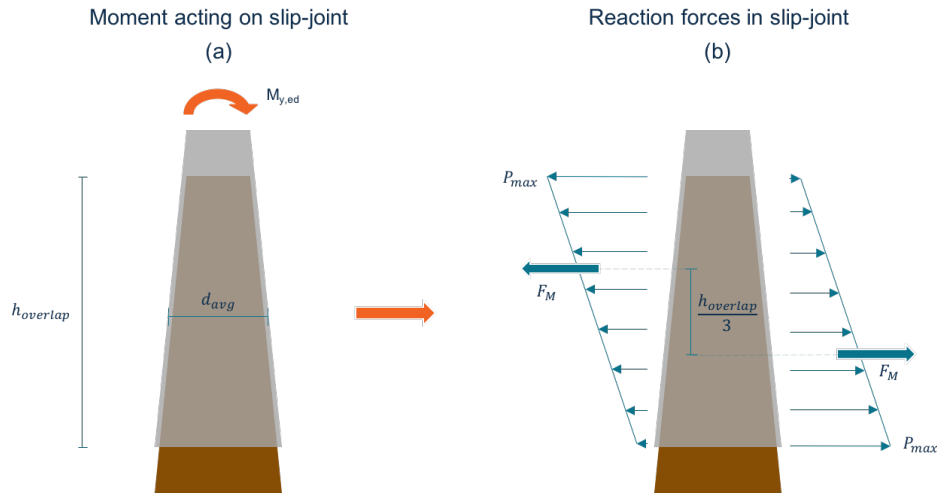


Figure 3.4: Internal forces resulting from moment on slip-joint

In this figure the linearly increasing contact forces resulting in a distributed pressure on the inside of the tower ranging from $P = 0$ to P_{max} . The summated contact forces F_M on both sides of the slip-joint are assumed to act on $\frac{h_{overlap}}{3}$ from the top of the linear profile. These summated forces F_M should be equal and in opposite direction to the moment acting on the slip-joint in order to be in equilibrium. This yields the following equation for the summated forces F_M :

$$F_M = \frac{M_{y,ed}}{\left(\frac{h_{overlap}}{3}\right)} [N] \quad (3.14)$$

Taking into account the linearly increasing triangular pressure profile, the maximum pressure $P_{w,max}$ induced on the inside of the tower can be expressed as:

$$P_{max} = \frac{2F_M}{h_{overlap}D_{t,i}} \left[\frac{N}{m^2} \right] \quad (3.15)$$

Substituting equation 3.14 in equation 3.15 yields the following relation for the maximum pressure P_{max} on the inside of the tower:

$$P_{max} = \frac{6M_{y,ed}}{h_{overlap}^2 D_{t,i}} \left[\frac{N}{m^2} \right] \quad (3.16)$$

Now, using equation 3.4a for the hoop stress resulting from an inside pressure, the following relation is obtained for the hoop stress σ_{hoop} in the tower resulting from the maximum pressure P_{max} introduced on the tower wall as a result of the bending moment $M_{y,ed}$:

$$\sigma_{hoop} = \frac{3M_{y,ed}}{h_{overlap}^2 t_{tower}} \left[\frac{N}{m^2} \right] \quad (3.17)$$

The latter equation shows that the main influences on the hoop stress as a result of a bending moment on the slip-joint are the wall thickness of the tower t_{tower} and the total overlap length of the slip-joint connection $h_{overlap}$. A inversely and quadratic inversely proportional relation respectively.

$$\sigma_{hoop} \propto \frac{1}{t_{MP}}, \quad \sigma_{hoop} \propto \frac{1}{h_{overlap}^2} \quad (3.18)$$

In the latter derivation it is assumed that there is a uniform contact area between the two cones and the diameter varies linearly over the height of the slip-joint. Furthermore, the tower and monopile are assumed to have a perfectly circular cross-section in the x-y plane. The latter assumptions can be questioned as shall be elaborated on in section 3.3.

Proposed alternative method

In stead of assuming horizontal reaction forces counter-acting the moment, one could also argue that there will be vertical reaction forces. These vertical reaction forces are the result of friction- and contact forces, as explained in 3.2.1. The moment essentially introduces two vertical equal but opposite forces on each side of the tower, split by the neutral line of the bending moment. This is depicted in figure 3.5.

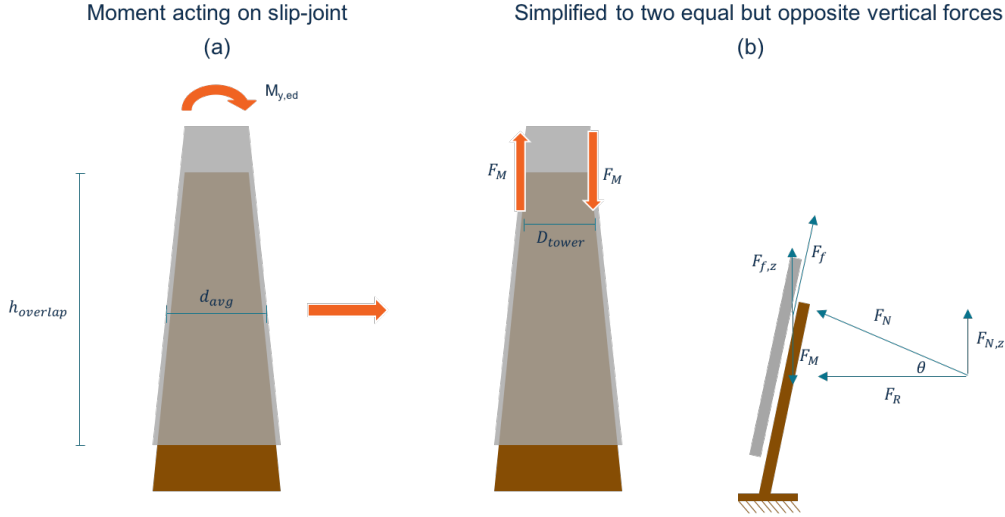


Figure 3.5: Internal forces resulting from moment on slip-joint

The value of this vertical forces can be readily obtained by dividing the moment by the distance separating the two forces, in this case the tower diameter at the top of the slip-joint:

$$F_M = \frac{M_{y,ed}}{D_{t,slip}} \quad [N] \quad (3.19)$$

The uniform pressure on the inside of the tower as a result of this vertical force can readily be obtained by equation 3.3 derived in section 3.2.1. However, this time the total radial force results in a pressure on only half of the total surface area i.e., the left or right side of the neutral line of the bending moment. This yields the following equation:

$$P = \frac{F_R}{h_{overlap} \cdot 0.5D_{t,i}\pi} \left[\frac{N}{m^2} \right] \quad (3.20)$$

In accordance with equation 3.11, the radial force that acts on the left or right side of the neutral line is given by:

$$F_R = \frac{F_M}{(\tan(\theta_{cone}) + \mu_s)} \quad [N] \quad (3.21)$$

Therefore, the uniformly distributed pressure acting on the tower wall is given by:

$$P = \frac{F_M}{h_{overlap} \cdot D_{t,i}\pi \cdot (\tan(\theta_{cone}) + \mu_s)} \left[\frac{N}{m^2} \right] \quad (3.22)$$

Combining equation 3.22 with equation 3.19 and substituting it in equation 3.4a, the following relation is found for the average hoop stress σ_{hoop} in the tower as a result of the bending moment:

$$\sigma_{hoop} = \frac{M_{y,ed}}{t_{tower} \cdot h_{overlap}\pi \cdot D_{t,slip} \cdot (\tan(\theta_{cone}) + \mu_s)} \left[\frac{N}{m^2} \right] \quad (3.23)$$

Apart from the assumptions stated in section 3.2.1, it is assumed in the preceding derivation that the pressure P resulting from the vertical force F_M is distributed uniformly both over the height and half of the circumference of the tower.

Discussion

It must be noted that both the methods named in the previous subsections are simplifications of the reality. In a real situation some of the assumptions might not be completely valid and even a combination of load transfer principle could be working within the slip-joint connection. However, the output of both methods differ. For comparison purposes a number of input values, established in sections 4.3 and 4.2, shall be used. These are listed in 3.1.

Table 3.1: Input values for hoop stress calculation

$M_{y,ed}$ [kNm]	t_{tower} [m]	$h_{overlap}$ [m]	$D_{t,slip}$ [m]	θ_{cone} [deg]	μ_s [-]
6145	0.015	5.200	3.165	1.738	0.210

With these input values the resulting hoop stress σ_{hoop} in the tower as result of the bending moment differs 38% between the two methods, with the alternative proposed method being the smallest. The hoop stresses via the literature method $\sigma_{hoop,l}$ and alternative method $\sigma_{hoop,a}$ were found to be:

$$\sigma_{hoop,l} = 44.41 \text{ [MPa]}, \quad \sigma_{hoop,a} = 32.20 \text{ [MPa]}, \quad \Delta\sigma_{hoop} = 38 \text{ [%]} \quad (3.24)$$

Therefore, operational data from the DOT500 turbine could give a clue on which of the load transfer mechanism is the most dominant. This shall be treated inspected in section 8.4.

Given these methods and formula's it is interesting to look at the minimal required overlap length for the DOT500 slip-joint based stresses caused by a bending moment and static vertical equilibrium. Using the dimensions and load cases as presented in table 3.1 and the yield strength of the tower as determined in section 4.2, $f_y = 275 \text{ MPa}$, the following overlap lengths are found:

$$h_{overlap,l} = 2.175 \text{ [m]}, \quad h_{overlap,a} = 1.289 \text{ [m]} \quad (3.25)$$

These values are quite striking as they differ severely from the proposed $h_{overlap} = 1.5D_{MP}$ in literature. However, these formula's assume perfectly tapered cones and a full uniform overlap of the slip-joint, which in an actual situation will not be the case. However, this evaluation gives reasons to believe that the ideal slip-joint overlap length might be shortened. Measurement data of the operational DOT500 turbine must be inspected to see if this hypothesis can be supported by actual stresses within the slip-joint.

3.3. Fabrication tolerances

As was explained in the previous sections, the main assumptions in all of the derivations on the resulting hoop stress in the tower are based on z-axisymmetric circular diameters in the x-y plane and perfectly linear increasing diameters over the height. This will of course never be the case in an actual fabricated conical tower section. On top of that, there is always some uncertainty in the actual diameter $D_{t,i}$, or circumference C_{tower} , of the actual fabricated product. These uncertainties have different causes in the fabrication process and their maximum or minimum deviation from the specified dimensions are established in fabrication tolerances. These tolerances can differ per manufacturer, product or situation. In this thesis the fabrication tolerances of DNV and GL for offshore structures shall be used [13], [20].

A circular cylindrical or conical tower is made up of different individual plate sections that are rolled through a press to create the desired curvature. These individual plates are subsequently welded together in both circumferential and longitudinal direction to create the final tubular, for example the DOT500 monopile as can be seen in figure 3.6.

In this process different effects can take place as a result of the fabrication. The different fabrication tolerances, relevant for the slip-joint connection evaluation, that will be discussed are graphically displayed in figure 3.7. They will be shortly elaborated on in the subsequent sections.



Figure 3.6: Individual plate sections make up the total monopile

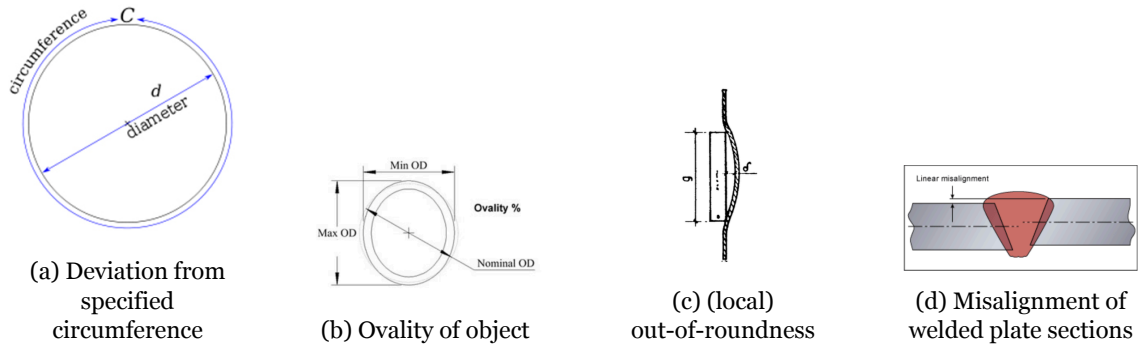


Figure 3.7: Different fabrication tolerances relevant for slip-joint design [13]

3.3.1. Deviation from specified circumference

A deviation of the circumference is a result of different sections that have been welded to each other, creating uncertainty in the total length of the welded circumference due to the variability of the weld length. This tolerance is of importance as the calculations presented in sections 3.2.1 and 3.2.2 require the input of a diameter of the tower $D_{t,i}$. If the actual diameter differs, this could cause a non-linearly increasing or decreasing diameter over the height of the object. Also, this effect could marginally influence actual angle of the cone, both locally and globally. The deviation from the specified circumference is simply defined as the actual circumference minus the specified circumference:

$$\Delta C = C_{actual} - C_{specified} \quad [m] \quad (3.26)$$

3.3.2. Ovality of the object

The ovality of a circular section is a specific kind of out-of-roundness, depicted in figure 3.7b. It can be a result of different bending radii of the individual plate sections. If a specific section of the cone shows some ovality, the assumption in the formula's that the circular sections are perfectly circular in the x-y plane is compromised. This influences the total contact area of the slip-joint. Ovality of a tower section is defined as the percentage that the minimal D_{min} or maximum D_{max} diameter deviates from the specified nominal diameter D_{nom} :

$$O = \frac{D_{max} - D_{min}}{D_{nom}} \quad [\%] \quad (3.27)$$

3.3.3. (local) out-of-roundness

The out-of-roundness, or local out-of-roundness, of a circular section is the (local) deviation of the actual material from the nominal bending radius. This local waviness of the material is depicted in

figure 3.7c. It can be a result of impurities of the plate section or can be caused by local buckling or non perfect bending at the edge of the plate, during the production process. These local imperfections again compromise the assumption that the cones are perfectly circular in the x-y plane. This can result in a non-uniform distribution of the contact area and thus, contact pressure P within the slip-joint. The out-of-roundness δ_o is simply defined as the distance between the nominal bending radius' line and the actual position of the material as displayed in 3.7c.

3.3.4. Misalignment of welded plate sections

Plate-to-plate misalignment is the result of a non-centred position of two plate sections that have been welded together, as is shown in figure 3.7d. This can easily happen during the process of welding two (conical) steel plates. In the case of a tubular section, this misalignment can be present in both the circumferential and longitudinal welds. Such a misalignment compromises the assumption of the perfectly linearly increasing diameter over the height of the cone. This could again influence the total contact area of the slip-joint, leading to a non-uniform distribution of the pressure between the two conical sections. The misalignment δ_{mis} is simply measured as the distance between the top, or bottom of the two plate sections welded together, as depicted in figure 3.7d.

3.3.5. Tolerances

The theoretical tolerances for the imperfections listed in the previous sections are displayed in table 3.2. They have been taken from DNV and GL design codes as specified. Furthermore, the (maximum) absolute value of the tolerance is also displayed in the table based on the dimensions of the DOT500 slip-joint as presented in 4.2. As most criteria are expressed as fractions of the wall thickness or diameter, the maximum value is presented based on the biggest diameter and wall thickness of the cone, which is $t_{tower} = 0.016\text{ m}$, $D_{t,i} = 3.612\text{ m}$ and $t_{MP} = 0.040\text{ m}$, $D_{MP} = 3.595\text{ m}$ respectively.

Table 3.2: Theoretical maximum fabrication tolerances of tower and monopile cone

Imperfection type	Tolerance criteria	Absolute (maximum) tolerance tower	Absolute (maximum) tolerance monopile
Circumference deviation	$0.001 \cdot C_{tower}$	11.3 mm	11.3 mm
Ovality	$0.003 \cdot D_{nom}$	10.8 mm	10.8 mm
Out-of-roundness	$0.10 \cdot t_{t,MP}$	1.57 mm	4.00 mm
Plate misalignment	$0.15 \cdot t_{t,MP}$	2.36 mm	6.00 mm

The actual imperfections of the two cones of the DOT500 will be discussed in section 4.2, whereas the effect of these imperfections will be elaborated on in section 6.3.

3.4. Slip-joint installation

As far as the installation of the slip-joint is concerned, multiple options are available which can best be divided into two main categories namely, non-forced and forced installation. Examples within these categories include, but are not limited to:

- Non-forced installation i.e., due to self-weight of the top cone only
- Forced installation
 - By controlled dropping of the upper cone
 - By introducing vibrations
 - By application of a static load
 - By local heating

From these installation methods at least two have been tested. The controlled dropping was tested on the Duinvogel slip-joint [27] and installation by introducing vibrations has been tested in a scale experiment on the TU Delft [16], [35]. Both installation methods shall be shortly elaborated on.

3.4.1. Controlled dropping

The idea behind this method of installation is that a certain drop height h_{drop} can be established, assuming uniform contact between the two cones, which is required to overcome the friction and secure a solid connection of the two cones. To calculate this drop height, the original design document of the Duinvogel slip-joint [27] proposes the following method based on energy balance. First of all, the required friction force F_f to assure a static vertical equilibrium is used as input. Given this friction force, the hoop stress σ_{hoop} in the tower can now be calculated according to the formula's presented in section 3.2.1. Given this hoop stress, the tower circumference will be stretched with the following quantity according to Hooke's law:

$$\delta_D = \frac{\delta_C}{\pi} = D_{t,i} \cdot \frac{\sigma_{hoop}}{E_{tower}} [m] \quad (3.28)$$

In order to reach this stretch, the tower has to travel an axial distance from the first point of contact to the final target level of δ_A , which results from the cone angle:

$$\delta_A = \frac{0.5\delta_D}{\tan(\theta_{cone})} [m] \quad (3.29)$$

To overcome this distance with zero to total friction, the total required energy is expressed as:

$$E_f = \frac{1}{2}\delta_A F_f [J] \quad (3.30)$$

This energy can be obtained from the potential energy E_p of the top cone hanging over the lower cone.

$$E_p = m_{cone} g h_{total} [J] \quad (3.31)$$

The potential energy should be equal to the energy that needs to be overcome due to the friction, therefore the total height at which the upper cone should hang above the lower cone, measured from the target overlap is:

$$h_{total} = \frac{E_f}{m_{cone} g} [m] \quad (3.32)$$

This means, that the drop height h_{drop} measured from the first point of contact is:

$$h_{drop} = h_{total} - \delta_A [m] \quad (3.33)$$

The maximum speed that the cone will reach i.e., the velocity that the winch of the crane should be able to reach, based on the total transformation of potential to kinetic energy is:

$$v_{cone} = \sqrt{2gh_{drop}} \left[\frac{m}{s} \right] \quad (3.34)$$

Using the latter equations and the input of the DOT500 slip-joint dimensions in section 4.4, the following drop height and maximum drop velocity can be determined:

$$h_{drop} = 5.545 [mm], \quad v_{cone} = 0.214 \left[\frac{m}{s} \right] \quad (3.35)$$

The validity of this simplified approach can be questioned. Nevertheless, it was shown in the DOWEC report [27] that the Duinvogel slip-joint that was installed in this manner was operational for 20 years experiencing little extra settlement over its lifetime. However, research [16] claims that installation via this method for bigger, offshore structures will not be feasible.

3.4.2. Introducing vibrations

On the TU Delft, a scale experiment has been performed in which two cones were installed by means of introducing vibrations in the top cone [35]. The theory behind this principle is that as the cone is vibrating, the friction force preventing the downward displacement of the top cone is drastically reduced. This allows for a much easier settlement of the top cone to target overlap. In the research it was concluded that the most important factor of the induced vibrations is the frequency of the vibration. Especially near input frequencies near the natural frequencies of the cones, the settlement was observed to be greater than near other frequency inputs. This means that as the cones get into resonance, the bigger amplitude deflections of the cone lead to bigger settlements. The input amplitude was found to be not of significant influence.

From the latter evaluation it can be concluded that the natural frequencies of the radial and circumferential modes are an important parameter when vibro-installing the slip-joint. These should be investigated when choosing this method of installation.

3.5. Conclusion

The theory of the slip-joint connection is discussed in this chapter, identifying the different relevant parameters related to the hoop stress in the cones. Both the static vertical equilibrium and an (extreme) bending moment have been considered. For the static vertical equilibrium of the joint, one can conclude that friction is a very important parameters. Any small value for the friction coefficient decreases the total stress in the cones of the slip-joint. For typical friction coefficients like $\mu_s = 0.10$, friction takes up 80% of the total vertical force. Furthermore, the stress in the cone is inversely proportional to the friction coefficient (μ_s), the wall thickness of the cone ($t_{t,MP}$), the total overlap length of the slip-joint ($h_{overlap}$) and the tangent of the angle of the cone ($\tan(\theta_{cone})$).

Secondly, the case of a bending moment is considered evaluating two different approaches. The first method, described in literature, assumes mainly horizontal reaction forces within the slip-joint as a result of a bending moment, whereas the second new proposed method assumes mainly vertical reaction forces. The latter method yields a 38% lower hoop stress in the cone with the same proportionality's to the parameters listed in the static equilibrium. The stress in the cone according to the literature method is inversely proportional to the wall thickness of the cone ($t_{t,MP}$) and inversely squared proportional the total overlap length of the slip-joint ($h_{overlap}$). In a real situation a combination of the two load transfer mechanism is to be expected and operational data of the DOT500 turbine is required to find which of the mechanisms is the dominant one. Also, based on these methods there is reason to believe that the slip-joint overlap length can be decreased from the typical $1.5D_{MP}$ stated in literature. For this purpose it is concluded that information of the stresses within the slip-joint is a crucial parameter that needs to be measured in the DOT500 measurement campaign. Also, the total settlement of the slip-joint should be measured in order to relate this to the total hoop stress increase.

Furthermore, fabrication imperfections have been examined as they can have an effect on the stress distributions in the slip-joint. These imperfections Uneven surfaces within the cones as well as welds, possibly causing misalignment of plates, can create uneven stress distributions or stress concentrations. The actual effect of this on the DOT500 slip-joint shall be discussed section 6.3. To minimise the chance and effect of these imperfections the total overlap length should be kept to a minimum and preferably be not any longer than one plate-width of steel.

Finally, two installation methods of a slip-joint have been considered namely forced installation via controlled dropping and vibrations. The important parameters for the installation of the DOT500 slip-joint with these methods, such as frequency of the vibrations and drop height, have been identified. Both installation methods are deemed feasible for the installation of the DOT500 slip-joint. However, introducing vibrations does require an extra installation step of applying a dynamic shaker. This reduces the elegance of the lean and time efficient installation procedure of the slip-joint concept in general. Furthermore, damage to stairs, lighting, doors and fatigue is not touched upon and should be considered.

DOT500 onshore test set-up

4.1. Introduction

The DOT500 project, is a project that has been created to prove the DOT concept on medium scale. To this end, a support structure was required, which could be used both on- and offshore in the later phases of the project. Furthermore, the DOT500 wind turbine was to be connected to the support structure (monopile) by means of a slip-joint connection. The mechanical behaviour of this joint is inspected in the measurement campaign.

The aim of the project is to provide the reader with the information on the project aspects relevant to the thesis. Furthermore, the dimensional data of the wind turbine, monopile and slip-joint will be presented accompanied with some notes on the design of the items. The different structural parts are presented in figure 4.1.

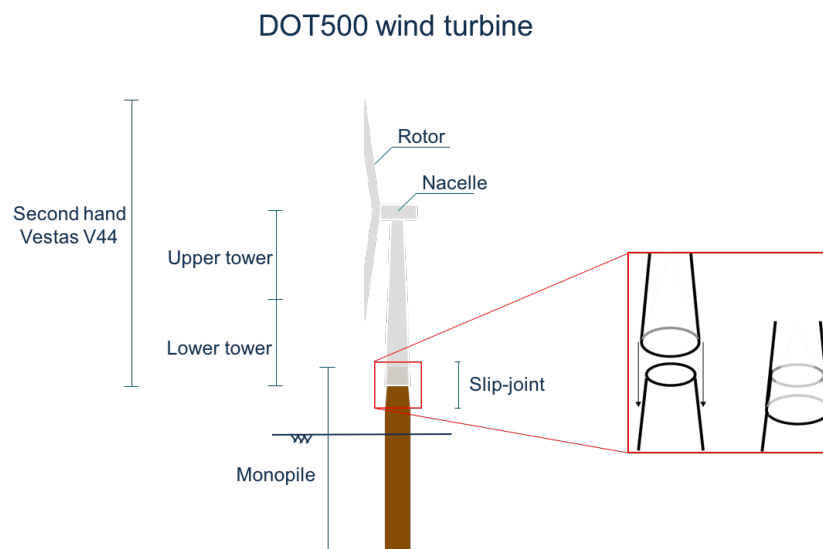


Figure 4.1: Overview of different structural components of the DOT500

First of all, the second hand wind turbine that has been bought for the project shall be inspected in section 4.2. Secondly, a monopile had to be design for the project that could also withstand the loads of a $3MW$ turbine in the North Sea for the future phases of the project. The design considerations and dimensions of this monopile shall be discussed in section 4.3. The slip-joint connection that will connect the wind turbine tower and monopile shall be discussed in section 4.4. Lastly, section 4.5 provides an overview of the test site and the actual erected wind turbine.

4.2. DOT500 Wind turbine tower and RNA

The wind turbine that is used in the DOT500 project is a second hand Vestas V44. The wind turbine was bought in Q4 2015, and transported to the workshop in Delft. For the design of the slip-joint and preparation of the measurement campaign, the relevant structural parameters of the turbine were required. Therefore, the following tests and measurements were performed to map this data from the second hand turbine:

- Diameter and wall thickness measurements of the two tower parts.
- Accurate laser tracker measurements of diameter and circumference on the bottom 6.00 m of the lower turbine tower, for the slip-joint purposes.
- Yields stress test of the tower material.
- Weight and centre of gravity measurement of the two tower parts.
- Weight and centre of gravity measurements of the nacelle and rotor.

They will be elaborated on in the subsequent sections.

4.2.1. Wind turbine tower information

The diameter measurements have been performed using a hand-laser. The diameters of the two towers have been measured in vertical direction and the first 6.00 m of the lower tower have also been cross checked and measured in horizontal direction. Furthermore, the wall thicknesses have been measured using Ultra Sonic measurements. Three measurements have been performed per plate section, which have been averaged to obtain the eventual wall thickness to calculate with. The details of these measurement can be found in appendix A, while a summary of the dimensions, per plate section, can be found in table 4.1a for the lower turbine tower table 4.1b for the upper turbine tower.

Table 4.1: Wind turbine tower dimensions

(a) Lower wind turbine tower dimensions			(b) Upper wind turbine tower dimensions		
Heights from bottom of cone [m]	Diameter [m]	Wall thickness [m]	Heights from bottom of cone [m]	Diameter [m]	Wall thickness [m]
0.00	3.580	15.3	0.000	2.518	10.7
1.750	3.455	15.4	2.932	2.450	10.8
5.490	3.251	10.2	5.828	2.382	10.8
8.230	3.129	10.3	8.630	2.316	9.00
11.00	2.922	10.3	11.66	2.244	9.00
13.78	2.741	10.1	14.60	2.175	9.00
16.07	2.605	10.4	17.54	2.105	8.40
18.94	2.518	10.4	20.47	2.035	8.40

The bottom 6.00 m of the lower tower has been measured more accurately for the slip-joint design. To this end, an extra hand-laser measurement was performed on a near-horizontal line and a laser tracker was used to scan this part of the tower. The details of this measurement can be found in appendix A and a summary of the dimensions of the slip-joint section on the tower measured from the bottom upward can be found in table 4.2. In this table, the diameters of both the vertical and near-horizontal measurements are presented accompanied by the difference between the two (horizontal – vertical). Furthermore, the ovality is shown based on these two measurements and the nominal diameter, which is taken from the laser-tracker measurement. Significant ovalities (< 0.15%) have been indicated in red in figure 4.2.1. The vertical and horizontal indications of the measurements are also presented in this figure.

Table 4.2: Detailed dimensions of tower slip-joint section

Height from bottom cone [m]	Diameter vert. [m]	Diameter hor. [m]	Difference [m]	Diameter nom. [m]	Ovality [%]
0.000	3.580	3.584	0.004	3.578	0.11
0.515	3.541	3.553	0.012	3.548	0.34
1.079	3.514	3.507	-0.007	3.513	0.20
1.555	3.488	3.485	-0.003	3.485	0.09
2.068	3.459	3.455	-0.004	3.454	0.12
2.499	3.340	3.426	-0.004	3.426	0.12
3.009	3.400	3.397	-0.003	3.396	0.09
3.508	3.376	3.368	-0.008	3.367	0.24
3.995	3.349	3.339	-0.010	3.338	0.30
4.516	3.320	3.310	-0.010	3.304	0.30
5.032	3.288	3.282	-0.006	3.273	0.18
5.517	3.258	3.256	-0.002	3.246	0.06

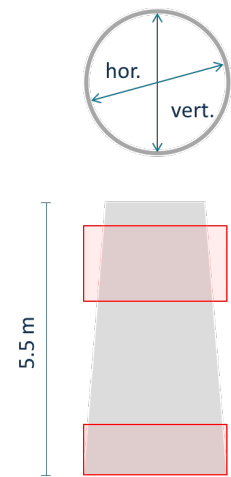


Figure 4.2: Ovality

From table 4.2 and figure 4.2.1 it can be observed that the tower shows ovality up to 0.30% in the regions from 0.000 – 1.000 m and 3.508 – 5.032 m measured from the bottom of the cone. This ovality was not caused by the gravitational force when the tower was down on the ground, since the horizontally measured diameter is smaller than the vertical measured diameter in these regions. This provides reasons to believe that this ovality will be even bigger when the turbine tower is upright. In some regions the ovalities exceed the theoretical maximum fabrication tolerance established in section 3.3. This is not surprising considering the fact that it is a second hand tower, but it should be noted and taken into account in sensitivities in the models in chapter 6.

Furthermore, from the laser-tracker measurements it was concluded that there is a significant plate-to-plate misalignment at the plate intersection at 5.490 m. The misalignment here was found to be in the order of 3.00 mm. It was decided to keep the slip-joint overlap under this misalignment to prevent stress concentrations due to this imperfection.

4.2.2. Additional tower information

The second hand wind turbine tower had to be refurbished to be suitable for the DOT500 project. These transformations included:

- Removal of the bolt flange of the lower tower.
- Removal and replacement of the entrance door from the bottom of the tower to the above the slip-joint interface.
- Addition of a small man-hole for hydraulics to exit the tower.

Using a piece of steel that was cut from the tower a tensile test and chemical analysis has been performed. The detailed report can be found in appendix A. The yield strength of the tower was found to be $f_y = 320 \text{ MPa}$. Therefore, the turbine tower could either be constructed with a poor S355 or strong S275 steel type. For the sake of conservatism, a steel type of S275 is used in design calculations.

As a final measurement on the turbine towers, the wind turbine towers have been weighed and their centre of gravity has been determined using the two overhead cranes in the hall and a load cell. The procedure and calculations of this measurement can be found in appendix A. The turbine towers and their centre of gravity are displayed in table 4.3.

Table 4.3: Weight and centre of gravity, measured from bottom of cone, of two tower pieces

	Weight [ton]	Centre of gravity from bottom [m]
Lower tower	16.91	6.590
Upper tower	13.11	11.11

4.2.3. Rotor and nacelle dimensions

The rotor and nacelle were also measured and weighed to get an indication of the dimensions of these items. To this end, a blade has been weighed with the overhead crane and a load cell and the centre of gravity has been determined in the same manner as was done with the tower sections. This has been done in order to more accurately calculate the rotational moment inertia of the blades and total rotor.

Furthermore, the nacelle is refurbished to house the DOT drive train system. This brings a weight reduction as the generator and gearbox are replaced with a pump. These items have been weighed and the total weight reduction was calculated to be 30%. The details can be found in appendix A. An overview of the masses and dimensions of the different RNA items can be found in table 4.4.

Table 4.4: Masses and dimensions of RNA

	Weight [ton]	Dimensions (LxWxH) [m]	Centre of gravity from bottom [m]
Blade	2.105	21.0	6.59
Hub	1.930	1.00 x 1.00 x 1.00	-
Nacelle (DOT)	13.88	1.89 x 9.43 x 9.63	-

4.3. DOT500 monopile

For the DOT500 project, a monopile had to be designed, which could be used in the 500kW onshore test, at the Maasvlakte II, but also in the future phases of the project until the North Sea conditions with a 3 MW wind turbine. Furthermore, it had to be connected to the wind turbine by means of a slip-joint, for which a conical top part was required. The designated offshore location is chosen as the wind park OWEZ, since a wind turbine demonstration area is present there. The future 3 MW turbine is chosen as the Vestas V90, as this type has relatively good availability on the second hand market.

In light of the preceding evaluations, a modular monopile was designed in which the top part could also be used onshore, without having to penetrate it very deeply into the soil. The simplified monopile design cycle was followed, as explained in chapter 2. The philosophy is that if the monopile can withstand the offshore loads with a 3 MW turbine, than it will certainly withstand the 500kW and onshore loads. The most important steps in this design cycle shall be elaborated on in this section, while the details can be found in appendix A. Also, the relevant load cases for the DOT500 onshore test shall be presented in this section. A schematic representation of the modular monopile can be found in figure 4.3.

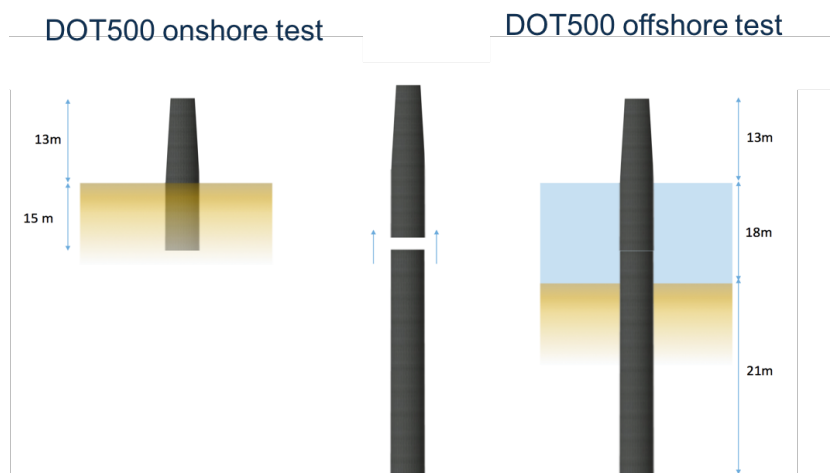


Figure 4.3: Schematic overview of modular monopile

The environmental data that was used in the design cycle was obtained via time series which were con-

sequently extrapolated in a Gumbel extreme analysis. The return-period values for the environmental parameters used in the design calculations, are presented in table 4.5. Detailed information, regarding environmental and structural parameters can be found in appendix A.

Table 4.5: Return periods values for different environmental load cases

Load Case	Wind [$\frac{m}{s}$]	Waves [m]	Current [$\frac{m}{s}$]	Ice	Water [m]
Load case 1	28.7	4.87	0.67	-	22.0
Load case 2	25.2	6.03	0.67	-	22.0
Load case 3	15.0	4.87	0.92	-	22.0

4.3.1. Design heights

The first step in the design cycle is to determine the design heights of the turbine at OWEZ with a 3 MW wind turbine. These heights are the leading design driver in the different phases of the project. The presented input parameters and structural information of the Vestas V90 was used to calculate the design heights presented in figure 4.4.

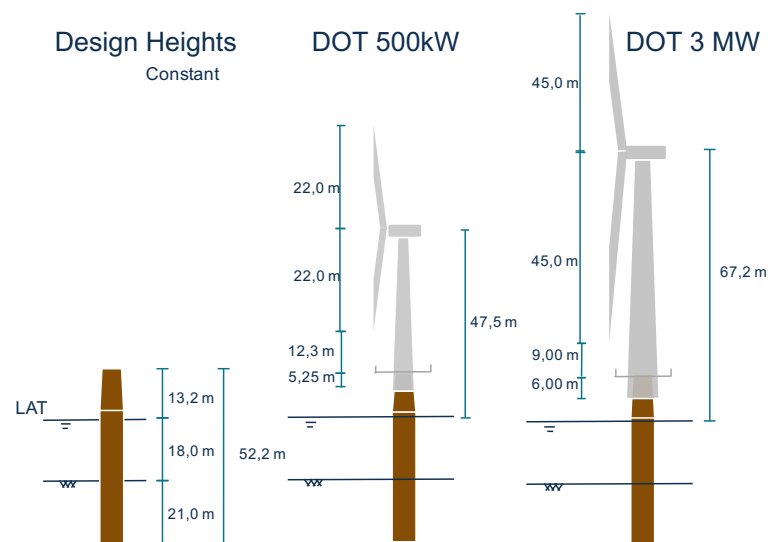


Figure 4.4: Schematic overview of design heights DOT500 and DOT3000 offshore

The platform clearance level, together with the geometrical information of the Vestas V44 cone angle, determined the length and size of the conical part of the monopile. This will be discussed in more detail in section 4.4. An overview of the DOT500 onshore test setup shall be presented in section 4.5.

4.3.2. Frequency analysis and monopile dimensions

With the design heights set, the preliminary monopile dimensions can be established, based on a frequency analysis as explained in section 2.4. The average diameter and wall thickness, combined with the given length input, have been calculated based on the stiffness criteria with a Vestas V90 as input turbine. The detailed information regarding this calculation can be found in appendix A. The optimal dimensions have been found as $D_{MP} = 4.00 \text{ m}$ and $t_{MP} = 0.055 \text{ m}$. This ensures that the DOT3000 offshore turbine fulfils the stiffness criterion. For both the DOT500 offshore and onshore test, this means that the stiffness criteria can not be fulfilled. Therefore, attention should be paid at operational ranges of the turbine near the first natural frequency of the bending modes of the turbine. For the DOT500 onshore case, this shall be investigated in section 6.2 while a short preliminary calculations is presented in figure 4.5.

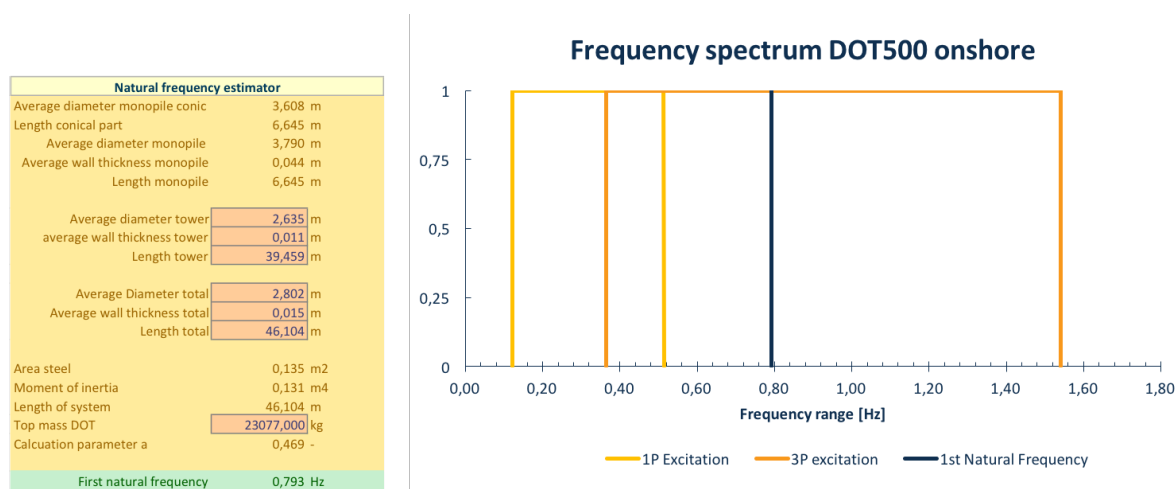


Figure 4.5: Frequency calculation and resulting spectrum of the DOT500 onshore wind turbine

The exact dimensions of the cone shall be elaborated on in section 4.4.

4.3.3. Loads and design checks

For the detailed design of the monopile, a reference case monopile is used to speed up the design process. The monopile that was used is from the Princess Amalia wind farm. This reference case was chosen for the following reasons:

- The water depth at OWEZ (15m – 20m) is shallower than at Amalia wind farm (19 – 24,50 m)
- While the top mass of the DOT 3MW turbine is equivalent to the Vestas V80 turbine used in the Amalia wind farm.
- The diameter matches the required 4.00 m.

Combining these two, it is expected that the monopile strength of the Amalia wind park foundation will suffice for the placement of a DOT 3MW wind turbine in the OWEZ wind farm. To verify this, the following checks and actions were performed:

- Adjust design heights to match OWEZ parameters, treated in section 4.3.1;
- Adjust top of the monopile to comply with new interface. The DOT system will use a slip-joint connection rather than a transition piece, treated in section 4.4;
- Check ultimate load case(s) to see if the strength suffices;

- Adjust penetration depth of monopile by checking bearing capacity and scour at OWEZ.

With the first two steps covered in the preceding sections, the load calculations can be performed, of which the details can be found in appendix A. The factored loads from the load cases that were used are presented in table 4.6 and the resulting reaction forces on the monopile of the governing load case and results of the strength and stability checks are displayed in figure 4.6. The governing load case for the offshore 3 MW turbine is the operational rated speed load case. Note that in the other load cases, the wind speed was above the operational range of the turbine, therefore no thrust force is present.

Table 4.6: Load cases for DOT3000 offshore

	Permanent load	Wind drag load		Thrust load		Hydrodynamic load	
	F_z [kN]	V_{ed} [kN]	$M_{y,ed}$ [kNm]	V_{ed} [kN]	$M_{y,ed}$ [kNm]	V_{ed} [kN]	$M_{y,ed}$ [kNm]
Load case 1	4628	155	10614	n.a.	n.a.	1056	16022
Load case 2	4628	119	8172	n.a.	n.a.	1352	20837
Load case 3	4628	42	2895	845	65934	1111	16891

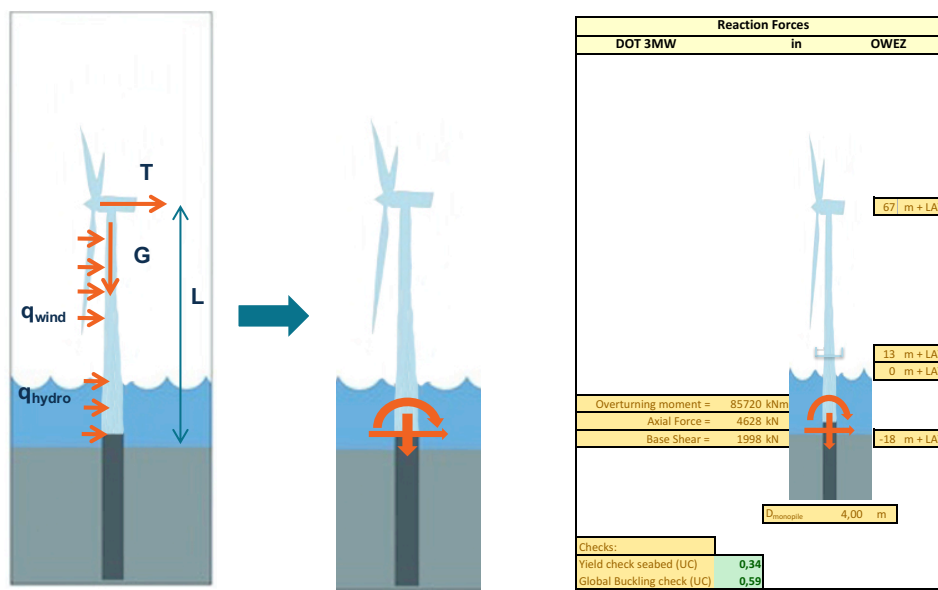


Figure 4.6: Governing load case and resulting strength and stability checks

Next to these checks, the penetration depth was checked and optimised, of which the details can be found in appendix A. The penetration depth was optimised to $z_{toe} = 18.0$ m. Since no scour protection shall be used, an extra $1 D_{MP}$ of penetration depth is added to anticipate the effect of a scour hole [37]. As can be seen in figure 4.6, the designed monopile is structurally safe considering the loads of the DOT3000 offshore test and the applied strength and stability checks, with a maximum unity check of $UC = 0.59$.

The actual monopile is based on this design cycle and the dimensions can be found in appendix A in figure A.8. The monopile was fabricated at SIF, Roermond.

4.4. DOT500 slip-joint

The monopile and the wind turbine should be connection via the slip-joint principle. The theory and working principle on which the design of such a connection is based, is treated in chapter 3. The cone of the monopile had to be designed in such a manner, that together with the wind turbine tower, a proper slip-joint connection can be created. Two main parameters had to be determined in this particular slip-joint design, namely the overlap length $h_{overlap}$ and the cone angle of the monopile θ_{cone} . This process will be elaborated on in section 4.4.1. Also, the 3D laser measurements performed on the monopile shall be described in section 4.4.2.

4.4.1. Slip-joint design

First of all, the cone angle of the monopile is chosen in such a manner that it fits with the wind turbine lower tower. Using the measurements of the lower wind turbine tower from section 4.2, a cone angle can be determined. However, since the measurements differ per type (vertical, horizontal and laser-tracker), different angles have been obtained, including:

$$\theta_{vert.} = 1.672^\circ \quad \text{and} \quad \theta_{hor.} = 1.703^\circ, \quad \text{and} \quad \theta_{laser} = 1.721^\circ \quad (4.1)$$

As was noted in an investigation at the TU Delft [16], it is advisable that the inner cone of the slip-joint has a slightly steeper angle than the outer cone. This creates a 'press-fit' and prevents the top part of the inner cone to drill through the outer cone. Figure 4.7 graphically displays this evaluation with figure 4.7a showing the angle notation and figure 4.7b and 4.7c showing a steeper and less steep inner cone angle, respectively.

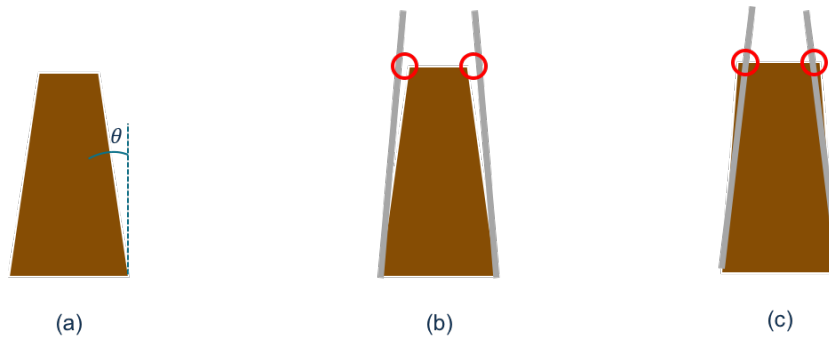


Figure 4.7: Different inner cone angles slip-joint

In combination with an overlap length, dimensional information of the wind turbine tower, assumed (perfect) diameter taper and the equations provided in section 3.2, different stress patterns over the height of the slip-joint are to be expected with varying cone angles and overlap lengths. Apart from the static stresses due to the target overlap length, additional stresses are to be expected from operational loads. As a governing load case, the rated speed conditions of the DOT500 in offshore conditions were used. The load case and resulting reaction forces are given in figure 4.8.

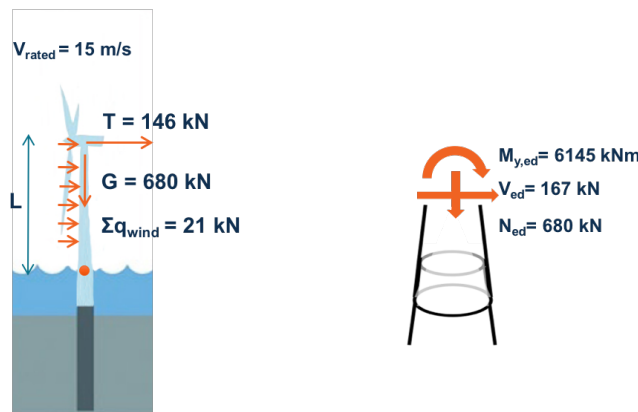


Figure 4.8: Governing load case for slip-joint design; DOT500 offshore conditions

Combining the above evaluations, an optimal cone angle at a given overlap length was determined, which leads to the most uniform stress distribution along the height of the slip-joint. This resulted in a cone angle of $\theta_{cone} = 1.738^\circ$ and an assumed overlap length of $h_{overlap} = 5.335$. This overlap length is based on a rule of thumb of $1.5D_{MP}$. A more detailed evaluation on the actual overlap length is presented in section 6.3.

4.4.2. 3D measurement monopile

Likewise the lower wind turbine tower, the monopile was measured using laser measurement technology to find the exact diameters and circumferences over the height of the cone. In the case of the monopile, this was done using 3D-scan technology when the monopile was in place. To this end, a laser scanner was positioned at three different positions around the monopile, each time taking a full scan of the surroundings. This results in three 3D scans which can be linked to each other by means of reference points that were marked on the monopile. After some post processing work, the three images can be combined to create a full 3D scan of the monopile.

The outcome of this scan can be found in figure A.9 in appendix A. Also, the monopile was tested on fabrication tolerances by the company itself of which the details can be found in the dimensional control document in figure A.20 in appendix A. From these measurements the following things can be concluded:

- The 3D scan technology was not accurate enough to gather information on the exact circumferences of the monopile over the height.
- However, from the 3D scan it was observed that the monopile showed almost no signs of ovality.
- Based on the dimension control report it can be concluded that the monopile cone was fabricated far within the fabrication tolerances. The maximum deviation from the circumference was found to be $\Delta C = 4 \text{ mm}$.

4.5. Test site set-up

The test site that was chosen for the DOT500 project is located at the Maasvlakte II, in Rotterdam. This location is chosen as it was available and the Port of Rotterdam was keen on having a demonstration project in this area. After the permitting process, the site was prepared for the project and the installation could begin, which is elaborated on in section 7.2. An overview of the test site and wind turbine can be found in figure 4.9.

An top view corresponding to the orientation in figure 4.9, accompanied with a side view of the actual test site can be found in figure 4.10.

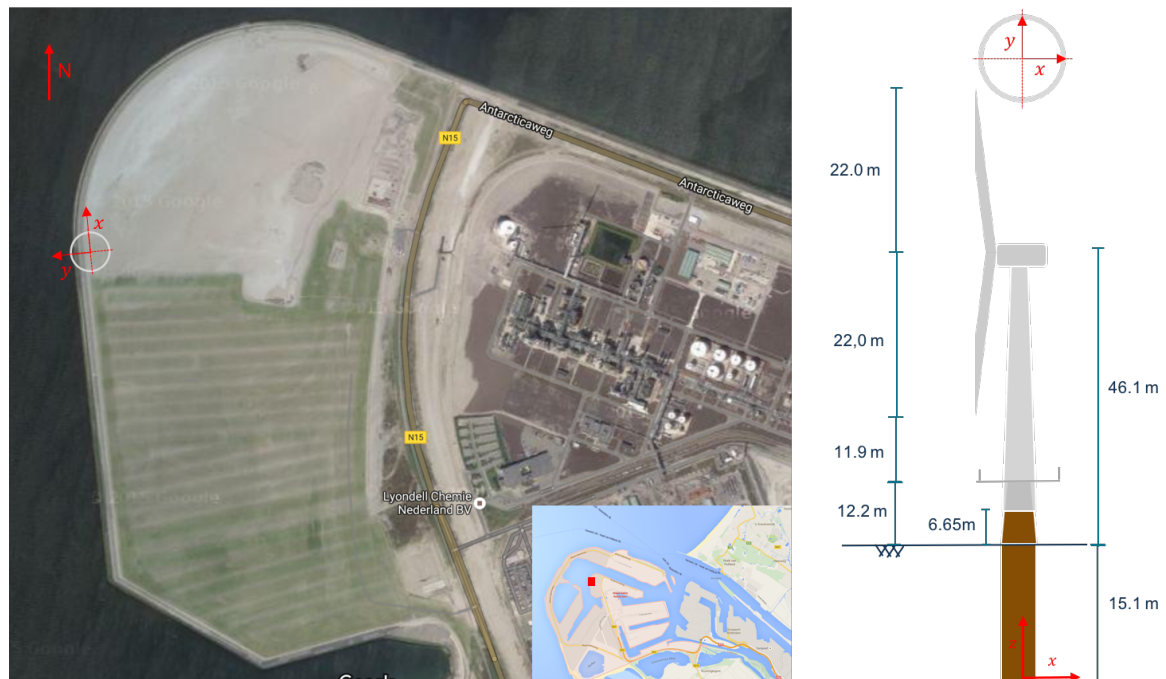


Figure 4.9: Schematic overview of DOT500 test site at Maasvlakte II

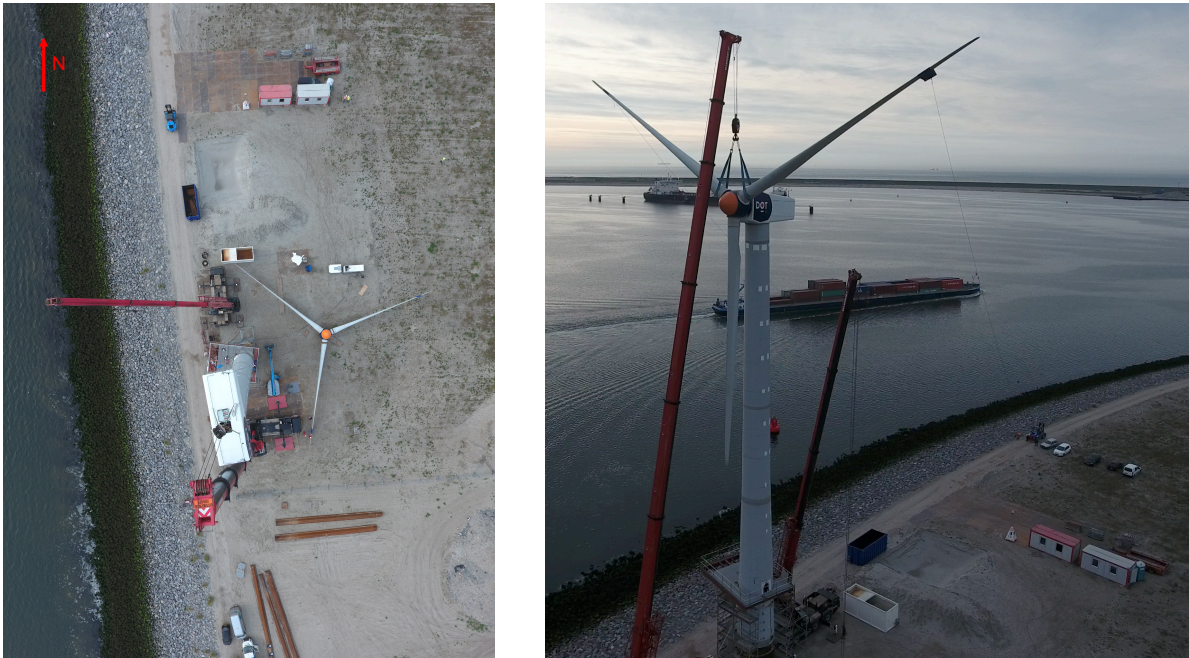


Figure 4.10: Overview of DOT500 test site at Maasvlakte II

4.6. Conclusion

In this chapter, the test site set-up was presented, elaborating on the dimensional information of the different structural parts of the DOT500 wind turbine, including the second hand wind turbine, the monopile and the slip-joint. Furthermore an overview of the test-site was provided. This structural input shall be used in the subsequent chapters. Important to note for further use in the thesis are the following items.

First of all, based on the laser measurements it can be concluded that the lower tower of the second hand wind turbine was far from perfectly conical. The towers shows significant ovality of $O = 0.30 - 0.35\%$ on multiple regions along the target slip-joint sections. Also, a significant plate-to-plate misalignment of 3.00 mm was found around 5.490 m measured from the bottom of the cone. This is beyond the theoretical maximum fabrication tolerance and should therefore be taken into account in the sensitivities of the models in section 6.3. A number of reconfigurations were performed on the lower tower to make it suitable for the slip-joint connection. This welding and cutting have most probably further increased the irregularities, yet the actual influence is unknown.

Secondly, the monopile that was designed by SIF was inspected with 3D laser scan technology and the inspection report of SIF was checked. It can be concluded that the monopile was fabricated well within fabrication tolerances, showing hardly any signs of ovality or misalignment. The biggest deviation from the specified circumference dimensions was found to be $\Delta C = 4\text{ mm}$. The slip-joint cone angle was based on the two laser measurements performed on both cones and was set to be $\theta_{\text{cone}} = 1.738^\circ$.

5

Measurement Campaign

5.1. Introduction

With the design of the DOT500 support structure and slip-joint dealt with, the next step in the process is the organisation of a proper measurement campaign. In light of the considerations discussed in chapters 2 and 3, and in line with the research approach, the measurement campaign will focus on three aspects, including:

- Identifying the first natural frequency of the total structure.
- Quantifying the settlement of the slip-joint.
- Identifying the stress distribution in the slip-joint connection.

Over the course of March through April 2016 different parties such as TNO, Fugro, HBM and Folmer Innovations have been approached to gather information on the right types of sensors and application techniques to fulfil the proposed measurement campaign. Eventually, Elbert Folmer from Folmer Innovations was chosen to be most suitable by DOT B.V. to assist during the measurement campaign.

The aim of this chapter is to provide the reader with the background information and motivations to the important decisions taken in the process of organising and preparing the measurement campaign. The different types of sensors that have been used, as well as the reason for these types, and the positioning of the different sensors will be clarified.

Sections 5.2 through 5.4 presents the above mentioned information on the different aspects of the measurement campaign. Furthermore, section 5.5 provides information on the calibration and zero-ing of the sensors and 5.6 will elaborate on the cable infrastructure and data acquisition system. Section 5.7 will provide an overview of the total measurement campaign, along with a coding of sensors that will be used for reference in the subsequent chapters. The details of the different sensors and information of the actual application process will be treated in appendix B.

5.2. Natural frequency identification

The goal of this part of the measurement campaign is to measure the first and second natural frequency corresponding to the first and second bending modes of the total turbine system. The relevance of accurately acquiring an estimate of this first natural frequency in an early design phase of an offshore wind turbine has already been stated in section 2.4. Therefore, the first natural frequency was modelled, as will be elaborated on in section 6.2, and will be measured during the campaign. This measured data provides valuable information to calibrate and validate this model. Hence, it can be of better use for future purposes.

5.2.1. Measuring natural frequency

A natural frequency is strictly spoken not a quantity that can be measured in itself. On a structural level, a natural frequency is just one of the endless possible frequencies at which a structure can vibrate as a result of an input vibration. However, when exciting a structure at the same frequency as its natural frequency, the response amplitude will dramatically increase as opposed to excitation at any other given frequency. This resonant behaviour has been explained in section 2.4.

Therefore, when trying to identify the natural frequency of a structure it is common practice to measure the structural response of the given structure, while excited by a force that contains any given frequency, including a structure's natural frequency. Such a force could possibly be a hammer impulse load, or in the case of a wind turbine one could use an emergency stop of the rotor to excite the tower with a range of frequencies. As an expected result, the vibrational response of the structure in the frequency domain, shows a distinct peak around the natural frequency, for the structure 'likes' to vibrate at this frequency.

A structures response can be measured by a time signal with any appropriate physical quantity. In the case of a wind turbine, this for example could be accelerations in the tower bending mode direction, or axial strains along the wind turbine tower structure. This time domain signal does not implicitly provide the information on the response at different frequencies yet and should therefore be converted to the frequency domain. A common way to do so is to use a Fast Fourier Transform. Such a Fourier transform filters out every frequency present in the time signal with its corresponding amplitude. Figure 5.1 graphically displays the transformation of a time signal to the frequency domain.

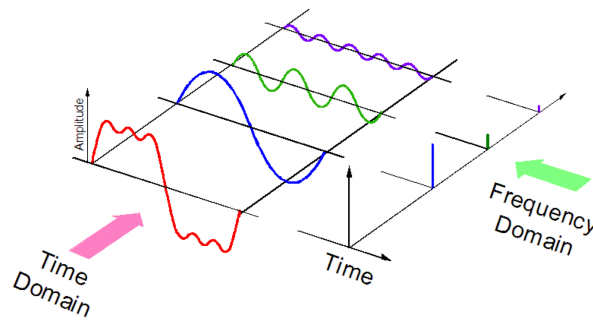


Figure 5.1: Fourier transformation from time- to frequency domain

At this point, it is of importance to note that the natural frequency obtained by using the above described method is a damped natural frequency. The influence of damping on the natural frequency is described by:

$$\omega_{0,d} = \omega_0 \sqrt{1 - \zeta_d} \quad (5.1)$$

In this equation, ζ_d is the damping ratio of the system and $\omega_{0,d}$ is the damped natural frequency. Since the damping of a wind turbine structure under no excitation is rather small, i.e. only structural damping of about 1% – 2%, the effect of this can be neglected [43].

5.2.2. Approach

As explained before, the goal of this part of the measurement campaign is to identify the first natural frequency of the total turbine system bending modes. In order to do so, a time signal of bending motion of the tower should be acquired. In this case, it is chosen to acquire two types of time signals, including:

- Accelerations of the nacelle in both fore-aft and side-side direction
- Strains in the axial direction of the turbine tower

These time domain signals can then be converted to the frequency domain in order to find the tower's response as a function of the vibration frequencies. A clear peak in the frequency spectrum of this signal

should be present at a natural frequency of the turbine structure. The reason to use both strains and acceleration signals is for cross-check purposes.

5.2.3. Chosen sensors

Both the strain gauges and the accelerometer have been selected to meet the following criteria:

- They should be able measure frequencies lower than 1 Hz, since the first natural frequency lies in the order of magnitude of $f_{nat,1} = 0.80$ Hz.
- The sensitivity of the accelerometer should be high enough to measure accelerations below 0.2 G. This is the maximum allowed acceleration in a wind turbine nacelle [15].
- The strain gauge should measure axial strains in the bending direction.
- The sampling frequency should at least be higher than 10 times the frequency that needs to be detected. This provides enough data points along one periode of the motion to accurately map its frequency.

These three criteria led to the selection of the following sensors types:

- A piezoresistive three-axis accelerometer with range of $\pm 2G$, type 'LSM303DLHC'.
- A full-bridge strain gauge , measuring axial strain along the tower.

The detailed specification of the sensors, as well as a detailed description of the working principle of these sensors, can be found in appendix B.

5.2.4. Sensor positioning

The sensors have been placed in such a manner that they are not in a node of the bending modes corresponding to the natural frequencies of interest. Furthermore, the sensors have been placed on position where the bending motions are significant enough to be detected.

This means that the accelerometer is positioned in the nacelle, aligning the x axis with the tower fore-aft bending motions and the y-axis with the side-side bending motion. During operation, this ensures significant accelerations to be measured due to the thrust force of the rotor. Also, the accelerometer is placed on a stiff structural part of the nacelle to minimise any large amplitude ambient vibrations to be detected, due to the machinery inside the nacelle.

The strain gauges have been placed with some distance from the stiffer slip-joint connection to avoid measuring irregular strain patterns due to stress concentrations. Furthermore, a total number of three strain gauges have been placed with a spacing of 120° in the circumferential direction. In this manner, there will always be two sensors that do not lie on the neutral bending line, thus not measuring any axial strains.

Figure 5.2 shows a schematic overview of the placement of the two types of sensor on the structure. Figure 5.3a indicates the actual positions of the sensor on the turbine structure, showing strain gauges in orange and accelerometer in dark blue. Figure 5.3b and 5.3c show a close up of the sensors used.

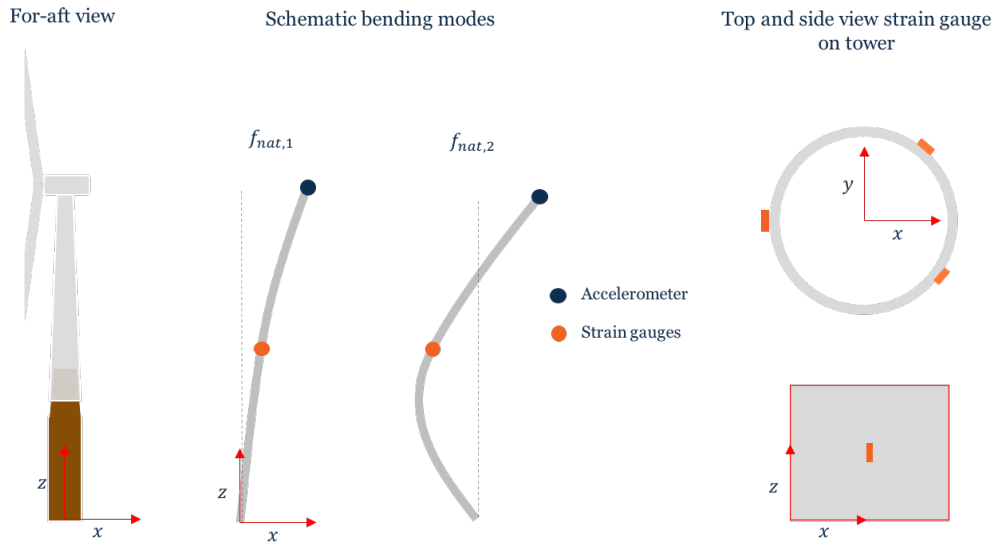


Figure 5.2: Schematic overview placement strain gauges and accelerometer



(a) Placement sensors



(b) Close up strain gauges



(c) Close up accelerometer

Figure 5.3: Natural frequency sensor overview

5.3. Slip-joint settlement

The goal of this part of the measurement campaign is to map the settlement of the slip-joint during installation and operation. The settlement of the slip-joint is measured in two ways, including:

- The absolute settlement of the slip-joint during different events at installation and operation.
- The development and nature of the settlement motion.

The first items present direct indications of settlement of the slip-joint and can be used to verify the slip-joint settlement calculations presented in section 6.3, while the latter might hold valuable information about the nature of this settlement, i.e. a jerky- as opposed to a smooth settlement motion.

5.3.1. Approach

To measure the stated items two types of sensors are used, supported by visual assistance. The quantitative settlement of the tower on the monopile will be measured by means of an analogue position sensor measuring the Δz in z-direction. Furthermore, a measuring staff with a camera is placed on the

outside of the monopile and the inside of the tower at target settlement height. This is an extra check on the output of the position sensor. The crucial factor in this measurement is the determination of an absolute zero-point. This zero-point has been determined during the installation. The tower was lowered gradually over the monopile and just when the tower touches the monopile, i.e. load drops from the crane hook, a zero-point is determined on both the position sensor and visually on the measurement staff.

To determine the nature of the settlement an accelerometer is used, measuring accelerations in the z-direction. The intensity and the time interval between the distinct acceleration peaks, due to the settlement of the tower on the monopile, is detected. It is anticipated that, due to the increasing normal force and resulting friction force when the tower settles over the monopile, the intensity of this motion will decrease. The decay in intensity, relative to the axial load applied during installation, could be used to possibly predict a final settlement of the slip-joint. The principle of this process is displayed in figure 5.4.

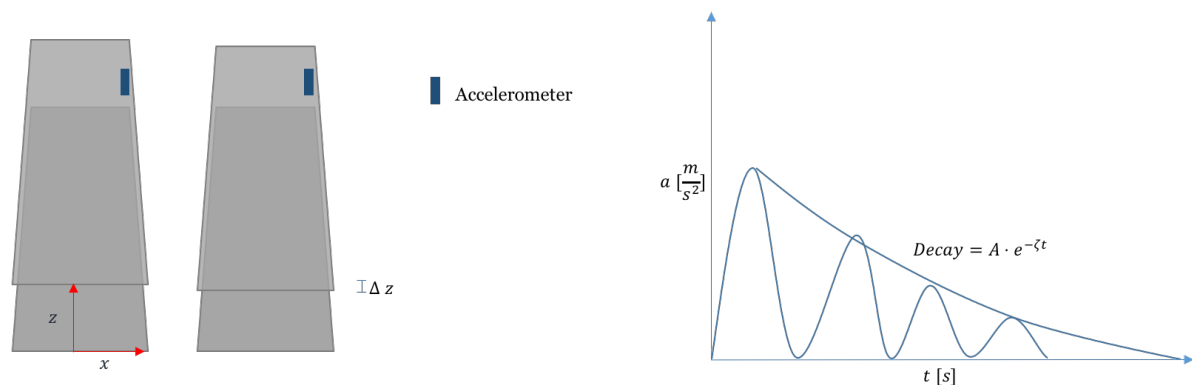


Figure 5.4: Schematic overview of decay in acceleration signal

Furthermore, the behaviour of the acceleration signal over time, combined with the settlement measured by the position sensor holds information about the nature of the motion. If the acceleration sensor shows a very peaked signal, this implies a jerky motion settlement of the tower on the monopile, whereas a smooth acceleration and settlement signal would imply a gradual settlement of the tower.

5.3.2. Chosen sensors

The sensors have been selected to meet the following criteria:

- The position sensor should have enough range to account for the uncertainties in predicted settlement.
- The accelerometer should have the right bandwidth to measure the possibly very low frequency motions of the settlement of the slip-joint.

These criteria have led to the selection of the following sensors:

- An analogue linear position sensor with 225mm reach, type 'Honeywell Smart'
- An piezoresistive accelerometer with range of $\pm 16G$, type 'LSM303DLHC'.
- Besides these sensors, a measuring staff is drawn on the monopile at the target overlap length and is monitored by a camera.

The position sensor has been placed inside a steel casing in order to easily spot-weld it to the tower. The detailed specification of the sensors, as well as a detailed description of the working principle of these sensors, can be found in appendix B.

5.3.3. Sensor positioning

The accelerometer is placed on a stiff structural part of the tower, i.e. the flench of the entrance door, in order to reduce the possibility of measuring large amplitude noisy ambient vibrations. The position sensor is placed on the tower, given the uncertainty of the point of first contact and further settlement on the monopile. Therefore, the position sensor itself is fixed and the anchor point on the monopile will be installed right after first contact point to act as a zero-point as indicated in section 5.3.1.

A schematic overview of the installed settlement sensors can be found in figure 5.5. The actual positions of the sensors on the turbine structure are shown in figure 5.6a, with orange marking the position of the accelerometer and red the position of the position sensor. Figure 5.6b and figure 5.6c show a close-up of the position sensor and accelerometer respectively.

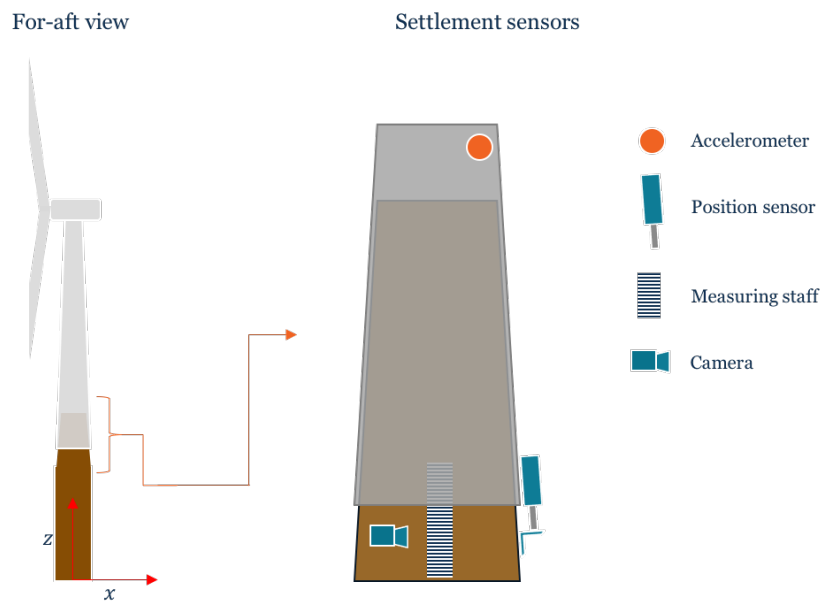
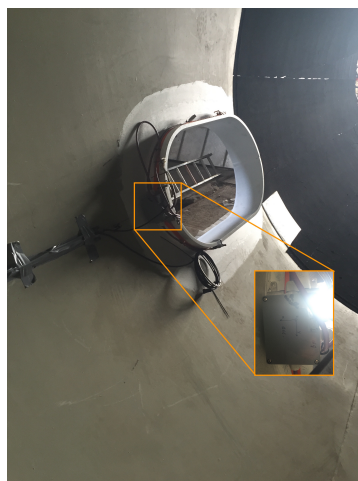


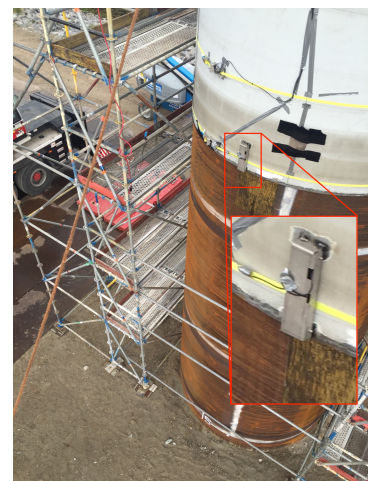
Figure 5.5: Schematic overview of settlement sensors



(a) Placement sensors



(b) Close up accelerometer



(c) Close up position sensor

Figure 5.6: Settlement sensor overview

5.4. Slip-joint stress distribution

The goal of this part of the measurement campaign is to identify the strains and resulting stresses within the slip-joint. Little is known about the internal stresses in the slip-joint during installation and operation. Carefully monitoring and analysing the strains could provide some valuable insights in the working principle and the structural integrity of this joint.

First of all, the strain distribution in the slip-joint could provide information about the contact area of the slip-joint. Any asymmetry seen on specific locations along the slip-joint indicate some kind of irregularity at that location of the slip-joint. This could for example be a non-contact area. This could in turn, provide a global indication of the total contact area of the slip-joint.

Secondly, the measurement of hoop strains, i.e. strains in the x-direction, along the slip-joint provide more detailed information on the working principle of the joint. It was shown in section 3.2 that the vertical stability in the joint is provided by the equilibrium of axial force on the slip-joint F_z , due to the self-weight, and the vertical component of the normal- and friction force, $F_{N,z}$ and $F_{f,z}$ respectively. This normal force has a radial component resulting in a hoop stress σ_{hoop} in the tower wall. Therefore, the measured hoop strains provide some insight in the forces and stresses within the slip-joint.

Finally, the measured strains provide an indication of the magnitude of the stresses in the slip-joint. This gives a rough indication whether or not the slip-joint's structural integrity can be guaranteed. As the tower was not purpose build for this joint, a monitoring system like this is essential.

5.4.1. Approach

To measure the strain distribution around the slip-joint connection, one ideally would like to place a number of strain gauges along the circumferential direction at multiple heights along the z-direction. However, this would be a costly solution since every strain gauge needs a conditioner and converter, which are quite costly. Therefore, a different solution was used to acquire the data. The measurement campaign here is threefold.

Strain gauges

On the slip-joint in the circumferential direction, every 2 m a strain gauge has been placed. The means a total number of six strain gauges per ring. A total number of three rings of strain gauges will be placed on the bottom, middle and top of the slip-joint as can be seen in figure 5.7. The primary goal is to acquire information on strains in the hoop direction. These strain gauge rings are aligned with the steel wires to check these measurements.

Steel wire with position sensors

On the same level as the strain gauges, as well as in the intermediate regions where no strain gauges are present, a steel taut wire has been placed, which is connected to a position sensor. This is displayed in figure 5.7 The wire is kept in place by means of conductors positioned on the tower. As is the case with the settlement position sensor, the sensor is placed inside a steel casing to easily mount it to the turbine tower. The taut wire is kept under tension by anchoring it to the casing and connecting it to the position sensor by means of a spring. The taut wire is chosen in such a way that it will not significantly elongate with the force introduced by the spring on the wire. In this manner the global hoop strain of one line in the circumferential direction is measured. This provides a global indication of the hoop strain over the height of the slip-joint. Furthermore, the strain gauges can be used to check this measurement and see if the values are somewhat reliable. A total number of seven taut wires with position sensors have been placed along the height of the slip-joint.

Acoustic measurement

The last item of this part of the measurement campaign is to perform an acoustic measurement on the slip-joint. It is anticipated that with the use of sound waves reflecting and transmitting through the two steel plates, an indication of the contact area can be obtained. This information is compared with the strain gauge data to see if any confirmation between the two results can be found.

The theoretical working principle behind this measurement is elaborated on in appendix E.5 and is based on the reflection and transmission coefficient, i_r and i_t respectively. Due to the difference in acoustic impedance of both steel and air the reflection coefficient greatly differs between a steel-air boundary and steel-steel boundary. Scanning different zones along the slip-joint and carefully monitoring the reflected energy could provide an insight in the contact area of the slip-joint.

5.4.2. Chosen sensors

The strain gauges and position sensors should meet the following criteria:

- The strain gauges should measure strain in one direction accurately.
- The accuracy of the strain gauge sensors should be within 5%. Anything lower than that is acceptable to get a proper indication of the distribution of the strains.
- The accuracy of the position sensor should, for the same reason, not be within 5%.

These criteria have led to the selection of the following sensors:

- An analogue position sensor with 75mm reach, type 'Honeywell Smart'.
- Full bridge, one direction strain gauges for the lower and the middle circumferences.
- A rosette configuration quarter bridge strain gauge, with a two dummy rosettes to compensate for temperature influences.

The details and working principle of these sensors can be found in appendix B. It must be noted here that the choice for a full bridge strain gauge and rosette was made as a cost versus benefit ratio. There are two main things to note on this matter.

Firstly, the full bridge strain gauge provides the most amplified signal and automatically compensates for temperature influences on both the steel and cable. A temperature difference of 20°C , already introduces a measuring error of 10%. When under the same circumstances this signal is sent through a copper cable of 5 m length, this measurement error is increased to 98%. Therefore, temperature compensation and a strain signal is a must, especially in an outdoor environment.

Secondly, the full bridge strain gauge measurement is only accurate when one principle stress is dominant. If the test specimen is undergoing a situation where two principle stresses are present, the influence of this effect cancel out the measured strain in the preferred measured direction. Therefore, they can only be used when the direction of the main principle stress is known and this principle stress is dominant. This situation is present at the bottom and middle of the slip-joint, but not at the top of the slip-joint, as the influence of the axial force increases the principle stress in the axial direction, compared to the bottom dominant hoop direction. Therefore, a rosette strain gauge is used at the top of the slip-joint. This rosette is temperature compensated with a dummy rosette on an unloaded piece of steel for earlier mentioned reasons.

5.4.3. Sensor positioning

The positioning and number of sensors has been decided on a cost versus benefit ground. The placement of six strain gauges along one circle in the circumferential direction spaces the strain gauges about 1.80 m apart on average. Furthermore, a total number of seven circles of measurements along the total height of the slip-joint, spaces the measurements 1.90 m apart.

A schematic overview of the installed strain distribution sensors can be found in figure 5.7. Furthermore, the actual installed strain gauges are displayed in figure 5.8b, with in red a close-up of the full bridge strain gauge and in orange a close-up of the rosette. Finally, figure 5.8c shows a close-up of the installed position sensors with taut wire.

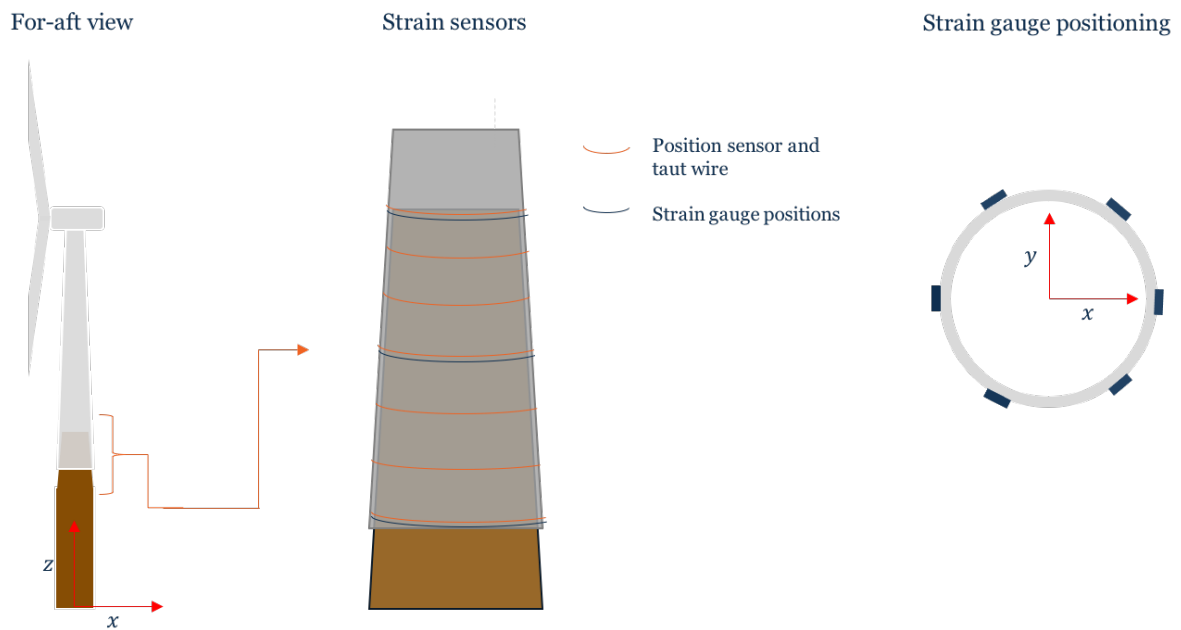


Figure 5.7: Schematic overview of placement of strain sensors



(a) Placement sensors



(b) Close up strain gauges



(c) Close position sensor

Figure 5.8: Strain distribution sensor overview

5.5. Calibration of the sensors

In order to be more certain about the measured values of the sensors, calibration is an important aspect. Also, a zero-point in the measurements is important to be able to relate the measured values to actual events that happened during the measurement. Although calibration is often done in the production process of the sensor itself it is of importance to check the provided calibration values.

5.5.1. Strain gauges

The strain gauge calibration was done by means of mounting a full bridge strain gauge and rosette strain gauge on a dummy steel strip. This steel strip was loaded with a calibrated force at the tip of the strip. By means of this exercise the strain gauge 'K-factor', was checked and found to be okay for both strain sensors.

Zeroing the strain gauge sensors is another important step while measuring with strain gauges. Since, the actual resistance of the Wheatstone bridge resistors and the cable resistance is never the same as calculated a proper zero-value has to be determined. This zero-point is the same as mentioned before, the point when the tower just touches the monopile. It is important to note here, that the measured values only provide information on the added stresses, due to the installation and operation of the slip-joint. This must be taken into account when making a judgement on the structural integrity of the joint.

5.5.2. Accelerometers

The calibration of the accelerometer can be done quite easily because of the fact that it is of the piezoresistive type. This means that it can detect accelerations up to 0 Hz , e.g. the gravitational acceleration. Therefore, the calibration process that has been performed was to place the accelerometer on a levelled plate on every one of its axis. The output signal should be precisely -1.0 G . The accelerometer was found to be calibrated correctly.

5.5.3. Position sensors

The position sensor calibration process was done by means of a simple measurement. Sliding the position sensor over a known distance x , should be equal to the output of the sensor. The position sensors were found to be calibrated correctly.

As is the case with the strain gauges, the position sensors' zero-point will be taken when the tower just touches the monopile during installation.

5.6. Sensor data acquisition

The data acquisition system is the system that acquires all the data from the different sensors and logs it to an external SD-card that can be read by the computer. The details of the sensor data acquisition system and working principle can be found in appendix B.

Every sensor sends its output signal to an analogue to digital (A/D) converter and in the case of the strain gauges an signal amplifier. Every A/D converter, or amplifier, has a total number of four channels. These converters, consequently send their data to the data logger, logging the data on a storage device. A maximum cable length of the strain gauges is set to 5 m , to minimise the negative influence of this effect on the quality of the signal. This determined the actual position of the converters, as displayed in section 5.7.

The sampling frequency for most sensors is set to 50 Hz . This provides enough data resolution for the measurement purposes, e.g. the frequency domain transformations. However, it does not generate too much data, overloading the data storage device and the communication cables. The only sensors that do not acquire data at 50 Hz , but at 25 Hz , are the position sensors, for a slightly lower resolution does not affect the purpose of the measurement.

Furthermore, the data acquisition system logs the data from the different sensors with identical time stamps. This makes it easier to compare the data in the processing stage, since every data point of every sensors has the same identical time stamp. Thus, all the data is transferred via one cable to the data logger. When the line is too busy, some sensors can not send their data. Therefore, a priority list has been made to prioritise the information sent to the data logger. This priority list is set as follows:

1. Position sensor
2. Stress distribution strain gauges
3. Natural frequency strain gauges
4. Settlement accelerometer
5. Natural frequency accelerometer

5.7. Conclusion

The measurement campaign with all the relevant aspects has been discussed in this chapter. Different approaches have been presented to measure the established relevant parameters of the DOT500 slip-joint, namely natural frequency, settlement and stresses within the connection. For this purpose an accelerometer and three strain gauges are equipped on the nacelle and tower to collect time signals for the identification of the natural frequencies of the tower. Furthermore, an accelerometer and a position sensor is mounted on the tower to map the settlement. Finally, multiple strain gauges shall be equipped on the turbine tower cone of the slip-joint to gather information on the stress distribution within the slip-joint.

The total overview of the total measurement campaign can be found in figure 5.10. In this figure the sensor coding can be found as well. The vertical grid lines '1' through '6' represent the position of the strain gauges in the vertical direction along the z-axis. The vertical line 'pos' represents the position of the position sensors and taut wires. Horizontal lines 'A' through 'G' represent the strain gauges measuring the strain distribution along the slip-joint. Horizontal line 'NF' represents the strain gauges measuring the natural frequency.

Furthermore, the blue lines are the cables connecting the strain gauges to the signal amplifiers and A/D converters. The pink lines are the cables connecting the position sensors to the A/D converters and finally, the cyan lines is the communication cable connecting the system to the data logger and power. The A/D converters are lettered 'A' through 'K' and 'M'. Furthermore, the letters 'L' and 'N' represent the accelerometers.

Figure 5.9 shows the same information in side and top view. Also the orientation of the wind turbine during installation is presented. Any further reference made to sensors in this thesis is done according to this coding.

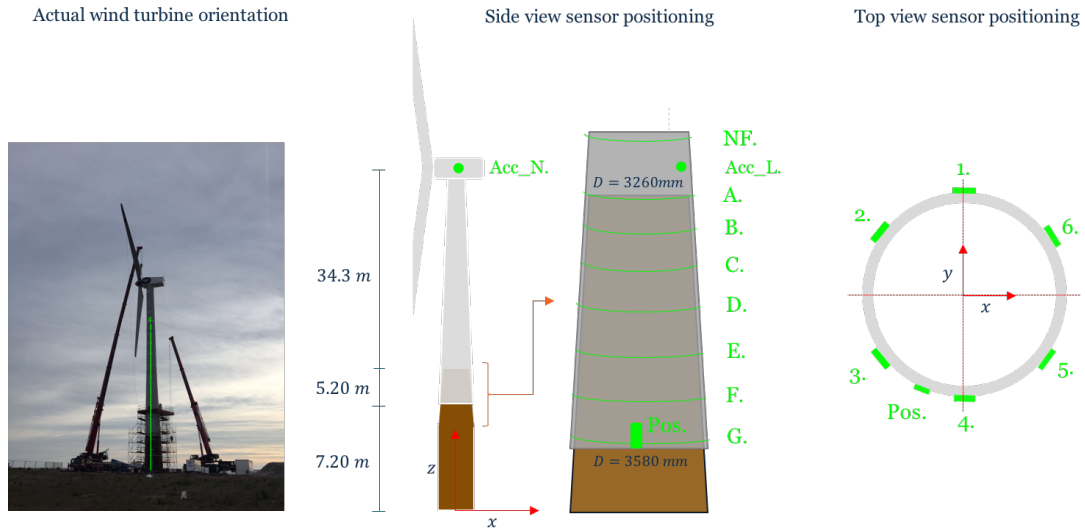


Figure 5.9: Overview of sensors on (actual) wind turbine structure

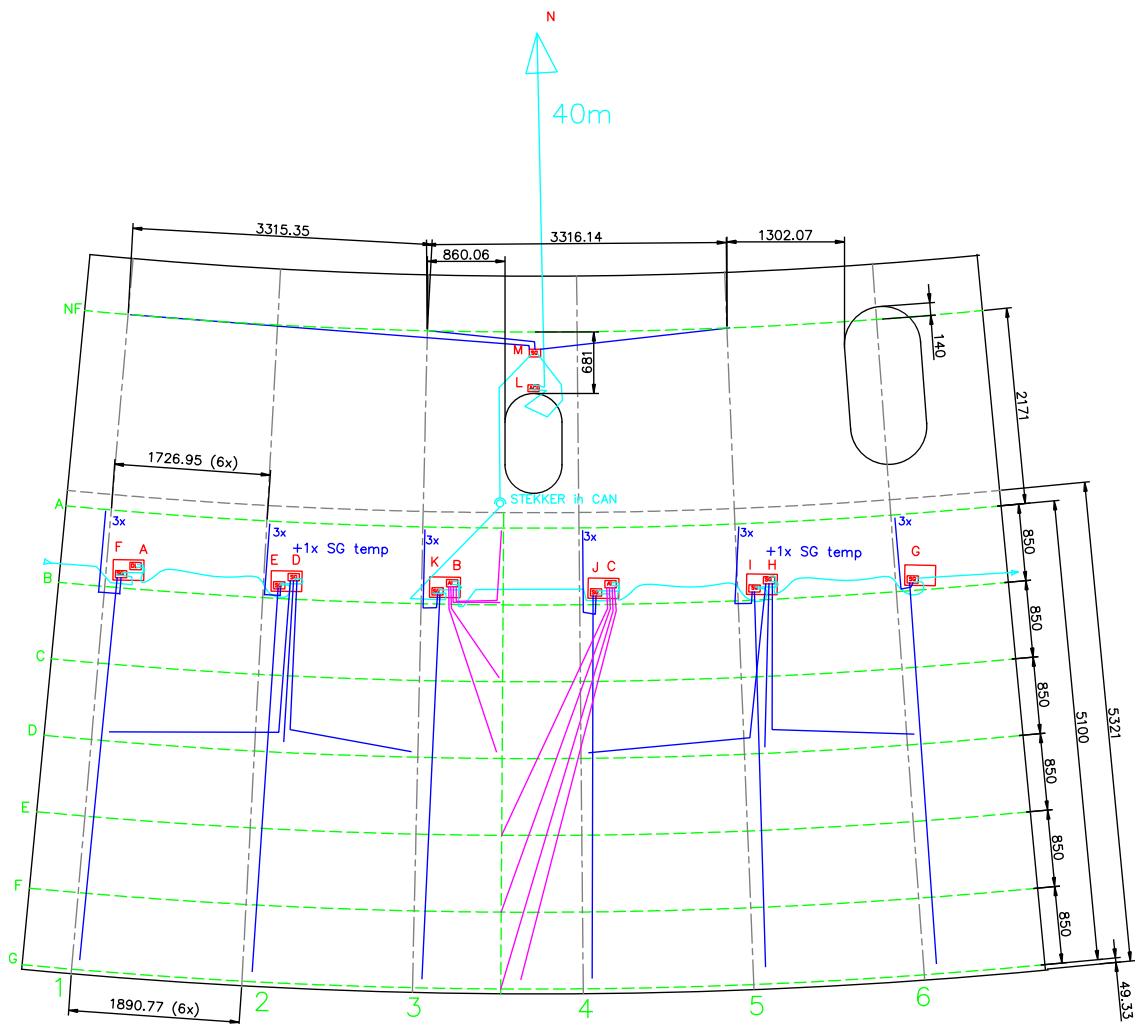


Figure 5.10: Schematic overview of the measurement instrument on the wind turbine tower

6

Modelling and predictions

6.1. Introduction

As for the next step in the process, an anticipated outcome of the different parts of the measurement campaign should be determined. As pointed out, the measurement campaign focusses on three points, including the natural frequency of the turbine system, the settlement of the slip-joint and the stress distributions within the slip-joint. Therefore, the focus of the models created in this chapter will coincide with the latter named items. Three models have been created, each predicting a possible outcome of the measurement campaign, which can be verified in a later stage of the project.

The aim of this chapter is to provide the reader with the basic concept behind the models and list the important assumptions and considerations taken while creating the model. The detailed information on the models can be found in appendix C, while the important steps, assumptions and outcome will be displayed in this chapter.

Section 6.2 provides information on the model that was used to identify the first natural of the total turbine system, while section 6.3 enlightens the model that was used to estimate the total settlement of the slip-joint after the installation process. Furthermore, the stress distributions, both globally and locally within the slip-joint, will be elaborated on in section 6.4 and 6.5. Every section is divided into subsections subsequently elaboration on (i) a description of the model (ii) assumptions in the model (iii) sensitivities within the model and (iv) the outcome of the model.

6.2. Natural frequency model

The identification of the first natural frequency of the first bending mode of the turbine structure was done by means of creating two models. One modelled in RFEM (a Finite Element program) and one in Bladed (commercial offshore wind turbine modelling software). The key feature in these models, is the creation of a tool that can conveniently take into account the soil-structure interactions to acquire a more accurate estimation of the first natural frequency. To this extend an excel-based tool was used to conveniently model this in both RFEM and Bladed. Modelling the monopile, tower and accompanying masses is fairly straight forward. However, modelling the foundation has an increased complexity in terms of unknown parameters and assumptions that need to be taken. The details of this feature will be discussed in the subsequent sections.

6.2.1. Model information

The start of both the RFEM and Bladed model is the tool that models soil-structure interaction. The aim of this tool is to take this effect into account by means of non-linear p-y curves acting as spring-supports in the lateral direction, as was explained in section 2.8. The input in this tool consists of the following items, which are shown in appendix C.2.:

- A soil layer distribution over depth
- The type of soil per layer
- Accompanying soil parameters per layer
- The monopile specifications per indicated soil layer
- A load combination if the displacement curve of the monopile is to be calculated by RFEM

With this information the tool creates the following output:

- A set of py-curves at every meter of depth that match the input soil layer and accompanying soil characteristics.
- Excel output sheets that can be read by RFEM as input to ease the process of creating the prescribed foundation in the Finite Element program.

With this output, the remainder of the RFEM and Bladed model can be conveniently created using the own built-in functions of the program. A flow-chart showing the above described steps is displayed in figure 6.1.

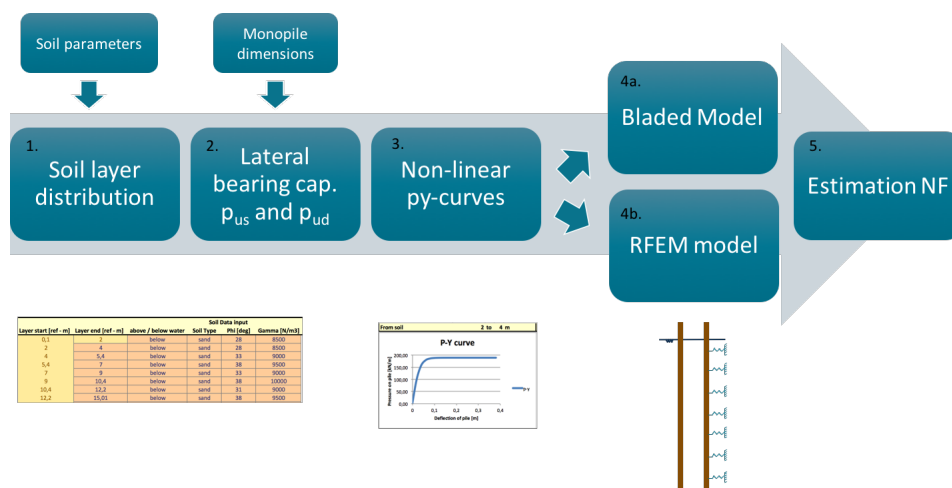


Figure 6.1: Schematic overview of foundation model for natural frequency

6.2.2. Assumptions and details

The assumptions and relevant details of the model will be discussed at every step of the model indicated by the numbers in figure 6.1.

1. Soil layer distribution

The first step in the model is the distribution of the soil at the designated site in different layers. The soil layers are to be entered with a maximum soil layer thickness of $\Delta z = 2.0 \text{ m}$. This discretisation of the continuous varying soil characteristics as a function of depth is required in order to end up with a finite number of spring-supports. This upper limit is chosen such that the spring-foundations in the eventual model can be placed every meter, as shall be explained in steps 2 and 3 of the model.

These soil parameters can either be obtained by externally conducted studies from professional parties, or they can be estimated from CPT-data, explained in section 2.8. The latter requires the use of several (semi-)empirical formula's and the interpretation of the executor. Since no externally conducted study has been performed at the DOT500 test site, the soil parameters had to be obtained via interpretation of the CPT data introducing an uncertainty in the obtained values.

2. Lateral capacity calculation

The next step within the tool is the calculation of the lateral bearing capacity of the soil at the distinct layers. This bearing capacity is calculated with the soil parameters and pile dimensions as input and according to the method described in section 2.8. This bearing capacity is depth dependent. At the top, the middle and the bottom of every soil layer the soil properties are calculated such that the maximum distance between two spring-foundations is $\Delta z = 1.0 \text{ m}$.

3. Non-linear py-curves

With the use of the calculated lateral bearing capacity of the soil layers at different heights the tool creates a set of py-curves according to the methods states in section 2.8. A cyclic loading pattern is assumed. Steps 1 through 3 are visualised in figure 6.2.

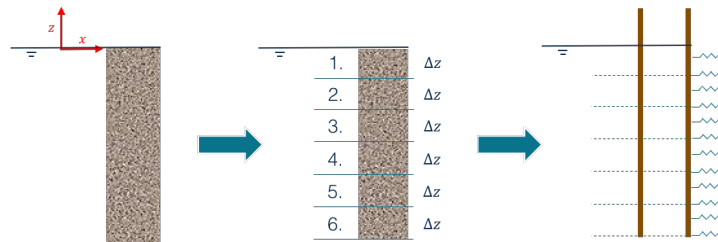


Figure 6.2: Schematic overview of discretisation steps in model

4a. Bladed model

The py-curves can be readily used as input in Bladed via lookup tables. This supports the structure in the lateral, x- and y-direction. The structure is fixed in the z-direction. The rest of the turbine tower has been modelled according to the dimensions specified in sections 4.2 and 4.3. Structural damping has been set 2%. In Bladed, the RNA is modelled as a top mass and inertia with different characteristics in fore-aft and side-side direction, to simulate the asymmetry introduced by the rotor.

4b. RFEM model

The tool creates output sheets that can be readily used as input in RFEM to create lateral support of the foundation. The turbine structure is fixed in the z-direction. The rest of the turbine is modelled according to the dimensions specified in sections 1.1.1 and 4.3. The RNA is modelled as a top mass in accordance with the total mass of the RNA, resulting in total axisymmetry about the z-axis.

Another feature of the tool is to create the deflection curve of the foundation as a result of a load case that can be specified in the input. The deflections and rotations of the pile can be exported to the tool. With this information the total foundation can be simplified and approximately be supported by a rotational and translational spring, with spring coefficients k_r and k_l of:

$$k_l = \frac{V_{ed}}{u_{seabed}} \left[\frac{N}{m} \right] \quad \text{and} \quad k_r = \frac{M_{y,ed}}{\phi_{seabed}} \left[\frac{Nm}{rad} \right] \quad (6.1)$$

This translational and rotational spring could be used as an approximation of the total lateral spring-supported foundation to ease the modelling process in Bladed. The approximation is valid as long as the py-springs stay in the linear area of the curve, which is the case for operational natural frequency predictions.

5. Estimation natural frequency

The models can now be used to estimate the natural frequencies of the bending modes of the turbine structure. Next to the estimation of the first natural bending frequency of the DOT500 turbine, an upper

limit is calculated. This provides a bandwidth between which the actual natural frequency should lie. This upper limit has been calculated by means of a infinitely stiff foundation i.e., a fixed support was incorporated in both models.

6.2.3. Sensitivities

The first and greatest sensitivity, is the input of soil parameters in the model. It is preferred to acquire these parameters from professional external parties as their experience and validated methods provide more reasonable estimates of the already complicated to model inhomogeneous material. In this case, an interpretation of the data obtained from a CPT was used to estimate the soil parameters. This introduces quite an uncertainty in the values of these parameters.

Secondly, the discretisation of the continuous depth-dependant characteristics of the soil bearing capacity introduces another sensitivity. The soil layer thickness Δz over which the characteristics are assumed constant, influences the outcome of the model.

6.2.4. Predictions

The outcome of both the Bladed and RFEM models is displayed in table 6.1. An upper limit and estimation is presented for the first natural bending frequency in both the fore-aft (x-direction) and side-side (y-direction). To avoid resonance problems, as explained in section 2.4, the 1P and 3P excitation zone should be avoided. They are shown in equation 6.2 for clarification. The first natural frequency of the bending modes lies in the middle of the 3P excitation zone at a rotor speed of around 16 RPM. Attention should be paid when operating at this rotor speed to monitor the tower's motion and possibly apply frequency skipping if the motion become to severe and show signs of resonant behaviour.

Table 6.1: First natural bending frequency estimations

	Direction	Estimation [Hz]	Upper Limit [Hz]
Bladed	fore-aft	0.795	0.988
	side-side	0.796	0.992
RFEM	fore-aft	0.823	0.983
	side-side	0.823	0.983

$$\text{Excitation ranges} \begin{cases} 1\text{P:} & 0.13 - 0.47 \\ 3\text{P:} & 0.40 - 1.40 \end{cases} \quad [\text{Hz}] \quad (6.2)$$

6.3. Slip-joint settlement

In order to gain insight in the target settlement of the slip-joint during the installation process, a first order static model was created. This model is based on the theory in section 3.2. The model is based on the equilibrium of the vertical forces working within the slip-joint. The details shall be discussed in the subsequent sections. In this section the following definitions shall be used:

- First point of contact, h_{foc} : height on z-axis measured from the top of the monopile at which the two cones contact each other for the first time
- Target overlap, h_{to} : height on z-axis measured from the top of the monopile at which the vertical equilibrium has been reached.
- Settlement, z_{settle} : the height along the z-axis between the target overlap and the first point of contact

These points are graphically displayed in figure 6.3 a through c respectively.

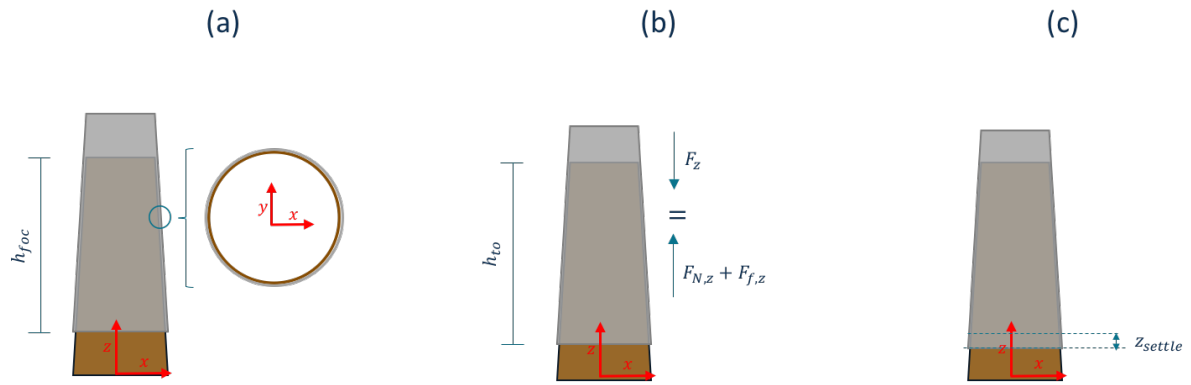


Figure 6.3: Graphical illustration of settlement parameters

6.3.1. Model information

The start of this model is based on the 3D measurements performed on the two cones of the DOT500 slip-joint structure. The two cones have been scanned along the area where they will overlap i.e., the monopile cone was scanned from the top downward and the wind turbine cone was scanned from the bottom upward. As explained in section 4.4, a target overlap of $1.5D_{MP}$ was used. Therefore, the cones were scanned over a distance of $6.00m$. Furthermore, the wall thicknesses have been measured at these areas. The input in the model consists of the following points, shown in appendix C.3:

- The diameters of the two cones as function of the height
- The wall thicknesses of the two cones as function of height
- The friction coefficient
- The total downward force i.e., the self weight of the structure

With this information the model creates the following output:

- The target overlap length
- The hoop stresses over the total height of the slip-joint

An overview of the model can be found in figure 6.4.

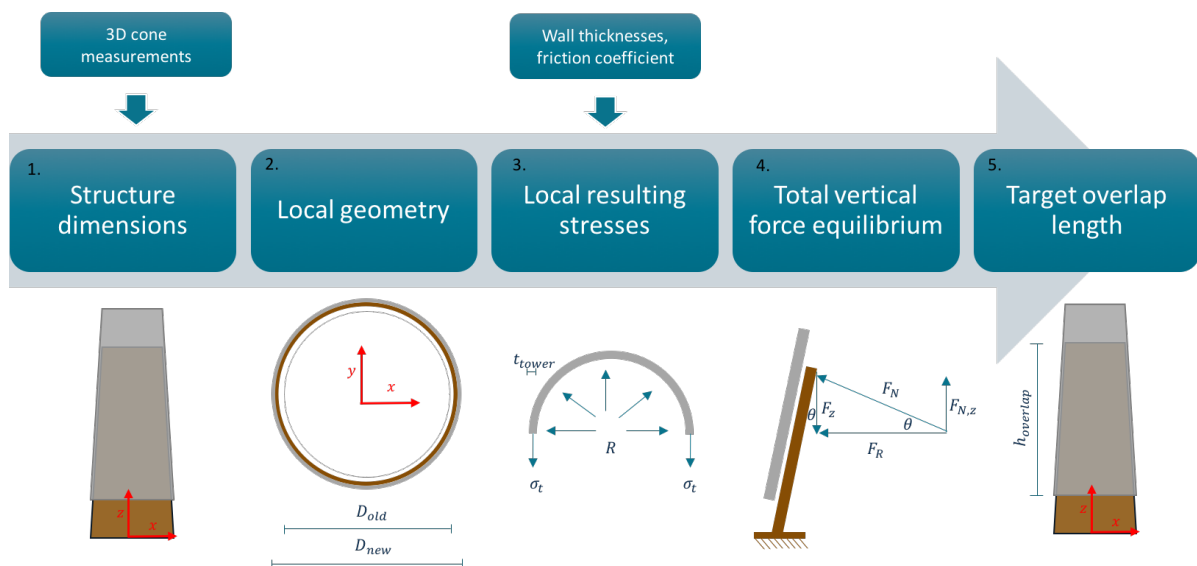


Figure 6.4: Schematic overview of settlement model

6.3.2. Assumptions and details

The details and assumptions of the model shall be discussed in this section, for every step as indicated in figure 6.4.

1. Structure dimensions

The model starts with the input of the structural dimensions of the two cones. Both of these were obtained using laser measurement technology. The resolution of these measurements and introduced sensitivities are different in both cases.

In the tower case, the measurements were performed by a laser tracker, situated at a known distance from the cone. The laser tracker scanned multiple points along the circumference at height intervals of $0.50m$. The accuracy of the laser tracker is within one-tenth of a millimetre, which does not contribute significantly to any sensitivities. However the intervals, both along the height and along the circumference of the cone, at which the measurements were taken do have an influence. The higher the resolution, the more accurate the actual shape of the cone is represented. Furthermore, the individual points, scanned by the laser tracker, are imported in a 3D-drawing application after which a perfect circle is fitted over these points to end up with the eventual diameter of the scanned circumference. The wall thicknesses of the tower have been scanned using Ultra Sonic technology. It is assumed that one plate of steel within the cone has the same wall thickness. This wall thickness is determined by means of averaging three points within one plate of steel, explained in section 4.2.

In the case of the monopile cone, a 3D measurement was performed. The accuracy of the device is around 1 mm . Likewise the laser tracker technology, the point-cloud that results from the 3D-scan is imported in a 3D-drawing application. Circles have been fitted in this point-cloud to determine the actual diameter of the cone at each specific location.

The obtained diameters as a function of the height of the slip-joint have been discretised along the height of the cones with a $\Delta z = 1\text{ mm}$. Any missing exact data has been linearly extrapolated. For both scans it is assumed that the measured circumference is a perfect circle, leading to a relation of:

$$D_{MP} = \frac{C_{tower}}{\pi} [m] \quad (6.3)$$

Any ovality in the shape of the cone is therefore neglected. It is reasonable to assume the the resistance to expand in the circumferential direction is much higher than to deform in the radial direction, therefore the friction build-up as a consequence of the latter is assumed not of great importance compared to the first.

2. Local geometry

At every discretised 1 mm circle, the local geometry is considered. As the two cones are lowered over each other, they will gradually start making contact on several circles along the height as the diameter of the monopile equals the diameter of the tower. At such a point, it is assumed that the diameter of the outer cone expands, while the diameter of the inner cone decreases. It is assumed that this deformation is proportional to the radial stiffness of the two cones, which almost has a linear relation with the wall thickness in the regions of $t = 0.015 - 0.040\text{ m}$ [16].

3. Local resulting stresses

Consequently, it is assumed that these circumferential deformations ($\Delta D_{T,MP}$) cause hoop stresses in the material that are linearly proportional to the strain in circumferential direction via Hooke's Law:

$$\sigma_{hoop} = \frac{\Delta D_{T,MP}}{D(z)_{T,MP}} \cdot E_{tower} \left[\frac{N}{m^2} \right] \quad (6.4)$$

For the ease of calculation it is assumed that the individual circle's deformation is uncoupled i.e., the deformation of one circle does not influence the deformation of another. In an actual deformation process, the one circle's deformation will influence another's creating more resistance to elongate in the circumferential direction. Therefore, this assumption gives an overestimation of the actual deformation.

4. Total vertical force equilibrium

Consequently, the stresses that result from the elongation in circumferential direction, will cause a radial pressure between the two cones. It is assumed that this pressure is given by the formulas presented in section 3.2. Therefore, this will result in an upward vertical friction force $F_{f,z}$ and the vertical component of the normal force $F_{N,z}$. It is important to note here that the formulas used for this friction force calculation are based on a uniform applied pressure and velocity independent friction force i.e., the Coulomb friction model [44]. For relatively low settlement velocities this latter assumptions is valid. The measurements should prove whether the first assumptions is valid for this model.

5. Target overlap length

The first point of contact is determined at the overlap distance where the first individual discretised ring of the cone makes contact and produces an upward force. From this point onwards the actual settlement starts.

The eventual target overlap is established on the basis of vertical equilibrium. The total vertical force of every individual ring, calculated in the previously described method, is summed over the total overlap length of the slip-joint. As soon as the magnitude of this upward vertical force equals the total downward force of the total structure the lowering is stopped. This point is determined as the target overlap length and the total settlement is the distance from the first point of contact to the target overlap length.

6.3.3. Sensitivities

The sensitivities of the model and effect of these shall be discussed. First of all, the uniform pressure distribution that is assumed to calculate the hoop stress and vertical upward forces is considered as a main sensitivity. The results of the measurements should prove whether or not this assumption is valid. If this is not the case, then the stresses could significantly deviate from the calculated ones using this model. Also, the assumption that the individual circle's deformation do not influence each other is a sensitivity in the model. The effect of this is not quantified, however it is noted that this assumption leads to an underestimation of the resistance to elongation, which in turn leads to an overestimation of the total settlement.

Secondly, the deviation from the structural dimensions, specifically the diameters of the cones, introduce quite a big sensitivity in the model. These deviations from the actual dimensions can be introduced by the inaccuracy of the 3D measurement and, or the post processing work. Furthermore, a temperature difference could also result in change of diameter in the two cones. If a linear thermal expansion is assumed, a temperature difference of $10^\circ C$ results in a diameter deviation of $\Delta D_{T,MP} = 0.50 \text{ mm}$. A deviation of $\Delta D_{T,MP} = 1 \text{ mm}$ is certainly within the expectations looking at the fabrication tolerances displayed in section 3.3. The quantification of these uncertainties is displayed in table 6.2. It can be observed that this introduces quite a big sensitivity.

Thirdly, the uncertainty in the friction coefficient between the two cones introduces another sensitivity in the model. For this model, a dynamic friction coefficient is assumed. Values for the dynamic friction between steel-steel range from $\mu_d = 0.20 - 0.50$ [9], [38]. A value of $\mu_d = 0.20$ is chosen. Although friction is quite important in the vertical force equilibrium it does not significantly contribute to the target overlap length. The sensitivity is looked at for an increased friction coefficient of $\mu_d = 0.50$. The quantification of this uncertainty is presented in table 6.2.

Fourthly, the known out of alignment of the monopile will have an influence on the first point of contact of the slip-joint. It is assumed that this inclination of the monopile does not further influence the target overlap length. To inspect this sensitivity an angle of the monopile of 0.1° is introduced. The quantification of this sensitivity is found in table 6.3.

Finally, ovality of the tower can increase the first point of contact considerably. Likewise the misalignment of the monopile, it is assumed that this does not influence the target overlap length. Considering the fabrication tolerances discussed in section 3.3 and 4.2, an ovality of 0.30% is inspected. If perfect ovality is considered i.e., $(D_{nom} - D_{min}) = (D_{max} - D_{nom})$, then the minimal diameter can be substituted in the ovality as a function of the maximum diameter via:

$$D_{max} = D_{nom} + (D_{nom} - D_{min}) [m] \quad (6.5a)$$

$$O = \frac{2D_{nom} - 2D_{min}}{D_{nom}} [\%] \quad (6.5b)$$

Consequently, equation 6.5b can be rewritten to find the maximum diameter as a function of the ovality and nominal diameter as in equation 6.6a. The difference in diameter $\Delta D_{T,MP}$ can then be found by subtracting the nominal diameter from the maximum diameter as in equation 6.6b.

$$D_{max} = -\frac{1}{2} \cdot (-2 + O)D_{nom} [m] \quad (6.6a)$$

$$\Delta D_{T,MP} = D_{nom} + \left(\frac{1}{2} \cdot (2 + O)D_{nom} \right) [m] \quad (6.6b)$$

If the average diameter of the cone of $D_{nom} = 3.414 m$ is used in combination with an ovality of 0.30 %, then an decrease in diameter of $\Delta D_{T,MP} = -5.12 mm$ is found. The quantification of this sensitivity is found in table 6.3.

Table 6.2: Influence of sensitivities on settlement parameters

Sensitivity Effect	Base Case [mm]	Diameter deviation $\Delta D_{T,MP} = 1 mm$		Temperature difference $\Delta T = 10^\circ C$		Friction coefficient $\mu_d = 0.50$	
		Absolute [mm]	Relative [%]	Absolute [mm]	Relative [%]	Absolute [mm]	Relative [%]
First point of contact	5223	-16.0	-0.31	-7.00	-0.13	0.00	0.00
Target overlap length	5232	-16.0	-0.31	-7.00	-0.15	-2.00	-0.04
Settlement	9.00	0.00	0.00	0.00	-11.1	-2.00	-22.2

Table 6.3: Influence of sensitivities on settlement parameters

Sensitivity Effect	Base Case [mm]	Monopile tilt $\alpha = 0.1^\circ$		Tower ovality $O = 0.30\%$	
		Absolute [mm]	Relative [%]	Absolute [mm]	Relative [%]
First point of contact	5223	-273	-5.23	-84.0	-1.61
Target overlap length	5232	5232	0.00	5232	0.00
Settlement	9.00	273	3.03E3	84.0	933

6.3.4. Predictions

The predictions of the first point of contact, target overlap length and accompanying settlement is displayed in tables 6.2 and 6.3 as the base case. These are the following values:

- First point of contact: 5.223 m
- Target overlap length: 5.232 m
- Settlement: 9 mm

6.4. Slip-joint global stress distribution

The global stress distribution in the hoop direction is a direct result of the model that was used to calculate the total settlement. Therefore, the reader is referred to sections 6.3.1 and 6.3.2 for information of the model and the assumptions and details. The sensitivities and predictions of the stress along the slip-joint will be treated in the subsequent section 6.4.1. In this section and in the model the stresses in the tower shall be considered, because these will be measured during the measurement campaign. The stresses in the monopile are significantly lower since the wall thickness is a little over twice the size.

6.4.1. Predictions and sensitivities

The sensitivities in the model are the same as described in 6.3.3, however the implication of these on the stresses shall be elaborated on here. The only sensitivity that have an influence on the stresses is an increased friction coefficient. The rest of the sensitivities do not influence the total settlement of the slip-joint, therefore no deviation of the stresses within the slip-joint shall be present. The effect of this sensitivity, with the same input-magnitude as presented in 6.3.3, is displayed in figure 7.8b and the base case stress distribution is displayed in figure 7.8a.

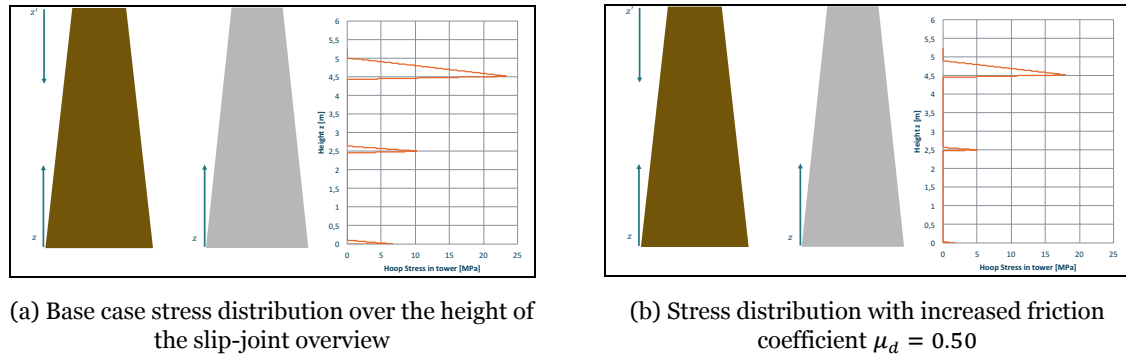


Figure 6.5: Stress distributions within slip-joint for base case and increased friction coefficient

Although other contributions to these stresses are present, as shall be elaborated on in section 6.5, this model suggest that the friction force that will support the slip-joint is effectively only created on limited areas of the total overlap length. Nonetheless, they can be considered insignificant of magnitude, as they are far below the tested yield stress of the material of $f_y = 320 \text{ MPa}$.

6.5. Slip-joint local stress distribution

The global stress distributions along the height of the slip-joint have been discussed in the preceding section. It is also important to look at the local stress distributions, especially the difference along one circumference of the slip-joint. The effect of non-uniform pressure and ovality is investigated. To this end, a Finite Element Model (FEM) was created, which will be treated in section 6.5.1. A discussion on the outcome of the model shall be treated in section 6.5.2.

6.5.1. Model information

To get insight in the stress distributions a number of FEM's were created, which can be ordered in two categories. Firstly, the effect of non-uniformly applied pressure on the insight of the outer cone shall be discussed and secondly the effect of an oval outer cone is discussed. The load cases and model information is treated in the subsequent subsections. It is important to note that these models were created not to get an actual representation of the magnitude of the stress distribution along the actual slip-joint. The purpose of these models is to get a feeling for the distribution of these stresses and acquire information on the type, tension or compression, of local stresses in the slip-joint.

Non-uniformly applied pressure

The model that was created to simulate the non-uniformly applied pressure is presented in figure 6.6.

In this model the lower 5.500 m of the actual slip-joint outer cone dimension i.e., the wind turbine lower tower, is used. The model is constrained at the top of the cone, in all directions. Furthermore, the model is created using several surfaces with intervals of $\Delta z = 0.500 \text{ m}$ over the height, and divided into six segments in the circumferential direction. The local axis system of all the surfaces are aligned to make inspection of the local hoop stresses more convenient.

With this model, three different load cases are run to see the influence of non-uniformly applied pressure. The load cases have been chosen to match the global stress distribution presented in section 6.4.

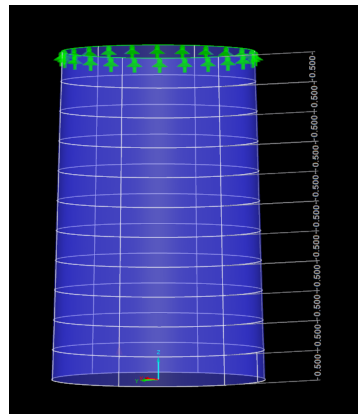
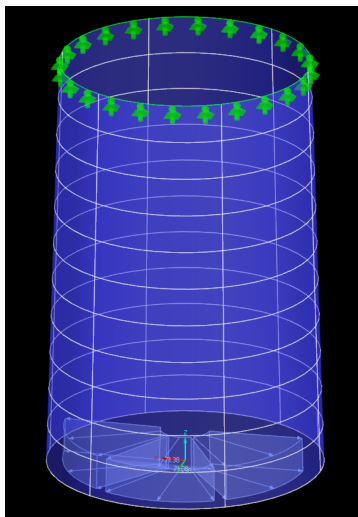
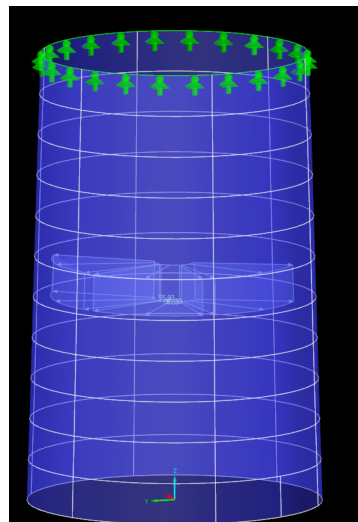


Figure 6.6: Schematic overview of FEM for non-uniform pressure application

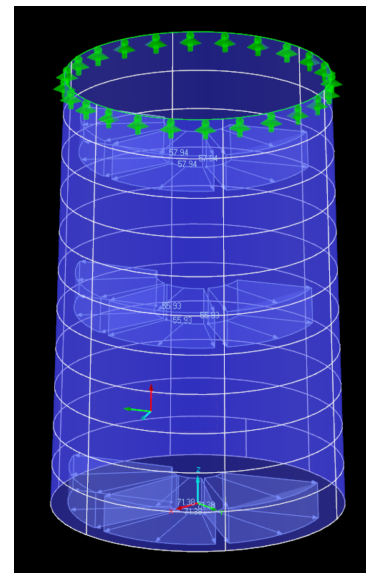
This means that a non-uniform pressure is applied over half the circumference on the levels $z = 5.00\text{ m}$, $z = 2.50\text{ m}$ and $z = 0.25\text{ m}$. This simulates the effect that the slip-joint slides on one side of the cone, for example due to the out of alignment of the monopile. These load cases are presented in figure 6.7. The outcome of the analysis is treated in section 6.5.2.



(a) Load case 1: non uniform pressure at bottom of slip-joint



(b) Load case 2: non uniform pressure at middle of slip-joint



(c) Load case 3: non uniform pressure at several heights

Figure 6.7: Different load cases simulating non-uniformly applied pressure

Ovality in outer tower

Another FEM was created to simulate the effect of uniformly applied pressure on an oval cylinder. To this end, an arbitrary ellipse was created with a nominal diameter of $D = 3.300\text{ m}$ and a height of 5.500 m . Likewise the previous model the model is made up of surfaces with aligned local axis systems to easily read the local hoop stresses. The ovality that is introduced is $O = 0.30\%$. On this oval an arbitrary uniform pressure was applied on the bottom of the oval, while the top of the oval was constrained in all directions. The model is presented in figure 6.8

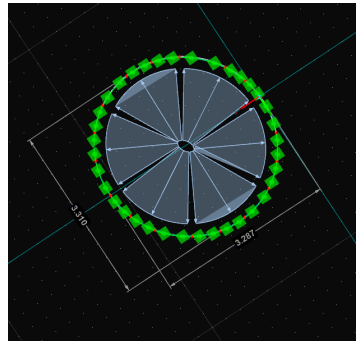
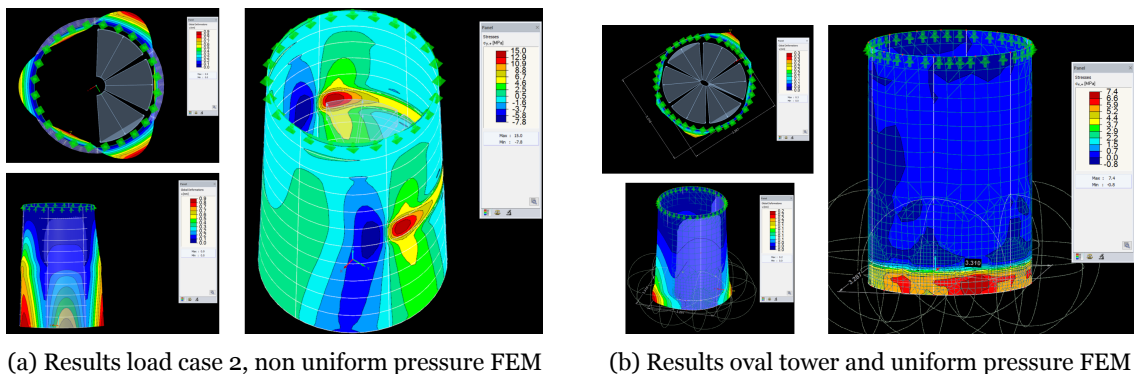


Figure 6.8: Schematic overview of FEM for oval tower simulation

6.5.2. Model outcome

The outcome of the two models showed interesting results. The hoop stresses and deformations of the non-uniformly applied pressure FEM with load case 2 and the ellipse FEM are presented in figure 6.9. The calculation output of the other models show similar behaviour and can be found in appendix C.4.



(a) Results load case 2, non uniform pressure FEM

(b) Results oval tower and uniform pressure FEM

Figure 6.9: Results of two FEM calculations

What can clearly be concluded from the results, is that the presence of both compression and tension is a possible effect of non-uniformly applied pressure or an oval section being loaded with a uniform pressure. Although the global circumference shows expansion and thus tension, the local stresses in the hoop direction show compression. The absolute magnitude of the stresses does not include any significant information. However, it is important to note that this magnitude may vary significantly over the circumference of the cone.

From the deformations in figure 6.9a and 6.9b it can be concluded that the steel has to deform in the negative radial direction for compression stresses to occur. In the actual situation the monopile will be positioned at the inside of the wind turbine cone, which prevents it from deforming significantly in the negative radial direction. Therefore, if compression stresses are to be found in the measurements on the wind turbine tower it means that the steel has to deform in the negative radial direction. This can only happen if there is nothing to resist it from moving inward i.e., the monopile and wind turbine tower cones are not in contact at that specific location.

6.6. Conclusion

This chapter has presented three models that have been created to anticipate the results of the measurement campaign and get a better insight in the different parameters that influence the slip-joint. First of all, a tool was created to ease the inclusion of a Winkler foundation py-springs in both a RFEM and Bladed model of the wind turbine structure. These models were used to estimate the first natural frequency of bending modes in the fore-aft and side-side direction of the wind turbine. An estimated

0.80 *Hz* was found in the RFEM model and 0.82 *Hz* was found in the bladed model, with very minor differences in fore-aft and side-side bending modes. These frequencies lie in the middle of the 3P excitation range, therefore attention should be paid around the 16 *RPM* operation speed of the turbine to check for signs of resonant behaviour.

Secondly, a first order static model based on vertical force equilibrium was created to predict the settlement and accompanying hoop stresses during installation of the slip-joint. It is anticipated that the target overlap of the slip-joint will reach 5.232 *m*, measured from the top of the monopile cone. The sensitivities in this model are concentrated on the deviations from the input dimensions of the cones and the uncertainty in the friction coefficient. Furthermore, the model does not incorporate the possibility of ovality in the cones, which introduces another sensitivity in the model. Simple geometry calculations show that this could lead to a discrepancy, between measured and modelled first point of contact, of up to 84 *mm*. Also, the monopile tilt could increase this first point of contact with an estimated 270 *mm* per tenth of a degree. The global stresses resulting from the settlement, are concentrated on limited areas within the slip-joint overlap, but can be considered of minor significance as they are in the order of magnitude of 10 – 30 *MPa*.

Finally, multiple FEM's were created to investigate the local stress distributions along the circumference and height of the slip-joint, especially as a result of non-uniform inside pressure and ovality of the outer cone. The results show that the stresses as a result of these load cases can vary significantly over the cone's circumference. Furthermore, compression is to be expected at positions where the monopile and wind turbine tower are not in contact. This can be caused by negative radial deformation of the wind turbine cone, due to non-uniform loading. This provides a method to identify the contact-area within the slip-joint

7

Results during installation

7.1. Introduction

In this chapter, the results of the measurements on the DOT500 support structure during the installation process are discussed. The installation took place in two phases. First of all the monopile was vibrated into the soil on the 6th of May and secondly, the rest of the DOT500 wind turbine was erected on the 18th and 19th of May 2016.

A great amount of data from the different installed sensors on the slip-joint, was gathered. This chapter presents the most relevant findings related to this research. To this end, the results are presented in this chapter while the post processing techniques and theory can be found in appendix D. Every graph is accompanied by a sketch of the slip-joint and the sensors, as explained in section 5.7. The sensors, corresponding to the presented data, are indicated in the figures with a red colour.

First of all, an overview of the total installation shall be presented in section 7.2. This provides the reader with the background on different events during the installation. Subsequently, the relevant results of the different sensors shall be presented in section 7.3 and 7.4. These sections will elaborate on the settlement as a result of the installation and the accompanying stresses within the slip-joint, respectively. Also, an acoustic measurement, that was performed after the installation, is treated in section 7.5. At last, section 7.6 lists the main findings and conclusions that can be drawn from the explored data.

7.2. Installation process

To get an overview of the steps taken during the installation, the different phases of the installation of the DOT500 turbine shall be presented. The installation took place over the course of three days. First of all, on the 6th of May the monopile was vibrated into the soil. On the next two days, the 18th and 19th of May, the wind turbine was erected.

7.2.1. Monopile installation day: 6th of May

On the 6th of May the monopile was installed using the vibro-hammering technique. After the installation, a 3D scan was made using the point-cloud scan as was discussed in section 4.2. The following installation steps were taken, which are also graphically depicted in figure 7.1.

- (a) The monopile was shipped to the project site at Maasvlakte two (MVII) and prepared for vibro-hammering installation.
- (b) The monopile was vibrated into the soil by means of the CV-320 VLT hammer.
- (c) Monopile installation was completed and 3D measurement was performed



Figure 7.1: Installation phases of day one, the 6th of May

The monopile was installed medium dense, to dense sand conditions to the target penetration depth of 15 meters. However, the actual installation time of about 80 minutes was longer than the predicted installation time of about 35 minutes, which was estimated based on a vibro-drivability study performed by Allnamics. Especially, the sections of about 9-10 meters penetration depth, and the final meter, lasted significantly longer than expected. A comparison and overview of these measured and predicted settlement speeds can be found in appendix E.2.

Furthermore, the monopile was installed with a slight offset from the vertical, based on the 3D measurements performed by Neitraco. The results of this measurement can be found in appendix A in figure A.9. The offset was found to be 0.77° in the negative y-direction and 0.90° in the negative x-direction in the defined axis system, also included in figure 7.1.

7.2.2. Wind turbine installation day one: 18th of May

The erection of the wind turbine was executed over the course of two days. On the first day, auxiliary equipment and the lower tower i.e., the slip-joint connection was installed. The following installation steps were taken, which are also graphically depicted in figure 7.2.

- (a) A scaffolding construction was made for easy access to the wind turbine and the slip-joint during the measurements and operation.
- (b) The leaking tray and the skid was installed on top of the monopile. The skid contains all the ground level equipment of the hydraulic drive train, such as the oil motor, the hydraulic power unit and the water pump.
- (c) The lower tower was installed on the monopile, by means of the slip-joint connection. From this point onwards, the measurement equipment started logging.



Figure 7.2: Installation phases of day two, the 18th of May

The slip-joint was to be installed via the controlled dropping principle, described in section 3.4.1. However, a miscommunication with the crane driver, during the lowering of the tower part over the monopile, had occurred. This led to the fact that the lower tower was lowered far below the first point of contact, which in turn resulted in the fact that the tower could not be lifted as the built-up friction was too large already. Therefore, the zero-point of the measurement equipment was established at this given instant of the installation. At this point, the hook load was reduced by 10 mT of the total 16.9 mT weighing lower tower. From this point onwards, the measurement equipment started logging and the tower settled due to self-weight only.

Apart from this fact, the slip-joint installation went smoothly and was completed within two hours. This included the delay due to the communication error. No real complication was experienced during the slip-joint installation, despite the slight out of alignment of the monopile.

7.2.3. Wind turbine installation day two: 19th of May

During the second day of the wind turbine installation, the remaining parts of the wind turbine were installed. In the morning, the rotor was assembled on ground level and the other items were prepared for lifting, which started after noon. The following installation steps were taken, which are also graphically depicted in figure 7.3.

- (a) The access platform was installed over the lower tower of the wind turbine.
- (b) The upper tower part was installed with the traditional bolted connection.
- (c) The nacelle was lifted and installed on top of the turbine tower.
- (d) The pre-assembled rotor was lifted in one piece and installed on the nacelle.



Figure 7.3: Installation phases of day two, the 18th of May

The masses of the individual subcomponents are listed in table 7.1.

Table 7.1: Masses of the subcomponents of the wind turbine

Subcomponent	Parameter	Value	Unit
Access platform	Mass	5.00	mT
Upper tower part	Mass	13.1	mT
Nacelle	Mass	13.8	mT
Rotor	Mass	9.20	mT

The installation of these components went smoothly and according to plan, except for the upper tower part. Some difficulty was experienced due to the slight out of alignment of the substructure. The mechanics experienced difficulties during the connecting process of the bolts between the two tower parts. This was caused by the fact that the bolt flange of the lower tower was at a slight angle from the vertical. The upper tower was lifted upwards and downwards to reposition it to allow for a secure connection.

7.2.4. Conclusion and discussion

From the installation process, a number of conclusions can be drawn. First of all, it can be concluded that the monopile was vibrated into relatively dense soil to the target penetration depth of 15 meters. However, this took substantially longer than expected. Furthermore, the 3D scan revealed that the monopile was installed with a slight out of alignment with the vertical axis of 0.77° in the negative y-direction and 0.90° in the negative x-direction. This results in a maximum out of alignment with the vertical axis of 1.18° .

Secondly, the installation of the slip-joint connection progressed smoothly, despite the slight vertical misalignment of the monopile. The installation of the item was completed within two hours, including a small delay due to communication error with the crane driver. However, the upper tower part, connected with a traditional bolted connection, did experience some difficulties during the installation. The out of alignment of the substructure, resulting in a slightly inclined bolt flange, hindered the connection of the bolts between the two tower parts. Although the 1.18° angle is far beyond the current industry requirement of 0.50° [15], it is important to conclude that this is not crucial for a slip-joint connection, in contrast to the traditional bolted connection.

7.3. Slip-joint settlement

The settlement of the slip-joint connection, during the installation process, was carefully mapped with both position sensor and visual assistance. The settlement behaviour during the installation is treated in section 7.3.1 and the additional settlement during the subsequent days is presented in section 7.3.2. Finally, a comparison of the predicted final settlement and overlap versus the actual measured quantities is evaluated in section 7.3.3.

7.3.1. Settlement during installation

In this section the settlement of the slip-joint due of the installation of the different subcomponents, as elaborated on in section 7.2, is treated. The zero-point of the settlement is determined as the point where the slip-joint was lowered over the tower with 10 mT of the tower's mass released from the hook, as described in section 7.2.2. Due to the miscommunication on wind turbine installation day one, no live data on this day is available. Only short time instances were logged.

Absolute settlement

The absolute value of the settlement of the slip-joint as a result of the different installed items was logged and is presented in table 7.2. This settlement was measured one hour after each component was released from the crane hook. Also, the relative absolute settlement per mT is presented to get an idea of the progressive behaviour of the settlement. Lastly, the cumulative settlement (including additional settlement between the installed items and overnight) over the course of these two days measured at the end of wind turbine installation day two, is presented in the bottom row.

Table 7.2: Settlement and relative settlement of slip-joint

Subcomponent	Installation day	Mass [mT]	Settlement [mm]	Relative settlement [$\frac{\text{mm}}{\text{mT}}$]
Lower tower (remaining mass)	Day one	6.90	-59.7	8.65
Access platform	Day two	5.00	-13.4	2.68
Upper tower part	Day two	13.1	-26.5	2.04
Nacelle	Day two	13.8	-14.2	1.03
Rotor	Day two	9.2	-2.1	0.23
cumulative settlement			-136	

It is noted that the relative settlement, defined as the settlement per mass-unit, decreases significantly with every additional component that is installed. Regardless of the absolute mass of the installed

item, the settlement of the slip-joint clearly converges to a final target level as a result of self-weight only. Furthermore, it is concluded that the additional settlement, which occurred between the installed items and overnight, accounts for an extra -20.4 mm leading to a total settlement of $z_{\text{settle}} = -136 \text{ mm}$.

Settlement behaviour

The nature of the settlement during the installation phases can be classified as very smoothly and no unexpected settlement or unexplained peaks in settlement velocity of the tower on the monopile can be detected. Figure 7.4 shows the settlement of the slip-joint on the second day of the wind turbine installation. The time instances at which the load of the installed component was released from the crane hook, are indicated. It is clear to see that the settlement progresses in a smooth manner and in a fashion one would expect.

Also, the numerically approximated settlement velocity of the slip-joint is presented for an arbitrary installed item, in this case the access platform. No unexplainable peaks or unexpected events can be identified during the installation of the four components.

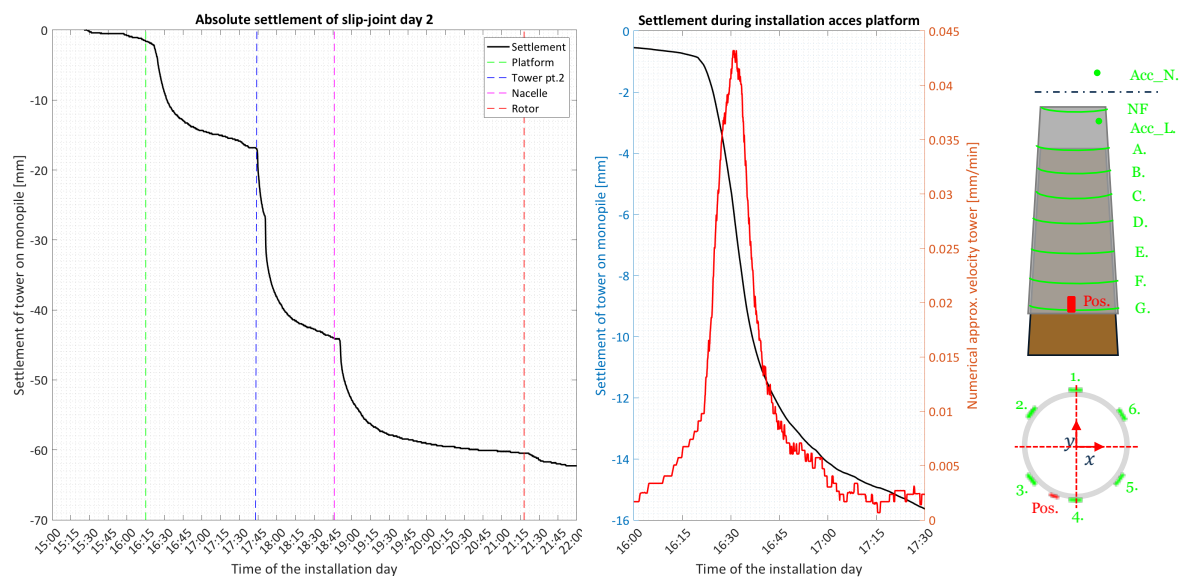


Figure 7.4: Settlement of slip-joint day two (left) and numerically approximated settlement velocity (right)

Finally, the accelerometer positioned in the lower tower measured the additional accelerations due to the settlement and installation of the different items. The signal-to-noise ratio (even after filtering) is found to be quite low, as can be observed in appendix E.3 in figure E.6. Therefore, limited information can be obtained from this sensor. Nevertheless, the highest peak in additional accelerations found in this time record, is in the order of magnitude of $1 G$. This happened during the beginning of the upper tower installation, and right after the upper tower load was released from the hook. Apart from these peaks, the accelerations during settlement are in the order of magnitude $0.25 - 0.50 G$ or below noise level, which is not considered very significant in terms of possible damage to equipment or personnel.

7.3.2. Settlement after installation

As was already noted in section 7.3.1, the slip-joint also settled progressively after the installation days. During the first night, from installation day one to installation day two, a settlement of $z_{\text{settle}} = -13.2 \text{ mm}$ was observed, followed by a settlement of $z_{\text{settle}} = -7.37 \text{ mm}$ during the second night. Over the course of the next three days an additional settlement of $z_{\text{settle}} = -3.82 \text{ mm}$ was observed. This clearly shows that the progressive settlement in the subsequent days is small and that the system converges to a final settlement level of $z_{\text{settle}} = -148 \text{ mm}$. This can also be observed by inspection of the graph in figure 7.5, which shows the total settlement of the slip-joint during the first weeks after the

installation. The clearly converging approximated settlement velocity per day is also shown by the red line.

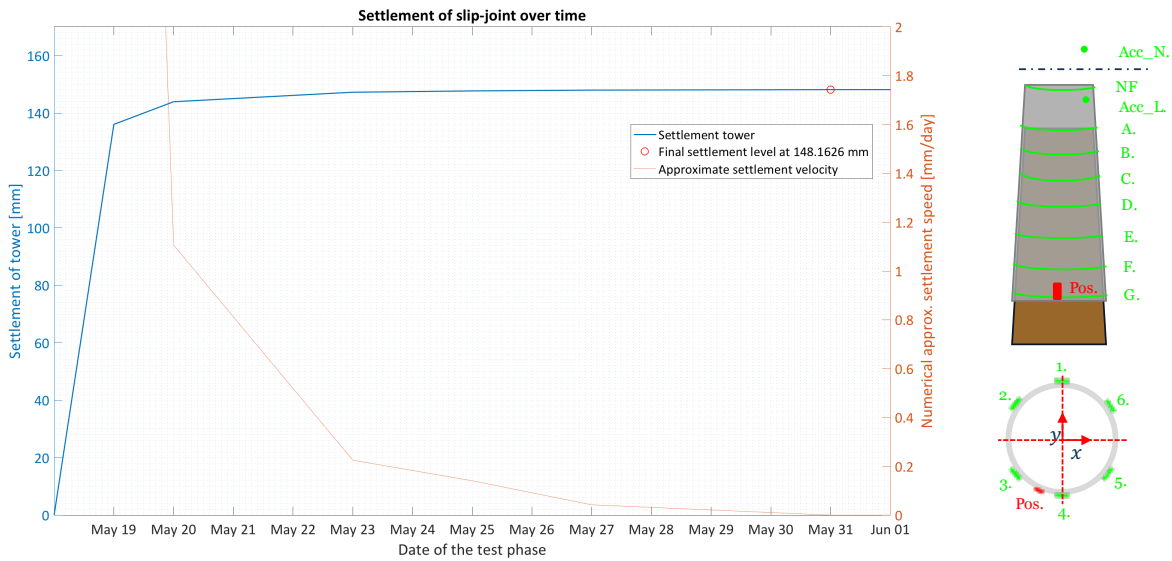


Figure 7.5: Total settlement of the slip-joint and approximated settlement velocity over the days

7.3.3. Final overlap compared to model

A first order static model, described in section 6.3, was created to predict the result of the slip-joint settlement. The predicted target overlap length was $h_{overlap} = 5.232 \text{ m}$. The zero-point of the measurements as discussed in section 7.2.2, was set at a height of 5.031 measured from the top of the monopile cone. It should be noted that this was not the actual first point of contact, however the real first point of contact is not known. An overview of the anticipated and measured values of the first point of contact h_{foc} , target overlap h_{to} and settlement z_{settle} can be found in table 7.3. The definitions are graphically displayed in figure 7.3.3.

Table 7.3: Measured and anticipated settlement values

	Predicted value [mm]	Measured value [mm]	Difference [mm]	Relative difference [%]
First point of contact	5223	5031	192	3.68
Target overlap	5232	5179	53	1.01
Settlement	9.00	148	139	-

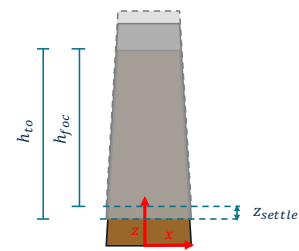


Figure 7.6: Settlement definitions

Two main observations can be made based on this data. First of all, the first point of contact was found to be earlier on in the lowering process than was predicted by the model. However, the model assumed two vertically aligned cones with no ovality. Taking into account the known significant ovality of the tower of $O = 0.35\%$ and the fact that the monopile has a maximum out of alignment with the vertical axis of $\alpha = 1.18^\circ$, the outcome is not surprising and well within the sensitivity limits that were established. Even a slight monopile angle, will cause the slip-joint to make an earlier contact of 273 mm.

Secondly, the target overlap is reasonably within the anticipated value taking into account the discussed sensitivities. The combined uncertainty in fabrication tolerances of the monopile and the inaccuracy in the laser measurements could easily lead to a mismatch in diameter of ΔD of 2 – 3 mm. This would already explain the 53 mm difference. Furthermore, the model does not account for any friction build-up due to ovality effects of the tower, or due to the out of alignment of the monopile. Given the fact

that these effects were actually present, and observed in terms of an earlier first point of contact, the outcome is to be expected.

The out of alignment direction, with respect to the position sensor, is displayed in figure 7.7 by the blue arrow in the x-y plane. Also, this figure provides a picture of the measurement staff that was applied on the monopile, which shows comparable overlap values with the measurement equipment. This data shows that the tower settled straightly over the monopile without introducing an additional misalignment between the two. This can also be observed in section 8.3.

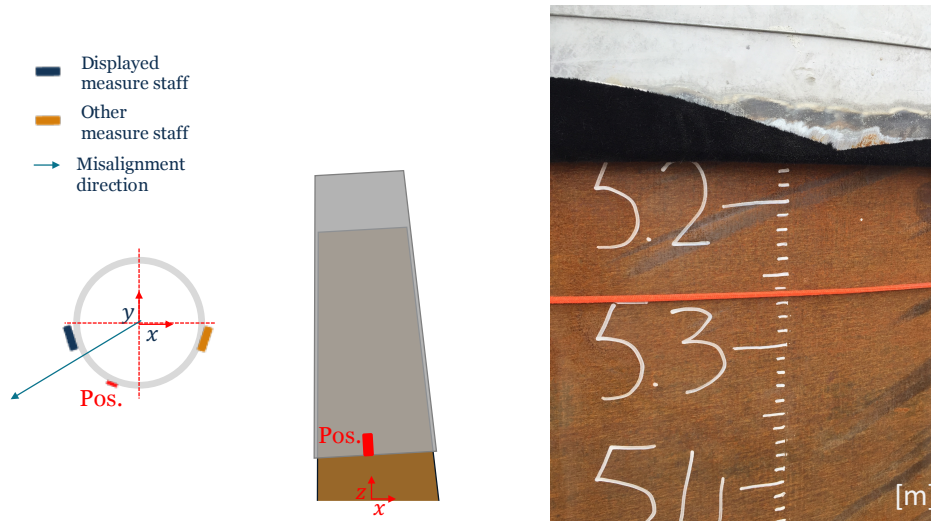


Figure 7.7: Schematic overview monopile misalignment direction (left) and measurement staff cross-check (right)

7.3.4. Conclusion and discussion

A number of conclusions can be drawn evaluating the data of the settlement of the slip-joint. First of all, the relative settlement of the slip-joint, as a result of the different installed components, significantly decreased with every additional installed item. This implies that there is a non-linear relation between the settlement and resulting friction force build-up, which ensures the vertical force equilibrium that supports the structure. This is understandable, since the friction force increases with increasing surface area as the overlap grows during the settlement. On top of that the friction force increases due to the growing normal force as a result of the outer cone's resistance to the expanding as it progresses down the inner cone.

Secondly, the settlement of the slip-joint showed a smooth and controlled behaviour. No unexpected settlements and settlement velocities have been observed. Furthermore, the accelerations were observed to be very low. This observation is in contrast to the observations from the TU Delft scale experiments [21], where sudden jumps in settlement were registered during application of a static vertical load and during the application of vibrations.

Thirdly, the settlement of the slip-joint in the subsequent days after the installation, was limited compared to the initial settlement during installation. Moreover, this progressive settlement significantly decreased over the days. It showed clear signs of convergence to a final and stable target settlement of $z_{settle} = -148 \text{ mm}$, due to the application of self-weight only.

Finally, the slip-joint experienced an earlier first point of contact than was anticipated, which can be readily explained by the out of alignment of the monopile and ovality of the tower. The final target overlap compares reasonably well with the anticipated value, however the actual overlap length is less than predicted. The conclusion on this is twofold. First of all, it might be explained by the sensitivities identified in section 6.3, including geometrical uncertainties of the cones and uncertainty in friction coefficient. On the other hand, the earlier reached vertical force equilibrium, might indicate that an additional mechanism was present, apart from the vertical friction build-up due to hoop expansion.

This can for example be friction build-up due the radial deformations, caused by the ovality of tower or the inclined monopile cone.

7.4. Slip-joint stress distribution

The stresses within the slip-joint have been monitored using strain gauges for local stresses. Furthermore, taut wires with position sensors have been used to identify the global strain distribution along the height of the slip-joint. Section 7.4.1 elaborates on the results with respect to the global stress distribution and section 7.4.2 evaluates the local stresses. Furthermore, section 7.4.3 presents the findings with regard to the principle stress calculations from the rosette strain gauges, located on the top of the slip-joint cone.

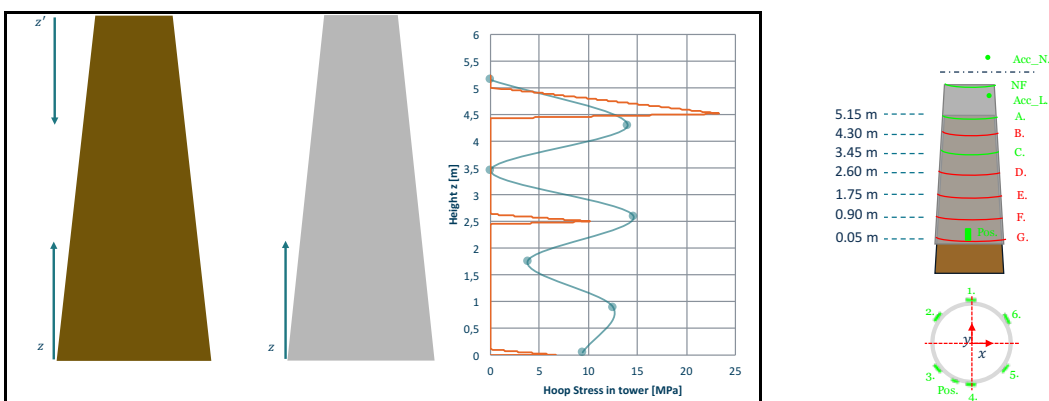
7.4.1. Global hoop stresses

The global elongations were measured by means of a taut wire, secured around the circumference of the slip-joint and fixed with a spring to a position sensor. In total, seven wires around the circumference have been installed over the total height of the slip-joint. Unfortunately, two of the sensors have been compromised during transport and installation of the slip-joint on levels 'A' and 'C'. The measured elongation in millimetres, is translated to global hoop stress via of Hooke's law. It should be noted that this method provides a rough estimate of the actual hoop stress in the tower. Therefore, the absolute values of the stresses are not that important. However, the distribution along the height of the slip-joint does provide valuable information.

The results of these global elongation measurements and the translation to stresses can be found in table 7.4. The presented values show the additional elongation in the hoop direction, due to the installation of all the wind turbine components. A graphical representation of the measured and anticipated values, including an overview of the positions of the sensors, is found in figure 7.8.

Table 7.4: Elongation of position sensors Pos A through Pos G

Parameter	Unit	Pos B	Pos D	Pos E	Pos F	Pos G
Elongation Δx	[mm]	0.72	0.76	0.20	0.68	0.52
Diameter of horizontal line	[mm]	3350	3401	3453	3556	3611
Additional strain $\Delta \epsilon$	[-]	6.84E-5	7.11E-5	1.84E-5	6.09E-5	4.58E-5
Additional stress $\Delta \sigma$	[MPa]	14.0	14.6	3.78	12.5	9.40



(a) Global measured hoop strains (light-green line) compared to anticipated distribution (orange line)

(b) Positioning of the elongation sensors

Figure 7.8: Global hoop elongations

Two things can be noted from this information. First of all, although the translated stresses from the measured elongations are a rough approximation, they do compare relatively well with the predicted

stress distribution. Especially in the top area of the cone, the values show significant resemblance. Compared to the stresses measured with the strain gauges, displayed in section 7.4.2, the values also match fairly well and are within the same order of magnitude.

Secondly, the distribution of the stresses along the height of the slip-joint matches the anticipated distribution fairly well, except for the bottom part of the cone. Also some measurement points at levels 'A' and 'C' are missing, therefore a real hard conclusion on this matter can not be provided.

7.4.2. Local hoop stresses

The local stresses have been measured using strain gauges on three circumferences - 'A', 'D' and 'G' - along the height of the slip-joint. The presented stresses are stresses in the hoop direction i.e., along the local x-axis of the tower cone. The presented values in figure 7.9, are additional stresses measured from the zero-point to the end of the installation of the total wind turbine structure i.e., the 19th of May. The actual time-series of this data, along with a number of observations, is presented in E.3.

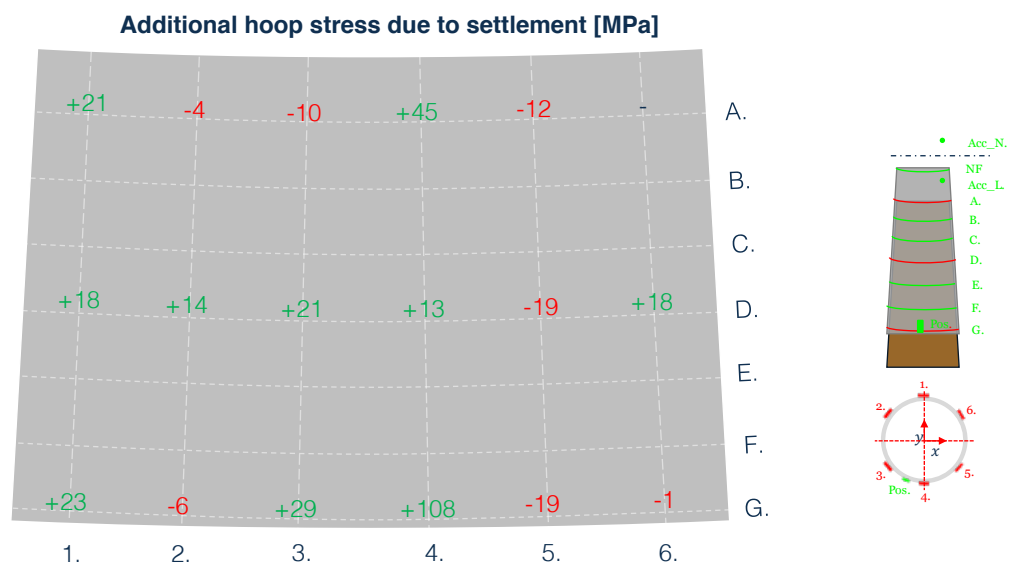


Figure 7.9: Additional hoop stresses due to settlement of the slip-joint

Four things can be noted from the data presented in figure 7.9. First of all, although in the same order of magnitude, the values are somewhat higher than was anticipated in the model. The most probable cause for this is that the measured stresses are not purely caused by strains in the hoop direction. Deformations in the radial direction, or introduction of shear stresses at these locations, could have influenced these measurements. In any case, almost all the measured hoop stresses in the tower wall, are in the region of $\sigma_{hoop} = 10 - 40 \text{ MPa}$. This is far below the yield stress of the material, which was tested at $f_y = 320 \text{ MPa}$. It can therefore be concluded that the additional stresses in the material, caused by the settlement of the wind turbine, are negligibly small.

Secondly, there is one striking value that stands out above the rest, which is sensor 'G4'. It shows a value of $\sigma_{hoop} = 108 \text{ MPa}$. Although this value is still well below the yield stress of the material, the magnitude is striking. The calibration factor of the strain gauge in the processing scripts was checked for any errors but these were not found. Therefore, this stress is either actually observed, or it could be the effect of an improper application process. Considering the fact that this particular sensor continuously provides deviating values compared to the rest of the sensor, the latter option is most probable. However, it could also be the result of a stress concentration. If this is the case, it can be found upon inspection after removal of the slip-joint.

Thirdly, the stress distribution along the total height and the circumferences of the slip-joint clearly shows no signs of axisymmetry. Neither along the vertical axis on a particular circumference, nor over the height of the different vertical lines. This means that no uniform loading was applied from the

inside of the tower cone. This could possibly be explained by the fact that the monopile has a slight out of alignment with the vertical axis, causing more pressure to be exerted on one side than the other. Also, the ovality of the tower could be a possible explanation to this non-axisymmetry. The tower was known to have significant ovality in the regions of sensors 'A' through 'C', and 'G'. Therefore, this could well explain the asymmetry.

Fourthly, in line with the non-axisymmetric stress distribution, also compression is observed at some strain gauges. This is rather counterintuitive, as one would expect only tensile stresses as a result of the inner cone applying pressure on the outer cone, which will therefore expand. However, the model in section 6.5, showed the same behaviour with the application of non-uniform radial pressure. Also, it showed that at these locations, the cone had to deform in the negative radial direction for compression to exist. This means that at the locations where compression is present, the cones are not in contact with each other. This hypothesis is backed up by the fact that at the region of sensor 'G5' and 'G6', where compressions is observed, a non contact area can be found between the tower and monopile depicted in figure 7.10.



Figure 7.10: Non-contact area between sensor 'G5' and 'G6'

Based on these evaluations, a highly superficial conclusion can be drawn on the total contact area within the slip-joint. Seven out of the eighteen strain gauges show compression i.e., a sign of a non-contact area. If this was to be extrapolated along the whole slip-joint, one can conclude that the slip-joint has a non-contact area of 38% over the total slip-joint overlap. If this was to be used in the calculation methods presented in section 3.2, the average hoop stress in the tower would amount to $\sigma_{hoop} = 14.61 \text{ MPa}$, which is in line with the observed hoop stresses presented in figure 7.9.

7.4.3. Principle stresses

The strain gauges installed on circumference 'A' are rosettes. These strain gauges measure strains in three directions, which enables the calculation of principle strains. The measured strains can be used as input in three equations, to calculate the two principle strains and their angle from the specified reference axis system [4]. This has been done for the rosettes on circumference 'A'. Unfortunately, strain gauge 'A6' was compromised during the welding of the platform keys on the tower, therefore no data is available from this rosette. The additional stress due to the settlement expressed as principle stresses and their accompanying direction can be found in figure 7.11.

A couple of things can be noted from this data. First of all, the values of the principle stresses differ slightly from the measured stresses in the hoop direction, displayed in figure 7.9. However, they are the same order of magnitude. Also, the distribution of compression and tension equals the observations from the local hoop strains. The maximum observed Von Mises equivalent stress was found at sensor

Additional stress expressed as principle strains and directions [MPa]

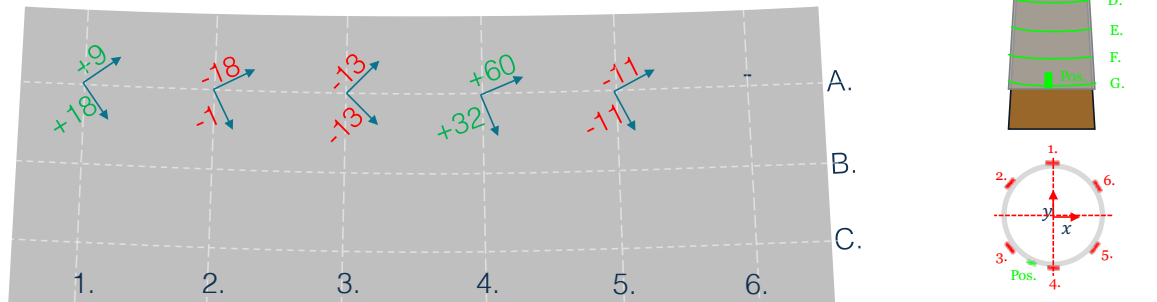


Figure 7.11: Principle stresses as result of slip-joint settlement

'A4' and amounts to:

$$\sigma_{VM} = \sqrt{32^2 - 32 \cdot 60 + 60^2} = 52 \text{ [MPa]} \quad (7.1)$$

This value, likewise the maximum observed hoops stress, is far below the yield stress of $f_y = 320 \text{ MPa}$.

Secondly, the direction of the principle stresses vary along the circumference, again indicating no axisymmetry along the vertical axis. However, no change in direction was found over time. This means that the total settlement of the slip-joint progressed in a smooth and controlled manner, effectively not changing the load pattern on the outer cone. This is in line with the observations found in section 7.3.1.

Finally, it can be observed that the direction of the principle stresses do not align with the hoop direction. Therefore, the stresses in the tower wall are not purely caused by expansion of the tower in the hoop direction. Local shear stresses are present, confirming the non-uniform load pattern on the tower, most probably caused by the non-contact areas within the slip-joint.

7.4.4. Conclusions and discussion

Three main conclusions can be drawn from the data of the strain gauges and global elongations along the slip-joint. First of all, the global stresses, translated from the global measured elongations, are within the same order of magnitude as the model predictions. Also, the values were found to be slightly smaller than the locally measured stresses. The explanation can be twofold. First of all, the steel taut wires also elongate slightly, due to the added tension in the wire as a result of the global hoop expansion. Secondly, the locally measured stresses also include the effect of locally induced shear stresses and radial deformations, which are not measured by the global method. The distribution of the global hoop stresses, along the height of the slip-joint, also matches the model predictions in the top part of the cone, but not in the bottom part. Some data points on circumference 'A' and 'C' are missing, due to broken sensors. Therefore, no hard conclusions can be drawn on this matter.

Secondly, the measured additional local hoop stresses, due to the settlement of the slip-joint, are all far below the yield stress. However, the distribution of these stresses show no signs of axisymmetry along the vertical and horizontal axis. This means that the stresses were not caused by pure uniform hoop elongation along the circumference. The tower was known to have some significant ovality and as the tower settled over the monopile, this could very well have caused this non-axisymmetry. Also, local compression has been observed. The existence of these are plausible, considering that the model, elaborated on in section 6.5, showed comparable results when applying non-uniform pressure or introducing ovality in the outer cone. This also implies that the cones are not in contact at the position where the sensors indicate compression. A superficial estimate of the total slip-joint contact area based on these evaluations is that at 39% of the total overlap area no contact between the two cones is present. An acoustic measurement shall be performed at these exact locations to see if the non-contact areas can be confirmed.

Thirdly, the principle strains calculated from the rosette strain gauges at circumference 'A' show the same values and distributions as the hoop stresses. The highest Von Mises equivalent stress is found at sensor 'A4' and amounts to 52 MPa , which is far below the yield stress of the material. The direction of the main principle stresses do not align with the hoop direction, implying that local shear stresses are present in line with previous observations. However, the direction of the principle strains do not change over time of the settlement. This means that the slip-joint settled in a smooth and controlled manner, without changing the inner load pattern.

7.5. Acoustic measurement

To try and measure and validate the existence of the non-contact areas within the slip-joint overlap, acoustic measurements have been performed on the DOT500 slip-joint. Also, the dismantled 'Duinvoegel' slip-joint was used as a test-case for the same purpose. A detailed measurement report was made, including all the relevant background information, pictures and explanations of the actual measurements and the conclusions of the tests. This report can be found in appendix E.5. A short summary and most important conclusions will be presented in this section.

7.5.1. Measurements

For these measurements, an ultra sonic device was used. This device sends acoustic waves through a pod and receives the reflected waves as they travel and reflect through the material it is placed on. The goal of the experiment was to try and find contact and non-contact areas along the slip-joint overlap. The theoretical working principle of this experiment is based on the reflection coefficient at the interfaces within the slip-joint. This is either a steel-steel, or a steel-air interface, indicating a contact or non-contact area, respectively. The difference in reflection coefficient is caused by the difference in acoustic impedance of the two different media. This principle is explained in more detail in appendix E.5.

The device displays the arrival times of the reflected sound waves, in terms of millimetres wall thickness. Also, the accompanying amplitude in decibel of the particular signal is presented. With a given frequency and wave speed, the travelled distance of the sound wave is measured. When properly calibrated, the reflection peaks correspond to the wall thickness of the tested specimen. An arbitrary signal can be seen in figure 7.12. Multiple peaks can be observed, referring to the higher harmonic reflections that get picked up by the device. These peaks correspond to multiples of the actual wall thickness of the specimen that is tested.



Figure 7.12: Response signal of acoustic device

If the pod moves over a section with a transition from contact area, to non-contact area, one would expect the location and magnitude of the displayed peaks to change. In the case of the DOT slip-joint, the wall thickness of the outer cone is $t_{tower} = 15.5 \text{ mm}$ and the wall thickness of the monopile is $t_{MP} = 40.0 \text{ mm}$. If there is non-contact area, one would expect reflection peaks at 15.5, 31.0, 46.5 etc.

However, if the pod moves to a contact area, one would expect another peak to appear near the region of $15.5 + 40.0 = 55.5 \text{ mm}$. Also, the magnitude of the other peaks should decrease. This is indicated in figure 7.12 by the orange arrows.

Unfortunately, it was not possible to detect the preceding described behaviour, in neither the DOT500 slip-joint nor the dismantled 'Duinvogel' slip-joint. The only output that was read from the device, were peaks at multiples of the wall thickness. Therefore, all of the sound wave's energy was reflected at the first boundary layer i.e., the inside of the outer cone. A number reasons can be found for this result, which are explained in detail in appendix E.5. The most important conclusions shall be listed in the subsequent section 7.5.2.

7.5.2. Conclusions and discussion

As pointed out, it was not possible to distinguish contact areas from non-contact areas using ultra sonic measurement techniques. Both in the decommissioned 'Duinvogel' slip-joint, as well as the DOT500 operational slip-joint no contact or non-contact areas could be verified. This can most prominently be explained by the significant difference in acoustic impedance of air and steel. Even the smallest air layer between the two steel plates, will cause virtually all the energy of the wave to reflect. Given the difference in acoustic impedance, the reflection coefficient at the first boundary layer between steel and air is $i_r = 0.99996$. This shows that practically all the measurable energy in the sound wave gets reflected at the first boundary layer in the slip-joint

However, it would be wrong to conclude that there is no contact between the cones whatsoever, given the fact that both the slip-joints have been, or are functioning properly. This means that enough friction is built up between the two cones to support the total structure above the joint. A possible explanation to this discrepancy is explained in figure 7.13. A schematic close up, on an arbitrary microscopic scale, of a piece of slip-joint in 'contact' is presented. The ragged surface of the steel causes points of the two plates to make contact, so friction can be built up. These points are often referred to as the nominal, or true contact area of two touching surfaces [42]. However, areas where the steel is not in 'contact' i.e., the air layers between the nominal contact area, are plentiful and will always be observed by the pod. In line with the preceding discussions, the energy of the sound wave, produced by the pod, will get reflected at these areas leading to the fact that a 'non-contact' area is observed.

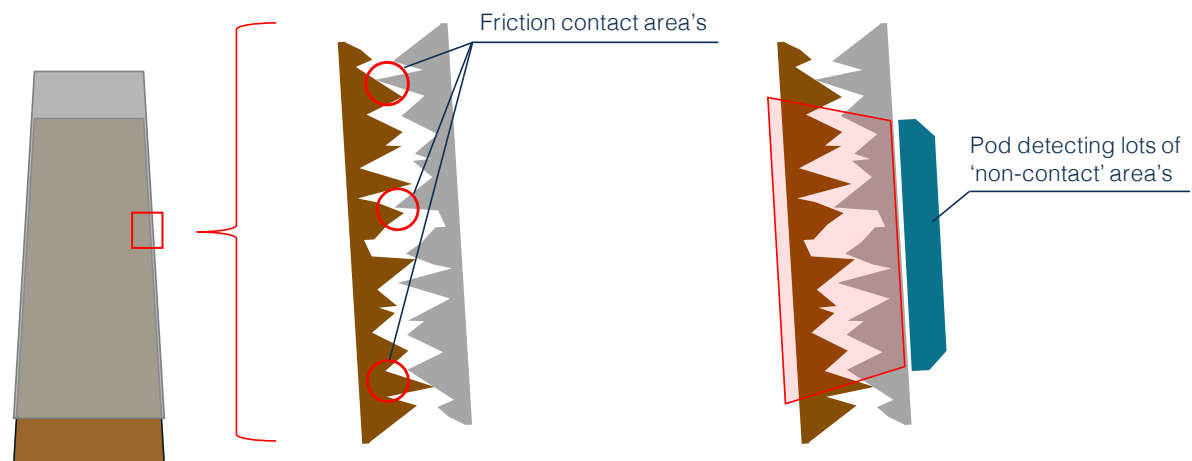


Figure 7.13: Difference in friction 'contact area' and measurable contact area

Another option to measure the contact and non-contact areas, could be by means of using eddy currents [7]. By inducing a magnetic field on a conductive material, eddy currents will be introduced in this material, which penetrate a short distance in the material. These eddy currents can be visualised and if a non-contact area is present this could be seen in the visualised eddy currents as the shape of the currents will be disrupted.

7.6. Conclusions

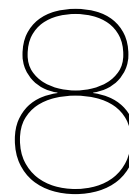
In this chapter, the results of the measurement data during the installation process has been discussed. The data from the installation, settlement and stress distributions has been analysed and a number of conclusions can be drawn from this evaluation.

First of all, it can be concluded that the monopile support structure of the DOT500 wind turbine was vibrated into relatively dense soil to the target penetration depth of 15 meters. The process took substantially longer than expected and resulted in an out of alignment with the vertical axis of 0.77° in the negative y-direction and 0.90° in the negative x-direction. This out of alignment did not cause substantial complications during the installation of the slip-joint connection i.e., the lowering of the lower turbine tower over the monopile. However, difficulties were experienced during the installation of the upper tower on the lower tower, during the connection process of the bolts. It can be concluded that a slight out of alignment of the monopile does not significantly affect the slip-joint connection. As a matter of fact, it brings a slight advantage over traditional bolted connections in terms of installation time.

Secondly, the settlement of the slip-joint as a result of the additional installed items, showed a smooth, controlled and anticipated behaviour. Also, the relative settlement, defined as the settlement per mT of added item, decreased with every installed item. The settlement, in the days after the installation, was limited and almost negligible compared to the initial settlement. Furthermore, the progressive settlement per day clearly decreased. Combing the latter three mentioned statements, it can be concluded that the system clearly convergences to a final stable settlement level and overlap length, due to self-weight only. This overlap length was found at $h_{overlap} = 5179 \text{ mm}$, measured from the top of the monopile cone. The first point of contact was found at $h_{foc} = 5031 \text{ mm}$, measured from the top of the monopile cone. The latter showed a significant discrepancy with the predicted value obtained from the models. This is readily explained by the fact that the wind turbine tower was known to have significant ovality and the fact that the monopile showed a slight out of alignment with the vertical axis. The final overlap length compares reasonably well with the anticipated $h_{overlap} = 5232 \text{ mm}$, taking into account the sensitivities due to the dimensional information. Also, the ovality of the tower and out of alignment of the monopile could have caused an earlier build-up of friction, reaching an earlier vertical force equilibrium. The combined effect of these can very well explain the discrepancy between the predicted and measured value.

Thirdly, the observed additional hoop stresses due to the settlement of the slip-joint at circumferences 'A', 'D' and 'G', are all well below the yield stress of the material and correspond relatively well with predicted values. Also, the principle stresses at circumference 'A', and resulting Von Mises equivalent stress, show comparable results. The direction of the principle stresses, do not change over time, indicating that the settlement progressed in a smooth manner without changing the inner load pattern of the slip-joint. The spacial distribution of the stresses show no signs of axisymmetry and display local compression at certain points on the slip-joint. In line with these observations, the directions of the principle stresses do not align with the hoop direction meaning that local shear stresses have been introduced. A non-uniform load pattern on the inside of the slip-joint could very well explain these asymmetries. The registered ovality and out of alignment of the monopile could have caused such a non-uniform load pattern. The presence of local compression implies that the cones are not in full contact at these specific locations, as the outer cone must deform in the negative radial direction in order for compression to occur. This phenomenon was observed at 38% of the total strain gauge sensors.

Fourthly, it was not possible to verify the presence of these contact and non-contact areas within the slip-joint, by means of ultra sonic measurements. At every tested location no transmission of sound was observed between the two steel plates within the cone. Due to the great difference in impedance between air and steel, virtually all the energy in a sound wave will reflect at a boundary of these two media. Therefore, the smallest film of air between the two steel cones will prohibit the transmission of the sound wave's energy into the next plate. A possible alternative to this measurement. could be the use of Eddy currents.



Results during operation

8.1. Introduction

Over the course of mid-May through mid-September, the turbine has been operational and the DOT drive train has been tested thoroughly. During these experiments, the sensors discussed in chapter 5 have also been logging data. This chapter will present the data obtained during this period.

The aim of this chapter is to present the most relevant data and conclusions that can be drawn from this operational period. The post processing techniques and theories can be found in appendix B, while the results can be found in this chapter. Every graph is accompanied by a sketch of the slip-joint and the sensors as explained in section 5.7. The sensors, corresponding to the presented data, are indicated in this figure with a red colour.

Section 8.2 elaborates on the results of the natural frequency measurement campaign. Section 8.3 shows the findings regarding the settlement of the slip-joint during the operational period and section 8.4 evaluates the stress distributions. Additional stresses due to the extra settlement as well as the (maximum) stresses during operation are discussed. Finally, section 8.5 list the main findings and conclusions that can be drawn from these evaluations.

8.2. Natural frequency

The natural frequencies of interest, are determined using time signals from the strain gauges, positioned above the slip-joint, measuring strains in the axial direction. These time signals are converted to the frequency domain using a Fast Fourier Transform algorithm in MATLAB. The frequency domain analysis of the time signals shall be investigated for a couple of cases, evaluated in the subsequent sections 8.2.1 through 8.2.3. Also, an estimation of the damping from three different decay tests are presented in section 8.2.4.

8.2.1. Heavy wind conditions and non operational

The first discussed signal, is an arbitrary signal of the tower, on the 6th of July, during heavy windy conditions. No other loading was present. The raw transformed signal shows clear peaks, however contains quite some white noise. Therefore, the signal is filtered using a butterworth filter of the 2nd order with a cut-off frequency of 0.4 Hz . This filter eliminates all signals with a higher frequency than 0.4 Hz in the frequency domain in a relatively flat manner [32].

Figure 8.1 shows the original and filtered frequency domain signals of the strain gauges. It is clear to see that the peaks at around 0.86 Hz of the different sensors indicate the first natural frequency of the bending mode. This corresponds relatively well to the approximate 0.81 Hz defined in section 6.2. The excitation was most likely caused by (several) severe wind gusts over the time record, giving the tower a displacement in any direction, after which it again enter a state of unforced vibration until it damps out.

Due to this, no hard conclusions can be drawn about directionality of the motions. Therefore, there is no information on which sensor regards the fore-aft or side-side mode in this case.

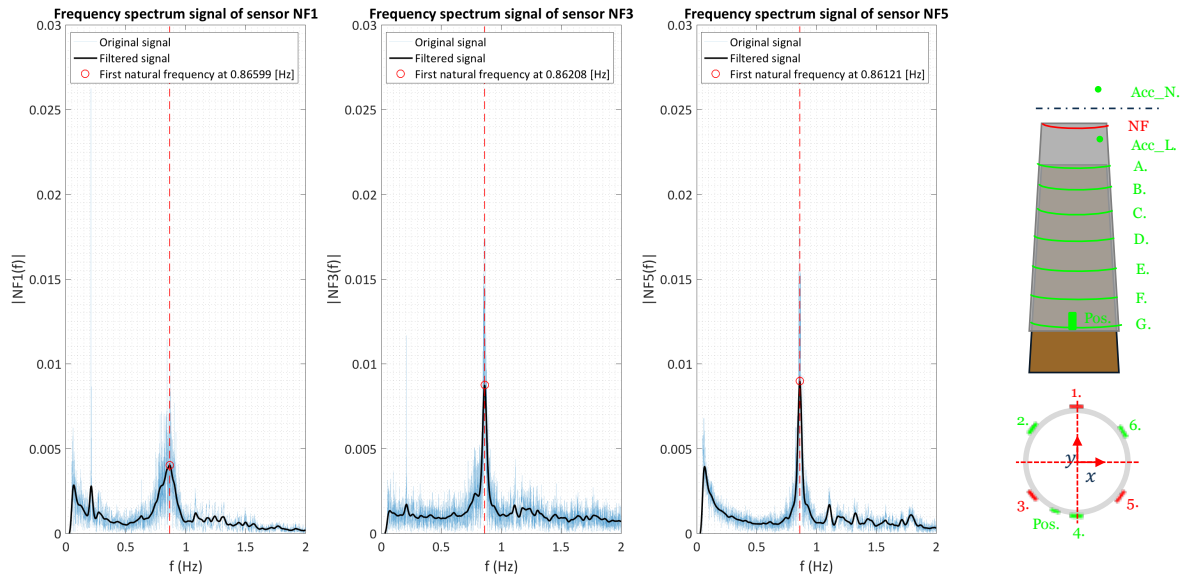


Figure 8.1: Frequency spectrum of NF strain gauges during heavy wind conditions

8.2.2. Operation conditions near rated speed

On the 3rd of August the wind turbine was operational at near rated speed conditions i.e., the rotor rotational speed was in the range of 24 RPM through 28 RPM. The wind direction during this time record was South-West, meaning that the NF5 sensor was directly in the fore-aft direction and that sensor NF3 and NF1 were almost in the side-side direction. The same filtering technique as in section 8.2.1 was applied. Figure 8.2 shows the frequency domain signals from strain gauges NF3 and NF5 in the described conditions, the orange arrow indicates the wind direction.

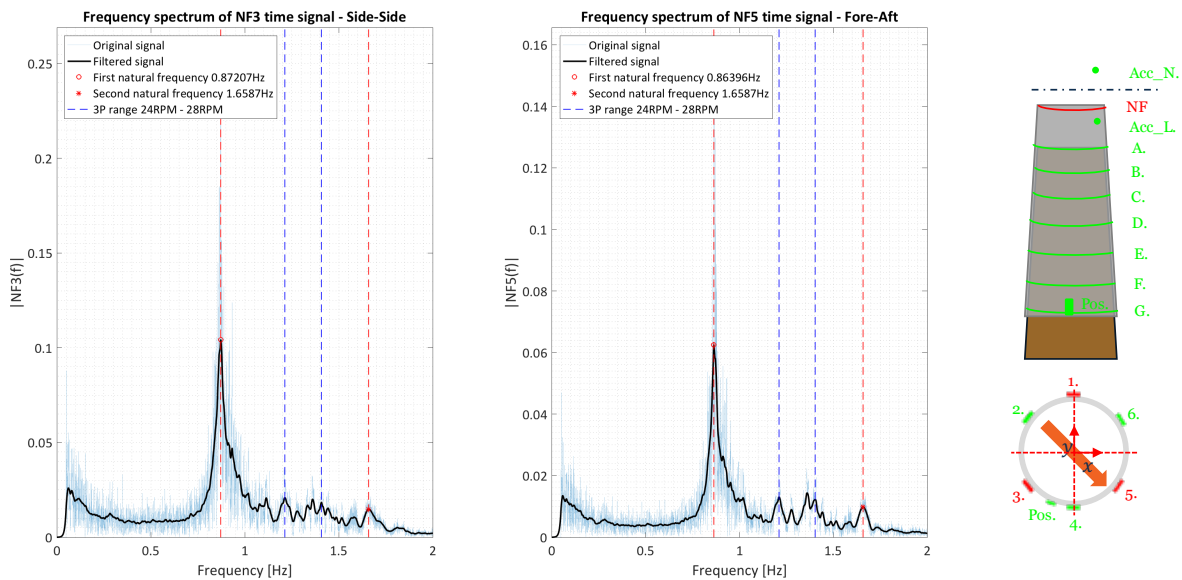


Figure 8.2: Frequency spectrum of NF3 and NF5 strain gauges during operational window

From figure 8.2, it is clear to identify the first natural frequency of the bending modes in both the fore-

aft and side-side mode. These are located at $f_{1,fa} = 0.864$ and $f_{1,ss} = 0.872$, respectively. The values correspond well with the predicted values, as well as the frequencies identified in section 8.2.1. The small difference between the two directions is readily explained by the aerodynamic damping that is only present in the fore-aft direction during operational intervals. In this specific case, it would amount to is 1%. Also, a small peak at 1.659 Hz is present, which could very well be the second natural frequency of the bending modes.

As far as excitation frequencies is concerned, the 3P excitations are clearly present around three times the operational frequency range. The 1P excitations however, are not present in this data record indicating that there was not such an excitation (due to rotor mass imbalance for example) in this record, or the energy in this excitation was negligible compared to the other excitations.

8.2.3. Emergency stop

The last time signal that is considered, is during the 29th of July. In this time record, multiple emergency stops have been performed with the turbine, testing the hydraulic emergency stop of the drive train. This was done by speeding up the rotor to the desired rotational speed, in this case around $24 - 26 \text{ RPM}$, and consequently applying resisting torque to the rotor by building up the pressure in the hydraulic drive train. This makes the rotor stop within ten seconds, after which the tower enters a state of free vibration until the motion damps out.

Figure 8.3 shows the time domain response of the strain gauges during these emergency stops. The peaks in the strain gauge response, clearly indicate the build up of thrust force and the fall back after the emergency stop sequence is activated. The black box indicates the emergency stop that is inspected to find the frequency domain response.

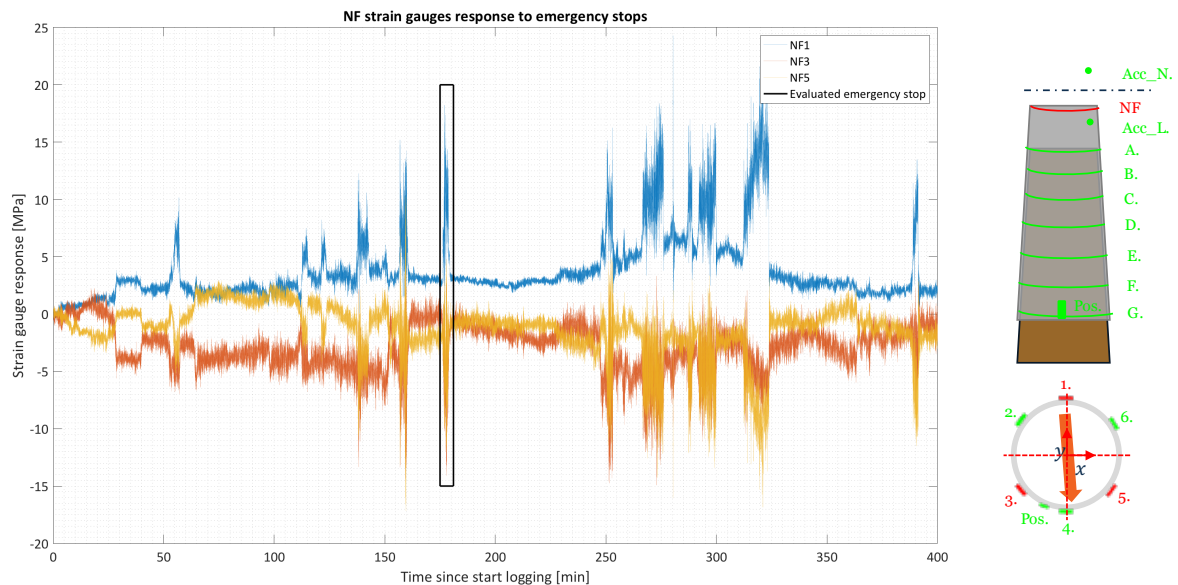


Figure 8.3: Time domain response of strain gauges during emergency stops

During these tests, the wind direction was mainly South-Western i.e., sensor NF1 is aligned with the fore-aft mode and sensors NF3 and NF5 are near the side-side mode. Figure 8.4 shows the response of the wind turbine in the frequency domain as a result of the above described emergency brake procedure. The same post processing steps as in section 8.2.1 were applied.

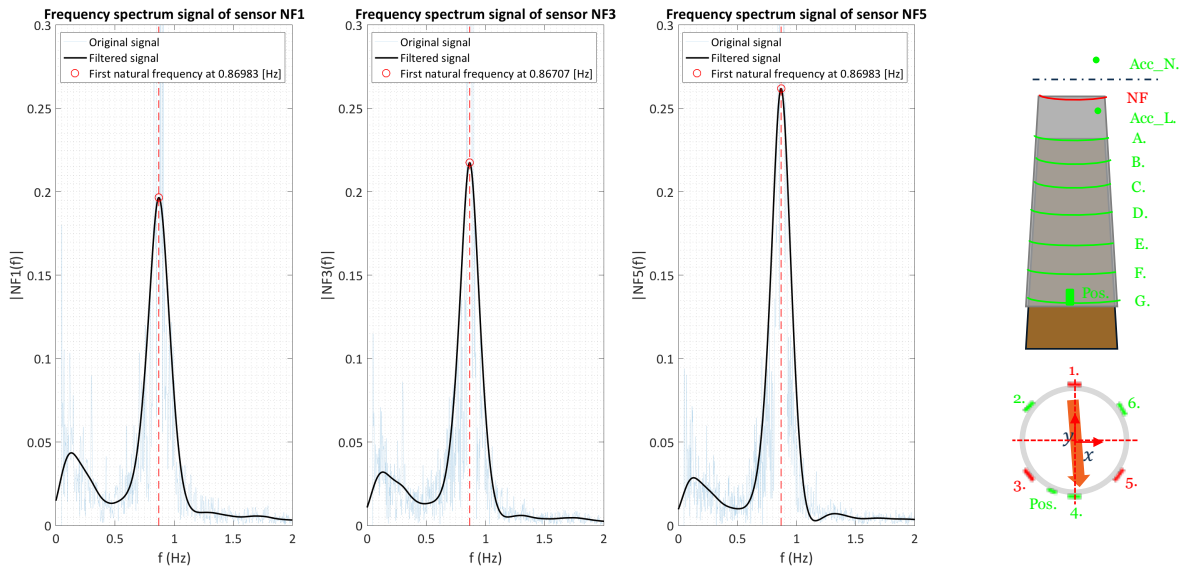


Figure 8.4: Frequency spectrum of strain gauge sensors during emergency stops

From figure 8.4, one can clearly identify one main peak in all the sensor responses, which is the first natural frequency located at around 0.87 Hz. Hardly any difference is observed in the different directional modes, which is readily explained by the absence of aerodynamic damping, ergo the damping in both directions is almost the same. Also, the amplitude of the peaks are in expected order, with the biggest response in the side-side direction (NF3 and NF5) as a result of the swift decrease of rotor-torque exciting the tower mainly in the side-side direction.

8.2.4. Damping estimation

The damping of the structure, during free vibration, can be estimated by means of a decay test. To this end, three different stops of the rotor have been analysed to inspect the damped free motion of the total structure. These stops are depicted in figure 8.5, which shows the time signal of the 'NF1' through 'NF5' strain gauges during operation on the 11th of August.

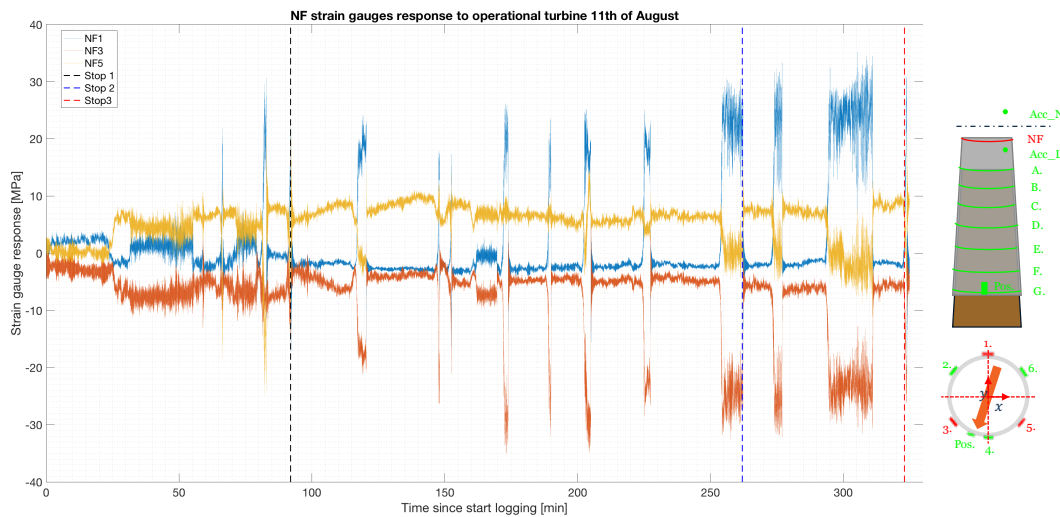


Figure 8.5: Three different (emergency) stops have been used for a decay test

After an (emergency) stop of the rotor, the tower enters a state free vibration as it is excited by the swift decrease of the rotor torque and thrust, in both side-side and fore-aft direction, respectively. The decay in amplitude of this unforced motion, holds valuable information regarding the damping in the total

structure. An exponential decay is expected, which is governed by an amplitude A and a damping ratio ζ_d , according to:

$$u_{decay} = A \cdot e^{(-\omega\zeta_d t)} [m] \quad (8.1)$$

In this equation, ω is the natural frequency of the damped motion. This can be determined by dividing the number of peaks, by the duration of the time interval. In this case, it amounts to $\omega = 0.86$. A curve fitting algorithm is used to determine the parameters A and ζ_d , in order to obtain a sound fit on the peaks of the decaying motion. The damping of the motion is presented by ζ_d . The results of three tests, can be found in detail in appendix E.4 in figure E.13 through E.15. The result of test three, is displayed in figure 8.6.

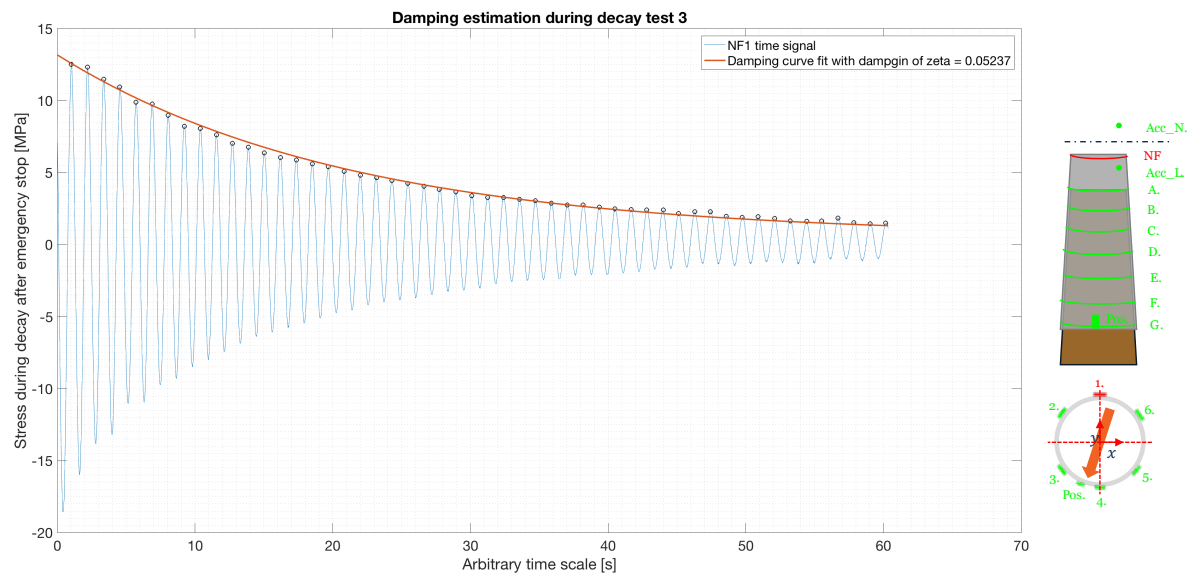


Figure 8.6: Fitted exponential decay in structure's response after (emergency) stop to obtain the damping. Test 3

Combining the results of the three test it can be concluded that the damping in this motion amounts to $\zeta_d = 0.045$ or 4.54%. It must be noted that this is total effective damping of the motion. Therefore, this value does not coincide with the pure damping ratio of the fore-aft motion only. Since the free motion is present in both directions, the vibration in the fore-aft motion gets influenced by the side-side motion and damping as well.

8.2.5. Conclusions and discussion

From the latter evaluations, it can be concluded that the first natural frequencies of the fore-aft and side-side bending mode are identified in three cases. In these cases, the identified natural frequencies coincided perfectly, indicating that there is little doubt about the fact that the registered peak frequency was indeed the first natural frequency.

Moreover, the found frequencies match reasonably well with the expected values discussed in section 6.2. Table 8.1 summarises the identified natural frequencies and predictions, including the relative error between the two. In this table the predicted values from Bladed are used for the operational turbine, whereas the predicted values of RFEM are used for the idle or emergency stop case.

Table 8.1: Identified and measured natural frequencies

Mode type	Case 1: Heavy wind conditions		Case 2: Operational turbine		Case 3: Emergency stop	
	fore-aft	side-side	fore-aft	side-side	fore-aft	side-side
Measured 1st natural frequency [Hz]	0.863	0.863	0.863	0.872	0.869	0.867
Predicted 1st natural frequency [Hz]	0.823	0.823	0.795	0.796	0.823	0.823
Relative error [%]	4.63	4.63	7.99	8.72	5.29	5.07

The differences are fairly small, especially for the idle and emergency stop cases. Overall, it can be concluded that the predicted frequencies are lower than the actual measured ones. This means that the structure, most probably the foundation, is modelled less stiff than on actual effect. A simple iteration on the interpretation of the soil parameters from the CPT can easily close the distance between reality and the model. The natural frequency is still within the 3P excitation zone at a rotor speed of 17 RPM. This minor shift does not have any significant influence on the control of the wind turbine. Furthermore, it should be noted that a first order estimate of the damping of the structure in free vibration was obtained using three decay tests. The average damping that was found amounts to $\zeta_d = 0.045$, or 4.54%. It must be noted that this is the effective damping ratio of the total motion of the structure and not the true damping ratio in one vibration direction. As vibrations, and damping, in both direction interact with each other, the calculated damping ratio is most probably 1 – 2 % higher than the true damping ratio in a single direction. A structural damping of 2% was assumed in models which corresponds well, taking into account the latter evaluation.

Finally, it can be concluded that the strain gauges were able to identify the natural frequency specifically well. Even with little excitation force e.g., heavy wind conditions, the sensitivity of the strain gauges was high enough to register the natural frequency. This was not the case with the accelerometer placed in the nacelle, which was not able to identify the natural frequency in case one. The frequency spectrum was too broad and presented an over-damped view. Unfortunately, during case two and case three the accelerometer was out of order so no cross check have been performed on these cases.

8.3. Slip-joint settlement

The settlement of the slip-joint has been carefully monitored during the operational period. The position sensor monitored the exact settlement in millimetres and two measuring staffs were used to cross-check the settlement values of the sensors. Section 8.3.1 discusses the magnitude of the settlement during the operational period, while section 8.3.2 elaborates on the nature of this settlement and the main causes for it.

8.3.1. Settlement during operational period

After the installation phase of the project, the slip-joint converged to a final and stable settlement level due to self-weight only. This has been explained in section 7.3.2. This static equilibrium was compromised during the operational phase of the project. Initiated by several instances during the operation phase, the slip-joint settled progressively. The instances which started the settlement of the slip-joint, were identified as follows:

- Start of the functional testing period. In this period some functional test were performed, including yaw tests and pitch tests. Also, the total hydraulic system was commissioned.
- Start of the failure testing period. In this period the emergency stop systems of the turbine were tested. Different alarms were commissioned and numerous emergency stops were performed in order to make sure that the turbine can function fully autonomously and shut-down if an emergency or failure happens. The procedure of such an emergency stop has been explained in section 8.2.3.
- Start of the operational testing period. In this period, the wind turbine was operational for almost every day during different time intervals. The performance of the drive-train was mapped in varying wind conditions.

The settlement of the slip-joint, as a result of the latter named operational phases, is displayed in figure 8.7.

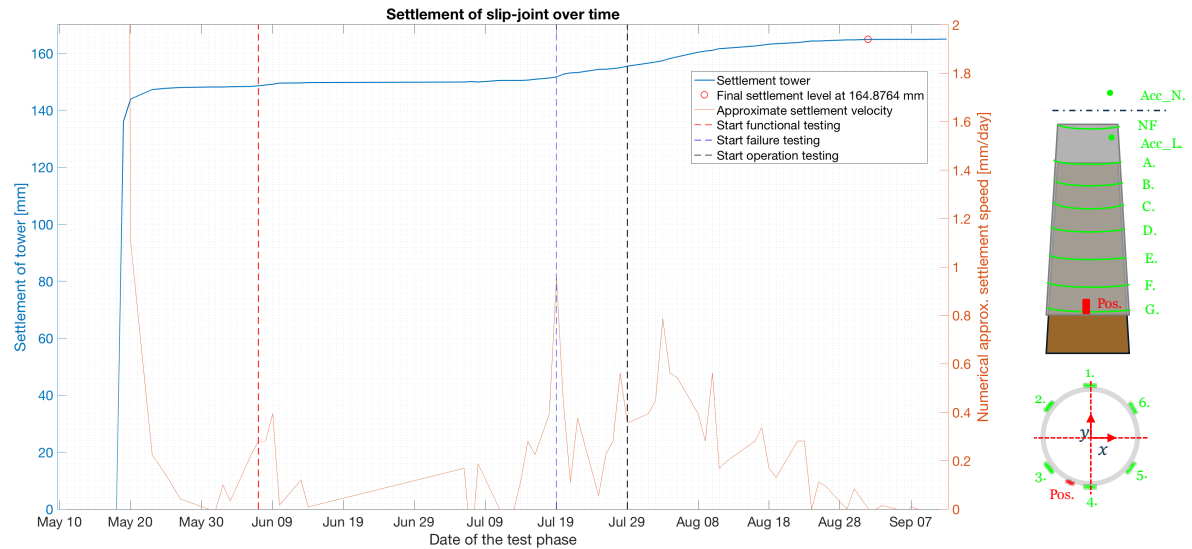


Figure 8.7: Settlement of the slip-joint over the total test phase

A couple of things can be noted from figure 8.7. First of all, as a result of the functional testing the slip-joint started settling a few extra millimetres, especially due to the yawing tests. The eccentricity of RNA mass introduces a moment on the slip-joint forcing it to settle. In the period after these tests, the settlement progressive towards a stable level again, indicating that an equilibrium has been reached. The extra settlement due to these tests, defined from the stable static equilibrium of $z_{settle} = -148 \text{ mm}$, was observed to be an additional $\Delta z_{settle} = -1.73 \text{ mm}$. Therefore, the stable settlement level after the functional testing period amounts to $z_{settle} = -150 \text{ mm}$.

Secondly, initiated by the failure testing and subsequently the operational testing, the slip-joint started to settling again. The loads from the emergency stops and thrust forces from the rotor, clearly cause the slip-joint to settle an additional amount. The actual settlement, indicated by the blue line in figure 8.7, progresses towards a plateau level. Even more so, the settlement velocity, indicated by the red line in figure 8.7, shows a clear decaying trend towards zero. This indicates that the mechanical system is converging to an equilibrium as a result of the operational loads. The thrust force at rated speed, which has been encountered several times in this period, is the biggest load case that the wind turbine will have to endure during operation. Therefore, no significant additional settlement is expected.

Thridly, the additional settlement due to the failure and operational testing period, amounts to $\Delta z_{settle} = -14.98 \text{ mm}$. This leads to a total settlement of the slip-joint of $z_{settle} = -165 \text{ mm}$. The total additional settlement due to the operational period of the DOT turbine is an extra $\Delta z_{settle} = -16.71 \text{ mm}$, which equals an extra 11% on top of the settle due to the self-weight only.

Finally, the final target overlap length of the slip-joint amounts to $h_{to} = 5196 \text{ mm}$. The two measuring staffs on the monopile confirm this overlap level, as can be seen in figure 8.8. Also, it can be observed that the tower settled on the monopile with hardly any misalignment. The two measuring staffs depict the same overlap length. Although it is hard to see, one could argue that the measuring staff on the South end, shows a slightly higher overlap length. If this is taken into account, the additional overlap length on this side would be about 5 mm , as can be observed in figure 8.8. This results in a (negligible) misalignment between the tower and monopile of:

$$\alpha = \arctan\left(\frac{\Delta z_{settle}}{D_{t,i}}\right) = \arctan\left(\frac{5}{3578}\right) = 0.08 \text{ [}^\circ\text{]} \quad (8.2)$$

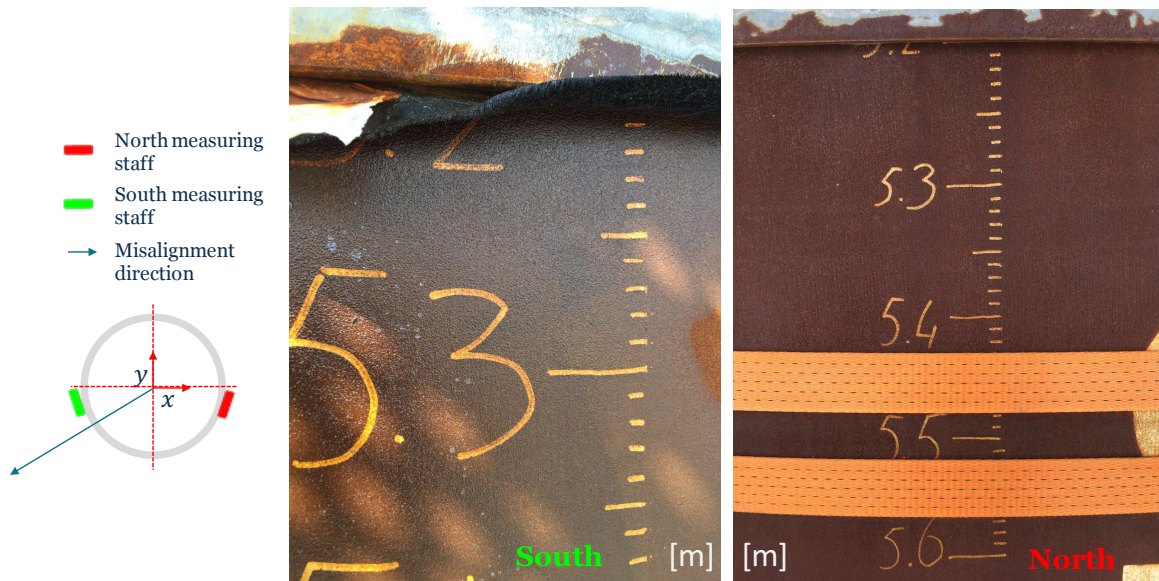


Figure 8.8: Total overlap length as can be read from the measuring staffs on the monopile

8.3.2. Settlement behaviour

By inspection of the settlement sensor in more detail, the behaviour of the settlement can be observed. Figure 8.9 shows the data from the settlement sensor and the time signal of strain gauge 'NF5', measuring strains in axial direction. For inspection, a time signal in which the turbine was operational, near the rated speed zone was chosen. The wind direction was West during this particular test. The strain gauge clearly shows the time instances at which the turbine was operational, as compression is observed in the tower due to the bending moment resulting from the thrust forces acting parallel to the wind direction.

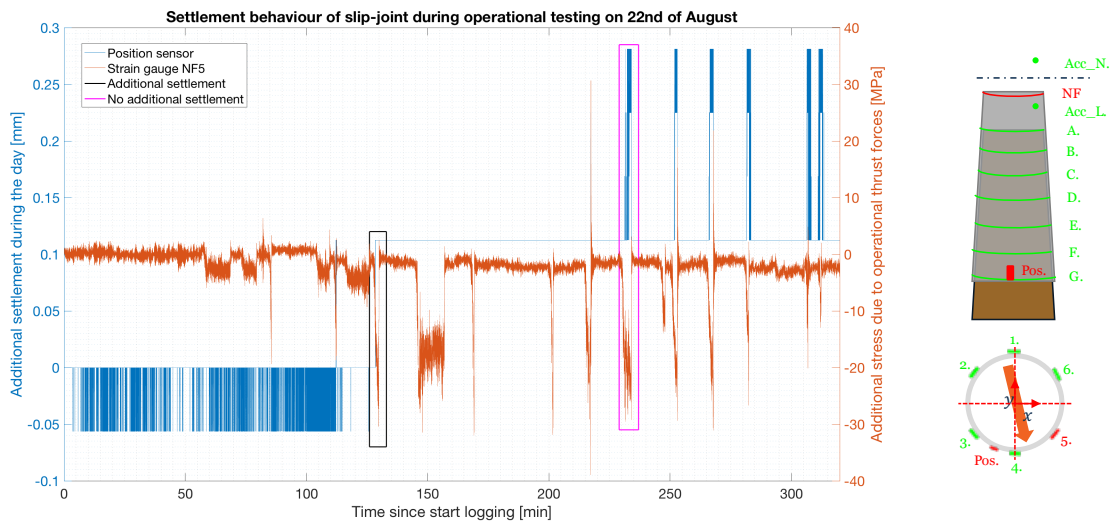


Figure 8.9: Settlement behaviour as a result of thrust forces

Two main observations can be made. First of all, the observed settlement on that specific day, happened right at a thrust force peak, as can be seen in the black box in figure 8.9. No other progressive settlement is observed. This means that the nature of the settlement shows a typical slip-stick behaviour. However, the slip behaviour is not initiated with every thrust peak that the rotor exerts on the tower. The thrust force initiated a slight settlement of the tower on one instance only.

Furthermore, during some instances the thrust force caused the tower to slightly misalign with the monopile for an instant whereafter the tower returns the original overlap level again. This phenomenon is observed during multiple instances in this specific time series and does not cause any permanent additional settlement.

8.3.3. Conclusions and discussion

A number of conclusions can be drawn from the evaluation of the settlement data during the DOT500 operational period. First of all, after a terminal settlement level was reached due to self-weight only, the slip-joint did settle an extra 16.71 mm, or 11%, during the operational period over the course of June through mid-September. This settlement mainly took place during the performance testing of the wind turbine i.e., the wind turbine was in (rated) power production mode during varying wind conditions.

Secondly, by inspecting both the absolute settlement level and the settlement velocity of the slip-joint during the operational phase it is plausible to assume that a final settlement level has been reached. Both clearly indicate that the system is converging towards a stable equilibrium. The slip-joint settled after every increasing load pattern, starting with a moment due to eccentricity of the top mass and subsequently the loads from emergency stops. Eventually, the turbine was exerted with a thrust force at rated speed after which very limited settlement was registered. Since the thrust force at rated conditions is one of the biggest load cases a wind turbine will encounter throughout its lifetime, it is reasonable to assume that a final settlement level can be reached after the endurance of this load case, likewise the observations in the measurements.

Thirdly, the final overlap length at this stable equilibrium amounts to $h_{overlap} = 5196 \text{ mm}$. This can also be observed from the measurement staffs on both the South and North side of the monopile. Furthermore, by inspection of these measurement staffs it follows that the tower settled over the monopile without any misalignment between the two.

Finally, by inspecting the daily settlement of the slip-joint, during operational time intervals of the wind turbine, it can be observed that the thrust force does indeed is the prime cause for the slip-joint to settle. It can be concluded that this happens in stick-slip like phases, rather than a smooth settlement. However, not every thrust force peak initiates additional settlement. Once available, more operational data is to be investigated to draw sound conclusions on the settlement behaviour of the slip-joint during operation of the wind turbine.

8.4. Slip-joint stress distribution

In this section the stresses within the slip-joint along circumference 'A', 'D' and 'G' are analysed during specific operational intervals. Section 8.4.1 evaluates the renewed stress distribution as a result of the additional settlement during the operational phase of the DOT500 wind turbine. Section 8.4.2 elaborates on the dynamic nature of the stresses during operational time intervals of the wind turbine, while section 8.4.3 evaluates the peak stresses as a result of the maximum thrust force at rated speed.

8.4.1. Additional stress due to extra settlement

As was noted in section 8.3, the slip-joint settled another -16.71 mm during the operational phase of the DOT500 project. This results in a new stress distribution over the total slip-joint overlap. The new distribution of hoop stresses in the tower wall, can be found in figure 8.10. The additional stresses due to the settlement during operation can be found in appendix E.4 in figure E.7.

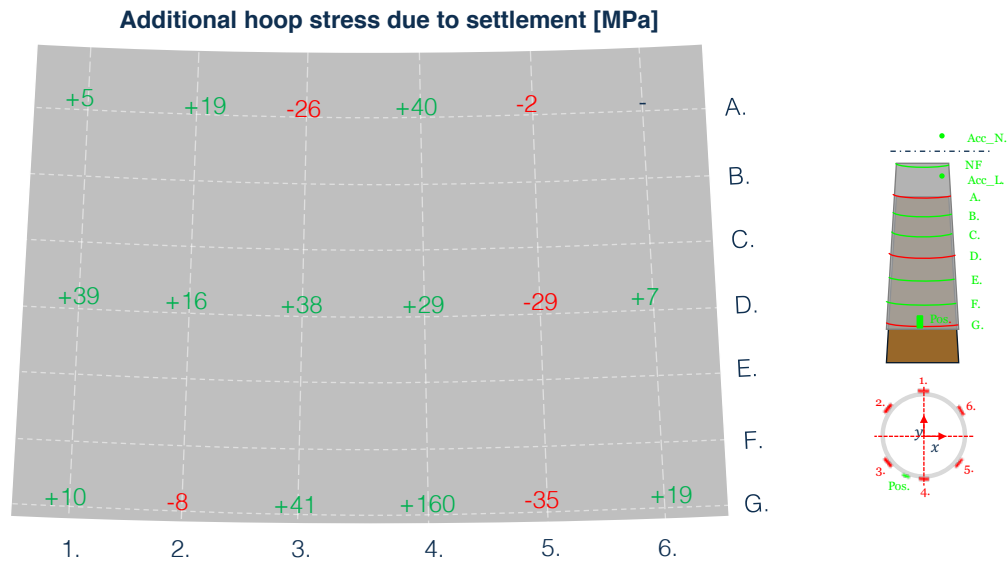


Figure 8.10: Hoop stress distribution after settlement during operation

A couple of things can be noted from figure 8.10. First of all, it can be observed that the stresses are well below the yield stress of the material. The average additional stress, over the total slip-joint overlap, is approximately $\Delta\sigma_{hoop} = 16 \text{ MPa}$. Likewise during the installation, sensor 'G4' shows an odd increase which is a number of times larger than all the other sensors. This increases the plausibility that the sensor is working improperly. However, after the decommissioning of the slip-joint, this location should be investigated to see if any anomalies can be observed.

Secondly, a number of sensors, including 'D2' and 'G6', show a transition from compression to tension. This indicates that the steel has deformed in the outward radial direction, or has been submitted to pure hoop elongation. A possible explanation for this could be that the former non-contact area is now actually in contact. Following this reasoning, it can be concluded that the contact area of the total slip-joint has increased with the additional settlement of the slip-joint during operation.

8.4.2. Analysis on dynamic stresses

In an effort to try and identify the difference between the contact and non-contact areas, an analysis on the time varying dynamic stresses is performed. These analyses have been performed on time instances at which the turbine was operational i.e., a time varying thrust force was present.

Two time signals have been evaluated. During the first time signal, the turbine was operating at a constant rotational speed for 15 minutes and the wind direction was Western. The second time signal that is chosen, is during an extreme seeking test. During this test, the wind turbine was operating below rated conditions and the optimal pitch angle was identified for every rotor speed during an incremental rotor speed test of 60 minutes. The wind direction was Southern during this test. An overview of the strain gauge's response during these operational intervals can be found in appendix E.4 in figure E.8 and E.10.

The additional stresses due to the thrust force have been analysed. It is anticipated that the standard deviation of the response of the strain gauge differs in the case of a contact and a non-contact area. In a contact situation, the standard deviation is expected to be lower than in a non-contact situation as the load transfer mechanism is more clean and fewer anomalies are expected. The standard deviation of the time signals have been determined and a normal distribution has been fitted on their histogram. The results of this can be found in appendix E.4 in figure E.9 and E.11. The standard deviations, presented in table 8.2, are normalised per circumference to more easily compare the values with one another.

$$\sigma_N = \frac{\sigma}{\sigma_{min}} \quad [-] \quad (8.3)$$

Table 8.2: Normalised standard deviations during operational interval

Normalised deviation $\left[\frac{\sigma}{\sigma_{min}}\right]$	1	2	3	4	5	6
	A	2.373	1.896	1.702	1.000	1.605
D	1.100	1.429	1.621	1.644	1.274	1.000
G	NaN	1.000	1.407	3.085	1.039	1.671

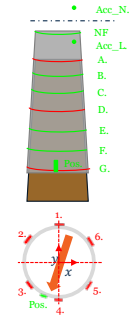


Figure 8.11: Sensor indication

From an inspection of these standard deviations, no real conclusions can be drawn. The sensor position that are assumed to be in a non-contact situation, as depicted in red in figure 7.9, do not show consistent correlation with a high standard deviation. Also, the values of the standard deviations are all quite close to each other.

However, by inspecting the mean values and histograms of the strain gauges, presented in appendix E.4 in figure E.9, the following can be noted. If the load transfer mechanism as explained in 3.2 is assumed, than sensors 'A1', 'A2', 'A5', 'G2' and 'G5' show anomalies in the mean value and their distribution. Apart from sensor 'A1' this is in accordance to the non-contact areas as defined in section 7.4.2. However, due to the lacking consistency and uncertainty in the method, no hard conclusions can be drawn on this matter.

8.4.3. Stresses due to peak loads

During the operational phase of the project, the thrust force is the main source of excitation on the tower and thus the slip-joint. As was noted in section 2.6, this force is the greatest near rated wind speed conditions. Unfortunately, rated wind conditions have not yet been reached with the turbine in full operation. However, the turbine has been operating near rated conditions on multiple occasions. The stresses within the slip-joint during these instances, are elaborated on subsequently. First of all, an estimation of the thrust force is provided. With this thrust force estimate, a comparison between measured and calculated hoop stresses along the slip-joint can be made. The interval that is chosen for analysis, depicted in figure 8.12, is on the 11th of August during a steady operational run with a west wind.

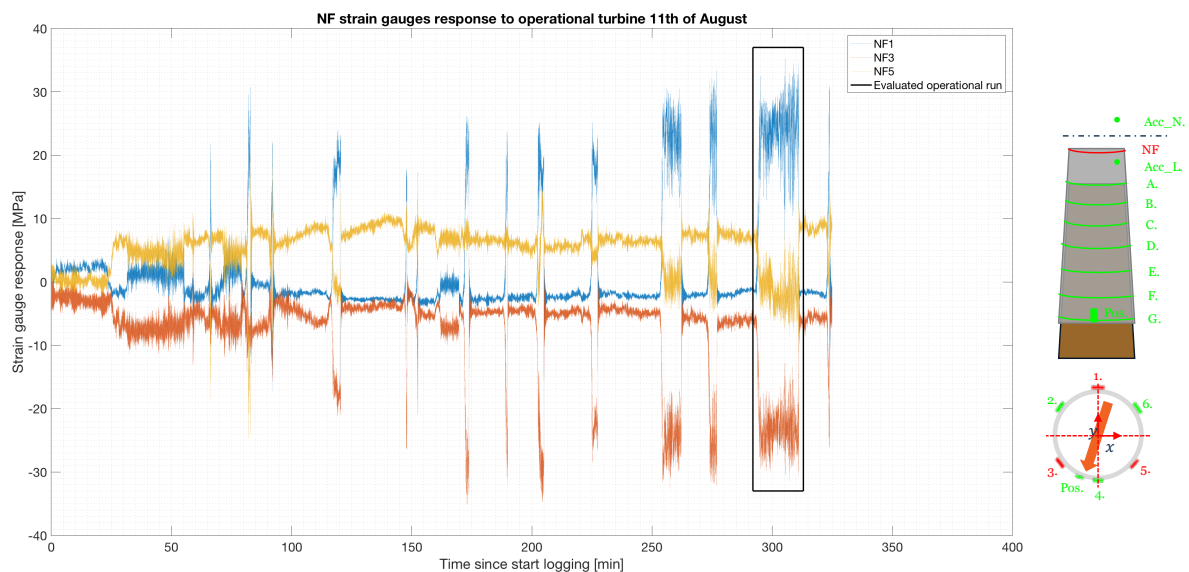


Figure 8.12: Evaluated operational interval

It is clear to identify the peaks in axial stress in the 'NF' strain gauges, as a result of the thrust force of the rotor. Also, the amplitude of these stresses matches with expectations based on the wind direction. In order to compare the measured values with predicted estimates, the thrust force of the rotor needs to be estimated. The obtained thrust force can be used as input in the stress calculations, according to the formulas presented in section 3.2.2. To determine this thrust force, the geometry of the tower and axial stress response of strain gauge 'NF3' is used. With a given stress response, the bending moment at the strain gauge position can be determined by:

$$M_{NF3} = \sigma_{m,NF3} \cdot W_{NF3} \quad [kNm] \quad (8.4)$$

To ease the calculation, it is assumed that this moment is caused by the thrust force only i.e., wind drag loads can be neglected. At low wind speeds this assumption is in line with the evaluations in section 4.3.3. The thrust force can then be estimated by:

$$T = \frac{M_{NF3}}{L_{NF3}} \quad [kN] \quad (8.5)$$

From the stress response of strain gauge 'NF3', an average compression of $\sigma_{m,NF3} = -17.58 \text{ MPa}$ is observed. Using this input, the corresponding estimated thrust force during the operational interval is $T = 42 \text{ kN}$. This obtained force can then be used to calculate the bending moment at the slip-joint connection, using equation 8.5 and changing the length L_{NF3} to the appropriate length between the slip-joint and rotor. The resulting moment at the slip-joint amounts to 1410 kNm .

This bending moment is subsequently used to calculate the hoop stresses in the tower wall by methods explained in section 3.2.2 and 3.2.2. The estimates for the maximum and average hoop stress, $\sigma_{hoop,l}$ and $\sigma_{hoop,a}$ respectively, are found to be:

$$\sigma_{hoop,l} = 10.83 \text{ [MPa]}, \quad \sigma_{hoop,a} = 7.25 \text{ [MPa]} \quad (8.6)$$

The measured hoop stresses on the vertical line number '3' within the slip-joint are presented in figure 8.13. Also, the vertical stress from strain gauge 'A3' and 'NF3' is presented. The mean values of the stresses over the total run are displayed in the legend.

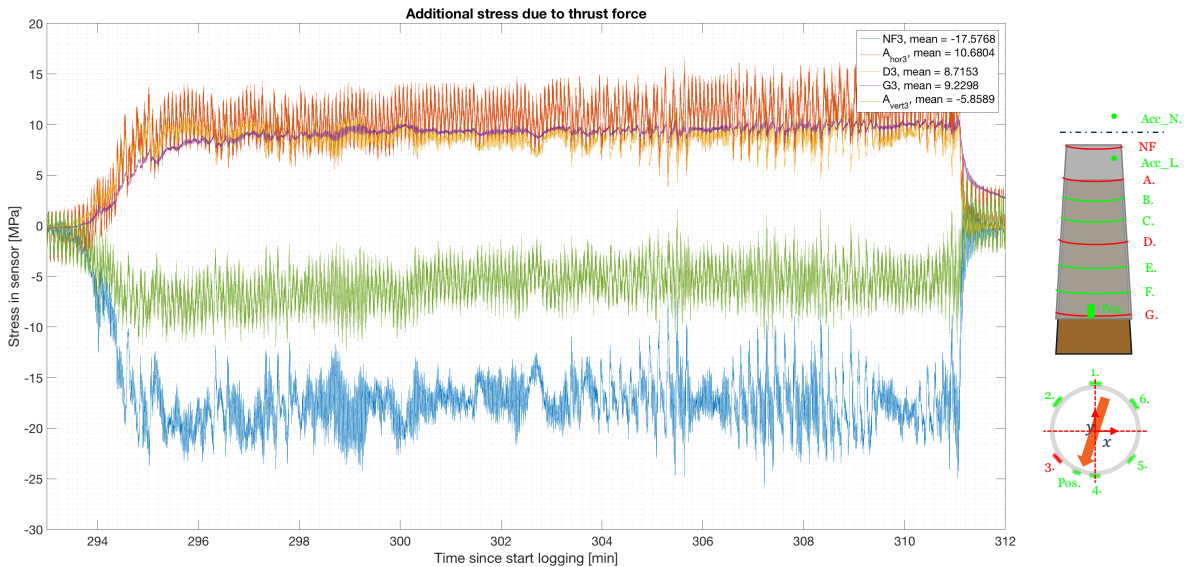


Figure 8.13: Additional hoop stresses within the slip-joint as result of thrust force

A couple of things can be noted when comparing these calculated values, to the measured values. First of all, the peak stress, $\sigma_{hoop,l}$, as calculated by the literature method corresponds remarkably well with the measured strain value in strain gauge 'G3'. This means that for this specific case, the calculated

values provide genuinely accurate predictions of the stresses within the slip-joint due to a bending moment.

Secondly, the average stress $\sigma_{hoop,a}$ in the slip-joint as a result of the bending moment, calculated with the alternative method, provides an accurate engineering prediction of the average hoop stress within the slip-joint as a result of the bending moment.

Thirdly, the vertical stress, as a result of this bending moment, at sensor 'A3' amounts to $\sigma_v = -5.86 \text{ MPa}$, as depicted in figure E.12. This is 33% of the total vertical stress registered in the 'NF3' strain gauge. This means that at sensor 'A' the friction force has taken up 67% of the total vertical load.

8.4.4. Conclusions and discussion

From the data of the strain gauges, evaluated during the operational intervals of the wind turbine, a number of conclusions can be drawn. First of all, it can be concluded that the additional stresses due to the total settlement of the slip-joint, including the additional settlement during the operational phase, are well below the yield stress. Also, two transitions from compression to tension have been observed. This could possibly mean that these locations moved from a non-contact to a contact situation. It must be noted that there is a sensitivity introduced in this evaluation. Since the sensors have no active temperature correction and shielding on the wires, their values may vary from day to day. This serves no problem when comparing measurements on a single day. However, when comparing stresses over multiple weeks, or months in this cause, attention should be paid to these sensitivities. From the data of the dummy strain gauges it can be observed that a stress range of $\Delta\sigma \approx \pm 10 \text{ MPa}$ is plausible.

Secondly, from the analysis on the standard deviation and probability distribution function of the time varying hoop stresses during two operational intervals, no real hard conclusions can be drawn. The values of the standard deviations are too close to each other and show no consistent correlation to the contact and the non-contact areas. Although the mean values and their histograms show some correlation, the resemblance is not big and consistent enough to base a solid conclusion on them.

Thirdly, by inspection of the amplitude of the stresses within the slip-joint connection, during an operational interval, it can be concluded that these stresses correspond genuinely well to the design calculation methods, established in section 3.2.2. The peak hoop stresses, due to the bending moment in the slip-joint, are well below the yield stress and correspond to the anticipated values. Furthermore, from the vertical stresses in sensor 'A3' it can be concluded that the friction forces within the slip-joint takes up roughly 67% of the total vertical force. It should be noted that only one time interval is analysed in detail in this section, however all the operational intervals in this day show the same behaviour. It is interesting to see if these relations will still hold with increasing thrust forces. If so, it can be concluded that the calculation methods can be used with confidence for design purposes. Up until now, this data is not yet available and it is therefore recommended to inspect this data in the same manner as in section 8.4.3, as soon as it becomes available.

8.5. Conclusion

In this chapter, the results of the measurements during the operational period from June 2016 through mid-September 2016 have been discussed. During this period the wind turbine has been fully operational in varying wind conditions, exciting the support structure with a range of loads. The data from the accelerometers, settlement sensors and strain gauges have been analysed and a number of conclusions can be drawn from this evaluation.

First of all, the natural frequencies of the first bending modes in both the fore-aft and side-side direction, have been identified using time domain signals from the strain gauge sensors. Three different excitations have been analysed, including heavy wind conditions, emergency stops and an operational interval. During all these instances, the natural frequency was identified around $f_{nat,1} = 0.86 \text{ Hz}$. As one would expect, the fore-aft and side-side directions showed a slight difference in the operational interval, caused by the presence of aerodynamic damping in the fore-aft direction. The natural frequencies during operation in the fore-aft and side-side direction were measured at $f_{1,fa} = 0.863 \text{ Hz}$ and $f_{1,ss} = 0.872 \text{ Hz}$, respectively. These values correspond relatively well with the anticipated first

natural frequencies, modelled in Bladed and RFEM. A maximum discrepancy of 8.72% was identified.

Secondly, after a stable settlement level was reached, due to self-weight only, the slip-joint did settle an additional -16.71 mm as a result of operational loads. Therewith, the total settlement of the slip-joint increased 11% from $z_{settle} = -148\text{ mm}$, to a final settlement level of $z_{settle} = -165\text{ mm}$. This was mainly caused by the thrust forces of the rotor exerting a moment on the slip-joint initiating the settlement. The absolute settlement and the settlement velocity, in millimetres per day, clearly show signs of a converging mechanical system to a stable equilibrium. Taking into account the fact that the slip-joint has endured its governing load case, it is plausible to assume that this settlement level is indeed a final and stable level. This means that the final target overlap of the slip-joint amounts to $h_{to} = 5197\text{ mm}$. The measurement staffs, located on the South and North side of the slip-joint, show comparable results. Furthermore, the measurement staffs present the same overlap lengths, indicating that the slip-joint settled without any misalignment between the tower and monopile.

Thirdly, considering the stresses within the slip-joint it can be concluded that the additional stresses due to the settlement in the operational phase, are well below the yield strength of the material. The average stress in the slip-joint wall is around 30 MPa . Furthermore, compared to the stress distribution right after the installation of the slip-joint, two transitions from compression to tension have been observed. This could possibly be explained by the fact that the cones moved from a non-contact to a contact situation. Following this reasoning, the total slip-joint contact area has increased as a result of the additional settlement.

Finally, it can be concluded that the stresses within the slip-joint, as a result of a bending moment, are well below the yields stress. Furthermore, the measured values correspond genuinely well with the predicted values within the analysed time intervals. Therefore, the calculation methods used in this thesis, prove to be well suited for design purposes. Of course, more data should be analysed, preferably at rated wind speed conditions, to increase the validity of the design calculations. However, at this point there is no reason to believe that the stresses at higher excitation forces, will significantly deviate from the evaluations in this section.

Conclusions and recommendations

9.1. Conclusions

Over the course of this master thesis, a full scale, four meter diameter, slip-joint has been installed at the Maasvlakte II, Rotterdam. This slip-joint connects a 500kW wind turbine to the monopile foundation as part of the DOT500 wind turbine demonstration project. The wind turbine was installed in May 2016 and has been operational over the course of June through September. During the installation and operation phases, different sensors, including strain gauges, accelerometers and position sensors, have monitored the mechanical behaviour of the slip-joint connection. Considering the data obtained and the analysis performed in this project, the following main conclusion can be drawn:

Main conclusion:

The mechanical behaviour of the slip-joint connection shows no significant complications during both the installation and operation phases of the project. The settlement, during installation and after a period of operation, was observed to be within predictable limits and converged to a stable level. The resulting stresses, both during installation and operation, are well below the yield strength of the material and correspond to the predicted values. This indicates that the calculation methods used, prove suitable for design purposes. Also, the measured stresses show that the contact area, within this particular slip-joint, was far from optimal. By using two purpose built cones this contact area could be improved, leading to an even more desirable stress distribution.

This conclusion is based on the following sub conclusions.

1. The monopile was vibro-hammered into relatively dense soil, to the target penetration depth of 15 meters, with a slight out of alignment with the vertical axis of 0.77 – 0.90 degrees. This did not cause significant complications during the slip-joint installation.

The installation took 80 minutes, which is substantially longer than the anticipated 35 minutes. However, target penetration was reached. Furthermore, the pile is slightly out of alignment, with respect to the vertical axis, by 0.77° in negative y-direction (East) and 0.90° in negative x-direction (South). This out of alignment did not cause substantial complications during installation of the slip-joint, it even performed better in terms of installation speed as compared to a traditional bolted connection.

2. The first natural frequencies of the fore-aft and side-side bending modes were modelled in Bladed and RFEM, and measured using strain gauge time signals. The predictions correspond reasonably well with the measurements and an average discrepancy of 5.9% was observed.

The modelling included a model in Bladed and RFEM, with the inclusion of soil-structure interaction in the foundation by means of py-spring supports in the lateral direction. To this end, an excel-based tool

was created, shortening the modelling time of the foundation significantly. The first natural frequencies of the first fore-aft and side-side bending modes were estimated at around 0.81 Hz and was measured to be 0.86 Hz and 0.87 Hz, respectively.

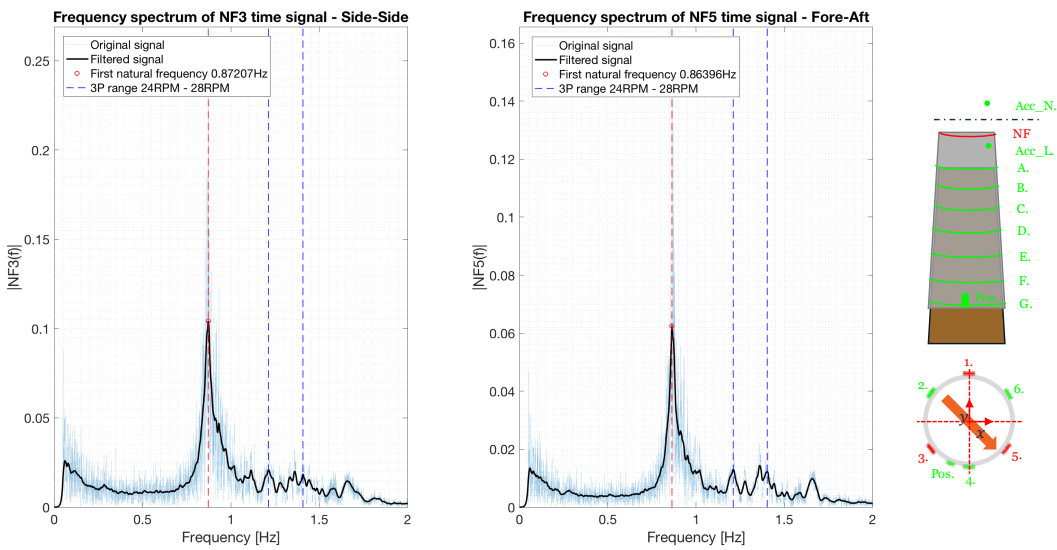


Figure 9.1: Frequency domain response of DOT500 turbine during operational interval at a rotor speed of 24-28 RPM

3. The settlement of the slip-joint, during the installation of four items, showed a smooth, controlled and anticipated behaviour. No unexpected jumps in velocity have been registered and the additional accelerations are considered insignificant, regarding damage to auxiliary equipment or personnel on the wind turbine.

After the lower tower was mounted on the monopile, four additional parts were installed, including: access platform, upper tower, nacelle and rotor. The settlement of the slip-joint, during the installation of these parts, showed a smooth behaviour without registering unexpected movements or jumps in settlement velocity. Also, the relative settlement, defined as the settlement per added tonne, clearly decreased during every component that was added. The additional accelerations registered during the settlement are in the order of magnitude of 0.25 – 0.50 G and considered insignificant.

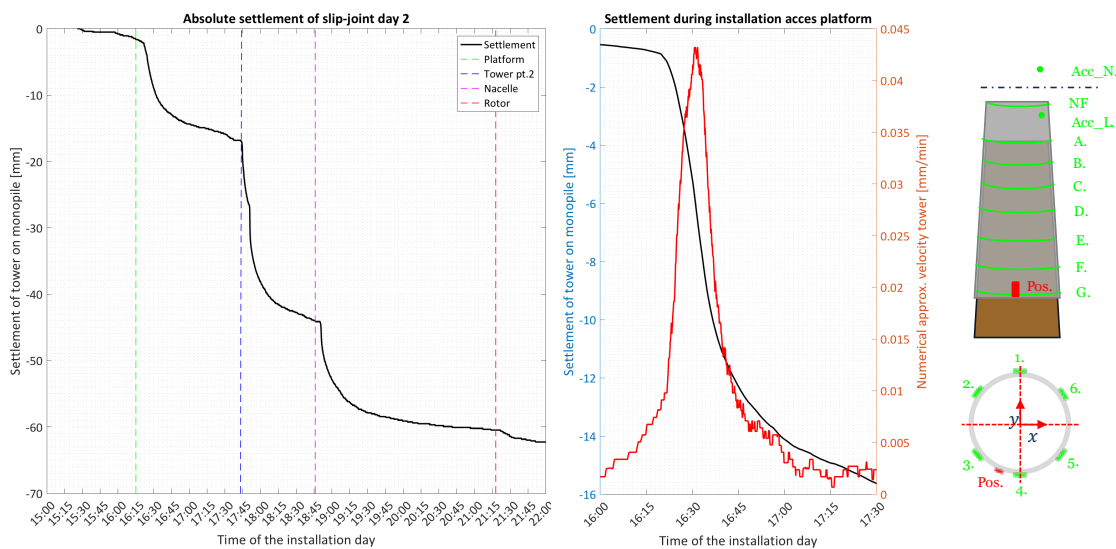


Figure 9.2: Settlement of slip-joint as result of additionally installed wind turbine items

4. In the subsequent days after the installation of the turbine, a negligible progressive settlement of 2% was registered. However, during operation, the turbine settled an additional 11%, after which the system converged to a stable settlement level of 165 millimetre.

Over the course of two weeks after the installation, a progressive settlement of -3.87 mm , or 2%, was observed due to self-weight only. A clear stable settlement level of $z_{settle} = -148\text{ mm}$ was reached. During operation, from begin July through mid-September, the slip-joint settled another -16.71 mm . The clearly decaying settlement velocity, indicates that the system is converging to a stable settlement level at around $z_{settle} = -165\text{ mm}$. Taking into account the fact that the slip-joint has endured its governing load case, it is plausible to assume that this settlement level is indeed a final and stable one. Furthermore, it can be concluded that the turbine tower settled on the monopile, without any misalignment between the two.

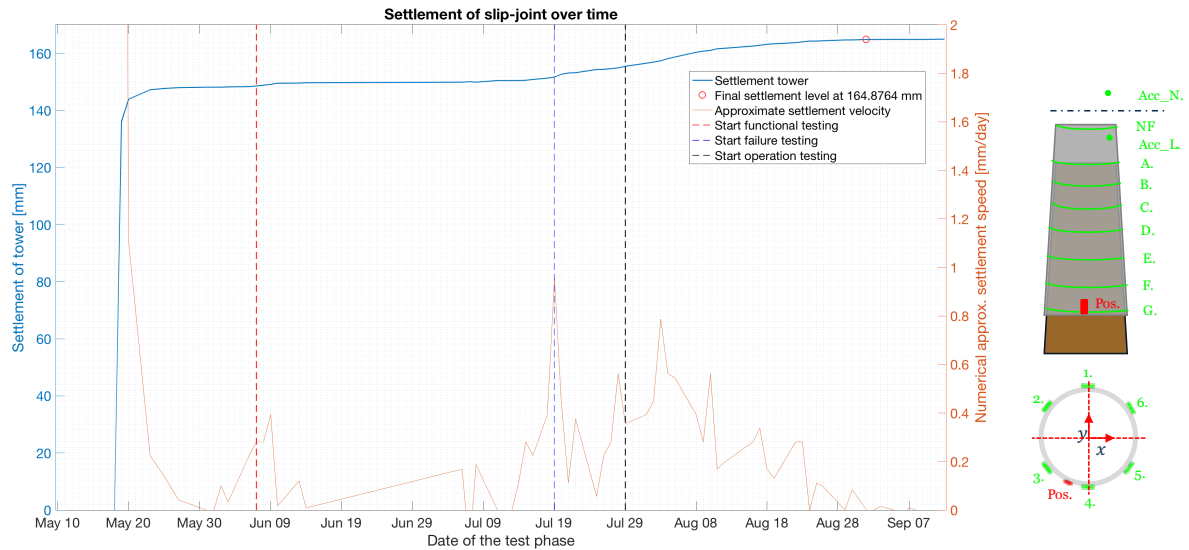


Figure 9.3: Settlement of the slip-joint over the total test phase

5. The estimated final overlap was within acceptable limits compared to the actual overlap, meaning that the prediction methodology is suitable to use in the design process.

A first order model was created, predicting the target overlap of the slip-joint, based on tower and monopile 3D laser measurements and vertical force equilibrium between contact forces and self-weight. The predicted target overlap length was 5.239m , which is not too far from the actual 5.196m , taking into account the sensitivities.

Table 9.1: Measured and anticipated settlement values

	Predicted value [mm]	Measured value [mm]	Difference [mm]	Relative difference [%]
First point of contact	5223	5031	192	3.68
Target overlap	5232	5196	36	0.69
Settlement	9.00	148	139	-

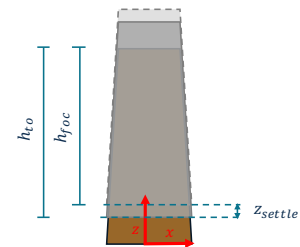


Figure 9.4: Settlement definitions

However, the total settlement, defined as the target overlap minus first point of contact, differed significantly. This was predicted to be 9.00 mm , compared to the measured 165 mm . This is readily explained by the fact that the tower was known to have significant ovality, leading to a much earlier first point of contact. Also, the out of alignment of the monopile contributes to this effect.

6. The measured hoop stresses, introduced in the tower by the expansion of the circumference as a result of the settlement, are far below the yield stress of the material and correspond with the predicted values.

During installation, hoop strains were measured using strain gauges on circumference 'A', 'D' and 'G'. These strains provide a reasonable estimate for the additional hoop-stress in the material as a result of the settlement. Almost all the stresses are found to be in the order of magnitude of 20 – 40 MPa, which is far below the yield stress of the material that was tested as 320 MPa. During the settlement in the operation phase, the average additional stress amounts to 16 MPa. The measured local hoop stresses correspond reasonably well with the predicted average values.

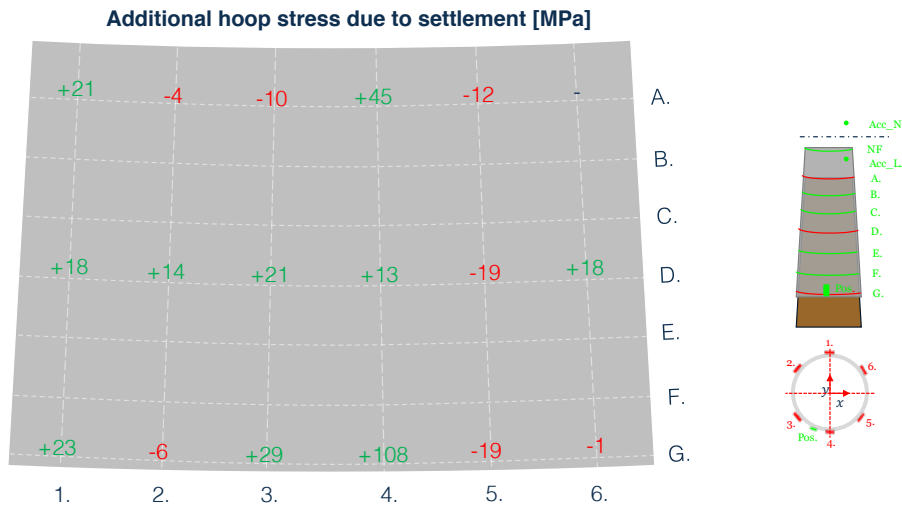


Figure 9.5: Additional hoop stress in tower wall due to settlement slip-joint

7. The stress distributions along the slip-joint overlap clearly show asymmetry along the vertical axis, indicating a non-uniform load pattern on the inside of the turbine tower and the presence of non-contact areas within the slip-joint.

Stress distributions show additional compression and tension during installation, at different locations along the circumference. A FEM was created to find out if compression, resulting from non-uniform contact-pressure, can occur within the slip-joint. The results of three different load cases, applying non-uniform pressure on the inside of the cylinder as well as uniform pressure on a cylinder with a slight ovality, confirmed the possible presence of local compression in the hoop direction. This implies deformation in the negative radial direction of the wind turbine tower wall.

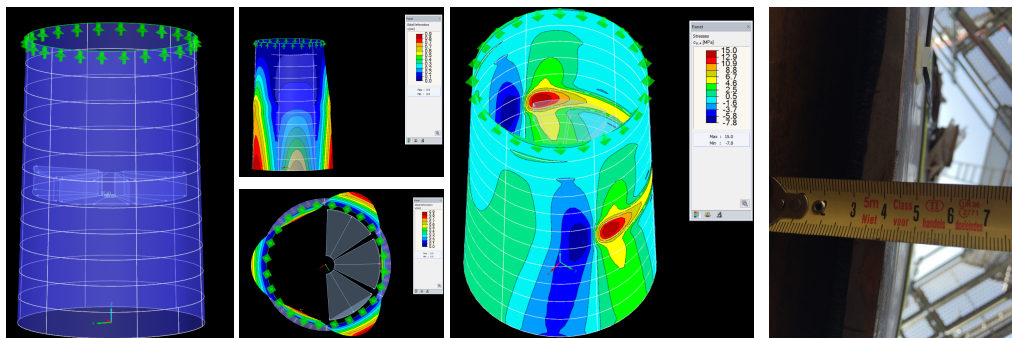


Figure 9.6: Modelled local strains (left) and observed non-contact area (right)

The observed negative stresses are plausible, confirming a number of non-contact areas along circumference 'A', 'D' and 'G'. Visual inspection and the presence ovality of the tower, increases the plausibility

of these non-contact areas. At sensors 'D2' and 'G6' a transition from compression to tensile stresses was observed during settlement in the operational phase, possibly indicating that the slip-joint contact area increased during the operational period.

8. The calculated principle stresses correspond to the measured hoop stresses and are far below the yield stress of the material. In line with conclusion seven, their direction does not align with the hoop direction. This implies the introduction of local shear stresses, most probably due to the non-uniformly applied inner pressure.

Principle stresses have been calculated from the rosette strain gauges at circumference 'A' and the Von Mises equivalent stress is far below the yield stress of the material. In line with the asymmetry observed in the local hoop stresses, the direction of the main principle stresses vary along the circumference and do not align with the hoop direction. However, the principle stress directions do not change during the installation, confirming a controlled and smooth settlement behaviour, as the inner load pattern on the slip-joint remained unchanged.

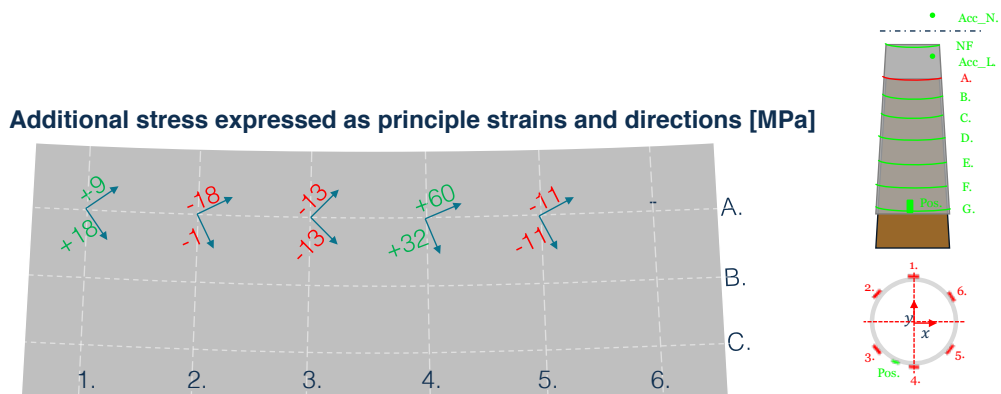


Figure 9.7: Principle stresses and direction after settlement of slip-joint

9. Verification of contact and non-contact areas was not possible using Ultra-Sonic technology. An alternative method could be by means of Eddy currents.

An ultrasonic test was performed to try and find contact and non-contact areas based on the difference in reflection coefficient of the steel-steel and steel-air boundary layers. On two slip-joints, the operational DOT500 and decommissioned 'Duinvoegel', it was not possible to confirm or exclude the existence of non-contact areas. The immense difference in acoustic impedance of both air and steel ensure that practically all the energy of the sound wave gets reflected, at even the smallest film of air between the two steel plates. On a microscopic scale, there are always non-contact areas present due to the ragged surface of the materials. A possible alternative measurement technique could be to make use of eddy currents.

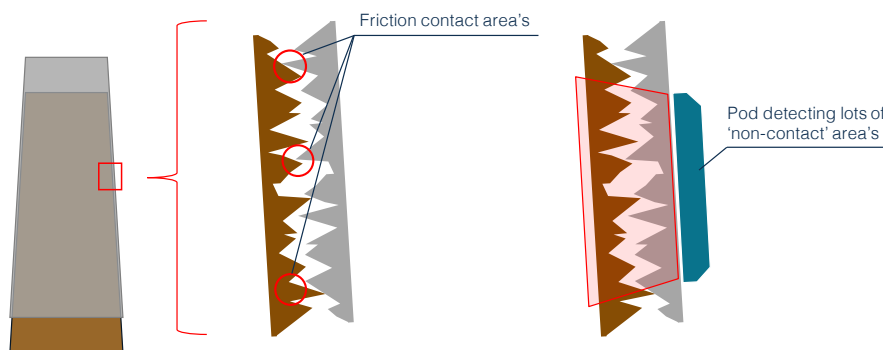


Figure 9.8: Most probable reason for not being able to detect a difference in contact and non-contact areas

10. The stresses within the slip-joint during operation are far below the yield stress and correspond well with the anticipated values. This implies that the calculation methods are practical for design purposes.

Based on the evaluated data in this research, it can be concluded that the stresses within the slip-joint as a result of a bending moment are well below the yields stress. Furthermore, the measured values correspond genuinely well with the anticipated values within the analysed time intervals. Also, it was found that friction takes up around 70 % of the vertical load at the top of the slip-joint, which is in line with the predictions. This means that the presented calculation methods in this thesis can be used for design purposes with confidence. More data should be analysed, preferably at rated wind speed conditions, to further increase the validity of the design calculations. However, at this point there is no reason to believe that the stresses at higher excitation forces will deviate significantly from the presented evaluations.

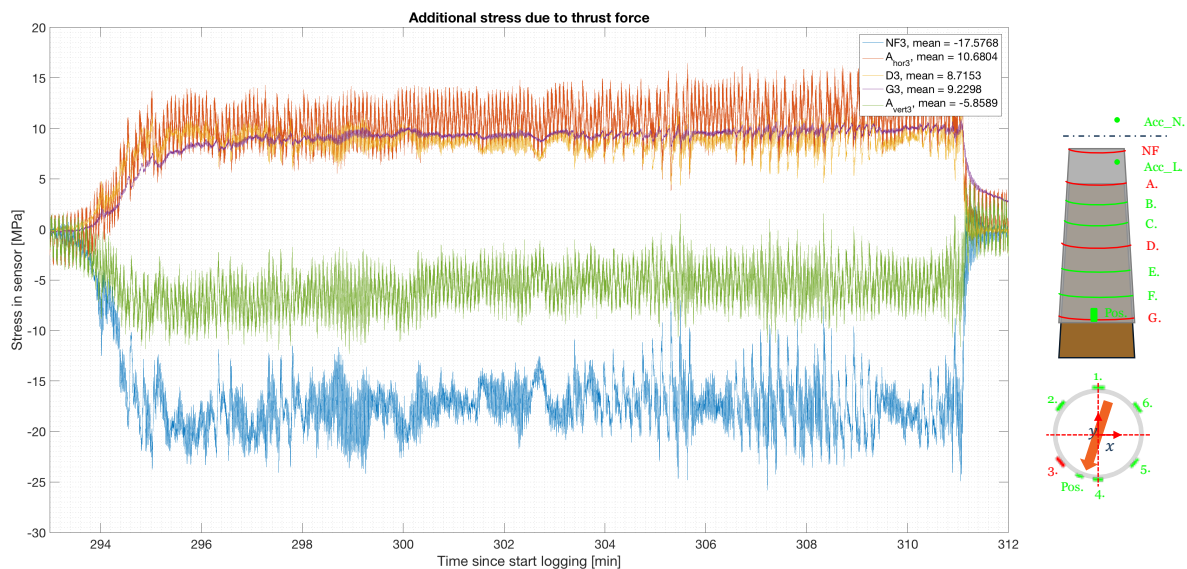


Figure 9.9: Additional hoop and vertical stresses in the slip-joint during operational interval

9.2. Recommendations and future research

Based on the research performed in this thesis a couple of recommendations are made. They are split in to three categories, including recommendations to the academic society, the industry and DOT B.V.

9.2.1. Recommendations to the academic society

1. Further research is advised on the effect of corrosion within the slip-joint.

The effect and monitoring of corrosion was not incorporated in this research. The non-contact areas and openings at the bottom of the slip-joint could allow for corrosion to form within the joint. The effect of this should be investigated. It could either solidify the connection, or 'eat' its way through the tower or monopile wall, possibly inducing significant local stress concentrations. It would be wise to check the DOT500 slip-joint after decommissioning on any signs of corrosion and the effect of this.

2. Future research is advised on the effect of fatigue within the slip-joint

Static stresses and ultimate load cases have been treated in this research. However, an analysis on fatigue damage due to the time varying loads of the operational wind turbine has not been investigated. Local stress concentrations might occur within the slip-joint due to non-uniform contact areas, which could lead to a decrease in fatigue lifetime of the wind turbine tower or monopile. Although, no significant problems can be foreseen based on this research, it is advised to verify this, possibly using the actual data gathered in this measurement campaign.

9.2.2. Recommendations to the industry

1. Based on the data of this research, the use of a slip-joint connection in (offshore) wind turbines is structurally feasible. It is recommended to use the concept in more (demonstration) wind turbine projects, to enlarge the number of samples and increase the validity of the concept.

The installation of the slip-joint was performed within two hours, considerably shortening installation time compared to a conventional transition piece connection. On top of that, even with a second-hand turbine tower, that was cut from and welded on, the connection was structurally safe without encountering any problems regarding stress and settlement during installation and operation. If two purpose built cones were to be used, likewise the satisfying conical monopile-top fabricated by Sif, the contact-area and thus mechanical behaviour will be improved.

2. The minor additional stresses in the slip-joint, due to the installation and operation of the wind turbine, combined with the knowledge regarding the far from ideal contact area within the slip-joint, provide reasons to believe that the desired total overlap length can be decreased. A possible decrease from $1.5D$ to $1D$ is anticipated

The additional stresses in the tower as a result of the settlement are far below the yield stress. Also, the stresses during operational loads were below the yield stress and were within predictable limits. Combined with the fact that the contact area of this particular total slip-joint was far from optimal, provides reasons to believe the target overlap can be shortened. In this case, a decrease to $3.00 m$ overlap, or approximately $0.9D$, seems plausible based on preliminary design calculations verified by this research.

It should be noted here that the diameter of the cone is not the one and only parameter on which the overlap length is dependant, as was already explained in section 3.2. Therefore, attention should be paid while expression overlap lengths, purely as a function of the diameter of the cone.

3. The use of vibro-hammering to install a monopile foundation presented no complications for the use of the slip-joint.

The out of alignment of $0.7 - 0.9$ degrees that resulted from the vibro-hammering installation, did not significantly affect the slip-joint performance. Although a more vertical alignment would be favourable, to further ease the installation process and provide a more uniform contact area, it is not crucial importance. Therefore, the current criterion of 0.1 degree out of alignment is well within practical acceptable limits.

9.2.3. Recommendations to DOT B.V.

1. It is recommended to continue monitoring the mechanical behaviour of slip-joint connection during the remainder of this phase and future phases of the DOT500 project.

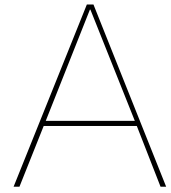
The actual data regarding the mechanical behaviour of a full-scale slip-joint connection, proved invaluable during this research. Promising conclusions have been drawn from this data and the inspection of more data, preferably near rated speed conditions, will increase the validity of the models, calculation methods and the slip-joint concept in general.

2. During future phases of the measurement campaign the following recommendations, regarding the used sensors, can be taken into account.

First of all, the accelerometers that were used did not prove to be too satisfactory. Their availability was limited and sometimes unpredictable and the signal-to-noise ratio was far from optimal in some cases. This could have been caused by the long cables from the nacelle to the data logger. Furthermore, the full bridge unidirectional strain gauges that were used to measure the natural frequency, proved very suitable. However, no direct directional information can be obtained from them, since the rotor moves independent of these strain gauges. This intensified the search for useful time series, yet did not create any real problems.

Secondly, the position sensor that was used to monitor the slip-joint's settlement performed well. One or two additional sensors could be positioned around the slip-joint's circumference to more accurately acquire information on the possible misalignment between the two cones during settlement. Furthermore, it is not advised to continue using the taut wires in combination with the position sensors to measure global hoop elongation. Their information was useful, however the construction proved to be fragile compromising the reliability of the measurement. Especially in an offshore environment, the sensors will be destined to break.

Finally, the spatial distribution of strain gauges along the slip-joint provided a satisfying image of the slip-joint's stress distribution. The full bridge unidirectional strain gauges performed very well in the outdoor environment, providing reliable values with little noise. However, shielding and shortening of the cables is advised if comparisons of values between long time instances are required. The rosette strain gauges provided very useful additional information regarding principle stresses, which would have been useful to have on multiple circumferences. However, they were manually configured in a half-bridge configuration, which showed in the signal to noise ratio and temperature sensitivity. Also, they are more expensive. This trade-off should be kept in mind when equipping the future slip-joint with strain gauges.



DOT500 support structure dimension

A.1. Introduction

In this appendix the dimensional and weight details of the different parts of the DOT500 support structure can be found. It includes information on:

- The lower tower dimensions and weight based on the 3D-scan and simple diameter and wall thickness measurements. Figure A.1 through A.4.
- The upper tower dimensions and weight based on simple diameter and wall thickness measurements. Figure A.5 and A.6.
- The report of the NDT that was performed on a piece of the tower. Figure A.7.
- The monopile dimensions based on technical drawing as well as 3D-scan data. Figure A.8 and A.9.
- The dimensions and weight of the different parts of the nacelle and rotor based on measurements and folder information. Figure A.10.

Also, information regarding the monopile design cycle is presented. It includes information on:

- The environmental and structural input parameters. Figure A.11 through A.13.
- Frequency analysis of the DOT500 and DOT3000 offshore turbine. Figure A.15 and A.14.
- Load calculations and strength checks for DOT500 and DOT3000 offshore test. Figure A.16 and A.17.
- Penetration depth optimisation for DOT500 onshore and DOT3000 offshore test. Figure A.18 and A.19.

Gemeten door Koen (vertikaal)					Gemeten door Thijs (op ongeveer 2/3 van onderste kwart)				
Afstand tot onderkant	Diameter	Links	Rechts	Omtrek	Afstand tot onderkant	Diameter	Links	Rechts	Omtrek
0,515	3,541	-1,7705	1,7705	11,124	0,514	3,553	-1,777	1,777	11,162
1,079	3,514	-1,757	1,757	11,040	1,082	3,507	-1,754	1,754	11,018
1,555	3,488	-1,744	1,744	10,958	1,557	3,485	-1,743	1,743	10,948
2,068	3,459	-1,7295	1,7295	10,867	2,073	3,455	-1,728	1,728	10,854
2,499	3,43	-1,715	1,715	10,776	2,500	3,426	-1,713	1,713	10,763
3,009	3,4	-1,7	1,7	10,681	3,009	3,397	-1,699	1,699	10,672
3,508	3,376	-1,688	1,688	10,606	3,514	3,368	-1,684	1,684	10,581
3,995	3,349	-1,6745	1,6745	10,521	3,993	3,339	-1,670	1,670	10,490
4,516	3,32	-1,66	1,66	10,430	4,519	3,310	-1,655	1,655	10,399
5,032	3,288	-1,644	1,644	10,330	5,034	3,282	-1,641	1,641	10,311
5,517	3,258	-1,629	1,629	10,235	5,520	3,256	-1,628	1,628	10,229
6,092	3,24	-1,62	1,62	10,179	6,096	3,218	-1,609	1,609	10,110
6,563	3,215	-1,6075	1,6075	10,100					
7,097	3,185	-1,5925	1,5925	10,006					
7,539	3,158	-1,579	1,579	9,921					
8,006	3,129	-1,5645	1,5645	9,830					
8,596	3,088	-1,544	1,544	9,701					
9,042	3,057	-1,5285	1,5285	9,604					
9,525	3,024	-1,512	1,512	9,500					
10,009	2,991	-1,4955	1,4955	9,397					
10,571	2,951	-1,4755	1,4755	9,271					
10,997	2,922	-1,461	1,461	9,180					
11,595	2,888	-1,444	1,444	9,073					
11,999	2,863	-1,4315	1,4315	8,994					
12,463	2,835	-1,4175	1,4175	8,906					
13,051	2,797	-1,3985	1,3985	8,787					
13,484	2,768	-1,384	1,384	8,696					
14,102	2,729	-1,3645	1,3645	8,573					
14,577	2,7	-1,35	1,35	8,482					
15,087	2,667	-1,3335	1,3335	8,379					
15,529	2,638	-1,319	1,319	8,288					
16,042	2,605	-1,3025	1,3025	8,184					
16,532	2,589	-1,2945	1,2945	8,134					
17,058	2,573	-1,2865	1,2865	8,083					
17,58	2,548	-1,274	1,274	8,005					
18,078	2,541	-1,2705	1,2705	7,983					
18,945	2,518	-1,259	1,259	7,911					

Figure A.1: Lower tower dimensional data based on simple diameter and wall thickness measurements

Wind turbine lower tower. Source: P093-C01b Calculation of the slip joint						
Ref bottom + m	Diameter [m]	Wall thickness [m]	Area [m2]	Mass [kg]	Extra mass [kg]	Total mass [kg]
6,645	3,580	0,0153	0,171	0,000	845,199	845,199
8,716	3,455	0,0154	0,166	4403,680	0,000	4403,680
12,098	3,251	0,0102	0,103	2071,073	0,000	2071,073
14,651	3,129	0,0103	0,101	4339,627	0,000	4339,627
20,129	2,768	0,0101	0,088	1757,195	0,000	1757,195
22,687	2,605	0,0104	0,085	1928,509	0,000	1928,509
25,585	2,518	0,0100	0,079	0,000	367,484	367,484
						15712,766

Figure A.2: Lower tower dimensional data based on simple diameter and wall thickness measurements with reference to actual site heights.

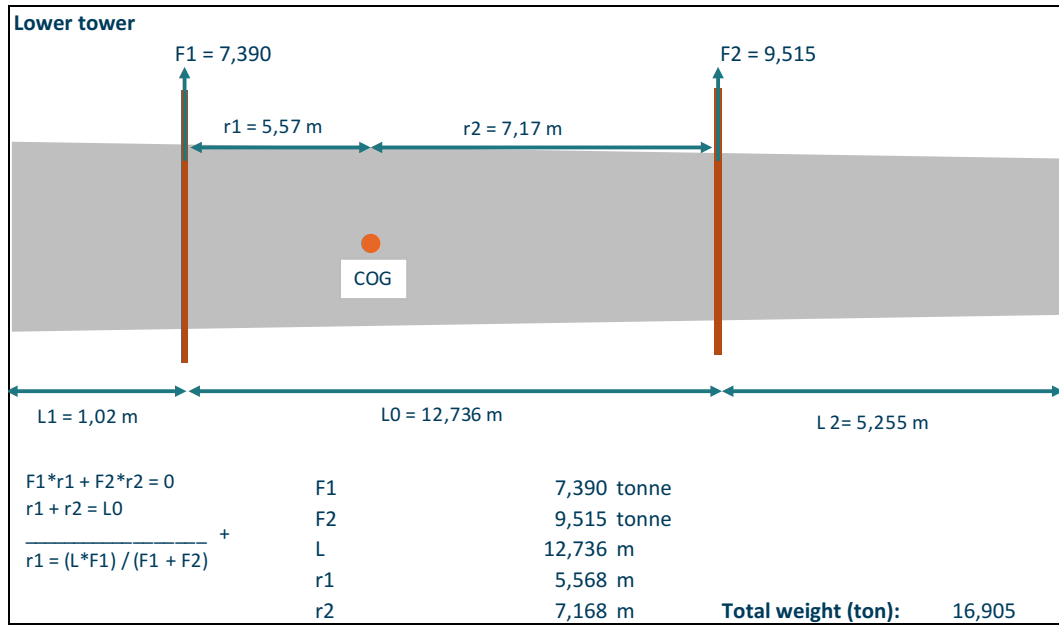


Figure A.3: Lower tower weight information based on test in workshop

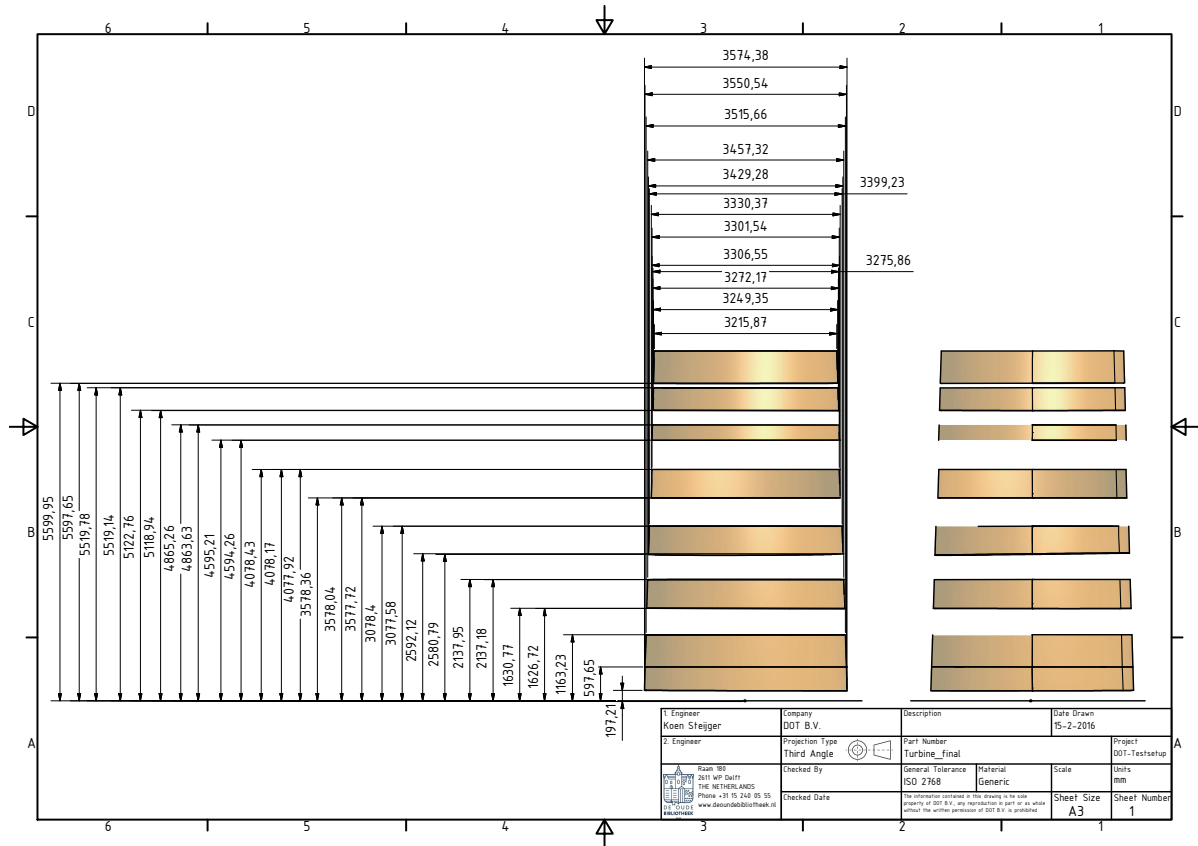


Figure A.4: Lower tower dimensional data based on 3D measurements

Wind turbine upper tower. Source: boventoren platen						
Ref bottom + m	Diameter [m]	Wall thickness [m]	Area [m2]	Mass [kg]	Extra mass [kg]	Total mass [kg]
25,633	2,518	0,0107	0,084	0,000	367,484	367,484
28,517	2,450	0,0107	0,082	1864,056	0,000	1864,056
31,413	2,382	0,0108	0,080	1769,338	0,000	1769,338
34,215	2,316	0,0108	0,078	1859,343	0,000	1859,343
37,244	2,244	0,0090	0,063	1457,968	0,000	1457,968
40,183	2,175	0,0090	0,061	1413,215	0,000	1413,215
43,123	2,105	0,0090	0,059	1387,026	0,000	1387,026
46,104	2,035	0,0084	0,053	0,000	250,660	250,660
						10369,089

Figure A.5: Upper tower dimensional based on simple diameter and wall thickness measurements

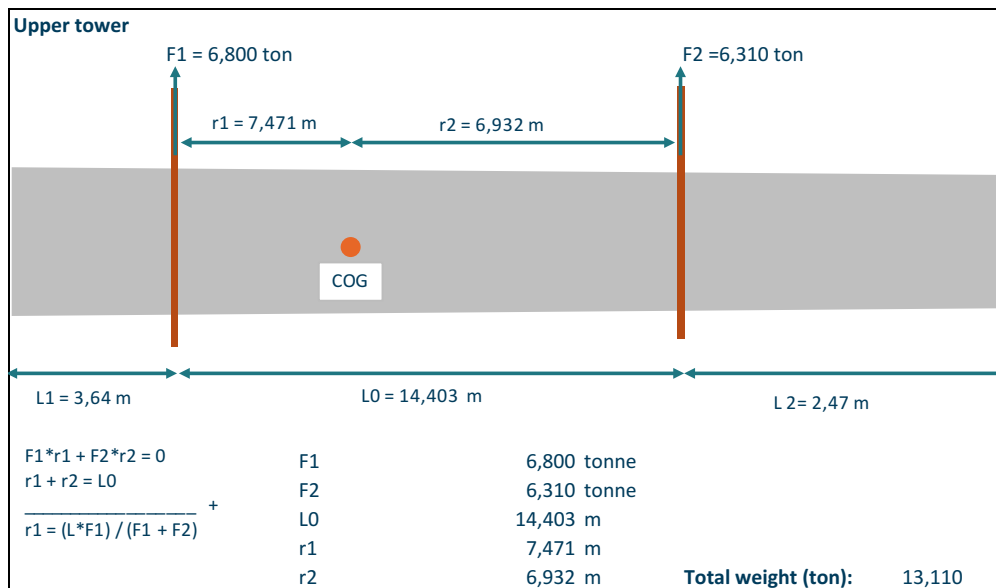


Figure A.6: Lower upper weight information based on test in workshop



MATERIAAL METINGEN TESTGROEP BV
Laboratorium

Report no. : 0532/1 page 1 of 1
Ref. Lab : 169.0532/1602221
Date : 16-02-2016

TEST REPORT

Customer	: DOT bv DELFT	Your Ref.	: DOT500 IST
Material	: Testpiece delivered by customer	Stamped by	: Customer
Examination	: Tensiletest, Impacttest and Chemical Analysis		
Requirements	: Not Specified		

TENSILE TEST		Acc.to NEN EN ISO 6892-1		Surf. area	Gauge length	*	Temp. °C	Yieldstrength ReH	Tensile strength	Elon - gation %	Reduction of area %	
Item	Heat number	Size mm	Dimensions testspec. mm	mm ²	mm			N/mm ²	N/mm ²			
01 *****	---	Plate 10	25.2 x 10.5	264	90	6	RT	321	421	33.0	--	---

Item	Flatt. Test	Drift exp. test	RingTen.Test	Ring Exp.test	Bend Test	IMPACT TEST		Type	Charpy-V			Values in Joule	
						Dimensions mm	* Temp °C	Acc.to NEN EN ISO 148-1	1	2	3	Average	
01 *****						55 x 10 x 7.5	6	-20	90	96	78	88	

CHEMICAL ANALYSES (OES)													own method acc.to ML 00260E		
Item	C %	Si %	Mn %	P %	S %	Cr %	Mo %	Ni %	Al %	Cu %	Ti %	V %			CEQ LF
01 *****	0.10	0.17	0.83	0.013	0.019	0.04	<0.01	0.03	0.044	0.01	<0.01	<0.01			0.254

Remarks :

* Direction testpieces : 1 = Longitudinal 2 = Transverse 3 = TTP 4 = Tangential 5 = Radial 6 = Not specified/Unknown 7 = Weld 8 = H.A.Z.


Laboratory :	Customer :	Witnessing Authority :
 Planner		

Figure A.7: Tensile and chemical test report turbine tower

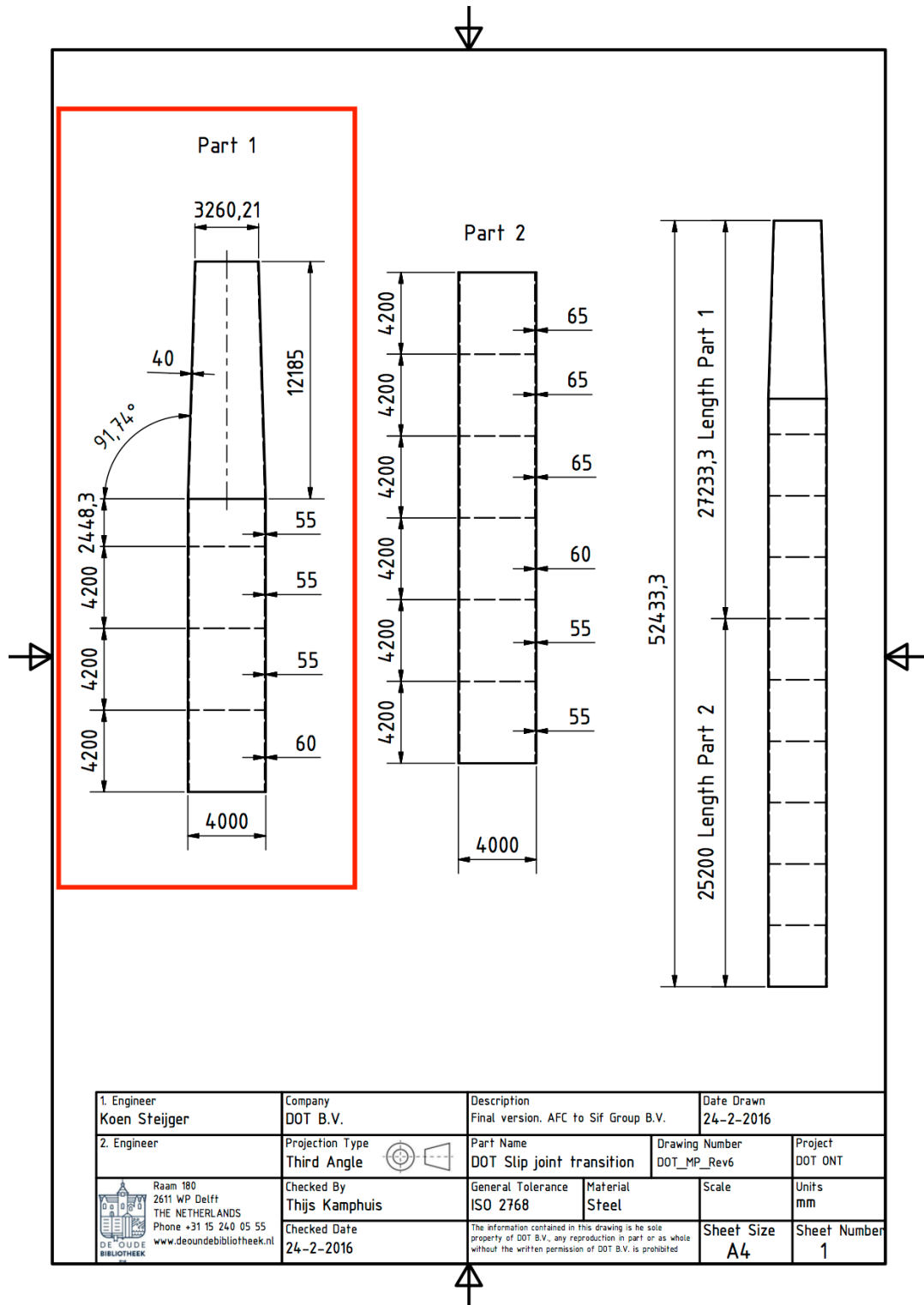


Figure A.8: Monopile dimensions according to technical drawing

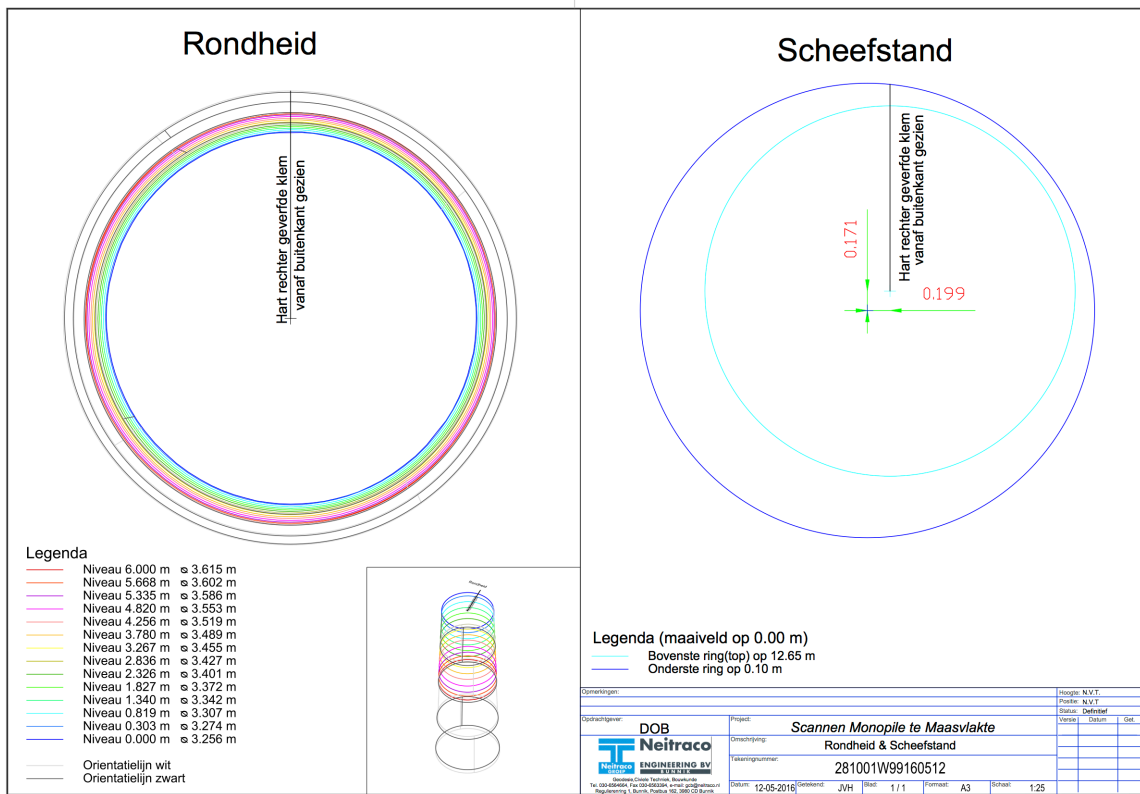


Figure A.9: Monopile dimensions according 3D-scan

Nacelle. Source: Weight control document DOT500		
item	mass [kg]	Source
Blade 1	2105	measured
Blade 2	2105	measured
Blade 3	2105	measured
Hub	1930	measured
Rotor Cover	120	estimated
Bolts	200	estimated
Unknown	635	From folder
Total RNA:	9200	
Generator	2990	measured
Cardan Shaft	100	estimated
Disc Brake	50	estimated
Gearbox	5420	measured
Remaining (structural) mass	11240	estimated
Total nacelle assembly:	19800	Calculation from folder
Hagglunds	1445	measured
Frame hagglunds	398,8	measured
Position tube	19,8	estimated
Brake disc	88,5	estimated
Hub with flange	323,2	estimated
Central shaft with hole	362	estimated
Total DOT nacelle assembly:	13877	Calculation
Total old top Mass	29000	kg
Total DOT top mass	23077	kg

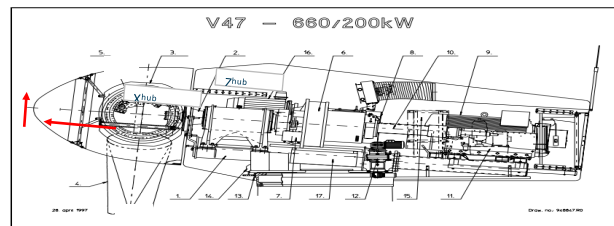


Figure 1 Structure of V47-660/200 kW. Only difference to V39/V42/V44-600kW, V47-660 kW : no. 16 and 17 is not present.

- | | |
|------------------|-----------------------------|
| 1. Base frame | 9. Generator (Gen 1) |
| 2. Main shaft | 10. Cardan shaft |
| 3. Blade hub | 11. Hydraulic power station |
| 4. Blade | 12. Yaw gear motor |
| 5. Blade bearing | 13. Yaw ring |
| 6. Gearbox | 14. Yaw control |
| 7. Gear tie rod | 15. VMP top control unit |
| 8. Disc brake | 16. Small generator (Gen2) |
| | - - Generator shift box |

Figure A.10: Nacelle and rotor weight information

Parameter	Value	Unit	Reference
Water depth (MSL)	18,0	m	OWEZ_R_141_20080215-General-Report
50y water level	22,0	m	Estimation (DNA)
50y potential wind speed (at 10m)	28.72	m/s	Excelsheet: Extreme value analysis and WW data (internal use only).xlsx
5y potential wind speed (at 10m)	25.23	m/s	Excelsheet: Extreme value analysis and WW data (internal use only).xlsx
50y wave height	6,03	m	Excelsheet: Extreme value analysis and WW data (internal use only).xlsx
Accompanying peak period	11,07	s	Excelsheet: Extreme value analysis and WW data (internal use only).xlsx
5y wave height	4,87	m	Excelsheet: Extreme value analysis and WW data (internal use only).xlsx
Accompanying peak period	9,87	s	Excelsheet: Extreme value analysis and WW data (internal use only).xlsx
50y current speed	0.92	m/s	Excelsheet: Extreme value analysis and WW data (internal use only).xlsx
5y current speed	0.67	m/s	Excelsheet: Extreme value analysis and WW data (internal use only).xlsx
Soil data	CPT	-	CPT's from Amalia wind park used

Figure A.11: Environmental input parameters OWEZ

Parameter	Value	Unit	Reference
Water depth	n.a.	m	-
50y water level	n.a.	m	-
50y potential wind speed (at 10m)	25,72	m/s	Excelsheet: Extreme value analysis and WW data (internal use only).xlsx
5y potential wind speed (at 10m)	22,32	m/s	Excelsheet: Extreme value analysis and WW data (internal use only).xlsx
50y wave height	n.a.	m	-
Accompanying peak period	n.a.	s	-
5y wave height	n.a.	m	-
Accompanying peak period	n.a.	s	-
50y current speed	n.a.	m/s	-
Soil data	CPT	-	CPT was performed

Figure A.12: Environmental input parameters Maasvlakte II

Parameter	Value	Unit	Reference
Tower bottom diameter	3,98	m	"950010R1_V90-GeneralSpecification"
Tower top diameter	2,30	m	"950010R1_V90-GeneralSpecification"
Tower wall thickness	0,02	m	Estimation (DNA)
Top mass (reduced):	82,8	ton	Calculation
- Blade mass (/ pcs)	6,60	ton	"950010R1_V90-GeneralSpecification"
- Hub mass	20,0	ton	"950010R1_V90-GeneralSpecification"
- Mass nacelle (incl. equipment)	68,0	ton	"950010R1_V90-GeneralSpecification"
- Assumed weight reduction DOT	25,0	ton	Due to exit: gearbox, generator, transformer
RPM minimal	8,60	RPM	"950010R1_V90-GeneralSpecification"
RPM maximum	18,4	RPM	"950010R1_V90-GeneralSpecification"
1P range (incl. buffer)	0,13 – 0,34	Hz	Excelsheet: "Design calculations_DOT PTS.xlsx"
3P range (incl. buffer)	0,39 – 1,01	Hz	Excelsheet: "Design calculations_DOT PTS.xlsx"

Figure A.13: Structural input parameters Vestas V90

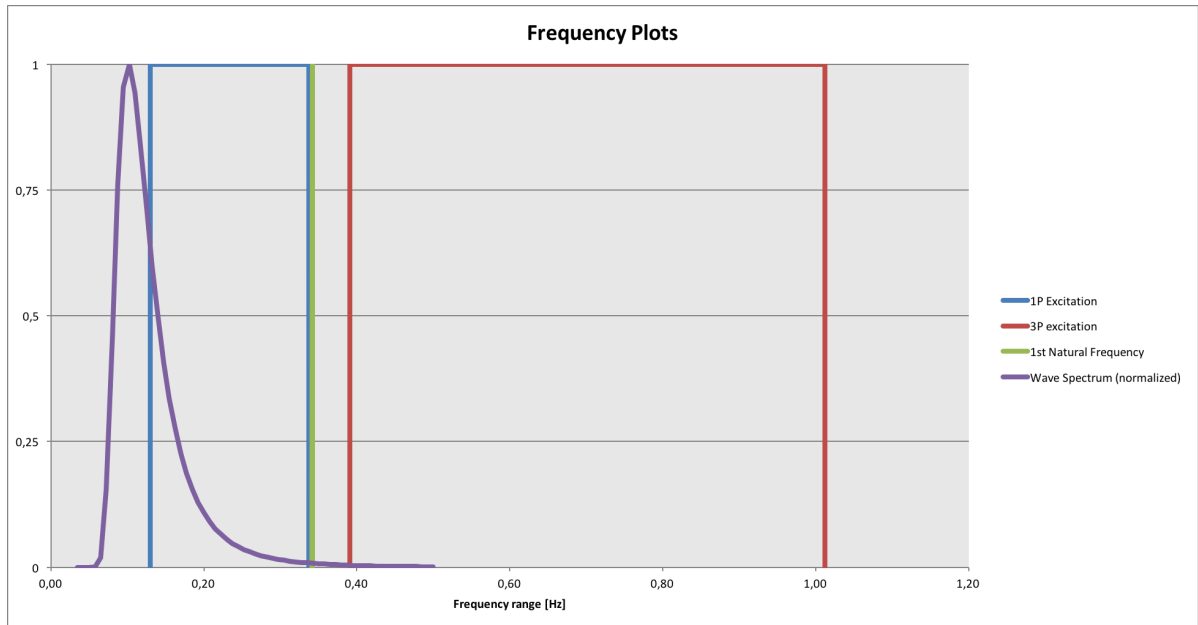


Figure A.14: Frequency spectrum of DOT3000 at OWEZ with average diameter of 4.00 m and wall thickness of 0.055 m

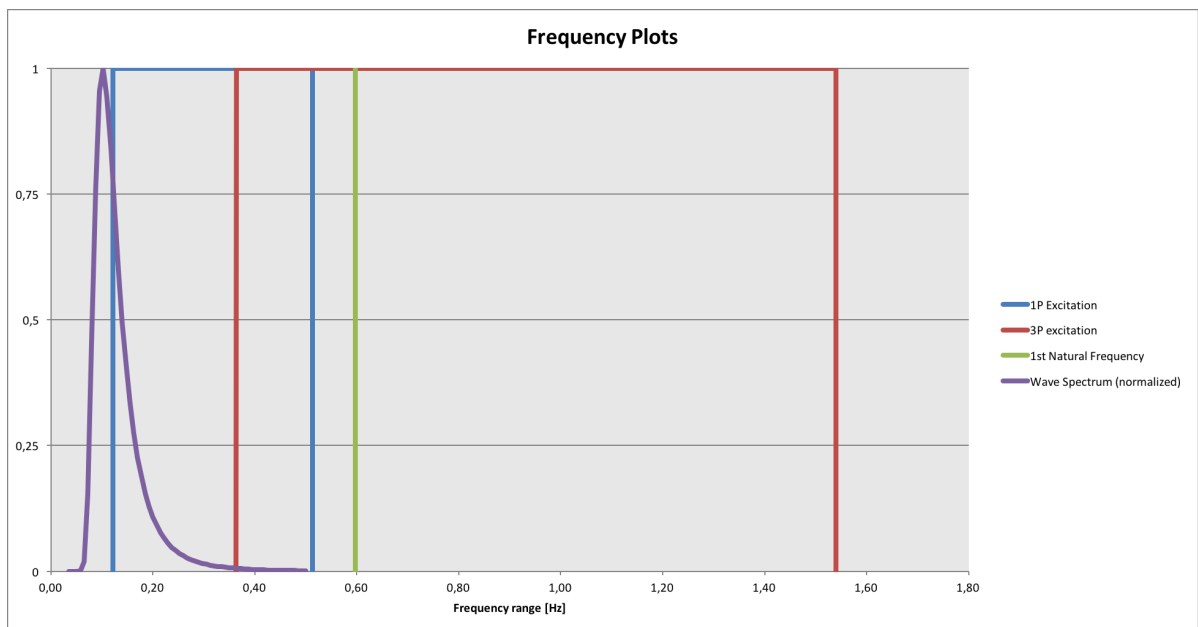


Figure A.15: Frequency spectrum of DOT500 at OWEZ with average diameter of 4.00 m and wall thickness of 0.055 m

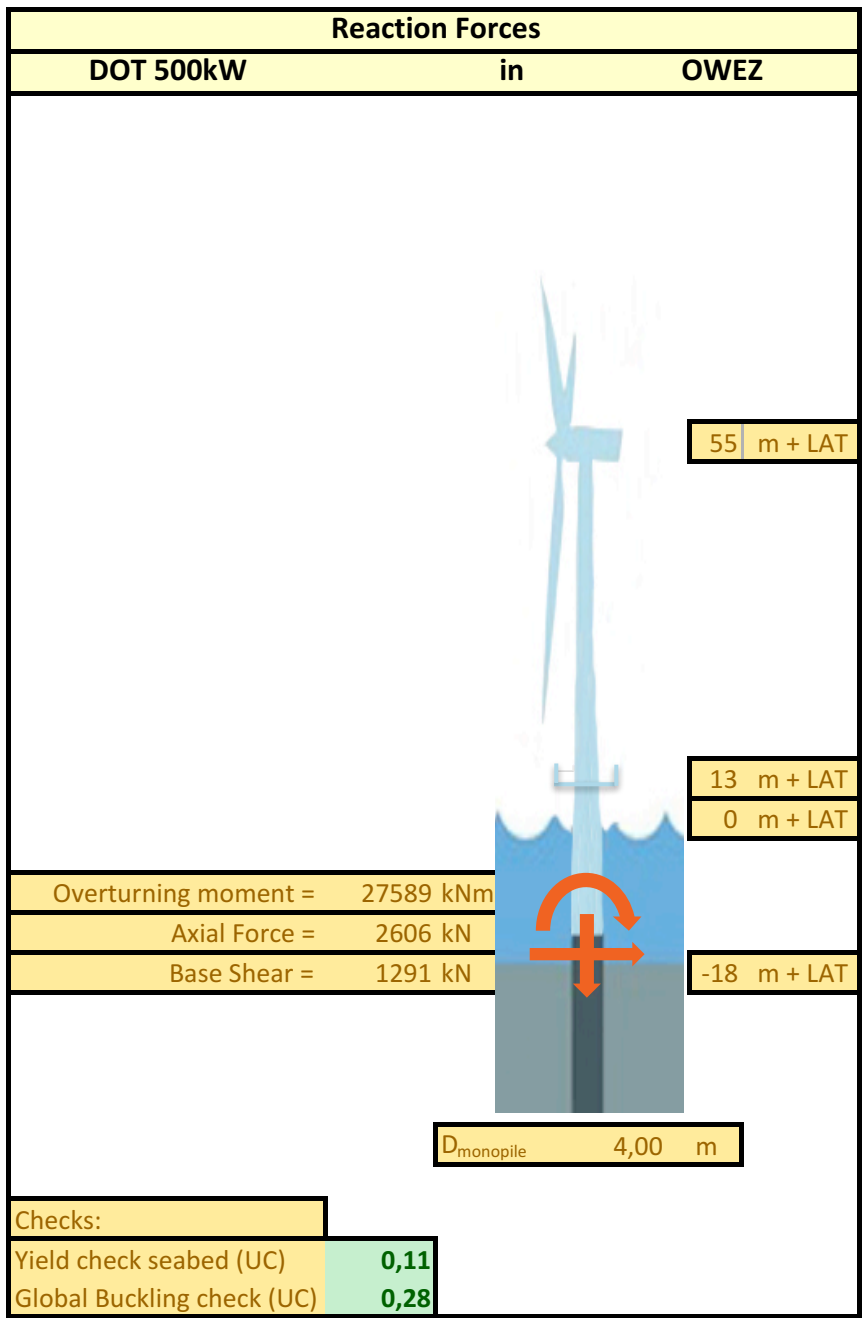


Figure A.16: Load calculation and strength checks for DOT500 offshore turbine

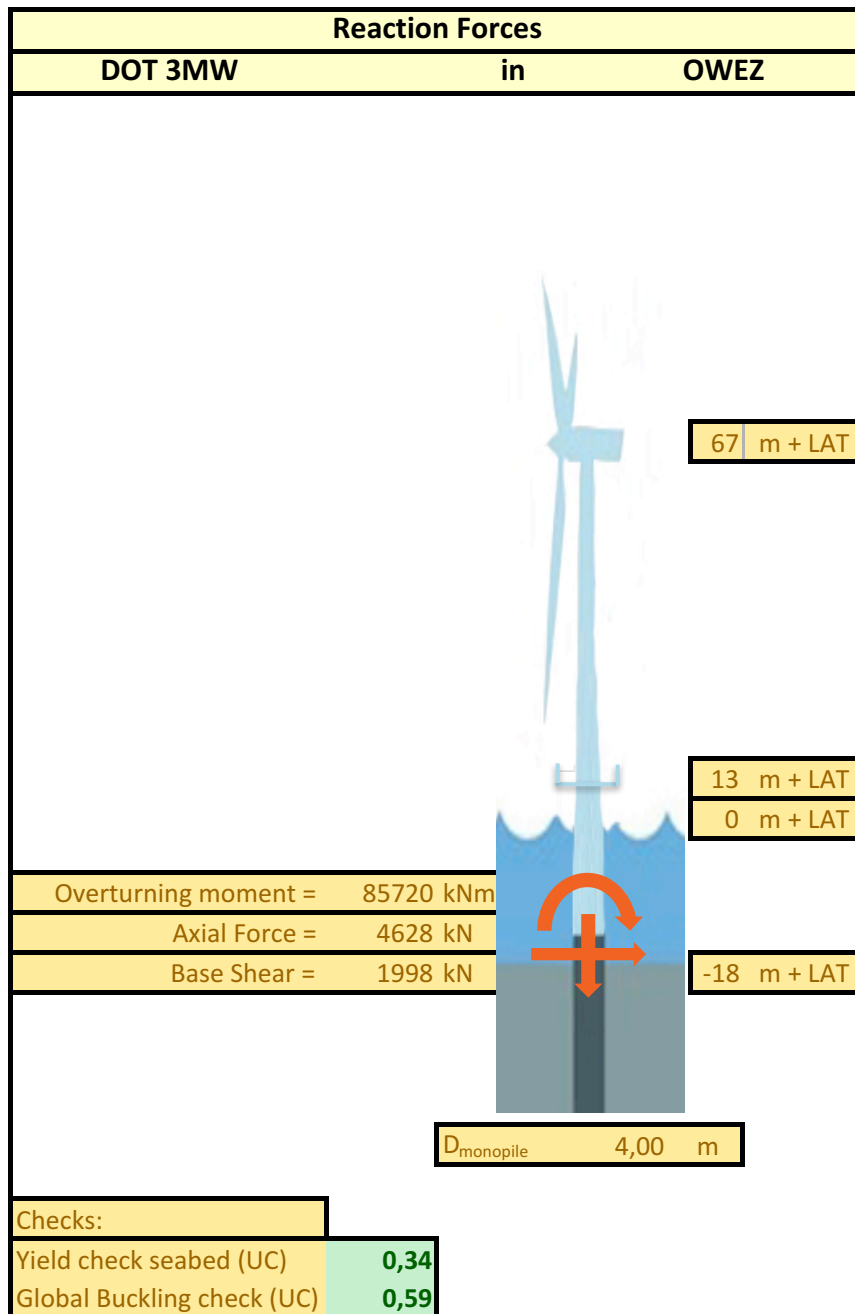


Figure A.17: Load calculation and strength checks for DOT3000 offshore turbine

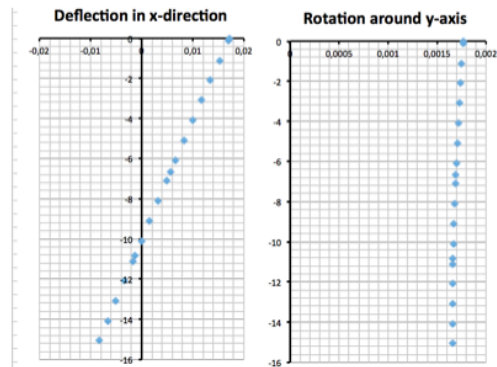
7.1.2 Onshore check

The onshore pile, which will be part 1 of the total monopile, has to be installed on the Maasvlakte II. At this point, little is known of the soil characteristics at this location. Therefore, a weak, loose soil profile is chosen for this matter. This soil profile consists of a uniform layer of loose sand with internal friction angle $\phi = 28^\circ$, submerged unit weight $\gamma = 8500 \text{ N/m}^3$. The penetration depth is chosen as equal to the straight part of the foundation pile part 1. The shortening of the pile is performed with subtracting total pieces of steel of 4,2 meter to ease fabrication processes at Sif.

This concludes that the penetration depth of 15,05 meters is sufficient enough to guarantee a safe design.

Step 1: 15.05 meter penetration depth

Parameter	Value	Criteria	Unit	Check?
u_{seabed}	17,1	120	mm	Yes
ϕ_{seabed}	0,0017	0,0087	rad	Yes
u_{toe}	8,24	20	mm	Yes
Natural frequency	0,967	-	Hz	-



Step 1: 10.85 meter penetration depth

Parameter	Value	Criteria	Unit	Check?
u_{seabed}	44,3	120	mm	Yes
ϕ_{seabed}	0,0061	0,0087	rad	Yes
u_{toe}	21,1	20	mm	No
Natural frequency	0,967	-	Hz	-

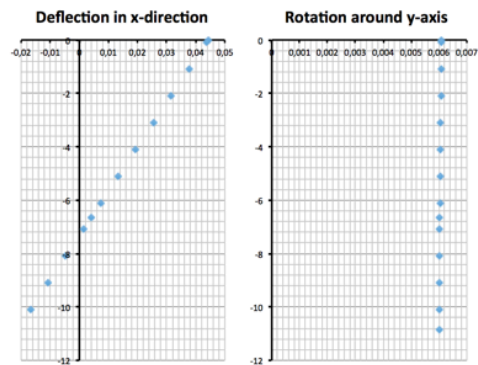


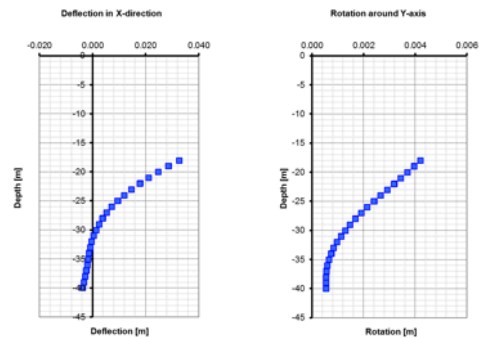
Figure A.18: Penetration depth optimisation for DOT500 onshore

7.1.1 Offshore

In this appendix the optimization process is displayed. The pile is shortened by shortening the original Amalia pile 3 meters every iteration step. In every step, the four design criteria are checked and the change on the natural frequency is assessed.

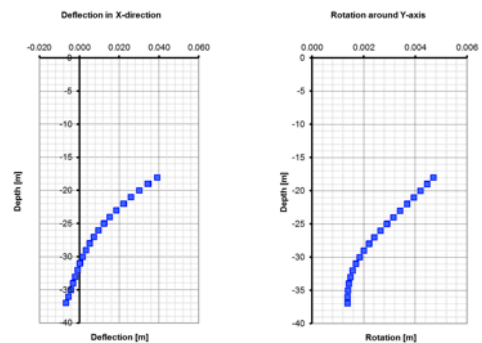
Step 1: 21 meter penetration depth

Parameter	Value	Criteria	Unit	Check?
u_{seabed}	32,6	120	mm	Yes
ϕ_{seabed}	0,0042	0,0087	rad	Yes
u_{toe}	3,80	20	mm	Yes
Natural frequency	0,425	-	Hz	-



Step 2: 18 meter penetration depth

Parameter	Value	Criteria	Unit	Check?
u_{seabed}	38,9	120	mm	Yes
ϕ_{seabed}	0,0047	0,0087	rad	Yes
u_{toe}	6,85	20	mm	Yes
Natural frequency	0,421	-	Hz	-



Step 3: 15 meter penetration depth



Parameter	Value	Criteria	Unit	Check?
u_{seabed}	76,1	120	mm	Yes
ϕ_{seabed}	0,0080	0,0087	rad	Yes
u_{toe}	20,8	20	mm	No
Natural frequency	-	-	Hz	-

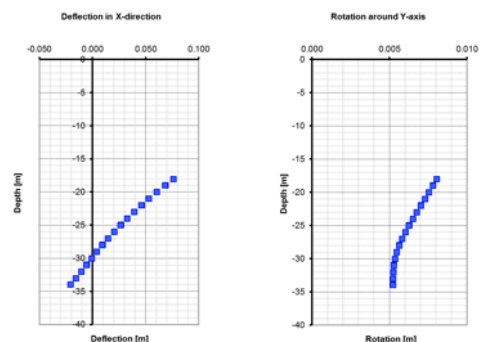


Figure A.19: Penetration depth optimisation for DOT3000 offshore



 Sif		<h2 style="margin: 0;">DIMENSIONAL CONTROL REPORT</h2> <h3 style="margin: 0;">Mono Pile</h3>		
PROJECT :	Demo Mono Pile Foundation	ITEM IDENT. NO. :	MP01	
FABRICATION OF :	Mono Pile	DATE :	23-3-2016	
CONTRACTOR :	Delft Offshore Turbine BV	QC INSPECTOR :	T. Willemsen	
SIF PROJECT NO. :	B2079	PROCEDURE :	DC-600-B2079	
SIF DRAWING NO. :	DRW-B2079- 001	TEMPERATURE :	15 / 20°C	
COMPONENT DIMENSIONS : OD : 3260/4000 mm L: 27233 mm w.t.: 40/60 mm				
DIMENSIONS		MEASUREMENTS		TOLERANCES
Length	Nominal : 27233 mm	Actual : 27.256 +23 mm		+50 /-25 mm
Circumference at ends	Top : 10241 mm	Top : 10244 3 mm		+/- 12 mm
	Bottom : 12566 mm	Bottom : 12565 -1 mm		
Circumference of complete item		Maximum : 4 mm		+/- 12 mm
		Minimum : -5 mm		
Ovality at ends		Top : 7 mm		10 mm
		Bottom : 8 mm		12 mm
Ovality of complete item		Maximum : 8 mm		10/12 mm
Straightness		Maximum : 2 mm		27 mm
TOLERANCES				
Circumference	+/- 12 mm			
Ovality (Dmax-Dmin)	Max. 0,3% of the nominal O.D.			
Out-of-straightness	Max. 0,001*L (L = length of MP)			
Local out-of-roundness	Max. 10% of the nominal wall thickness.			
Misalignment	LW: max. of 2 mm CW: max. of 4 mm			
Longitudinal weld orientation	+/-3°			
All dimensions are within specified tolerances: <input checked="" type="checkbox"/> Yes. <input type="checkbox"/> No, see remarks. All other dimensions are within tolerance.		Remarks:		
FINAL REVIEW / QUALITY CONTROL / SIF GROUP BV  DATE: 23-3-2016		DATE:		

Figure A.20: Dimensions control report SIF monopile

B

Measurement campaign details

B.1. Introduction

In this appendix the details of the sensors can be found. This appendix contains three sections describing the three different types of sensors that were used, including:

- Strain gauges
- Accelerometers
- Position sensors

Both the working principle of the sensor will be explained as well as the details of the sensor such as bandwidth, sensitivity etcetera.

B.2. Sensor details

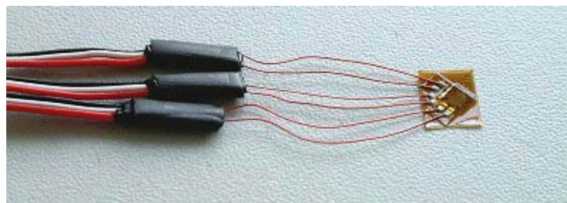
B.2.1. Strain gauges

The specification sheet of the rosette strain gauge that has been used can be found in figure B.1.

DMS-Rosette C2A

DMS-Rosette (0°, 45°, 90°) als Stack mit Anschlusskabel für die Spannungsanalyse.

Anwendung: Spannungsanalyse an Leiterplatten, Schaltschränken.
Messung von Schwingungsamplituden an Bauteilen.



c2a-06-062ww-350; Abmessungen 8,3 x 6,7mm; Grid Länge: 1,57mm; Widerstand: 350 ± 1%; Kabellänge: 3m

c2a-06-125ww-350; Abmessungen 9,5 x 7,8mm; Grid Länge: 3,18mm; Widerstand: 350 ± 1%; Kabellänge: 3m

Figure B.1: Rosette strain gauge specification sheet



Dehnungsmessstreifen DA-FAE4



Die DMS Vollbrücken DA FAE4-A6355J werden mit 5m Anschlusskabel und einer Kabelschelle geliefert, die als Zugentlastung und Installationshilfe dient.

Damit lassen sich mechanische Beanspruchungen besonders auf großflächigen Bauteilen, wie z.B Füße von Silos, Maschinengestelle etc. mit geringem Zeitaufwand im Rahmen der Entwicklungstätigkeit ermitteln. Die Installation erfolgt mit einem geeigneten Cyanacrylat-Klebstoff wie z.B. M-Bond 200. Als Anzeigeeinheit wird vorzugsweise der Messverstärker GSV-2TSD-Di eingesetzt. Bei mehr als 2 Kanälen wird der 8-Kanal Messverstärker GSV-1A8 empfohlen.

Für den dauerhaften Einsatz zur Maschinenüberwachung oder zur Prozessregelung werden Dehnungsaufnehmer oder heißhärtend geklebte Sensoren eingesetzt mit aufwändigem Schutz der Verdrahtung und entsprechendem Schutz gegen Öl und Feuchte.

Installationsanleitung

1. Kabelschelle ankleben, so dass der Dehnungsmessstreifen bezüglich Lage und Richtung ausgerichtet ist. Das verbleibende Kabel zwischen Kabelschelle und Dehnungsmessstreifen dient als Scharniergelenk für den nachfolgenden Klebevorgang.
2. Dehnungsmessstreifen mit Aktivator einstreichen und trocknen lassen.
3. Bauteiloberfläche mit Aktivator einstreichen.
4. Dehnungsmessstreifen mit M-Bond 200 Cyanacrylat benetzen und evtl mit einem Holzstäbchen, Zahnstocher o.ä. verteilen.
5. Dehnungsmessstreifen mit Teflonfolie für mindestens 20 Sekunden auf die Bauteiloberfläche andrücken.
6. Sichtkontrolle: Der Dehnungsmessstreifen muss ganzflächig und ohne Lufteinschlüsse mit der Bauteiloberfläche verbunden sein.
7. Funktionskontrolle: Zwischen den Anschlüssen der Brückenspeisung (rot-schwarz) und zwischen den Anschlüssen des Brückenausgangs (grün-weiß) sind jeweils 350...420 Ohm zu messen.
8. Das Ausgangssignal liegt innerhalb $\pm 1,5\text{mV}$ pro Volt Speisespannung. Durch direktes Andrücken und Scheren der Messgitter z.B. mit einem Radierstift bleibt die Änderung des Ausgangssignals deutlich unter $0,1\text{mV/V}$.

Achtung: Zwischen dem Einstreichen der Bauteiloberfläche mit Aktivator (Schritt 3) und dem Andrücken des Dehnungsmessstreifens (Schritt 5) sollten nur wenige Sekunden vergehen. Alle Materialien sind vorher bereitzulegen, alle Bewegungsabläufe sollten

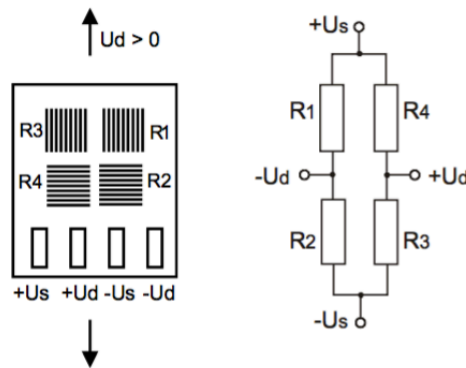
Figure B.2: Full bridge strain gauge specification sheet part 1



vorher eingeübt werden.

Anschlussbelegung

+Us	positive Brückenspeisung	rot
-Us	negative Brückenspeisung	schwarz
+Ud	positiver Brückenausgang	grün
-Ud	negativer Brückenausgang	weiß



Für die Berechnung der Brückenverstimmung U_D/U_S aus dem k-Faktor, der Dehnung ϵ und der Querkontraktionszahl μ gilt in guter Näherung:

Gleichung für die Viertelbrücke	• Faktor	für die Brückenart:
$U_D/U_S = 1/4 \cdot k \cdot \epsilon$	• 4	Vollbrücke
	• 2	Halbbrücke
	• 1	Viertelbrücke
	• $(2+2\mu)$	Vollbrücke, 2 Gitter Längs-, 2 Gitter Querdehnung
	• $(1+1\mu)$	Halbbrücke, 1 Gitter Längs-, 1 Gitter Querdehnung

Mit $\mu=0,3$ und $k=2,0$ ergibt sich für einen Messverstärker mit ± 5 Volt Ausgangsspannung:

Dehnung ϵ	Brückenverstimmung U_D/U_S	Eingangsempfindlichkeit des Messverstärkers	Ausgangssignal des Messverstärkers
$\pm 1538 \mu\text{m/m}$	$\pm 2 \text{ mV/V}$	$\pm 2 \text{ mV/V}$	$\pm 5 \text{ Volt}$
$\pm 769 \mu\text{m/m}$	$\pm 1 \text{ mV/V}$	$\pm 1 \text{ mV/V}$	$\pm 5 \text{ Volt}$

1 $\mu\text{m/m}$ entspricht ca. 0,2 N/mm² bei Stahl mit einem Elastizitätsmodul von 200.000 N/mm²

Figure B.3: Full bridge strain gauge specification sheet part 2

B.2.2. Accelerometers

The specification sheet of the used accelerometers can be found in figure B.4.

LPMS Reference Manual

DEVICE SPECIFICATIONS

V. DEVICE SPECIFICATIONS

Currently a packaged version of the LPMS-CU with plastic casing is available. Please see the below table of the summary of sensor specification. Please refer to the section “X. MECHANICAL INFORMATION” for detail introduction of package layout.

Wired Interface	CAN Bus	USB 2.0
Maximum baudrate	1Mbit/s	921.6Kbit/s
Communication protocol	LpCAN	LpBUS
Size	37 x 28 x 17 mm	
Weight	12.8 g	
Orientation	360° about all axes	
Resolution	< 0.05°	
Accuracy	< 2° RMS (dynamic), < 0.5°(static)	
Accelerometer	3-axis, ±20 / ±40 / ±80 / ±160 m/s ² , 16 bits	
Gyroscope	3-axis, ±250 / ±500 / ±2000 °/s, 16 bits	
Magnetometer	3-axis, ±130 ~ ±810 uT, 16 bits	
Pressure sensor	300 ~ 1100 hPa *	
Data output format	Raw data / Euler angle / Quaternion	
Sampling rate	0 ~ 500 Hz.	
Power consumption	165 mW	
Supply voltage (Vcc)	2.5 ~ 18 V DC	
Connector	Micro USB, type B	
Casing material	Polystyrol Plastic	
Temperature range	- 40 ~ +80 °C	
Software	C++ library for Windows, Java library for Android, LpmsControl utility software for Windows, Open Motion Analysis Toolkit (OpenMAT) for Windows	

* The pressure sensor is optional and can be added on LPMS-CU, which depends on the requirement from users. Please contact us for more information about this.

Figure B.4: Accelerometer specification sheet

B.2.3. Position sensors

The specification sheet of the used position sensors can be found in figure B.5.

SMART Position Sensor, 35 mm, 75 mm and 225 mm Linear Configurations

ISSUE 4
50046793

Table 1. Specifications

Characteristic	Component	Parameter				
		35 mm analog (SPS-L035-LATS)	75 mm analog (SPS-L075-HALS)	225 mm		
				analog (SPS-L075-HALS)	digital (SPS-L225-HDLS)	
Sensing range	sensor only	0 mm to 35 mm [0 in to 1.38 in]	0 mm to 75 mm [0 in to 32.95 in]	0 mm to 225 mm [0 in to 8.86 in]		
Resolution		0.04 mm [0.0016 in]	0,05 mm [0.002 in]	0,14 mm [0.0055 in]	0,0035 mm [0.000137 in]	
Supply voltage		4.75 Vdc to 5.25 Vdc		6 Vdc to 24 Vdc		
Output		0.55 Vdc to 4.15 Vdc		0 Vdc to 5 Vdc		RS 232-type digital
Supply current		20 mA max.		32 mA max.	34 mA max.	88 mA max.
Linearity ¹		±1.0% full scale output		±0.4% full scale output		
Reverse polarity		-5 V		26.4 V at 125 °C [257 °F]		
Sensitivity		103 mV/mm typ.		50 mV/mm typ.	17.78 mV/mm typ.	282.16 counts/mm typ.
Update rate		476 µs		400 µs		3200 µs
Baud rate				-		576 kbits/s
Initial startup time		5 ms		30 ms		
Termination		TYCO Super Seal 282087-1 integral connector		flying leads		
Cable bend radius		-		40 mm [1.6 in] min.		
Operating temperature		-40 °C to 125 °C [-40 °F to 257 °F]				
Storage temperature		-40 °C to 150 °C [-40 °F to 302 °F]				
Air gap		8,5 ±1,0 mm [0.334 ±0.039 in]		3,0 ±2,5 mm [0.118 ±0.098 in]		
Sealing	IP67, IP69K					
Radiated immunity	100 V/m per ISO 11452-2		-			
Conducted immunity	100 mA BCI per ISO 11452-4		-			
Shock	50 G half sine wave with 11 ms duration					
Vibration	20 G from 10 Hz to 2000 Hz		10 G from 10 Hz to 2000 Hz			
Housing material	thermoplastic					
Approvals	CE					
Mounting: screws recommended torque	¼-20 or M6 6 N m to 10 N m [53.1 in lb to 88.5 in lb]					
Material	magnet ac- tuator only	neodymium iron boron				
Strength		13,500 Gauss	10,000 Gauss			

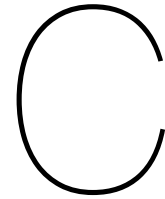
Note:

1. Percent linearity is the quotient of the measured output deviation from the best fit line at the measured temperature to the full scale output span.

NOTICE

- Ferrous metal within a 100 mm [3.9 in] radius of the magnet actuator may affect sensor performance.
- Always use fresh, non-magnetic stainless steel washers when mounting the sensor.

Figure B.5: Position sensor specification sheet



Model details

C.1. Introduction

C.2. Natural Frequency

This section shows the details of the model that was used to estimate the first natural frequency of the first bending mode of the wind turbine structure.

C.2.1. Model input

The first input is the overview of soil layers at the location where the monopile is to be modelled, shown in figure C.1. As an example the soil parameters at the DOT500 project are used.

General Input	
Diameter Pile	4,00
Pile toe	-15,048

		Soil Data input									
Layer start [ref - m]	Layer end [ref - m]	above / below water	Soil Type	Phi [deg]	Gamma [N/m3]	plim [Pa]	k [N/m3]	cu [Pa]	e50 [%]		
0,1	2	above	sand	33	9500		17200000				
2	3	above	sand	31	8500		17200000				
3	5	above	sand	33	9500		17200000				
5	7	above	sand	33	9500		17200000				
7	9	above	sand	31	8500		17200000				
9	11	above	sand	31	8500		17200000				
11	12	above	sand	31	9000		17200000				
12	14	above	sand	33	9500		17200000				
14	15,048	above	sand	31	8000		17200000				
15,048							#N/B				
0							#N/B				
0							#N/B				
0							#N/B				
0							#N/B				
0							#N/B				
0							#N/B				
0							#N/B				
0							#N/B				
0							#N/B				
0							#N/B				
0							#N/B				

Figure C.1: Input sheet soil interaction model - soil parameters as function of depth (brown is input, yellow is calculated)

The second input sheet concerns the structural data of the monopile and possible load case if deflection curves need to be calculated, shown in figure C.2.

Monopile data		Member data				Load information		
Node	depth [m]	Lines	Connects	Section depth [m]	Diameter [cm]	wall thicknes [cm]	Base shear [kN]	Overturning Moment [kNm]
1	0,1	1	1 and 2	0	-	-	300	3000
2	0	2	2 and 3	-1	400,00			
3	-1	3	3 and 4	-2	400,00			
4	-2	4	4 and 5	-2,5	400,00			
5	-2,5	5	5 and 6	-3	400,00			
6	-3	6	6 and 7	-4	400,00			
7	-4	7	7 and 8	-5	400,00			
8	-5	8	8 and 9	-6	400,00			
9	-6	9	9 and 10	-7	400,00			
10	-7	10	10 and 11	-8	400,00			
11	-8	11	11 and 12	-9	400,00			
12	-9	12	12 and 13	-10	400,00			
13	-10	13	13 and 14	-11	400,00			
14	-11	14	14 and 15	-11,5	400,00			
15	-11,5	15	15 and 16	-12	400,00			
16	-12	16	16 and 17	-13	400,00			
17	-13	17	17 and 18	-14	400,00			
18	-14	18	18 and 19	-14,524	400,00			
19	-14,524	19	19 and 20	-15,048	400,00			
20	-15,048							

Figure C.2: Input sheet soil interaction model - dimensions monopile (brown is input, yellow is calculated)

C.2.2. Model output

Bladed Output

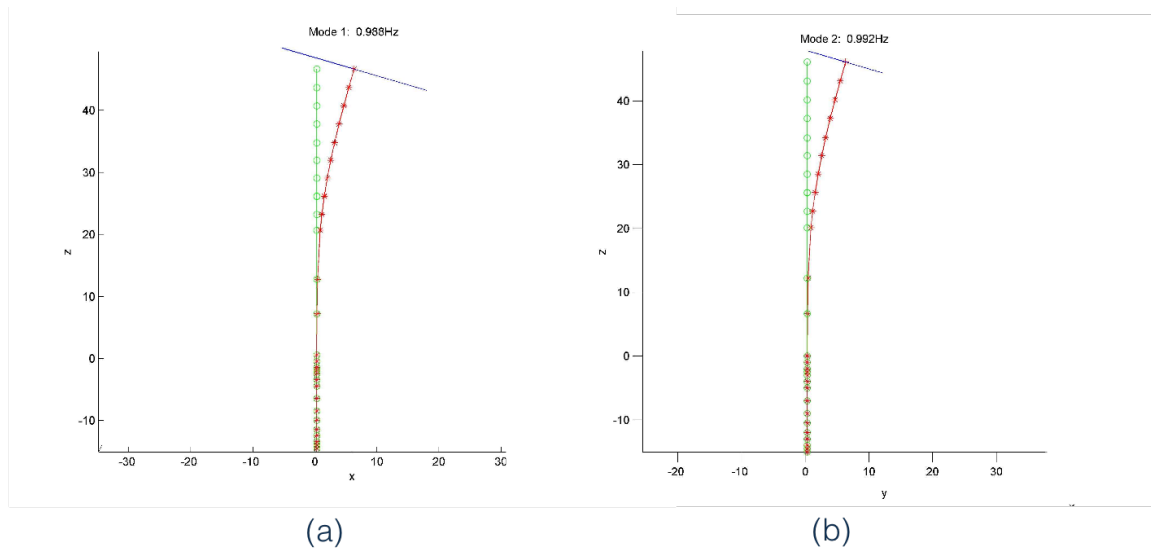


Figure C.3: Output Bladed natural frequency calculation with clamped foundation fore-aft (a) and side-side (b) direction

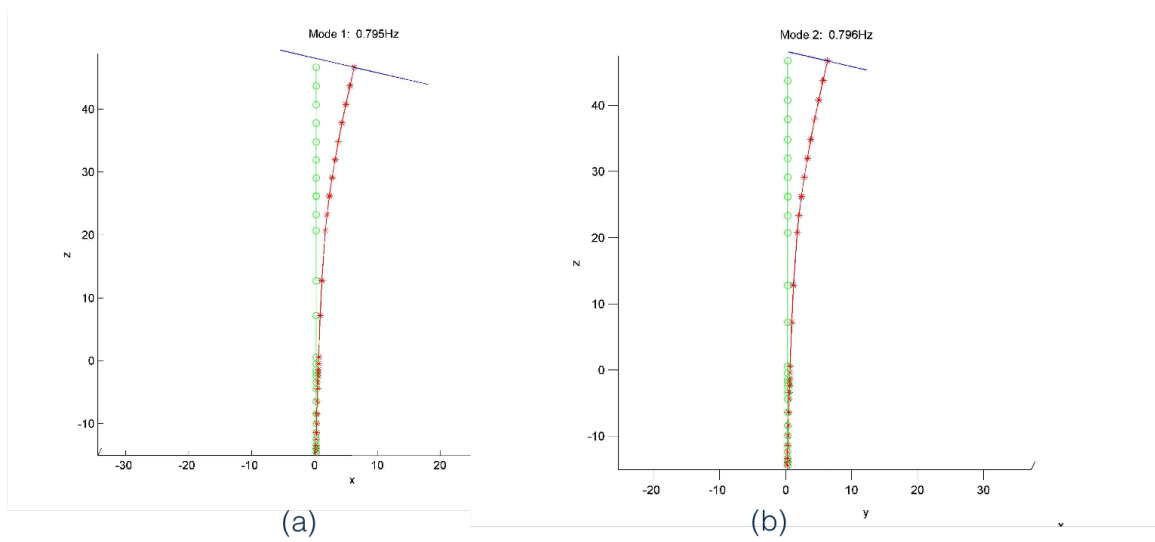
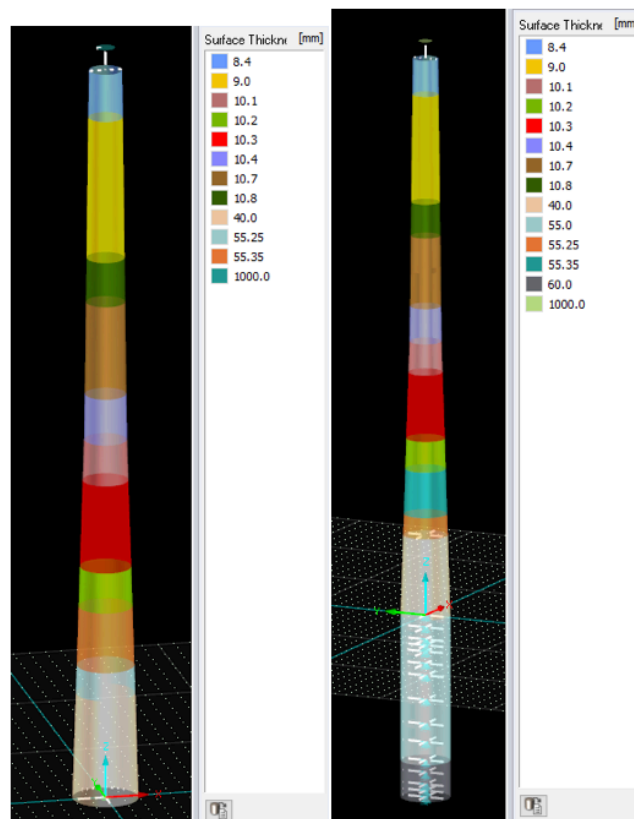


Figure C.4: Output Bladed natural frequency calculation with spring-foundation fore-aft and side-side direction

RFEM Output



■ 5.1 NATURAL FREQUENCIES CLAMPED NVC1

Mode No.	Eigenvalue λ [$1/s^2$]	Angular frequency ω [rad/s]	Natural Frequency f [Hz]	Natural Period T [s]
1	38.120	6.174	0.983	1.018
2	38.123	6.174	0.983	1.018
3	1416.524	37.637	5.990	0.167
4	1416.583	37.638	5.990	0.167

■ 5.1 NATURAL FREQUENCIES SPRING-FOUNDED NVC1

Mode No.	Eigenvalue λ [$1/s^2$]	Angular frequency ω [rad/s]	Natural Frequency f [Hz]	Natural Period T [s]
1	26.770	5.174	0.823	1.214
2	37.447	6.119	0.974	1.027
3	481.472	21.942	3.492	0.286
4	1501.967	38.755	6.168	0.162

Figure C.5: Output RFEM natural frequency calculation with clamped and spring-foundation (no difference in direction)

C.3. Slip-joint settlement

This section shows the details of the model that was used to estimate the target overlap and settlement of the slip-joint connection.

C.3.1. Model input

The input in the model consist of the dimensions of the two cones, friction coefficient and the total vertical downward force i.e., the self-weight of the structure.

Tower dimensions			Monopile dimensions			
z [m]	Inner diameter [m]	Wall thickness (measured) [m]	z [m]	z' [m]	Outer diameter [m]	Wall thickness (drawing) [m]
0	3,578	0,016	12,185	0,000	3,261	0,040
0,515	3,548	0,016	11,671	0,515	3,292	0,040
1,081	3,513	0,016	11,105	1,081	3,326	0,040
1,556	3,485	0,016	10,629	1,556	3,355	0,040
2,071	3,454	0,016	10,115	2,071	3,386	0,040
2,500	3,426	0,016	9,686	2,500	3,412	0,040
3,009	3,396	0,016	9,176	3,009	3,443	0,040
3,511	3,367	0,016	8,674	3,511	3,474	0,040
3,994	3,338	0,016	8,191	3,994	3,503	0,040
4,518	3,304	0,016	7,668	4,518	3,535	0,040
5,033	3,273	0,016	7,152	5,033	3,566	0,040
5,453	3,250	0,016	6,732	5,453	3,592	0,040
5,519	3,246	0,010	6,667	5,519	3,596	0,040
6,094	3,213	0,010	6,091	6,094	3,631	0,040

Target settlement [m]	5,232
Friction Coefficient [-]	0,2
Total downward force	574,79
Total vertical force	613,43

Figure C.6: Input scheme of target penetration model

C.3.2. Model output

The model shows the total build-up friction force from which the target overlap length can be determined. Furthermore, the accompanying stresses as a result of this settlement are shown.

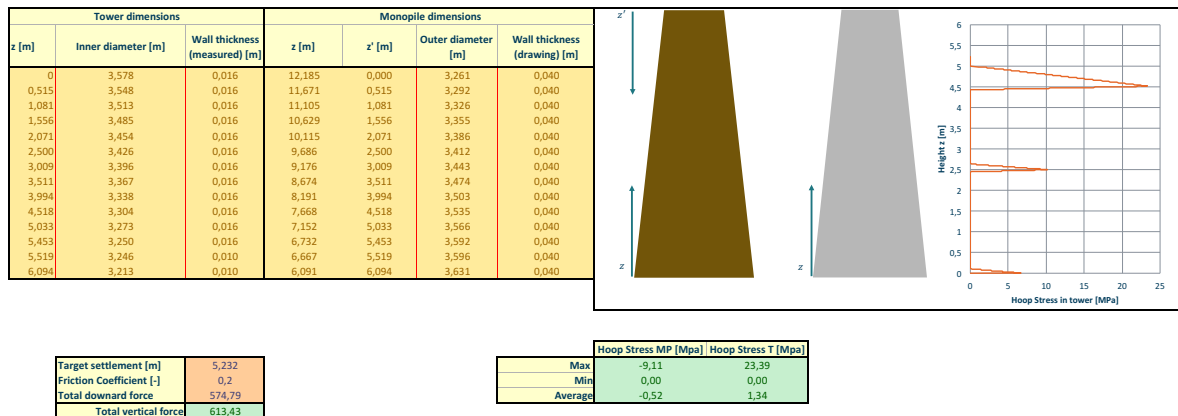


Figure C.7: Output of the model: target overlap length and accompanying hoop stresses

C.4. Local stress distribution

The outcome of the FEM's to find the local stress distributions as a result of non-uniformly applied pressure can be found in figure C.8 through C.10. Furthermore, the deformations and stresses from the oval lower tower with uniformly applied pressure can be found in figure C.11.

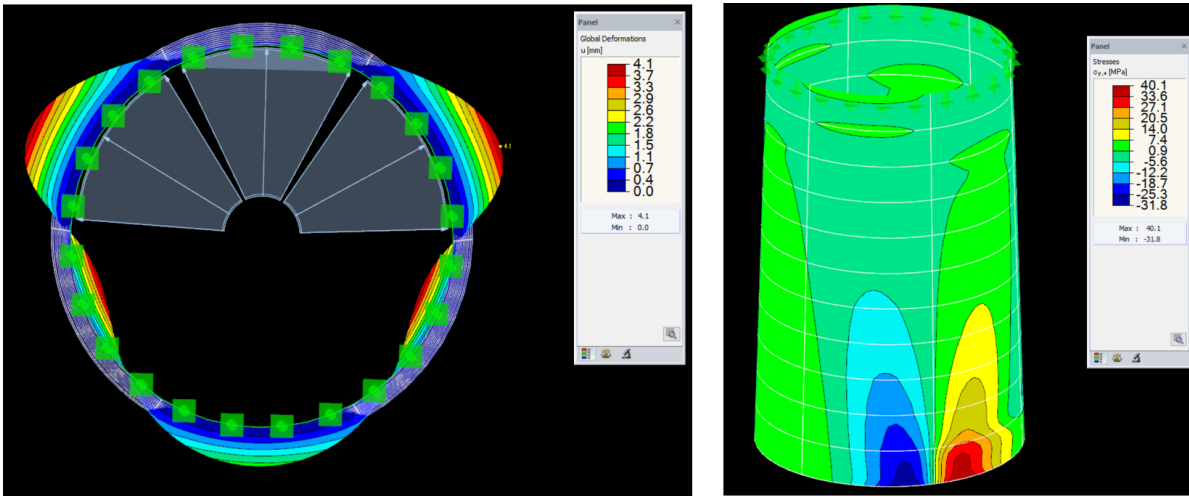


Figure C.8: Deformations (left) and accompanying stresses as result of load case 1 in RFEM

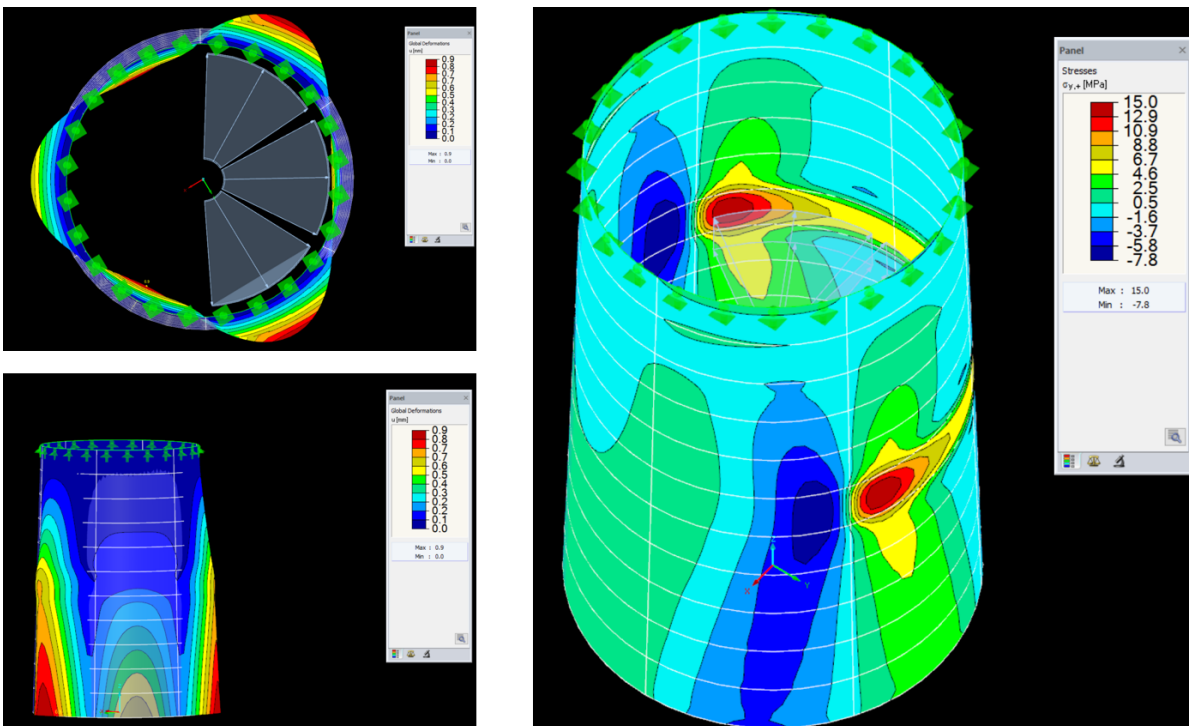


Figure C.9: Deformations (left) and accompanying stresses (right) as result of load case 2 in RFEM

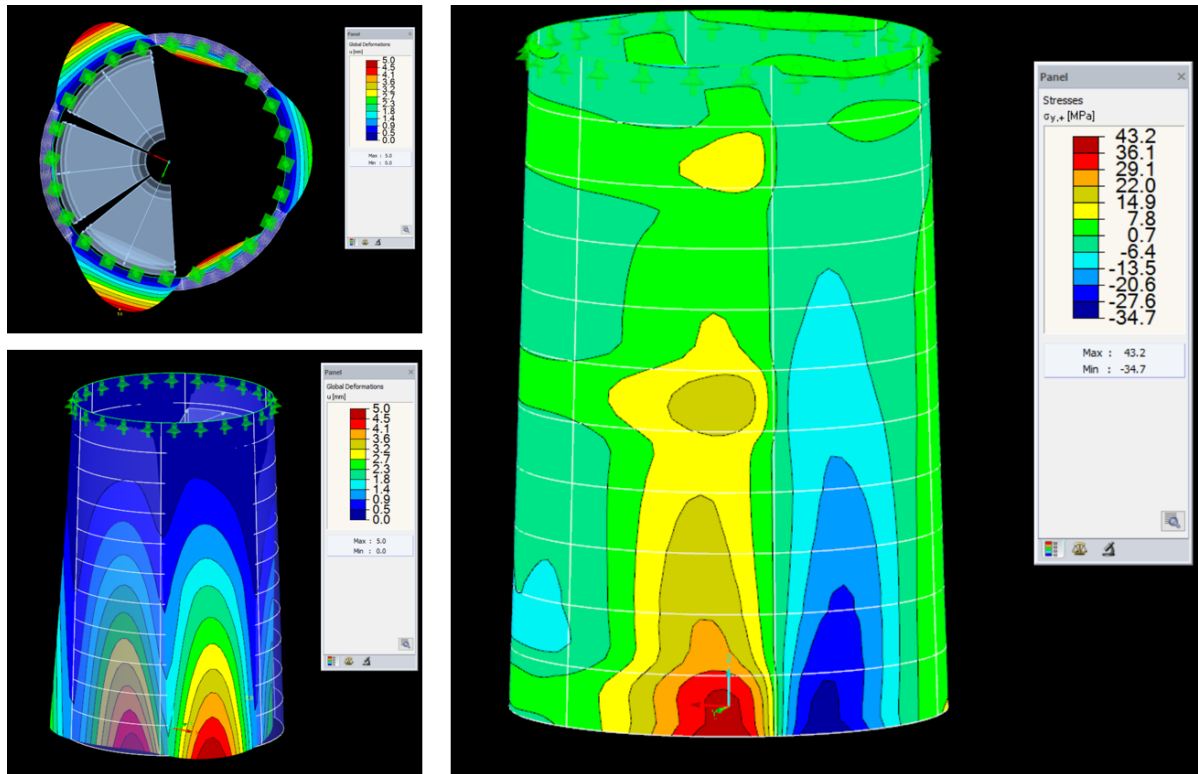


Figure C.10: Deformations (left) and accompanying stresses (right) as result of load case 3 in RFEM

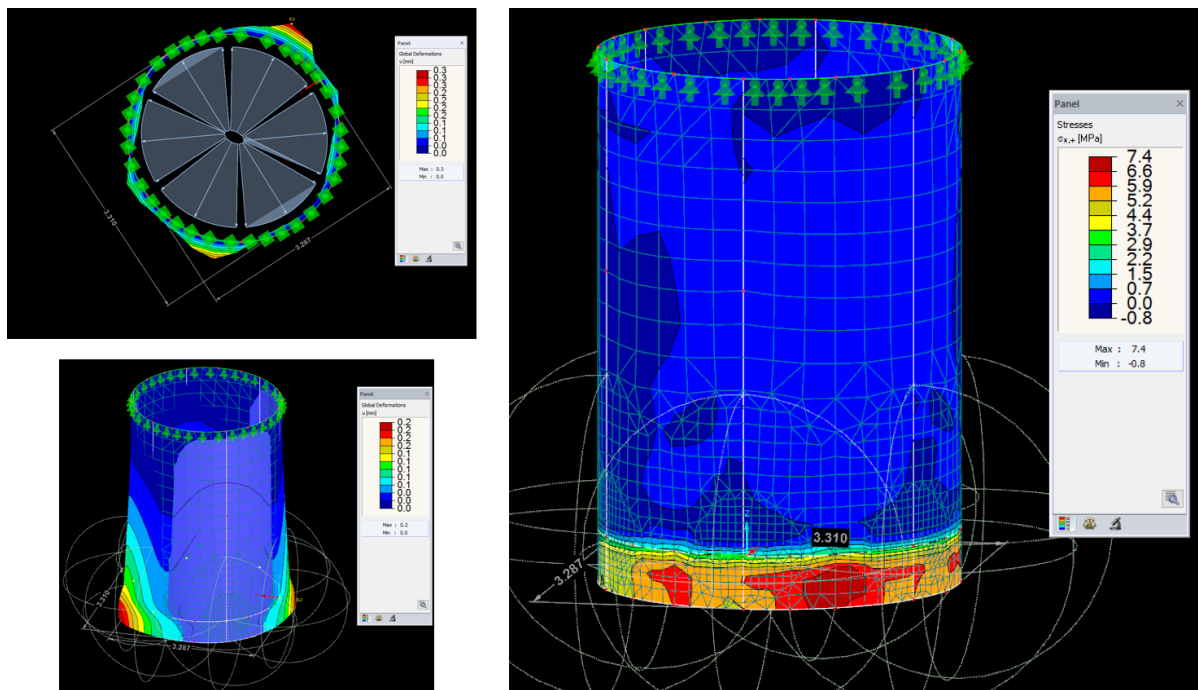
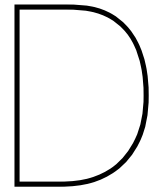


Figure C.11: Deformations (left) and accompanying stresses (right) as result of oval tower case



Post processing tool details

D.1. Introduction

In this appendix the theory behind the post processing strategies taken in the report shall be presented. First of all the decompression tool of the raw data is treated in section D.2. Secondly, section ?? presents the post processing theory and tools related to the measurement of the different elements including the natural frequency, slip-joint settlement and stresses within the slip-joint.

D.2. Decompression and decoding tool

The data that was logged by the data logger is compressed in order to save data storage space on the storage device, a SD-card. The compression has been done by means of hexadecimal characters. An example of a couple of log lines can be found in figure D.1.

```
H 8dmQ >}&T* ,; 7!  
B 8dmR )E @w )D ?S  
K 8dmR +- -n&@R 00  
D 8dmU /J 2F&MÄ 2Ç  
M 8dmW R&A0 0&&Ft  
G 8dmX&4*&G'&Fg&FS
```

Figure D.1: Example of a couple of log lines directly obtained from the data logger

In such a log line, the first character represents the tag of the A/D-converter that has sent the signal. The following four characters represent the time stamp of the measured data line. Every next set of three characters represent the sensor output values in unsigned format of channels one through four of the A/D-converter. This processing is done by means of a MATLAB script. The main function file is presented in figure D.2. Within this function file three other functions are nested that (i) decompress the values from hexadecimal to actual values (ii) order these values of the different sensors in different arrays with corresponding sensor names (iii) process the output values in mV to the required values required for processing. This scripts are displayed in figures D.4 through D.6.

```
function [ S ] = f_main(ID,txt,C_time)  
%Data processing file %%%%%  
%Thijs Kamphuis  
%26-05-2016  
  
% Call decompressing file  
%Acquiring the data matrix  
[decompressed]=f_decompress(ID,txt);  
  
% Call sensor ordering function  
%The decompressed matrix will be ordered to get arrays per sensor.  
[SENSORS]=f_order_per_sensor(decompressed);  
  
% Call processor function  
%The sensor arrays will be processed to give their actual values rather  
%than values in millivolts. The function calls for different conversion  
%factors and offsets in the beginning of the script. Enter these values in  
%the function file.  
[S,SENSORS] = f_processor( SENSORS,C_time );  
end
```

Figure D.2: Main function file decompression and decoding tool

```

function [AA] = f_decompress (ID,txt)
%% Preperatory
%Choose Directory: 1= separate text, 2=Merged text files

if txt == 1;
x_directory='/Users/Thijsk/Documents/2. Educatie/3. Master Offshore/2e jaar/1. Afstuderen/06 Measurements/1. Data/2. Processed
data/1. Processed text files'; %Directory where raw data is placed
else
x_directory='/Users/Thijsk/Documents/2. Educatie/3. Master Offshore/2e jaar/1. Afstuderen/06 Measurements/1. Data/2. Processed
data/1.1 Merged text files'; %Directory where raw data is placed
end

files=dir([x_directory]); %Provides all files that are present in this folder
filenames={files.name}; %Stores all names of the files present in the folder

name_file=fullfile(x_directory,filenames{ID}); %Choose which file you want to load. Later -> make loop

%% Opening
fileID=fopen(name_file); %Create file ID
A=textscan(fileID,'%18c'); %Read 18 characters per line and store n matrix A
code=A{1}; %Extract matrix with every column a character

unit_nummer_c=code(:,1); %Store unit number in character style
deel_tijd_c=code(:,2:6); %Store time in character style
waarde1_c=code(:,7:9); %Store value of sensor 1 in character style
waarde2_c=code(:,10:12); %Store value of sensor 2 in character style
waarde3_c=code(:,13:15); %Store value of sensor 3 in character style
waarde4_c=code(:,16:18); %Store value of sensor 4 in character style

%% Decompressing and decoding
%Convert all character arrays into number arrays. The result is 10 arrays
%with the different values of the time and the 4 sensor values in signed
%and unsigned manner
deel_tijd=( double((deel_tijd_c(:,1))-32)*100000000) + (double((deel_tijd_c(:,2))-32)*1000000) + (double((deel_tijd_c(:,3))-32)
*10000) + (double((deel_tijd_c(:,4))-32)*100) + (double((deel_tijd_c(:,5))-32)) );

%Unsigned values
waarde1_unsigned=( double((waarde1_c(:,1))-32)*10000) + (double((waarde1_c(:,2))-32)*100) + (double((waarde1_c(:,3))-32)) );
waarde2_unsigned=( double((waarde2_c(:,1))-32)*10000) + (double((waarde2_c(:,2))-32)*100) + (double((waarde2_c(:,3))-32)) );
waarde3_unsigned=( double((waarde3_c(:,1))-32)*10000) + (double((waarde3_c(:,2))-32)*100) + (double((waarde3_c(:,3))-32)) );
waarde4_unsigned=( double((waarde4_c(:,1))-32)*10000) + (double((waarde4_c(:,2))-32)*100) + (double((waarde4_c(:,3))-32)) );

%Signed values
waarde1_signed=zeros(length(waarde1_unsigned),1);
for i=1:length(waarde1_unsigned)
if waarde1_unsigned(i) > (65536/2)
waarde1_signed(i)=waarde1_unsigned(i)-65536;
else waarde1_signed(i)=waarde1_unsigned(i);
end
end

waarde2_signed=zeros(length(waarde2_unsigned),1);
for i=1:length(waarde2_unsigned)
if waarde2_unsigned(i) > (65536/2)
waarde2_signed(i)=waarde2_unsigned(i)-65536;
else waarde2_signed(i)=waarde2_unsigned(i);
end
end

waarde3_signed=zeros(length(waarde3_unsigned),1);
for i=1:length(waarde3_unsigned)
if waarde3_unsigned(i) > (65536/2)
waarde3_signed(i)=waarde3_unsigned(i)-65536;
else waarde3_signed(i)=waarde3_unsigned(i);
end
end

waarde4_signed=zeros(length(waarde4_unsigned),1);
for i=1:length(waarde4_unsigned)
if waarde4_unsigned(i) > (65536/2)
waarde4_signed(i)=waarde4_unsigned(i)-65536;
else waarde4_signed(i)=waarde4_unsigned(i);
end
end

%%Creating matrix with all data in 1
AA=zeros(length(deel_tijd),10); %Create empty matrix

%Fill matrix with the values
AA(:,1)=unit_nummer_c; %First column = converter letter (in number format)
AA(:,2)=deel_tijd; %Second column = logging time in [ms]
AA(:,3)=waarde1_unsigned; %Third column = values sensor channel 1 (unsigned)
AA(:,4)=waarde2_unsigned; %Fourth column = values sensor channel 2 (unsigned)
AA(:,5)=waarde3_unsigned; %Fifth column = values sensor channel 3 (unsigned)
AA(:,6)=waarde4_unsigned; %Sixth column = values sensor channel 4 (unsigned)
AA(:,7)=waarde1_signed; %Seventh column = values sensor channel 1 (signed)
AA(:,8)=waarde2_signed; %Eighth column = values sensor channel 2 (signed)
AA(:,9)=waarde3_signed; %Ninth column = values sensor channel 3 (signed)
AA(:,10)=waarde4_signed; %Tenth column = values sensor channel 4 (signed)
end

```

Figure D.3: Script that decompresses the data to actual numeric values


```

function [ SENSORS ] = f_order_per_sensor( decompressed )

%Explanation goes here

AA=decompressed;

%% Order the strain gauges. See master slip-joint excel for explanation of the sensors codes
%Sensor NF1: strain gauge; values in [mV]
SENSORS.NF1_mV=zeros(length(AA),3);
for k=1:length(AA);
    if AA(k,1) == double('M');
        SENSORS.NF1_mV(k,1)=AA(k,2);           %First column presents the time in ms since start logging
        SENSORS.NF1_mV(k,2)=AA(k,3);           %Second column presents the unsigned value of the sensor
        SENSORS.NF1_mV(k,3)=AA(k,7);           %Third column presents the signed value of the sensor
    end
end
SENSORS.NF1_mV( all(~SENSORS.NF1_mV,2), : ) = []; %Delete all zero rows from the file to get clean array

%Sensor A_hor1: strain gauge; values in [mV]
SENSORS.A_hor1_mV=zeros(length(AA),3);
for k=1:length(AA);
    if AA(k,1) == double('F');
        SENSORS.A_hor1_mV(k,1)=AA(k,2);           %First column presents the time in ms since start logging
        SENSORS.A_hor1_mV(k,2)=AA(k,4);           %Second column presents the unsigned value of the sensor
        SENSORS.A_hor1_mV(k,3)=AA(k,8);           %Third column presents the signed value of the sensor
    end
end
SENSORS.A_hor1_mV( all(~SENSORS.A_hor1_mV,2), : ) = []; %Delete all zero rows from the file to get clean array

%Sensor A_sch1: strain gauge; values in [mV]
SENSORS.A_sch1_mV=zeros(length(AA),3);
for k=1:length(AA);
    if AA(k,1) == double('F');
        SENSORS.A_sch1_mV(k,1)=AA(k,2);           %First column presents the time in ms since start logging
        SENSORS.A_sch1_mV(k,2)=AA(k,5);           %Second column presents the unsigned value of the sensor
        SENSORS.A_sch1_mV(k,3)=AA(k,9);           %Third column presents the signed value of the sensor
    end
end
SENSORS.A_sch1_mV( all(~SENSORS.A_sch1_mV,2), : ) = []; %Delete all zero rows from the file to get clean array

%Sensor A_vert1: strain gauge; values in [mV]
SENSORS.A_vert1_mV=zeros(length(AA),3);
for k=1:length(AA);
    if AA(k,1) == double('F');
        SENSORS.A_vert1_mV(k,1)=AA(k,2);           %First column presents the time in ms since start logging
        SENSORS.A_vert1_mV(k,2)=AA(k,6);           %Second column presents the unsigned value of the sensor
        SENSORS.A_vert1_mV(k,3)=AA(k,10);          %Third column presents the signed value of the sensor
    end
end
SENSORS.A_vert1_mV( all(~SENSORS.A_vert1_mV,2), : ) = []; %Delete all zero rows from the file to get clean array

%Sensor D1: strain gauge; values in [mV]
SENSORS.D1_mV=zeros(length(AA),3);
for k=1:length(AA);
    if AA(k,1) == double('D');
        SENSORS.D1_mV(k,1)=AA(k,2);           %First column presents the time in ms since start logging
        SENSORS.D1_mV(k,2)=AA(k,5);           %Second column presents the unsigned value of the sensor
        SENSORS.D1_mV(k,3)=AA(k,9);           %Third column presents the signed value of the sensor
    end
end
SENSORS.D1_mV( all(~SENSORS.D1_mV,2), : ) = []; %Delete all zero rows from the file to get clean array

%Sensor G1: strain gauge; values in [mV]
SENSORS.G1_mV=zeros(length(AA),3);
for k=1:length(AA);
    if AA(k,1) == double('F');
        SENSORS.G1_mV(k,1)=AA(k,2);           %First column presents the time in ms since start logging
        SENSORS.G1_mV(k,2)=AA(k,3);           %Second column presents the unsigned value of the sensor
        SENSORS.G1_mV(k,3)=AA(k,7);           %Third column presents the signed value of the sensor
    end
end
SENSORS.G1_mV( all(~SENSORS.G1_mV,2), : ) = []; %Delete all zero rows from the file to get clean array

%Sensor A_hor2: strain gauge; values in [mV]
SENSORS.A_hor2_mV=zeros(length(AA),3);
for k=1:length(AA);
    if AA(k,1) == double('E');
        SENSORS.A_hor2_mV(k,1)=AA(k,2);           %First column presents the time in ms since start logging
        SENSORS.A_hor2_mV(k,2)=AA(k,4);           %Second column presents the unsigned value of the sensor
        SENSORS.A_hor2_mV(k,3)=AA(k,8);           %Third column presents the signed value of the sensor
    end
end
SENSORS.A_hor2_mV( all(~SENSORS.A_hor2_mV,2), : ) = []; %Delete all zero rows from the file to get clean array

```

Figure D.4: First part of the ordering script. The rest is the same for all sensors

```

function [ S,SENSORS ] = f_processor( SENSORS,C_time )
%This Matlab function processes the values of the sensors in mV's to their
%actual output. This is done by means of the conversion factor specified in
%the MSc Thesis report.

%% Specify conversion factors:
%These are the conversion factor for the different sensors. They can be
%found and verified in the MSc Thesis report.

%Strain gauges conversion factor from mV's to Stresses [MPa]
C_sg_T=0.10063; %Conversion factor for the temperature Strain Gauge (half bridge) [MPa]
C_sg_fb=0.039687; %Conversion factor for the Full Bridge single direction Strain Gauge [MPa]
C_sg_r=0.050293; %Conversion factor for the Rosette Strain Gauge (full bridge) [MPa]

%Position sensors conversion factors from mV's to displacement [mm]
C_pos_MP=0.05625; %Conversion factor for the monopile settlement position sensor [mm]
C_pos=0.02; %Conversion factor for the rest of the position sensors [mm]

%Acceleration sensors conversion factors from digital signal to
%accelerations [m/s^2]
C_acc_r=0.001; %Conversion factor for the raw acceleration signal [m/s^2]
C_acc_l=0.000102; %Conversion factor for the linear acceleration signal [m/s^2]
C_ang=0.0572957795; %Conversion factor for the Eulerian angle signals [deg]
C_gyr=1; %Conversion factor for the gyroscopic signals [..]
C_q=1; %Conversion factor for quaternion [..]

%% Specify offsets
%These are the offsets that determine the sensors final zero-point value of
%the sensor. The origin of these values are explained in the MSc thesis
%report.

%Strain gauge offsets
O_NF1=0; %Offset sensor NF1 [MPa]
O_A_hor1=0; %Offset sensor A_hor1 [MPa]
O_A_sch1=0; %etc. [MPa]
O_A_vert1=0;
O_D1=0;
O_G1=0;
O_A_hor2=0;
O_A_sch2=0;
O_A_vert2=0;
O_D2=0;
O_G2=0;
O_NF3=0;
O_A_hor3=0;
O_A_sch3=0;
O_A_vert3=0;
O_D3=0;
O_G3=0;
O_A_hor4=0;
O_A_sch4=0;
O_A_vert4=0;
O_D4=0;
O_G4=0;
O_NF5=0;
O_A_hor5=0;
O_A_sch5=0;
O_A_vert5=0;
O_D5=0;
O_G5=0;
O_A_hor6=0;
O_A_sch6=0;
O_A_vert6=0;
O_D6=0;
O_G6=0;
O_TempD=0;
O_TempH=0;

%Position sensor offsets
O_posA=-11.2; %Offset position sensor A [mm]
O_posB=-11.2; %Offset position sensor B [mm]
O_posC=-11.2; %Etc.
O_posD=-11.2;
O_posE=-11.2;
O_posF=-11.2;
O_posG=-11.2;
O_posMP=-28.125;

%Acceleration sensor offsets
%Bottom accelerometer sensor
O_raccxb=0;O_raccyb=0;O_racczb=0;O_gyrxb=0;
O_laccxb=0;O_laccyb=0;O_lacczb=0;O_gyryb=0;
O_angxb=0;O_angyb=0;O_angzb=0;O_gyrzb=0;
O_qwb=0;O_qxb=0;O_qyb=0;O_qzb=0;

O_raccxt=0;O_raccyt=0;O_racczt=0;O_gyrxt=0;
O_laccxt=0;O_laccyt=0;O_lacczt=0;O_gyryt=0;
O_angxt=0;O_angyt=0;O_angzt=0;O_gyrzt=0;
O_qwt=0;O_qxt=0;O_qyt=0;O_qzt=0;

%% Processing Strain gauges
%This part of the script processes the data in the sensor arrays to their
%actual values.

```

Figure D.5: Script that processes the the sensor signal into required output values, pt1.

```

%Process strain gauge values
%Sensor NF1 conversion:
S.NF1=zeros(length(SENSORS.NF1_mv),3);           %Create zero matrix to replace mV values to actual values
S.NF1(:,1)=SENSORS.NF1_mv(:,1).*C_time;         %Convert the time column to specified unit
S.NF1(:,2)=SENSORS.NF1_mv(:,2).*C_sg_fb+0_NF1;  %Convert unsigned sensor value to stresses [MPa]
S.NF1(:,3)=SENSORS.NF1_mv(:,3).*C_sg_fb+0_NF1;  %Convert signed sensor value to stresses [MPa]

%Sensor A_hor1 conversion:
S.A_hor1=zeros(length(SENSORS.A_hor1_mv),3);     %Create zero matrix to replace mV values to actual values
S.A_hor1(:,1)=SENSORS.A_hor1_mv(:,1).*C_time;   %Convert the time column to specified unit
S.A_hor1(:,2)=SENSORS.A_hor1_mv(:,2).*C_sg_r+0_A_hor1; %Convert unsigned sensor value to stresses [MPa]
S.A_hor1(:,3)=SENSORS.A_hor1_mv(:,3).*C_sg_r+0_A_hor1; %Convert signed sensor value to stresses [MPa]

%Sensor A_sch1 conversion:
S.A_sch1=zeros(length(SENSORS.A_sch1_mv),3);    %Create zero matrix to replace mV values to actual values
S.A_sch1(:,1)=SENSORS.A_sch1_mv(:,1).*C_time;  %Convert the time column to specified unit
S.A_sch1(:,2)=SENSORS.A_sch1_mv(:,2).*C_sg_r+0_A_sch1; %Convert unsigned sensor value to stresses [MPa]
S.A_sch1(:,3)=SENSORS.A_sch1_mv(:,3).*C_sg_r+0_A_sch1; %Convert signed sensor value to stresses [MPa]

%Sensor A_vert1 conversion:
S.A_vert1=zeros(length(SENSORS.A_vert1_mv),3);  %Create zero matrix to replace mV values to actual values
S.A_vert1(:,1)=SENSORS.A_vert1_mv(:,1).*C_time; %Convert the time column to specified unit
S.A_vert1(:,2)=SENSORS.A_vert1_mv(:,2).*C_sg_r+0_A_vert1; %Convert unsigned sensor value to stresses [MPa]
S.A_vert1(:,3)=SENSORS.A_vert1_mv(:,3).*C_sg_r+0_A_vert1; %Convert signed sensor value to stresses [MPa]

%Sensor D1 conversion:
S.D1=zeros(length(SENSORS.D1_mv),3);            %Create zero matrix to replace mV values to actual values
S.D1(:,1)=SENSORS.D1_mv(:,1).*C_time;          %Convert the time column to specified unit
S.D1(:,2)=SENSORS.D1_mv(:,2).*C_sg_fb+0_D1;    %Convert unsigned sensor value to stresses [MPa]
S.D1(:,3)=SENSORS.D1_mv(:,3).*C_sg_fb+0_D1;    %Convert signed sensor value to stresses [MPa]

%Sensor G1 conversion:
S.G1=zeros(length(SENSORS.G1_mv),3);           %Create zero matrix to replace mV values to actual values
S.G1(:,1)=SENSORS.G1_mv(:,1).*C_time;         %Convert the time column to specified unit
S.G1(:,2)=SENSORS.G1_mv(:,2).*C_sg_fb+0_G1;   %Convert unsigned sensor value to stresses [MPa]
S.G1(:,3)=SENSORS.G1_mv(:,3).*C_sg_fb+0_G1;   %Convert signed sensor value to stresses [MPa]

%Sensor A_hor2 conversion:
S.A_hor2=zeros(length(SENSORS.A_hor2_mv),3);    %Create zero matrix to replace mV values to actual values
S.A_hor2(:,1)=SENSORS.A_hor2_mv(:,1).*C_time;  %Convert the time column to specified unit
S.A_hor2(:,2)=SENSORS.A_hor2_mv(:,2).*C_sg_r+0_A_hor2; %Convert unsigned sensor value to stresses [MPa]
S.A_hor2(:,3)=SENSORS.A_hor2_mv(:,3).*C_sg_r+0_A_hor2; %Convert signed sensor value to stresses [MPa]

%Sensor A_sch2 conversion:
S.A_sch2=zeros(length(SENSORS.A_sch2_mv),3);    %Create zero matrix to replace mV values to actual values
S.A_sch2(:,1)=SENSORS.A_sch2_mv(:,1).*C_time;  %Convert the time column to specified unit
S.A_sch2(:,2)=SENSORS.A_sch2_mv(:,2).*C_sg_r+0_A_sch2; %Convert unsigned sensor value to stresses [MPa]
S.A_sch2(:,3)=SENSORS.A_sch2_mv(:,3).*C_sg_r+0_A_sch2; %Convert signed sensor value to stresses [MPa]

%Sensor A_vert2 conversion:
S.A_vert2=zeros(length(SENSORS.A_vert2_mv),3);  %Create zero matrix to replace mV values to actual values
S.A_vert2(:,1)=SENSORS.A_vert2_mv(:,1).*C_time; %Convert the time column to specified unit
S.A_vert2(:,2)=SENSORS.A_vert2_mv(:,2).*C_sg_r+0_A_vert2; %Convert unsigned sensor value to stresses [MPa]
S.A_vert2(:,3)=SENSORS.A_vert2_mv(:,3).*C_sg_r+0_A_vert2; %Convert signed sensor value to stresses [MPa]

%Sensor D2 conversion:
S.D2=zeros(length(SENSORS.D2_mv),3);            %Create zero matrix to replace mV values to actual values
S.D2(:,1)=SENSORS.D2_mv(:,1).*C_time;          %Convert the time column to specified unit
S.D2(:,2)=SENSORS.D2_mv(:,2).*C_sg_fb+0_D2;    %Convert unsigned sensor value to stresses [MPa]
S.D2(:,3)=SENSORS.D2_mv(:,3).*C_sg_fb+0_D2;    %Convert signed sensor value to stresses [MPa]

%Sensor G2 conversion:
S.G2=zeros(length(SENSORS.G2_mv),3);           %Create zero matrix to replace mV values to actual values
S.G2(:,1)=SENSORS.G2_mv(:,1).*C_time;         %Convert the time column to specified unit
S.G2(:,2)=SENSORS.G2_mv(:,2).*C_sg_fb+0_G2;   %Convert unsigned sensor value to stresses [MPa]
S.G2(:,3)=SENSORS.G2_mv(:,3).*C_sg_fb+0_G2;   %Convert signed sensor value to stresses [MPa]

%Sensor NF3 conversion:
S.NF3=zeros(length(SENSORS.NF3_mv),3);         %Create zero matrix to replace mV values to actual values
S.NF3(:,1)=SENSORS.NF3_mv(:,1).*C_time;       %Convert the time column to specified unit
S.NF3(:,2)=SENSORS.NF3_mv(:,2).*C_sg_fb+0_NF3; %Convert unsigned sensor value to stresses [MPa]
S.NF3(:,3)=SENSORS.NF3_mv(:,3).*C_sg_fb+0_NF3; %Convert signed sensor value to stresses [MPa]

%Sensor A_hor3 conversion:
S.A_hor3=zeros(length(SENSORS.A_hor3_mv),3);    %Create zero matrix to replace mV values to actual values
S.A_hor3(:,1)=SENSORS.A_hor3_mv(:,1).*C_time;  %Convert the time column to specified unit
S.A_hor3(:,2)=SENSORS.A_hor3_mv(:,2).*C_sg_r+0_A_hor3; %Convert unsigned sensor value to stresses [MPa]
S.A_hor3(:,3)=SENSORS.A_hor3_mv(:,3).*C_sg_r+0_A_hor3; %Convert signed sensor value to stresses [MPa]

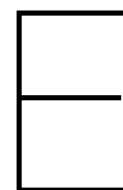
%Sensor A_sch3 conversion:
S.A_sch3=zeros(length(SENSORS.A_sch3_mv),3);    %Create zero matrix to replace mV values to actual values
S.A_sch3(:,1)=SENSORS.A_sch3_mv(:,1).*C_time;  %Convert the time column to specified unit
S.A_sch3(:,2)=SENSORS.A_sch3_mv(:,2).*C_sg_r+0_A_sch3; %Convert unsigned sensor value to stresses [MPa]
S.A_sch3(:,3)=SENSORS.A_sch3_mv(:,3).*C_sg_r+0_A_sch3; %Convert signed sensor value to stresses [MPa]

%Sensor A_vert3 conversion:
S.A_vert3=zeros(length(SENSORS.A_vert3_mv),3);  %Create zero matrix to replace mV values to actual values
S.A_vert3(:,1)=SENSORS.A_vert3_mv(:,1).*C_time; %Convert the time column to specified unit
S.A_vert3(:,2)=SENSORS.A_vert3_mv(:,2).*C_sg_r+0_A_vert3; %Convert unsigned sensor value to stresses [MPa]
S.A_vert3(:,3)=SENSORS.A_vert3_mv(:,3).*C_sg_r+0_A_vert3; %Convert signed sensor value to stresses [MPa]

%Sensor D3 conversion:
S.D3=zeros(length(SENSORS.D3_mv),3);            %Create zero matrix to replace mV values to actual values
S.D3(:,1)=SENSORS.D3_mv(:,1).*C_time;          %Convert the time column to specified unit

```

Figure D.6: Script that processes the sensor signal into required output values, pt2., rest is same for all sensors



Measurement results details

E.1. Introduction

In this appendix some additional and detailed data shall be presented. The different sections correspond to the different measurement phases as where explained in chapter 7 and 8. In this appendix, the following data is presented:

1. Section E.2, figure E.1: The measured and predicted penetration speed of the monopile with respect to the soil characteristic. Predictions were done by means of a vibro-drivability study performed by Allnamics. The soil characteristics have been obtained by a CPT.
2. Section E.3, figure E.2 through E.5: Settlement sensor and horizontal strain gauge response due to installation of different components. The settlement and increase in hoop stress is observed to be smoothly as each subcomponent gets installed. Only during the tower installation some irregular response can be seen. This was result of a minor complication as the tower needed to be lifted up and down again to secure the bolts on the slightly misaligned substructure. Also the accelerations in the lower tower due to the installation of the different components is presented in figure E.6.
3. Section E.4, figure E.7. Shows the additional stresses due to the extra settlement of the tower over the monopile during the operational period of the DOT500 project.
4. Section E.4, figure E.8 through E.11. Shows the statistical analysis of the dynamic stresses due to operational loads. Figure E.12 shows the stresses due to an operational thrust load, including vertical stresses.
5. Section E.4, figure E.13 through E.15. Shows the results of the three decay tests that have been performed to determine the damping.
6. Section E.5, figure E.16 through E.26: the acoustic measurement report that provides all the relevant theoretical background, results and conclusions of the acoustic measurement campaign.

E.2. Monopile installation

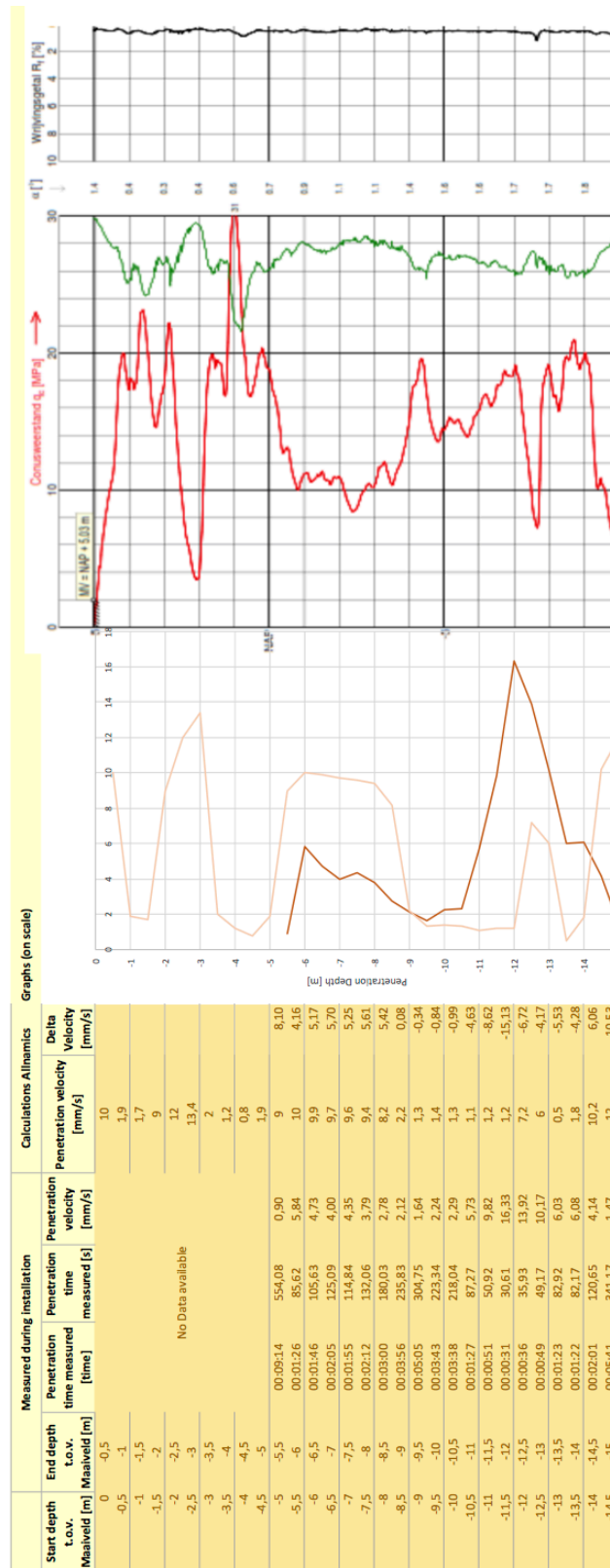


Figure E.1: Predicted and measured penetration speed in relation with soil characteristics

E.3. Slip-joint installation

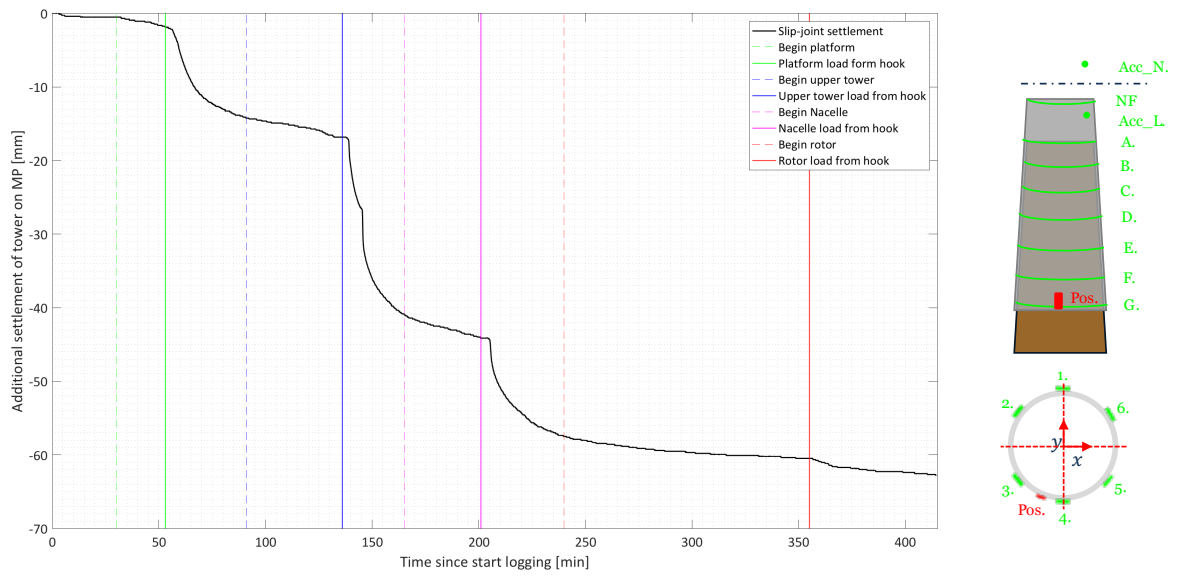


Figure E.2: Slip-joint settlement as result of different subcomponents installed

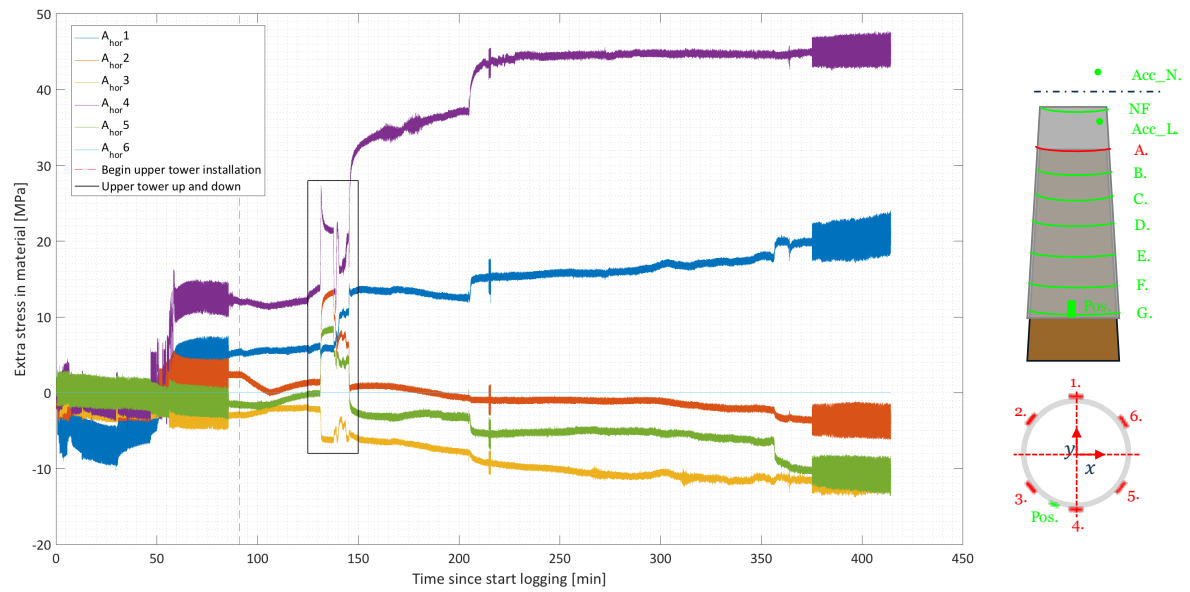


Figure E.3: Horizontal strain gauge ring A response as result of installation of subcomponents

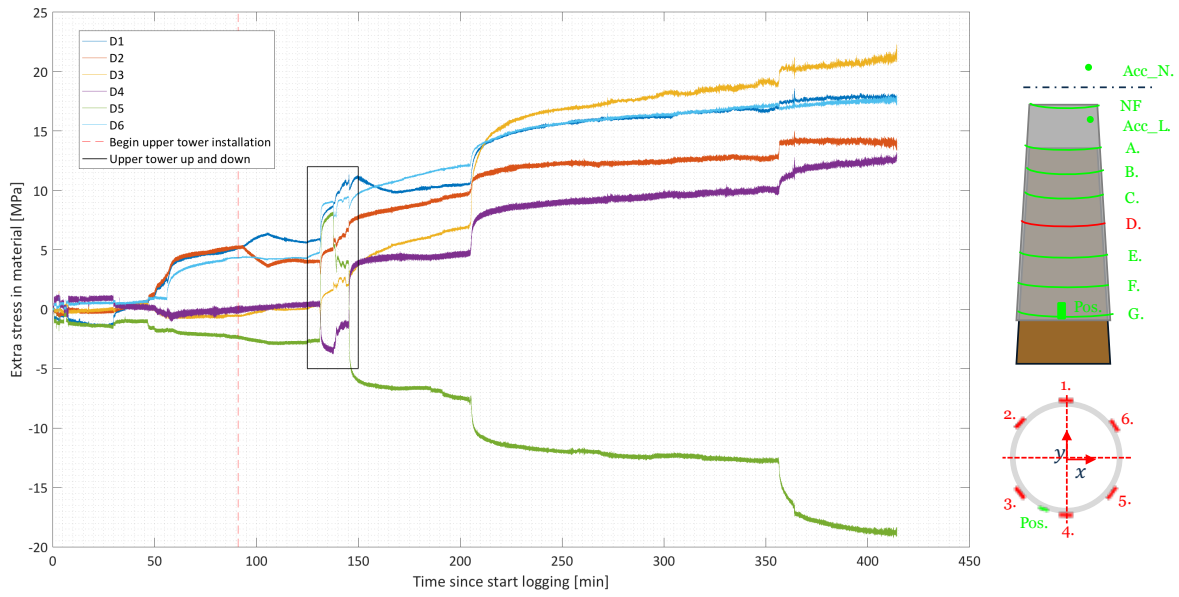


Figure E.4: Horizontal strain gauge ring D response as result of installation of subcomponents

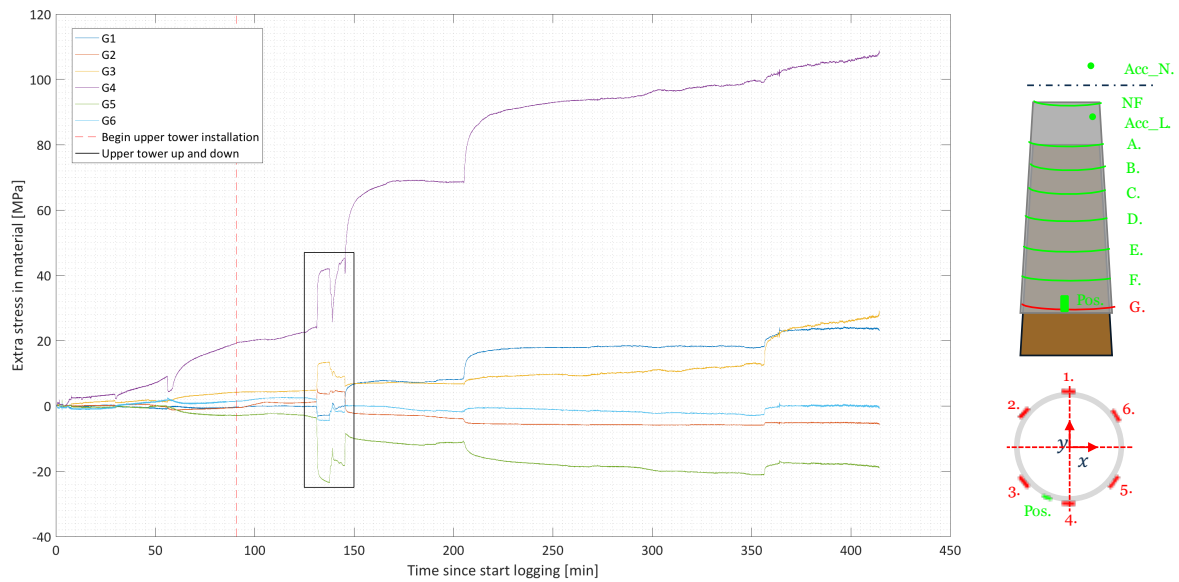


Figure E.5: Horizontal strain gauge ring G response as result of installation of subcomponents

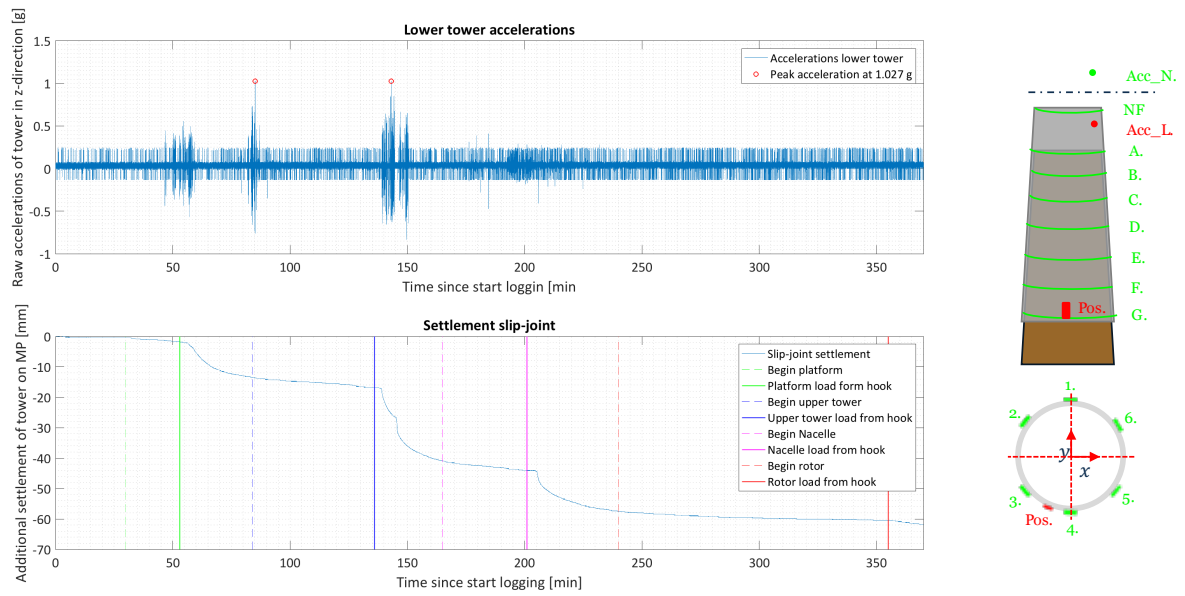


Figure E.6: Acceleration of slip-joint during installation of different subcomponents

E.4. Measurements during operation

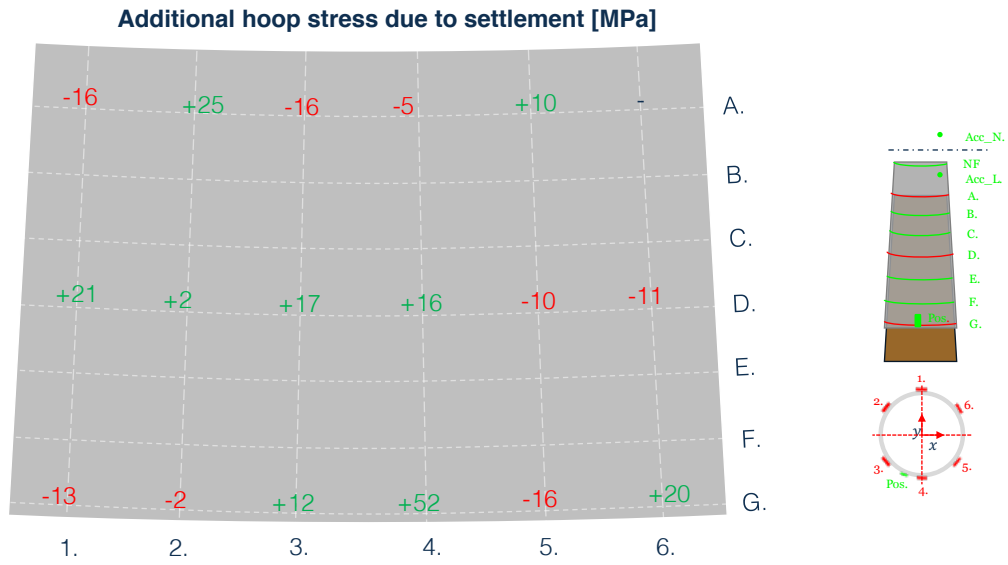


Figure E.7: Additional stresses due to settlement during operation interval

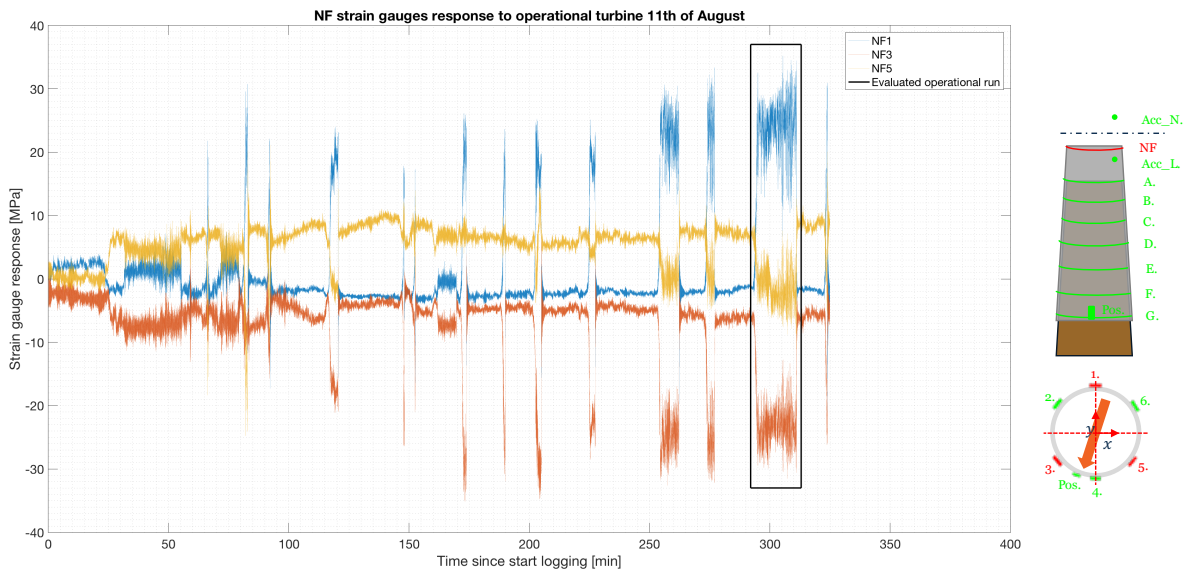


Figure E.8: Additional stresses due during operation interval on 11th of August

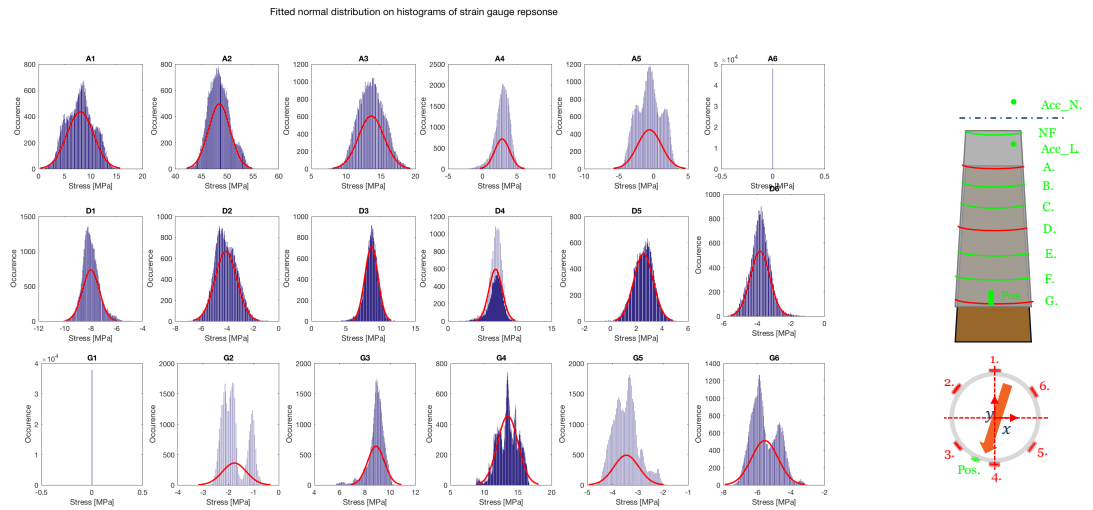


Figure E.9: Histogram and fitted normal distribution of additional stress due to operational interval on 11th of August

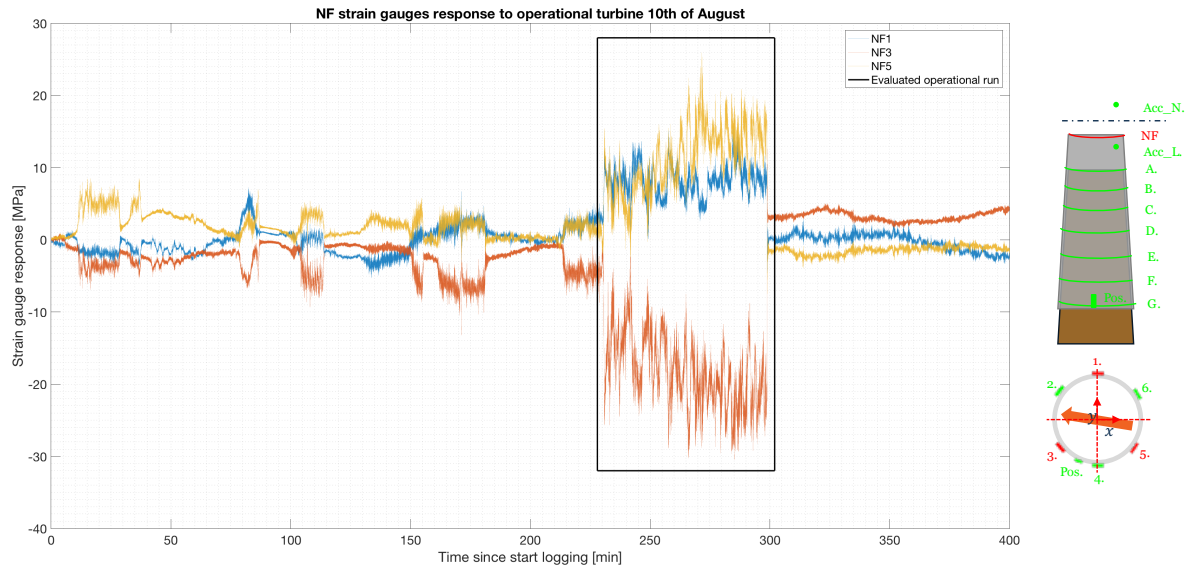


Figure E.10: Additional stresses due during operation interval on 10th of August

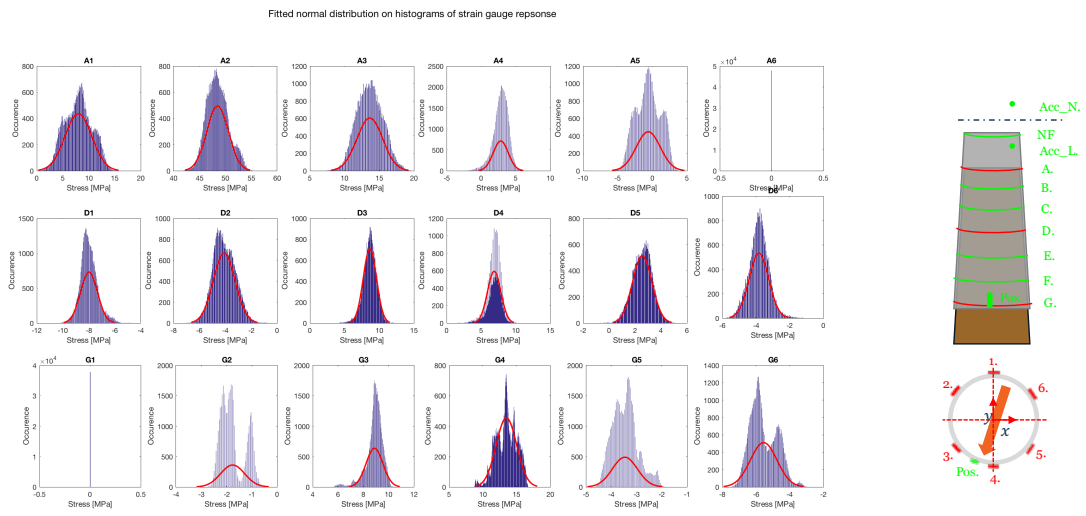


Figure E.11: Histogram and fitted normal distribution of additional stress due to operational interval on 10th of August

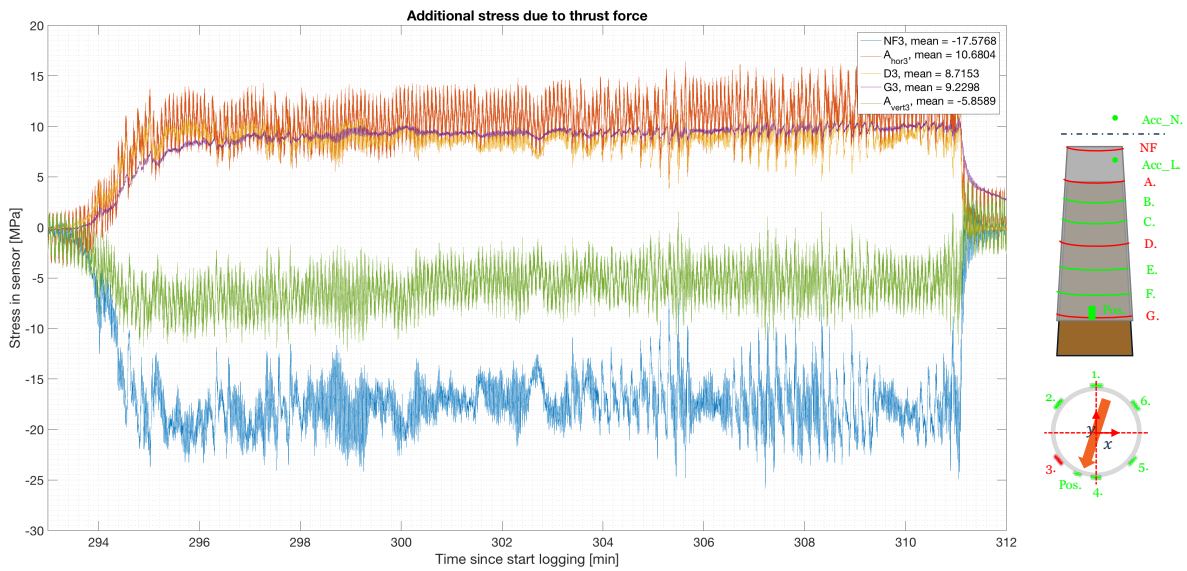


Figure E.12: Stresses within slip-joint as result of thrust force near rated conditions

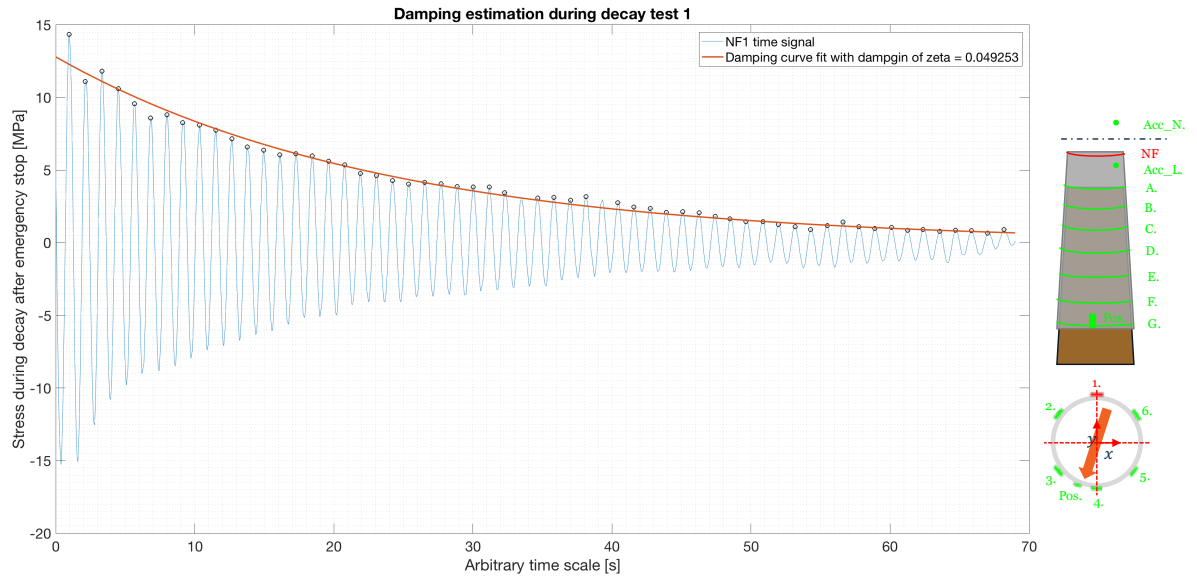


Figure E.13: Fitted exponential decay in structure's response after (emergency) stop to obtain the damping. Test 1

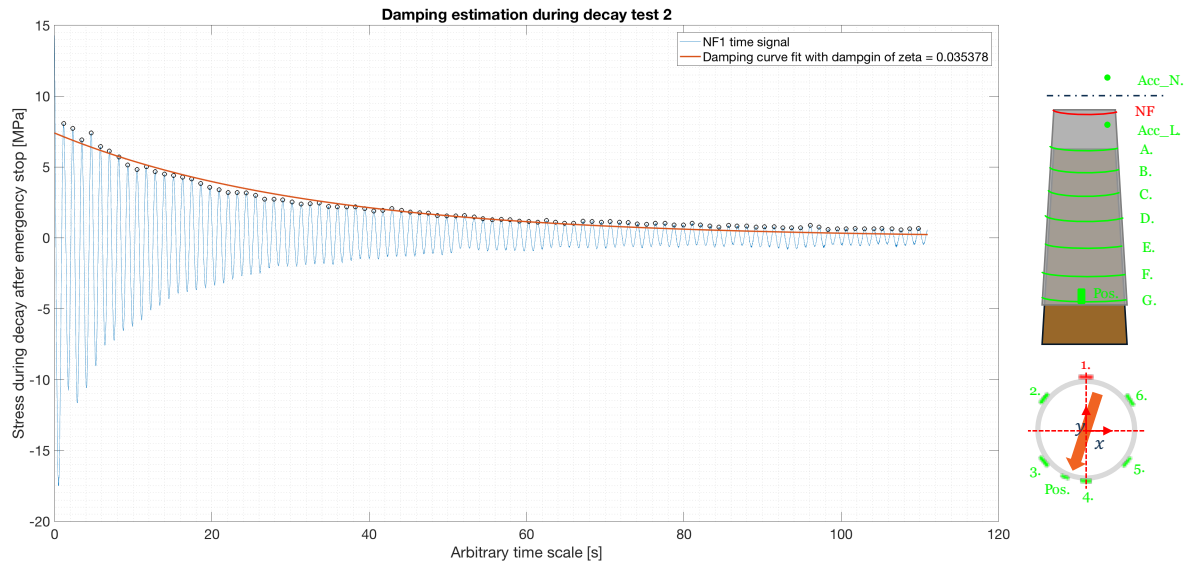


Figure E.14: Fitted exponential decay in structure's response after (emergency) stop to obtain the damping. Test 2

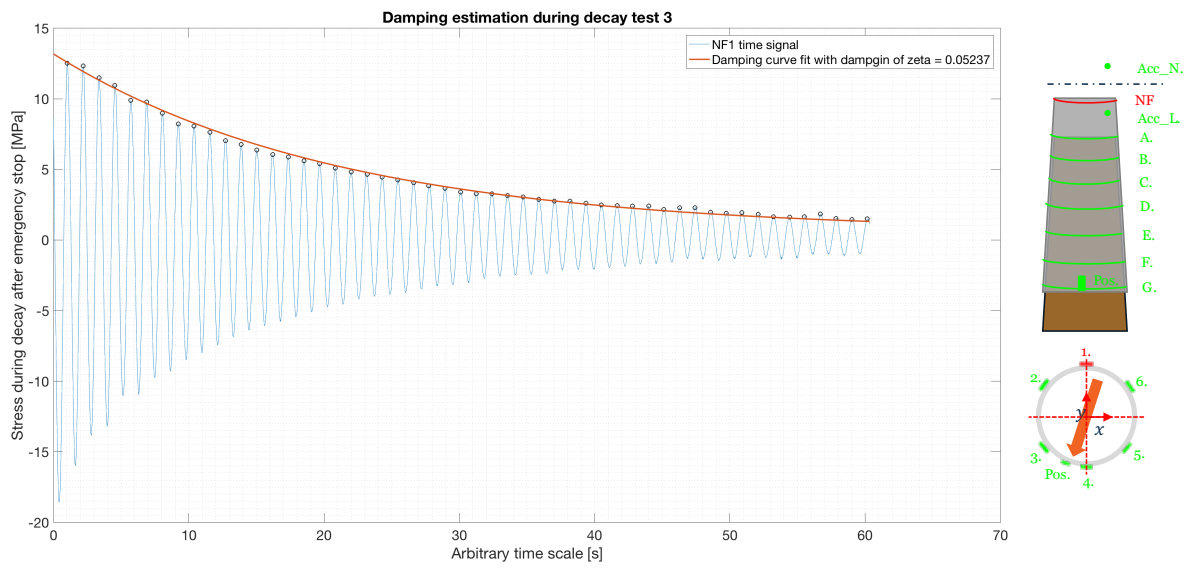


Figure E.15: Fitted exponential decay in structure’s response after (emergency) stop to obtain the dampging. Test 3

E.5. Acoustic measurement report



Acoustic measurement report

26-07-2016

T.P.J. Kamphuis

1 Introduction

As part of the MSc Thesis of Thijs Kamphuis an acoustic measurement was performed on two slip-joint connections. The first connection that has been tested was part of the wind turbine 'Duinvogel', which has been operational for about 20 years and was eventually decommissioned. The slip-joint section has been separated from the rest of the turbine and now lies on the Van Oord yard in Zuilichem, displayed in Figure 1. This test will be elaborated on in chapter 2.



FIGURE 1. SLIP-JOINT CONNECTION AT VAN OORD

Secondly, the slip-joint of the DOT wind turbine at the Maasvlakte II was tested. This slip-joint connects the operating DOT wind turbine to its foundation as displayed in Figure 2. This test will be elaborated on in chapter 3.



FIGURE 2. DOT SLIP-JOINT AT MAASVLAKTE 2

The goal of these measurement was to identify the global contact area of the two overlapping circular sections and get an indication whether there is full steel-steel contact as opposed to a non-contact area

Delft Offshore Turbine B.V.

Raam 180, 2611 WP Delft, The Netherlands

VAT NL 853 445 217 B01 | COC 59 370 114 | BANK NL 45 RABO 0195 2451 13

— PAGE 1



due to local non-linear deformations of any kind. Identifying these non-contact points is important to the structural integrity of the slip-joint as its stability greatly depends on frictional forces that are present between the two steel plates.

Ultrasonic pulses will be sent through the slip-joint and the difference in reflection coefficient from an air-steel transition as opposed to a steel-steel transmission could give a clue of the contact area of the slip-joint. This difference is to be expected since the acoustic impedance of air is far smaller than that of steel, resulting in a considerable difference in amplitude of the received sound wave that has travelled between the two media. The general principle of this measurement is explained in Figure 3.

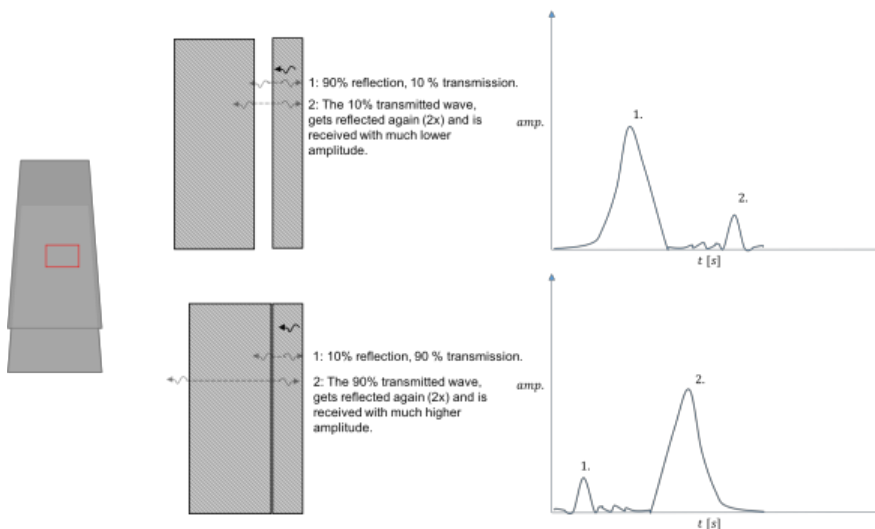


FIGURE 3. US MEASUREMENT PRINCIPLE

2 Measurements ‘Duinvogel’ slip-joint

2.1 Measurement 1: Individual plate wall thickness

First of all, the wall thickness of the individual plates was measured. This was done by means of a 2Mhz, 20mm pod. A contact fluid was applied on the location to be tested to secure a good contact between the pod and the steel. The wall thicknesses that were found are summarised in

Table 1 in rounded numbers. The plates sections that are in overlap at the actual slip-joint both have an equal wall thickness of 12mm.

Delft Offshore Turbine B.V.

Raam 180, 2611 WP Delft, The Netherlands

VAT NL 853 445 217 B01 | COC 59 370 114 | BANK NL 45 RABO 0195 2451 13

PAGE 2

Figure E.17: Acoustic report page 2



TABLE 1. WALL THICKNESSES SLIP-JOINT SECTIONS

Cone plate section	Wall thickness [mm]
1. "Male" cone	15
2. "Male" cone	12
3. "Female" cone	12



2.2 Measurement 2: Point measurements for contact area

The second part of the measurement was to try and measure the contact and non-contact areas of the slip-joint on individual points at the overlapping sections. A pod with a frequency of 2 MHz and 20mm pod diameter was used. First of all, the measurement was performed on the coated outer surface of the steel with use of the contact fluid. After that, the coating was removed at a couple of spots to perform the measurement directly on the blank steel. Measurements were taken both from the outside of the sections as well as from the inside. Figure 4 shows the performance of these measurements.



FIGURE 4. POINT CONTACT MEASUREMENTS

On all of the spots the US measurements showed distinct peaks at about 12mm wall thickness. Also, peaks at multiples of these, i.e. 24mm, 36mm, etc. were detected as can be seen in the right picture of Figure 4. Since the wall thickness of both plates of the slip-joint where 12mm, no real conclusions can be drawn from this measurement. The peak at 24mm could be a second reflection of the first 12mm plate as well as a reflection of the bottom of the second plate, i.e. a total wall thickness of 2 times 12mm. The difference in the first and second peak was not pronounced enough to conclude or exclude on any of the cases.

2.3 Measurement 3: Line measurements for contact area

The next part of the measurement was to perform the same acoustic measurements as in measurement 2, but now moving the pod while the measurement is ongoing. Several lines have been measured on different locations, both on the in- and outside of the slip-joint. Also, measurements have been

Delft Offshore Turbine B.V.

Raam 180, 2611 WP Delft, The Netherlands

VAT NL 853 445 217 B01 | COC 59 370 114 | BANK NL 45 RABO 0195 2451 13

— PAGE 3



performed on the coating as well as directly on the blank steel, including the use of the contact fluid. A pod with a frequency of 2 MHz and 20mm diameter was used.

The goal of this measurement was to observe the development of the reflection peaks at 12mm and 24mm. If the amplitude of the two peaks vary simultaneously with the same amplitude along the scanned line, one would expect no transmission from the first steel plate to the second. However, if the second peak, at 24mm, would increase in amplitude while the first peak, at 12mm, remains the same or even decreases than this would indicate a point of full contact. This is because the pod then receives more reflections at 24mm whilst receiving less reflections at 12 mm indicating that a higher portion of soundwave's energy has travelled through the two plates, implying a full contact. This is graphically displayed in Figure 5.



FIGURE 5. DIFFERENCE NON-CONTACT SITUATION (LEFT) VERSUS CONTACT SITUATION (RIGHT)

Figure 6 shows the execution of these measurements. Multiple locations on the slip-joint have been measured as well as a variety of pulse-frequencies and pod diameters, including:

- 4MHz, 10 mm
- 2 MHz, 10 mm and 20 mm
- 1 MHz, 20 mm

Delft Offshore Turbine B.V.

Raam 180, 2611 WP Delft, The Netherlands

VAT NL 853 445 217 B01 | COC 59 370 114 | BANK NL 45 RABO 0195 2451 13

PAGE 4



FIGURE 6. LINE MEASUREMENTS

During these measurements no significant increase in amplitude of the second peak and simultaneous remaining or decreasing amplitude of the first peak has been observed. Figure 7 shows a specific location that was tested where, judged by the eye, the plates go from non-contact to contact situation. Also at this location, no satisfying results have been detected.



FIGURE 7. NON-CONTACT TO CONTACT SITUATION

The two most plausible reasons for the non-satisfactory results are the following.

2.3.1 Loose connection

First of all, it must be noted that the slip-joint has been cut-out from the rest of the wind turbine tower structure as can be observed from the cutting marks at the edge of the cone in Figure 1. During this process the radial stiffness of the circular sections has been drastically decreased, making it easier to deform in the radial direction as a result of lifting and transportation loads. Due to these radial deformations, the radial forces between the two steel sections will decrease leading to a more loosened connection. This hypothesis is supported by the fact that the two conical sections of the slip-joint have been welded prior to transport, presumably because there was movement between the two cones.

Delft Offshore Turbine B.V.

Raam 180, 2611 WP Delft, The Netherlands

VAT NL 853 445 217 B01 | COC 59 370 114 | BANK NL 45 RABO 0195 2451 13

— PAGE 5



FIGURE 8. WELDS (ORANGE ARROWS) HOLD THE TWO SECTIONS TOGETHER

This loosened connection allows for small air layers between the two plates. Acoustic impedance, or specific acoustic impedance, is a measure of the opposition that a system has to the acoustic flow as a result of acoustic pressure. The absolute value of the specific acoustic impedance (z_0) is a function of the speed of sound (c) through, and density (ρ) of the specific material.

$$z_0 = c\rho,$$

Since air has a much lower density than steel and sound waves travel more slowly through air than through steel, the acoustic impedance of air is considerably smaller than that of steel, i.e. an approximate factor of $1e5$:

$$z_{0,air} = 340 \cdot 1.23 = 4.18e2 \left[\frac{Pa \cdot s}{s} \right], \quad z_{0,steel} = 6100 \cdot 7800 = 4.76e7 \left[\frac{Pa \cdot s}{s} \right],$$

$$\Delta z_0 = \frac{z_{0,steel}}{z_{0,air}} = 1.15e5$$

Due to the great difference in impedance, almost all of the sound waves will be reflected at the boundary of the two media [1]. Therefore, detecting sound waves that travel through both steel plates with a (small) air layer in between will be virtually impossible in practice as the detectable sound wave's amplitude is so drastically reduced. When the sound wave meets the boundary the particle velocity and local particle pressure must be continuous across this boundary. Using this interface condition in d'Alembert's solution for the pressure wave the reflection coefficient can be written in terms of the impedance of the different media as [2]:

$$R = \frac{p^-}{p^+} = \frac{\frac{Z_2}{Z_1} - 1}{1 + \frac{Z_2}{Z_1}}$$

Sound is measured in terms of intensity which has a cubic relation to the pressure, therefore the measurable reflection coefficient is:

$$R = \left(\frac{\frac{Z_2}{Z_1} - 1}{1 + \frac{Z_2}{Z_1}} \right)^2 = \frac{(Z_1 - Z_2)^2}{(Z_1 + Z_2)^2}$$

Filling in the specific acoustic impedance for the two media, steel and air, yields the following result:
 $R = 0.99996$, with $Z_{steel} = 4.76e7$, and $Z_{air} = 4.18e2$

Delft Offshore Turbine B.V.

Raam 180, 2611 WP Delft, The Netherlands

VAT NL 853 445 217 B01 | COC 59 370 114 | BANK NL 45 RABO 0195 2451 13

PAGE 6



This means that already at the first boundary, practically all the energy in the sound wave gets reflected.

2.3.2 Plate thicknesses

Secondly, the identical plate thicknesses of the two plates, 12mm, overlapping at the slip-joint create an extra uncertainty in the measurement. Even if a reflected sound wave that has travelled through the two plate sections was to be observed it will show a peak at the exact same location as a second reflection of a sound wave travelling through the first plate only. Adding the effect of item 1 makes it virtually impossible in this case to detect sound waves that have travelled through both plates.

3 Measurements DOT slip-joint

3.1 Measurement 1: Individual plate wall thickness

In the same way as the measurement at the Duinvogel slip-joint, the first step in the measurement was to identify the wall thicknesses of the individual steel plates that overlap at the slip-joint location. The measurement was done directly at the coated tower and the uncoated monopile with application of the contact fluid using a pod with a frequency of 2MHz and diameter of 20mm. The tower wall thickness was measured at a location where obviously no contact was made between the two steel plates as can be seen in Figure 9. The measured wall thicknesses can be found in Table 2. They are in accordance with the monopile specifications and previously measured wall thickness of the turbine tower.

TABLE 2. WALL THICKNESS OF SLIP-JOINT PLATE SECTIONS

Cone plate section	Wall thickness [mm]
1. "Male" cone	40
2. "Female" cone	15.5



FIGURE 9. WALL THICKNESS MEASUREMENT

3.2 Measurement 2: Contact area measurement

The next part of the measurement was to scan multiple lines along the slip-joint to try and get an indication of the contact and non-contact areas within the slip-joint. It is important to note at this point that the inside of the wind turbine tower has been equipped with a special kind of nylon-film layer, Micanti, to ease the removal process of the two steel sections, since the slip-joint will be reused for later purposes. The implication of this will be discussed later on.

Delft Offshore Turbine B.V.

Raam 180, 2611 WP Delft, The Netherlands

VAT NL 853 445 217 B01 | COC 59 370 114 | BANK NL 45 RABO 0195 2451 13

— PAGE 7



The measurement was performed at different locations on the slip-joint. These locations have been chosen using the strain gauge measurements. At locations where the strain gauges imply solid contact between the two plates, i.e. substantial hoop stresses, the US measurements were performed. A pod with a frequency of 2 MHz and 20mm diameter was used. The wall thickness of the first plate was 15.5mm, therefore peaks at around 15.5, 31, 46.5 and 62mm will be expected as these are first and higher order reflections of the first plate. If the acoustic wave transfers energy through both steel plates, i.e. full contact of the two steel plates, then a peak at around 55.5mm is to be expected and simultaneous lowering of the reflection peaks of the first plate, as graphically depicted in Figure 10. Figure 11 shows the execution of these measurements at the different locations.



FIGURE 10. CONTACT AREA INDICATION



FIGURE 11. EXECUTION OF CONTACT AREA MEASUREMENTS

During these measurements no significant peak was detected around the 55.5mm region. On some occasions, some small disturbances around the 55.5 mm region were detected, however these also showed up at the other locations between the peaks of the first plate reflection, between 15.5 and 31, etc. This means that these were not measured sound waves that travelled through both plates, but reflections due to a defect of some kind in the first plate. The two most probable reasons for this result will be explained in the subsequent sections.

Delft Offshore Turbine B.V.

Raam 180, 2611 WP Delft, The Netherlands

VAT NL 853 445 217 B01 | COC 59 370 114 | BANK NL 45 RABO 0195 2451 13



3.2.1 Not enough radial pressure

The most obvious reason for this unsatisfactory result again lies in the possibility of the presence of small air films between the steel and micanti layers. Although this slip-joint is connecting an operational turbine, the radial forces that are present might still be too small to eliminate any small air films between the two steel plates and the Micanti layer. However, this hypothesis cannot be confirmed or falsified since there is an extra uncertainty in the equation, the Micanti layer. This material also has quite an impedance difference compared to steel, which will be elaborated on in section 3.2.2.

To conclude on this matter with more certainty it is proposed to perform a small scale experiment. Two steel plates with different wall thicknesses must be pressed to each other with equivalent pressure that one will find in an operational slip-joint. An US measurement will be performed on these two steel plates. If there is still no transmission of sound wave energy to be detected it is safe to conclude that US measurement is not a reliable and effective way to measure the contact and non-contact area in a slip-joint connection.

3.2.2 Micanti layer

The second reasons for not measuring any transmitted waves through the steel plates can be found in the impedance difference between Micanti and steel. The density and speed of sound of Micanti have been obtained using the values for Nylon 6-6, $c_{nylon} = 2400 \frac{m}{s}$ and $\rho_{nylon} = 1.1 \frac{kg}{m^3}$ respectively. When applying the formulas explained in section 2.3.1 the values for the specific impedance for both Micanti and steel are:

$$z_{0,steel} = 4.76e7 \left[\frac{Pa \cdot s}{s} \right], \quad z_{0,micanti} = 2.64e3 \left[\frac{Pa \cdot s}{s} \right], \quad \Delta z_0 = \frac{z_{0,steel}}{z_{0,micanti}} = 1.80e4$$

This impedance difference results in the following reflection coefficient, according to section 2.3.1:

$$R = 0.999787$$

This means that practically all the energy of the sound wave gets reflection at the first boundary layer. So even if the radial pressure in this particular slip-joint was high enough to prevent any air films from existing between the boundary layers, the impedance difference between the Micanti and steel would still be considered too large to detect any portion of the sound wave that has travelled through both steel plates, with the Micanti layer in between.

This problem can theoretically be overcome by applying contact fluid between these impedance mismatching materials, effectively reducing the impedance mismatch. Therefore, a piece of Micanti was soaked in the contact fluid and applied with firm pressure on the outer wall of the tower, as can be seen in Figure 12. In this manner, it was possible to measure transmitted sound waves through the Micanti and the first steel plate. Conclusively, if the impedance mismatching boundary layers, in this particular case Micanti and steel, are lubricated with the contact fluid it is possible to measure through the different layers.

Delft Offshore Turbine B.V.

Raam 180, 2611 WP Delft, The Netherlands

VAT NL 853 445 217 B01 | COC 59 370 114 | BANK NL 45 RABO 0195 2451 13

— PAGE 9



FIGURE 12. MICANTI MEASUREMENT

4 Conclusion

An acoustic measurement has been performed on the Duinvogel slip-joint as well as the DOT500 slip-joint to try and get an idea of contact- and non-contact areas within a slip-joint connection. In order to do so, the wall thicknesses of the individual plates have been measured, furthermore the US sound wave's amplitude and development of this amplitude along the slip-joint have been observed.

It was not possible to conclude on contact or non-contact areas within the slip-joint as no satisfactory results have been obtained in the measurements. No contact areas, as defined in section 1, have been detected. It is highly unlikely that this means there is no contact at all between the plates, since the DOT500 slip-joint actually supports an operational wind turbine, meaning that there is enough contact between the plates to generate sufficient friction for a stable connection. Therefore, the reason for this unsatisfactory result must lie somewhere else.

At the Duinvogel slip-joint one of the possible reasons to this was found to be the equivalent wall thicknesses of both plates within the slip-joint. This problem was not present in the measured at the DOT500 slip-joint. However, the DOT500 introduced another complication, namely a small Micanti layer between the two steel plates with a high impedance mismatch to steel.

The most important learnings concern radial force, i.e. pressure between the steel plates, as well as impedance matching:

1. Sufficient radial force and thus pressure between the two plates is of utmost importance. This decreases the possibility of small films of air between the two conical sections, eradicating the effect of impedance mismatch between air and steel. Future studies should indicate how small this air layer must be, i.e. how high the pressure between the steel plates must be, in order to transmit enough energy through the steel plates. Moreover, a small scale experiment is proposed to simulate typical slip-joint pressure and see if this is enough for the US measurement to be effective.

Delft Offshore Turbine B.V.

Raam 180, 2611 WP Delft, The Netherlands

VAT NL 853 445 217 B01 | COC 59 370 114 | BANK NL 45 RABO 0195 2451 13

PAGE 10



2. Impedance matching is crucial factor in order to transmit enough energy through boundary layers of materials with varying density and speed of sound. The most obvious impedance difference being that of air and steel in the form of the presence of small air films between the steel plates as discussed above. It has been proven that by applying contact fluid between these boundary layers, i.e. effectively reducing the impedance mismatch, it is possible to transmit enough energy through the two layers to measure contact or non-contact areas.

5 References

[1] A. Coppins, A. Frey, L. Kinsler, J. Sanders, (2000). *Fundamentals of Acoustics*. New York: John Wiley & Sons, Inc.

[2] A.V. Metrikine, A.C.W.M. Vrouwenvelder, (2005). *Structural Dynamics; Part 2: Wave Dynamics*. Lecture Notes CT 4140. Delft: Delft University of Technology.

Delft Offshore Turbine B.V.

Raam 180, 2611 WP Delft, The Netherlands

VAT NL 853 445 217 B01 | COC 59 370 114 | BANK NL 45 RABO 0195 2451 13

— PAGE 11

Figure E.26: Acoustic report page 11

Bibliography

- [1] 4COffshore. London array offshore wind farm, 2016. URL <http://www.4coffshore.com/windfarms/london-array-united-kingdom-uk14.html>.
- [2] 4COffshore. Vindeby offshore wind farm, 2016. URL <http://www.4coffshore.com/windfarms/vindeby-denmark-dk06.html>.
- [3] API. *Recommended Practice for Planning, Designing and Constructing Fixed Offshore Platforms—Working Stress Design*. American Petroleum Institute, America, 2000.
- [4] M.C.M. Bakker. *Measurement technique for materials and structures*. TU Delft, 2006.
- [5] A. Betz. *Das maximum der theoretisch möglichen Auswendung des Windes durch Windmotoren Zeitschrift für gesamte Turbinewesen*. Germany, 1920.
- [6] J.E. Bowles. *Foundation Analysis and Design*. McGraw-Hill, Columbus, United States of America, 2001.
- [7] NDT Research center. Eddy currents, 2014. URL <https://www.nde-ed.org/EducationResources/HighSchool/Electricity/eddycurrents.htm>.
- [8] S.K. Chakrabarti. *Hydrodynamics of Offshore Structures*. Computational Mechanics Publications, Southampton, United Kingdom, 1987.
- [9] Dirac Delta Consultants. Friction. URL <http://www.diracdelta.co.uk/science/source/f/r/friction/source.html#.V8gIOWW7DgI>.
- [10] K. Davids. Successful and failed transitions. a comparison of innovations in windmill technology in britain and the netherlands in the early modern period. Article, June 2008.
- [11] N.F.B. Diepeveen. *On Fluid Power Transmission in Offshore Wind Turbines*. PhD thesis, Delft University of Technology, August 2013.
- [12] DNV. *Foundations - Classification notes NO. 30.4*. Det Norske Veritas, Norway, 1992.
- [13] DNV. *Fabrication and testing of offshore structures*. Det Norske Veritas, Norway, 2010.
- [14] DNV. *Fatigue Design of Offshore Steel Structures*. Det Norske Veritas, Norway, 2011.
- [15] DNV. *Design of Offshore Wind Turbine Structures*. Det Norske Veritas, Norway, 2014.
- [16] M.L.A. Segeren E. Lourens. Investigation of a slip joint connection between the monopile and tower of an offshore wind turbine. Paper, 2013.
- [17] A.C.W.M. Vrouwenhelder E.C. Klaever, J.M.J. Spijkers. *Structural Dynamics; Part 1: Structural Vibrations. Lecture Notes CT 4140*. Delft University of Technology, Delft, the Netherlands, 2005.
- [18] Hasselmann et al. Measurements of wind wave growth and swell decay during the joint north sea wave project deutsche hydro. Article, 1973.
- [19] EWEA. The european offshore wind industry - key trends and statistics 2015. Article, February 2016.
- [20] GL. *Guideline for the Certification of Offshore Wind Turbines*. Germanischer Lloyd, Germany, 2012.
- [21] K.W. Hermans. Slip-joint experimental set-up, October 2013.

- [22] L. H. Holthuijsen. *Waves in Oceanic and Coastal Waters*. Cambridge University Press, New York, United States of America, 2007.
- [23] IEA. Projected cost of generating electricity. Article, August 2015.
- [24] IEA. World energy outlook 2015 factsheet. Article, November 2015.
- [25] IEA. Key world energy statistics. Paper, 2015.
- [26] ISO. *ISO 19902 - Petroleum and natural gas industries – Fixed steel offshore structures*. International Organization for Standardization (ISO), Germany, 2007.
- [27] B. Lutje Schipholt J. van der Tempel. The slip-joint connection - alternative connection between pile and tower. Paper, October 2003.
- [28] P.K. Robertson K.L. Cabal. Estimating soil unit weight from cpt. Paper, 2010.
- [29] H.K.T. Kuijper. *Probabilities in Civil Engineering, Part 1: Probabilistic Design in Theory*. Stichting CUR, Gouda, the Netherlands, 1997.
- [30] et al. L. Arany. Dynamic soil-structure interaction issues of offshore wind turbines. Paper, July 2014.
- [31] W.J. Pierson L.A. Moskowitz. A proposed spectral form of fully developed wind seas based on the similarity theory of s.a. kitaigorodshii, j. geophys. Article, 1964.
- [32] R. Sharma M. Bansal, P. Grover. Performance evaluation of butterworth filter for signal denoising. Paper, December 2010.
- [33] P. W. Mayne. Cone penetration testing state-of-practice. Paper, February 2007.
- [34] M.A. Miner. Cumulative damage in fatigue trans. Article, 1945.
- [35] K.W. Hermans M.L.A. Segeren. Experimental investigation of the dynamic installation of a slip joint connection between the monopile and tower of an offshore wind turbine. Paper, 2014.
- [36] OceanWeatherInc. Hindcast approach, 2001. URL <http://www.oceanweather.com/research/HindcastApproach.html>.
- [37] S.A. Hughes PhD. Scour and scour protection. Report.
- [38] Inc. Poly-Tech Industrial. Nylon 6/6 (polyamide), 2011. URL <http://www.polytechindustrial.com/products/plastic-stock-shapes/nylon-66>.
- [39] et al. T. Burton. *Wind Energy Handbook*. John Wiley & Sons Ltd, England, 2001.
- [40] UNFCCC. United nations framework convention on climate change, May 1992. URL http://unfccc.int/essential_background/convention/status_of_ratification/items/2631.php.
- [41] UNFCCC. Adoption of the paris agreement, December 2015. URL <http://unfccc.int/resource/docs/2015/cop21/eng/109r01.pdf>.
- [42] Brown University. Review of forces and moments. Excerpt, 2014.
- [43] J. van der Tempel. *Design of Support Structures for Offshore Wind Turbines*. PhD thesis, Delft University of Technology, April 2006.
- [44] V. van Geffen. A study of friction models and friction compensation. Report, December 2009.
- [45] Jan. H. Vugts. *Handbook of Bottom Founded Offshore Structure*. Eburon Academic Publishers, Delft, the Netherlands, 2013.
- [46] J.D. Wheeler. Method for calculating forces produced by irregular waves. Article, 1970.
- [47] J. Wieringa. Gust factor over open water and built-up country boundary layer meteorolog. Article, March 1973.